A cryogenic buffer-gas cooled beam of barium monohydride for laser slowing, cooling, and trapping

Geoffrey Zerbinatti Iwata

Submitted in partial fulfillment of the
requirements for the degree of
Doctor of Philosophy
in the Graduate School of Arts and Sciences

Columbia University
2018

ABSTRACT

A cryogenic buffer-gas cooled beam of barium monohydride for laser slowing, cooling, and trapping

Geoffrey Zerbinatti Iwata

Ultracold molecules promise a revolutionary test bed for quantum science with applications ranging from experiments that probe the nature of our universe, to hosting new platforms for quantum computing. Cooling and trapping molecules in the ultracold regime is the first step to unlocking the wide array of proposed applications, and developing these techniques to control molecules is a key but challenging research field. In this thesis, we describe progress towards a new apparatus designed to cool and trap barium monohydride (BaH), a molecule that is amenable to laser cooling and has prospects as a precursor for ultracold atomic hydrogen. The same complexity that makes molecules interesting objects of study creates challenges for optical control. To mitigate some of these challenges, we first cool the molecules using cryogenic techniques and technologies. Our apparatus uses a cryogenic buffer gas to thermalize BaH within a contained cell. The molecules are extracted into a beam with millikelvin transverse temperature, and forward velocities <100 m/s. The BaH beam in this work is the brightest hydride beam to date, with molecule density and kinetic characteristics well suited for laser cooling and trapping.

This thesis presents preliminary studies of BaH's suitability for laser cooling, details of the design and construction of our molecular beam source, experiments that uncover the hyperfine properties of the molecules, and describes ongoing work for laser slowing, cooling, and trapping of the molecules. Finally, we discuss the possibility of using our molecules to create trapped ultracold atomic hydrogen – a long-standing goal of atomic, molecular, and optical physics.

Contents

Acknowledgments

I was once told that graduate school is where you learn how little you really know, and indeed, there is a quote that has been on my mind as I write this thesis,

"An expert is one who knows more and more about less and less until he knows absolutely everything about nothing." - Nicholas Bulter

When I first visited Columbia back in 2012 during visit week, I grabbed an everything bagel from Absolute Bagels on my way to my appointment at the Zelevinsky lab, and finished just a few moments before meeting with Chris Osborn and Mickey McDonald, the two graduate students working there. Some combination of the delicious bagel and Mickey and Chris's enthusiasm for the work they were doing was entirely thrilling to me, filling me with the sense of great curiosity and wonder at the science of ultracold molecules. Seeing them bounce around the lab, showing me the immensely complicated apparatus around creating ultracold strontium dimers, and the novel experiments they were attempting, cemented in my mind that I too wanted to be in this burgeoning new field.

Now, five and a half years later, I find myself still excited at the prospect of controlling molecules. Professor Tanya Zelevinsky gave me the opportunity to work on that Sr experiment that ignited my interest, at a particularly productive and exciting time to contribute. Soon after, she entrusted me with the reigns on designing and constructing a brand new experiment, on which this thesis is based. I am so grateful to have had these two experiences. Working with molecules has given me a deep appreciation for how much you can study and

still be absolutely baffled by nature. Building a new experiment requires more foresight and patience than I may have had when I entered graduate school, but I am proud of the work that we have accomplished, and I look forward with the confidence to approach and tackle any scientific challenges ahead.

That being said, these past years would not have been possible without some very special people.

In my first years in the lab, I had the privilege of working alongside Mickey McDonald, a fellow graduate student, who taught me many basic lab skills (and lab expressions "beast factor?"), and was always there to bounce fun ideas off. His determination and ingenuity took the Sr experiment to incredible places under his stewardship as the senior grad student. His positivity and work ethic are infectious, and made taking data late into the night something to look forward to. He also is an incredible musician, and I encourage you to look him up on iTunes!

Marco Tarallo joined the lab as a post-doc just as we began to start thinking about a new experiment. Marco has a immense knowledge of many fields of physics, and his expertise led the way for my stumbling in the dark. As long as he wasn't streaming Italian soccer games, Marco was dedicated to the experiment and as a mentor to me. Almost all the stories I can think of about Marco involve inappropriate Italian phrases that would make my mother upset, but suffice to say that for the two years working with him, it felt as though I was working alongside a true friend. His input in almost every aspect of the design has surely avoided so many pitfalls down the line.

Alongside Marco, Bart McGuyer was another post-doc who would cheerfully and patiently explain concepts over and over again to me. Bart's meticulousness, good humor, and incredible knowledge of physics helped me understand countless mysteries I could not figure out alone. I also want to thank him for teaching me how to play with high voltage (somewhat safely).

While Rees joined the lab less than two years ago, he has learned the BaH remarkably quickly, leaving me sure that the experiment is in great hands moving forward. His experimental skills have helped bring the apparatus to a new level of sophistication and technical excellence, and I appreciate his willingness to take risks and implement all sorts of new ideas. Rees has also made the frustration that is synonymous with molecular experiments, a lot more bearable - forever will BaH have a funk and hip-hop soundtrack in my mind.

Damon Daw and Cole Rainey, undergrads while working with us, gave so much time and effort to understand and contribute to our experiment, providing valuable electronics and machining of various parts.

There are so many members of ZLab who need to be thanked for their hard work and attitude that has made it a joy to work alongside. Post-doc Andrew Grier joined ZLab for a short year, but left a strong impression on me as just about the most humble and soft-spoken damn good physicist around. Chih-Hsi Lee, Stan Kondov, and Kon Leung have upgraded the Sr experiment to new and exciting heights - their dedication and seemingly weekly discoveries are inspirational to what we could achieve in our experiment. Konrad Wenz has always been willing to lend his valuable time whenever I needed a helping hand to lift the absurdly heavy parts of our cryostat into place.

Fabian Sorenson and Florian Apfelbeck, visiting Masters' students from Germany, put in immense effort to accomplish incredible progress within a year. I look forward to seeing them both next year! I also need to thank Fabian for helping me find a special drink on a certain night. For three successive summers we had students visiting from French universities: Katerina Vertelesky, Leila Abbih, and Paul Pouyanne all constructed external cavity diode lasers with amusing names.

All the wonderful science that has been possible is due to Professor Tanya Zelevinsky, who has fostered an atmosphere of passion for excellent experiments. Tanya's guidance and expertise has truly formed me into the scientist I am today. She offered me an incredible

idea for an experiment, and I am so grateful that she entrusted us with so much freedom to design the experiment as we saw fit, to learn from our mistakes and encourage our successes.

The supporting staff of the physics department also deserve great thanks for their work - without them, none of this could be possible. Specifically, George Leou, Nelson Rivera, and Michael Adan have all helped out at various points to offer advice, encouragement, and their respective expertise to make this work feasible.

I also want to thank Dave Patterson and Nick Hutzler for some extremely helpful email correspondence early on, that helped get the project off the ground and avoid some serious mistakes.

Thank you to my parents, who have always driven me to pursue that which I love doing. They have always been a source of unwavering love, guidance and support, as I move farther and farther from home. I know how hard you have worked to give me the opportunity to pursue and study what I want, and I have felt invincible in the face of challenges knowing that I will always have your wisdom and love to guide me through.

Thank you to my friends in New York City who have listened to my ramblings and musings and kept my spirits high. I couldn't have maintained my optimism and sense of purpose without them in my life.

Most importantly, I owe gratitude to Lyka Sethi. We started dating before I began graduate school, and you have given me love and strength throughout this half-decade endeavor. With a patient heart and a clear mind, you have constantly encouraged and supported me through the highs and inevitable lows of graduate school, and words cannot express the gratitude I have for you. From late night Chinese take-out to 5-star feasts at New York's finest; from autumn walks along Riverside park to 2AM dollar-pizza slices; from dates in Cold Spring to getting married at City-Hall this year; you have made graduate school some of the best years of my life, full of love, excitement, curiosity, and bagels. While physics may be my obsession in life, Lyka, you are the passion that makes it all worthwhile.

To my patient and loving Lyka, without whom my sanity would surely be far from my mind.

Chapter 1

Introduction

1.1 Ultracold Molecules: A New Laboratory for Quantum Science

With the recent achievement of laser cooling and trapping of two species of diatomic molecules (CaF and SrF) in a three dimensional magneto-optical trap (MOT) [1–3], ultracold science is ready to explore a world beyond atoms. Ultracold atoms remain incredibly fruitful in expanding numerous fields and new applications, reaching unprecedented precision in optical clocks [4], as test beds of quantum simulations in quantum gas microscopes [5, 6], spearheading the understanding of Fermi liquids [7] and Bose condensates [8, 9] - the list goes on, certain to interest scientists from all fields. The study of ultracold molecular gases is a natural place to extend the methods and expertise amassed over the last 25 years; the greater complexity and chemical diversity in molecular systems offer unique directions of study. The applications include controlled, coherent, ultracold chemistry [10, 11], quantum information processing and computing [12], studies of dipolar physics and condensed matter systems [11–13], understanding of astrophsyical spectroscopy [14–16], and fundamental precision measurement [12, 17]. Many of these applications are being explored with new

experiments that complement the physics probed in ultracold atomic experiments. Furthermore, as experimentalists rapidly overcome the technical challenges associated with taming molecules, experiments that aim to cool and trap polyatomic molecules are already underway [18–20], paving the way for truly bridging the fields of physics and chemistry.

In this thesis, we discuss the design and construction of a new apparatus (Figure 1.1) for creating a trapped sample of an ultracold diatomic molecule, barium monohydride (BaH). This new apparatus contributes to the broader field by advancing cooling techniques for molecules, offering chemical diversity in studies of ultracold dipolar quantum gases, and establishing a novel technique to access ultracold samples of hydrogen.

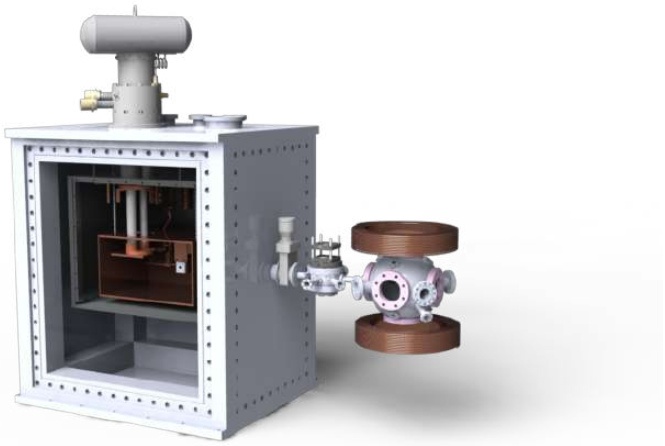

Figure 1.1: 3D rendering of the barium monohydride cooling and trapping apparatus, showing a cryogenic source region, diagnostic region, and proposed magneto-optical trapping chamber.

Systematic effects in measurements of trapped, ultracold molecules and atoms are either strongly suppressed or well characterized, making these systems ideal for precision measurements and tests of fundamental physics. Compared to atoms, molecules have new mechanisms governing their internal motion, such as the vibration and rotation modes. This difference means that precision measurements of transitions between the internal states of molecules are sensitive to different physics than analogous measurements in atoms, opening

up new directions for precision science. Examples include the study of subradiant states, arising from the symmetry in homonuclear molecules [21], or studies of violations of fundamental symmetries such as parity or time-reversal, enhanced due to the sensitivity of molecular transitions to nuclear effects [22,23]. Even comparisons between electronic and vibrational transitions in a molecular clock probe different fundamental interactions, enabling precision tests of possible time-variation of fundamental constants [24, 25].

Another prominent example is the measurement of the electron's electric dipole moment (EDM) - which would constrain theoretical extensions to the Standard Model (SM) [26, 27]. The sensitivity of this measurement is greatly enhanced in polar molecules versus atoms, due to the very large internal fields in molecules [28]. Additionally, some molecules allow for an effective field reversal simply by state selection - an immense benefit for canceling out systematic effects [29]. Experiments with YbF, PbO, and ThO have already provided some of the tightest constraints [17, 29, 30], while further experiments are underway with YbF, TlF, [23, 31] and even triatomic YbOH [20].

These ensembles of polar molecules could also offer fascinating insights into strongly interacting gases, since the dipole-dipole interaction is both long range and anisotropic [11]. These forces govern many fundamental interactions such as van der Waals forces [32–34], collisional dynamics in few-body systems [12], many-body radiative heat transfer [33, 35], and Rydberg blockade [36,37], and have been proposed as the basis for quantum information protocols [38,39]. Molecules are particularly well suited to study these types of interactions because they have tunable experimental parameters not found in neutral atoms: the electric dipole moment can be induced by DC or AC electric fields, and thereby coupled to individual rotational states within the molecule, allowing the experimenter to effectively tailor dipole-dipole interactions to be short or long range [40].

While molecules may be an attractive playground for study, the same complexity that offers such new possibilities also presents significant challenges to production and quantum

control. However, overcoming the challenges presented by the complexities in molecules offers an opportunity to extend a more powerful and broader toolbox to cooling an array of quantum objects from atoms and diatomic molecules, to polyatomic molecules and ions.

So far, there have been two main approaches to creating ultracold ensembles of molecules, both of which have enjoyed considerable success and are useful for quantum control experiments because molecules are formed with μK energies.

1.1.1 Ultracold Molecules from Ultracold Atoms

In the first technique, external fields are used to combine ultracold atoms into molecules. For this to happen, the scattering length between trapped ultracold atoms is tuned using magnetic fields so that the atoms pass through a so called Feshbach resonance, where a bound molecular state energy of the atoms is tuned by the external field to match the scattering energy. By ramping the external field slowly across the resonance, atoms are adiabatically converted into molecules [41]. The Feshbach resonance technique has been employed with great success to make a variety of ultracold molecules [42–46].

A closely related process to Feshbach resonances is photoassociation, where two colliding atoms are illuminated by a photon and form an excited, bound molecule, where the energy of the molecular bound state is the sum of the kinetic energy of the colliding atoms and the photon energy [47]. The resulting excited molecule can then emit another photon, and either dissociate back into two atoms, or in some special cases, fall into the lower energy molecular ground state. In addition to studying BaH, our lab employs this technique in a $^{88}Sr_2$ experiment with high efficiency, where ultracold Sr atoms are trapped in a 1D optical lattice and photoassociated into an electronically excited vibrational state, from where they rapidly decay into excited vibrational levels in the electronic ground state. The molecules are trapped in the optical lattice, where they enjoy long lifetimes for precision spectroscopy [48]. Photoassociation has had considerable success for molecules that do not

have readily accessible Feshbach resonances [48–51].

1.1.2 Direct Cooling

The second approach to creating an ultracold ensemble is through direct cooling and trapping of molecules using a combination of technologies. In some ways, this approach is more broadly applicable, since it is not constrained to constituent atoms that can be laser cooled. To achieve the same level of quantum control in the high phase space density regime, this technique ultimately relies on optical methods.

The same complexity that leads to the richness of molecular structure also creates daunting challenges for laser cooling and trapping, which relies fundamentally on the ability to cycle many photons on a single atom or molecule. At first glance, molecules seem to be far less amenable to optical cooling methods, since more degrees of freedom means more states, including those without strict selection rules. These factors make it practically impossible to find a truly closed, two-level system. Yet we will see that there are a number of diatomic molecules, and even polyatomic ones, which are quasi-closed, requiring the addition of one or two extra lasers to close any losses [15]. The advent of diode laser technology has made adding two, three or even more lasers far more palatable, and taming the molecule is becoming more a technical challenge than a fundamental roadblock.

Nevertheless, optical slowing of molecules from oven temperatures requires hundreds of thousands of photon cycles, and the number of molecules remain at the end of a slowing and cooling experiment would be unworkable, due to 'leaks' to unaddressed states. Therefore, the approach is to utilize a number of other technologies to bring the molecules from oven or ablation temperatures down to the 'cold' regime (100 mK $<$ T $<$1 K), and then bring in laser cooling to do the rest of the work. The main workhorse for this experiment has been the buffer-gas cooled beam source, which we utilize in this thesis.

Buffer-Gas Cooled Beams

Cooled molecular and atomic beam sources are not exactly a new technology - effusive molecular beams have been utilized at least since experiments by Dunoyer in 1911 [52] and the techniques of cooling via supersonic expansion have been widely used since it was proposed by Kantrowitz and Grey in 1951 [53]. The cryogenic buffer-gas cooled method is a relatively recently developed technique, in which molecules are produced inside a cryogenic cell which is filled with a cryogenic, inert buffer gas, such as helium. The molecules rapidly thermalize with the He via elastic and inelastic collisions, losing their translational and internal energy within a few milliseconds. The cell has an aperture in through which helium flows out into vacuum, carrying with it the molecular species of interest. At the aperture, the buffer-gas cell operates in a hydrodynamic region characterized by a collision rate between molecules and the buffer gas between zero (effusive) and fully fluid (supersonic) [54].

A combination of cell design parameters and the flow dynamics allows the cell to operate in the hydrodynamic regime. The advantage of the cryogenic cell is in the brightness and coldness of the beam. Thermalizing with the cold buffer gas means that the molecular beam actually has a low transverse temperature right when it exits the cell, rather than due to a cut from a skimmer. As a result, the beam can be much brighter, since more molecules are actually moving forward. In the longitudinal direction, the beam has much narrower velocity spreads than in an effusive beam, indicative of the hydrodynamic effects near the exit aperture. And yet, the mean forward velocity, typically centered around 80-100 m/s, is significantly slower than that of a supersonic beam, which may have narrow velocity spreads, but typically is moving forward at several hundred meters per second.

The development and proliferation of affordable cryogenic techniques has enabled this new technology. In particular, cryocoolers, such as pulse tube refrigerators and Gifford-McMahon cryocoolers are essentially plug-and-play devices (as far as experimental physics goes), which means that cooling a copper cell and He buffer gas down to 4 K is no longer a

heroic endeavor requiring experts in cryogenics and years of development and design, not to mention a prohibitively expensive amount of helium.

The cryogenic buffer gas beam source is thus a vital step to achieving complete quantum control of molecules, as it allows for high molecule numbers combined with a significant head start towards ultracold temperatures. After all, a typical molecular oven runs at 700 °C, so starting out at 4 K has already removed 99.6% of the translational energy (in at least two dimensions)!

Slowing the Beams

While the temperature of buffer-gas cooled molecules may be low, the molecular beam still has a forward velocity between 50 and 150 m/s. This is much slower than a supersonic source, but presents a problem for trapping. For atomic beams, the Zeeman slower is the most effective tool to reduce the forward velocity to MOT capture velocities (<10 m/s), and works by using a position dependent magnetic field that compensates changing Doppler shifts of atoms that are being slowed with radiation pressure. The Zeeman slower is well suited for atoms, is continuous, and compresses the longitudinal velocity distribution, allowing all atoms to stop at the same point, regardless of initial velocity [55]. However, the Zeeman slower technique usually relies on the Zeeman shift of a single hyperfine state. To date, all diatomic molecules that are considered amenable to laser cooling have a complex level structure and a combination of magnetic g-factors that make Zeeman slowing not applicable [56].

Of course, many other techniques have been developed to slow molecular beams, including Stark decelerators [57–60], counter-rotating nozzles [61–63], rotating centrifuges [18], secondary slowing cells [64], and even Zeeman decelerators [65, 66]. In addition, there are also purely optical techniques of chirped light [2] and broadband, or "white-light" slowing [67,68].

In our proposed scheme, we will use the "white-light" slowing technique, where the cooling

lasers are sent counterpropagating to the molecular beam, and are broadened using electro-optical modulation to address changing Doppler shifts and the multiple velocity classes. While this does not compress the velocity distribution, it has been shown to be an effective method to put a non-negligible fraction of the molecular beam below the capture velocity of the MOT [2, 67, 68].

Slowing the molecular beam while retaining many molecules remains an ongoing challenge in the field of ultracold molecular physics and is an area requiring much research.

1.2 Why BaH?

1.2.1 Favorable Molecular Properties

Many of the diatomic molecules that have been laser cooled thus far have been chosen primarily based on their amenability to laser cooling. That is to say that they most closely resemble the two level system that we are able to find readily in alkali and alkaline-earth metal atoms. Even in the simplest model of a molecule, it is difficult to find resemblance to any atom. In particular, there is no atomic analog to the diatomic molecular picture of two heavy balls connected by a spring. While the basic mechanics of electron orbitals may be familiar, this vibrational degree of freedom between the two nuclei is thorny because there are no explicit rules governing how an excited state vibrational state will decay into a ground vibrational state. The determining factor is in how well the probability distribution of the electron in the excited vibrating mode overlaps with a ground state vibrating mode of interest. The measure of this overlap is known as the Franck-Condon Factor (FCF). From the FCF one can calculate the particular branching ratio, or probability that a given excited state will fall into a single ground state. A "good" candidate molecule will have that probability close to 1.

In BaH, in turns out that the probability is excellent for a couple of excited electronic

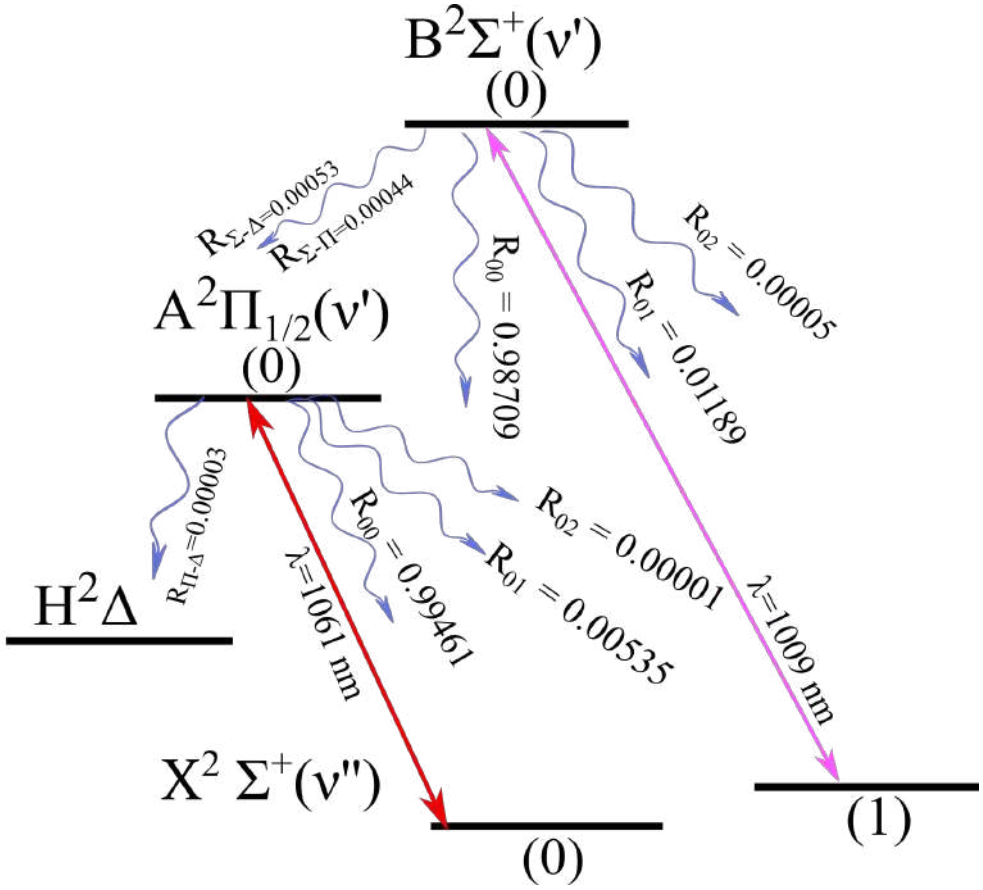

Figure 1.2: Proposed laser cooling scheme for BaH, showing vibrational branching ratios for the two excited states of interest. Adapted from Ref. [69]

states. In Figure 1.2, two possible excited electronic states are shown with their respective vibrational branching ratios, calculated by Moore *et. al.* [70]. For each of the two states, we see that they have close to 100% probability of return to the ground vibrational state, and ever smaller probability of falling into other vibrational states or a low-lying excited state. These two states of interest, $A^2\Pi_{1/2}$ and $B^2\Sigma^+$ have been fairly well studied over the past hundred years or so, including two particularly in depth spectroscopic studies by Kopp *et. al.* on the $A^2\Pi_{1/2}$ state [71] and Appelblad *et. al.* on the $B^2\Sigma^+$ state [72]. While these studies were comprehensive at the time, the technical resolution of both studies is limited to the fine-structure of the molecule, while complete knowledge of the hyperfine structure is necessary for laser-cooling ambitions.

The $A^2\Pi_{1/2}$ state in Figure 1.2 shows almost 99.5% probability of decay into the ground vibration state. In a laser cooling experiment, where 1061 nm light is used to excite the ground state as shown in the figure, this corresponds over 100 photon cycles before the molecule will fall into the next most likely place, which is the $v'' = 1$ level in the ground state where the 1061 nm light is no longer resonant with it. With the addition of a repump laser at 1009 nm, as shown, the molecule can be sent to the $B^2\Sigma^+$ state where it will have a 98.7% chance of returning to the original ground state, and undergo another 100 cycles.

In BaH, the wavelengths from $X^2\Sigma^+$ to $A^2\Pi_{1/2}$ and $B^2\Sigma^+$ are 1061 nm and 905 nm respectively, which are convenient for diode lasers. This significantly lowers costs of the experiment, since other types of laser technologies (solid-state, dye lasers) can be very costly. In particular, the 1061 nm wavelength is convenient because of the large amount of technology developed around Nd:YAG lasers at 1064 nm. As a result, specialized optical components are available at this wavelength with excellent optical qualities at relatively low prices.

The alkaline-earth hydrides all appear to have respectable FCFs, but the lower mass candidates (BeH, MgH, CaH) suffer from predissociative losses, where relevant rovibrational levels within the electronic excited states lie above the ground state dissociation limit, which causes these states to dissociate non-radiatively [73]. SrH and BaH remain the possible candidates, and choosing between them comes down to questions of transition wavelengths, lifetimes, branching to low-lying states, mass and preference. We ultimately choose BaH because the higher mass differential between constituent atoms is beneficial for considerations in producing ultracold hydrogen, as discussed in Section 1.2.3.

1.2.2 Diatomic Hydrides

Laser-cooled BaH would represent a new class of ultracold diatomic molecule. So far, there has been much success with two alkaline-earth-fluoride molecules, and significant progress with Yttrium Oxide (YO) [74], but hydrides, despite having good FCFs and being accessible

to computational techniques, have not been laser cooled. Expanding the scope of techniques to include hydrides opens the toolbox at hand for future ultracold molecule researchers to play with. Furthermore, at 2.7 Debye, the estimated dipole moment of BaH is in an ideal range to study dipole interactions in an ultracold gas [70] which would add chemical diversity to studies of quantum gases, which is currently limited to molecules that have constituent atoms which can be laser cooled. The description of the source region, comprising a major part of the present work, will provide detailed documentation for other hydride experiments to follow.

We note that laser cooling BaH would be "narrow-line" compared to the previously explored fluorides. Developing "narrow-line" cooling of molecules is important for taming other diatomic molecules with this property, such as those used in EDM measurements.

1.2.3 Route to Ultracold Hydrogen

Hydrogen has clear importance as the principle atomic system for experimentally testing our understanding of the physical universe. As both the most abundant and simplest element in nature, there is a fundamental need to apply physical theories to it while at the same time have corresponding experimental accuracy and precision on its properties. However, hydrogen has shown to be elusive to use in the workhorse of such precision measurements, the MOT, because the principal Lyman-α ($1^2S \rightarrow 2^2P$) line for cooling is at a wavelength (121 nm) at which current laser technology cannot generate enough power. Moreover, the recoil temperature for hydrogen cooled at such a wavelength is 2.4 mK [75], well above the μK regime needed for precision experiments.

Cooling a molecular hydride such as BaH offers an alternative route to ultracold hydrogen, where the cooled molecule can be precisely photodissociated, adding minimal excess energy, and leave behind an ultracold gas of hydrogen and barium atoms. Breaking the molecular bond in this way has the added benefit of a cooling effect, where the mass difference leaves

the kinetic energy of the small mass partner far reduced from that of the parent molecule [73]. BaH is thus not only a viable molecule to study in itself, but also offers a unique method to cool atoms which have previously been elusive to traditional techniques. Details of this scheme are discussed in Chapter 8.

1.2.4 Some Complexities of BaH

The lifetime of the cooling state determines the speed of the cooling cycle, which ideally we want to be as fast as possible. Only the lifetime of a single rovibrational level within the $B^2\Sigma^+$ excited electronic state has been directly measured (Ref. [76]) to be 125±2 ns, corresponding to a maximum scattering rate of $1/\tau = 4 \times 10^6$ s^{-1}. This is about an order of magnitude slower than for SrF or CaF, but is still workable, as we will see in Chapter 7. The lifetime of the $A^2\Pi_{1/2}$ state is predicted to be 136 ns [70], providing similar numbers for the scattering rate. These longer lifetimes also correspond to weaker optical trapping forces in a MOT, thus requiring a lower capture velocity than one might need for other diatomics. One upside to the longer lifetimes of BaH is that the Doppler temperatures are smaller, resulting in a colder possible MOT temperature.

A complication in BaH arises from the presence of a low-lying $H^2\Delta$ state, which, if branching to it is significant, can remove molecules from the cooling cycle. It would be difficult to pump out of this state, since the wavelengths to $A^2\Pi_{1/2}$ and $B^2\Sigma^+$ are in the mid IR, and transitions directly to the ground state are parity forbidden. The presence of this state was first inferred from measurements in Ref. [71], and later confirmed via direct spectroscopy in Refs. [77, 78]. Calculations from Moore *et. al.* [70] indicate that in fact, the branching to this state should be small enough to ensure at least 57000 laser cooling cycles.

The mass of BaH, at 138 amu, makes it quite a bit heavier than the other cooled diatomics, CaF (59 amu) and SrF (106 amu). This means that the radiative force required to slow down the molecule is greater, leading to longer slowing regions. Again, the possible upside here is

the lower recoil temperature from a single photon kick, which scales as m^{-1}.

While these are some potential roadblocks to using BaH, we are optimistic that they are tractable problems, and that the end goals of the experiment are worth the effort.

1.3 A Survey of the Playing Field

During the course of this thesis work, significant advances have been made toward the goal of cooling and trapping diatomic, and even polyatomic molecules. On one hand, it has been thrilling to see the extent of the interest in working with similar systems, and on the other hand, daunting to hear of all the trials and tribulations that our friends in other groups experienced. I would be remiss to not say that I am extremely indebted to the advice of so many people, from the long, technical emails and Skype calls, to the tidbits of information gleaned from offhand remarks made at conferences. The more successful of diatomic molecules thus far attempted to be laser cooled and controlled remain the fluorides, typically paired with an alkaline-earth atom. Similarly to the hydrides, they present the diagonal level structure that is so important, and easily accessible laser wavelengths. They too have been studied, if not in much more detail than hydrides, then at least to the same extent, and the fluorides have proven to be reliably straightforward to produce in stable quantities, and work well with buffer gas cooling. Table 1.1 lists current, published work being carried out towards molecular MOTs.

One begins to wonder why the hydrides have not experienced such success and widespread use, and the answer is not for a lack of trying. In particular, the Tarbutt and Hinds groups at Imperial College have attempted experiments with lithium hydride [59], but have found that the ablation yield is insufficient for laser cooling and trapping. Calcium monohydride was cooled using a buffer gas and magnetically confined inside the buffer gas cell at several hundred millikelvin [79], but optical access was insufficient to do additional laser cooling.

Molecule	Institution	Status	Temperature (approx.)	Ref.
CaF	Imperial College	MOT	50 μK	[2]
	Harvard University	MOT	340 μK	[3]
SrF	Yale University	MOT	250 μK	[81]
YO	CU Boulder	MOT	100 mK	[74]
BaF	Zhejiang University	Cryogenic Beam	K	[82]
SrOH	Harvard University	Cryogenic Beam	750 μK	[20]
BaH	Columbia University	Cryogenic Beam	100 mK	

Table 1.1: Various buffer gas cooled molecule experiments around the world.

Finally, as mentioned previously, the light partner alkaline-earth hydrides suffer from predissociative losses, precluding them from the possibility of laser cooling.

The results of my work with BaH molecules are published in Refs. [69, 80]

1.4 $^{88}Sr_2$ in an Optical Lattice

In my first two years in the ZLab, I worked on a different ultracold molecule experiment, which I would be remiss not to describe, as it informed much of the motivation for what I find interesting in molecules. This experiment was the ultracold Strontium dimer experiment, where $^{88}Sr_2$ molecules trapped in a one-dimensional (1D) optical lattice are probed and manipulated with exquisite precision. The work I contributed to in the following sections is published in Refs. [10, 21, 83, 84].

This Sr_2 experiment has set the standard for coherent molecule-light interactions [10, 21], and serves as a testbed for the ultracold photodissociation techniques [85, 86] that in the future could be applied to laser-cooled molecules such as BaH.

Entire theses should be (and have been [87–89]) dedicated to the ultracold strontium dimer experiment, and so I highly encourage the interested reader to look to those references for details, insights, and the wonderful physics.

1.4.1 Apparatus

The Sr_2 experiment is a complicated device, to say the least, but we can try and break it down with a brevity that does not give justice to the subtleties and effort that went into each piece. An overview of the experiment and the ultracold molecular spectroscopy that we did can be found in Ref. [10].

Sr atoms begin in an oven heated to around 600° C, where they are vaporized from a solid source. After traveling through capillary array to collimate a beam, they fly down a permanent magnet Zeeman slower [90], and into an ultrahigh-vacuum science chamber where they are captured in a MOT operating on the $^1S_0 - ^1P_1$ (461 nm) strong laser cooling transition in Sr. With a short natural lifetime of 5 ns, this transition provides strong trapping forces, but an ultimately high MOT temperature of a few mK. The 461 nm light is generated by sending amplified light from an 922 nm ECDL through a nonlinear crystal in a resonant cavity, which doubles the frequency through second harmonic generation. To get colder, the atoms are transitioned into a MOT operating on the narrow, $^1S_0 - ^3P_1$ (689 nm) spin-forbidden transition, which has a final temperature in the μK range.

As a final step of confinement, the Sr atoms are loaded into a 1D optical lattice - a standing wave of light where atoms are trapped within the high-field regions of the light field via optical dipole forces resulting from off resonant AC Stark shifts, forming a series of flat planes of Sr atoms [6, 91]. However, that same AC Stark shift can incur undesirable broadening effects for the measured transitions: since the polarizability of the ground and excited states are different, the AC Stark shift is different for each state. However, the polarizability is wavelength dependent, and there is an optimal wavelength for the $^1S_0 - ^3P_1$ transition at which the polarizabilities are the same, and the shifts in the ground and excited states cancel out [92]. This is known as the "magic" wavelength, and is a remarkable and useful tool for precision science. In Sr, the lattice is chosen at the magic wavelength in order to not affect subsequent experiments.

Now we get to making molecules! The procedure is outlined in Figure 1.3 and the experimental arrangement is shown in Figure 1.4. Sr atoms in the lattice are photoassociated directly into weakly bound vibrational states near the asymptote of the excited molecular potential. These weakly bound states have excellent wavefunction overlap with weakly bound ground states in the molecular ground state, leading the molecules to decay quickly into them (Figure 1.3(b)). Any non-associated atoms are wiped away with a 461 nm pulse. From this starting point, we can perform experiments with these ultracold Sr_2 molecules. Subradiant-state optical spectroscopy of Sr_2 (described below) puts the limit on the resulting spectroscopy <200 Hz, likely limited by optical fiber noise.

To detect the molecules, we recover them through the reverse process where we excite ground-state Sr_2 to very weakly bound excited vibrational states or directly to the $^1S_0 - ^3P_1$ asymptote, from where they spontaneously decay into atoms which can then be imaged. For details of this scheme, readers should consult Ref. [48].

1.4.2 Thermometry in Optical Lattices

This section regards work published in Ref. [83]. When the lattice-trapped ultracold molecules undergo optical transitions, they do so in the Lamb-Dicke regime, where the coupling between the light field and the motional states of the trap is strongly suppressed, meaning that we can drive transitions without changing the trap state of the molecule [93–95]. Additionally, the molecules are also in the resolved sideband regime, meaning that we can resolve the central carrier transition from the red or blue sidebands, as shown in Figure 1.5.

Under these assumptions, the carrier lineshape can be derived analytically by considering the differential light shift W due to the lattice light, which has both thermal (W_r) and non-thermal (W_0) contributions that depend on the ratio of polarizabilities between the excited and ground states, α'/α. This derived lineshape has the form of a Boltzmann distribution in a 3D harmonic trap, which is asymmetrically broadened by the thermal components of

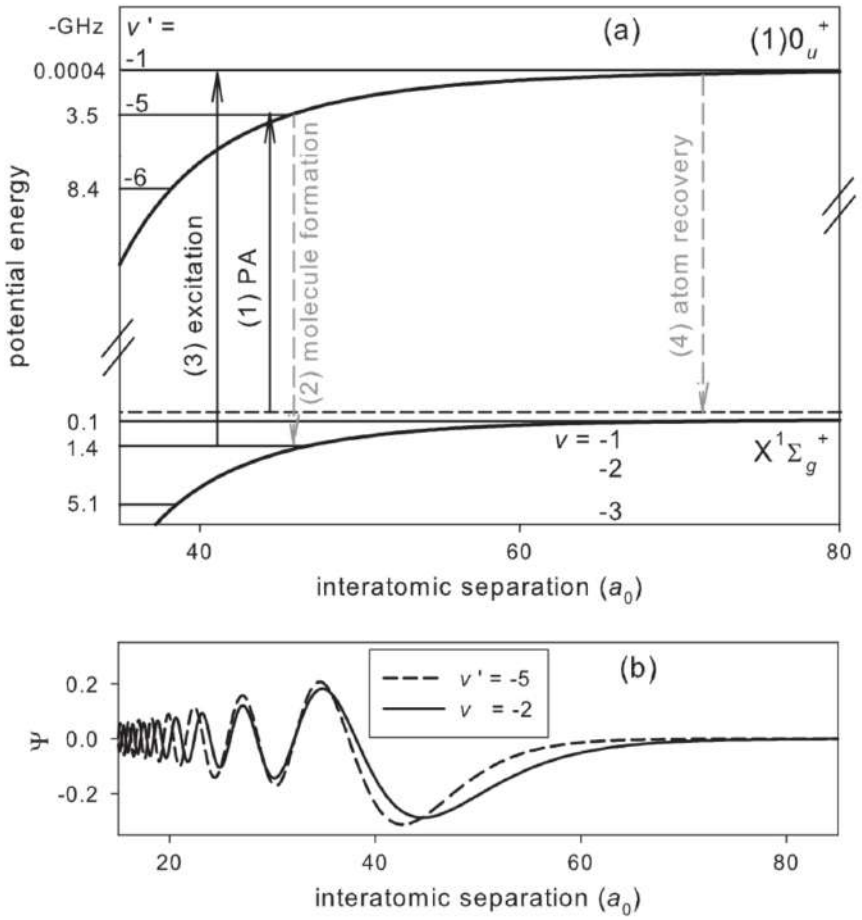

Figure 1.3: Sr_2 molecule production and atom recovery. (a) 1. Photoassociate Sr + Sr to v'=-5 (or -4) excited-state Sr_2 near the 689 nm $^1S_0 - ^3P_1$ intercombination line. 2. Spontaneous decay to v=-2 (or -1) ground-state Sr_2 (J=0 or 2) via a large Frank-Condon overlap of wavefunctions. 3. Excite ground-state Sr_2 molecules to very weakly bound excited vibrational states or directly to the $^1S_0 - ^3P_1$ asymptote. 4. Efficient spontaneous decay to trapped ground state Sr atoms, detected by absorption imaging. (b) Wavefunction overlap of excited and ground state molecular states, leading to large FCFs that facilitate ground-state molecule production. The notation (v, J) specifies the vibrational level and total angular momentum of the molecule. Adapted from Ref. [10].

the light shift. The measured carrier FWHM, Γ_C, can be related to the temperature of the molecules probed by the carrier as,

$$T_C \approx \frac{0.295\Gamma_C}{|\sqrt{\alpha'/\alpha} - 1|}\frac{h}{k_B}. \tag{1.4.1}$$

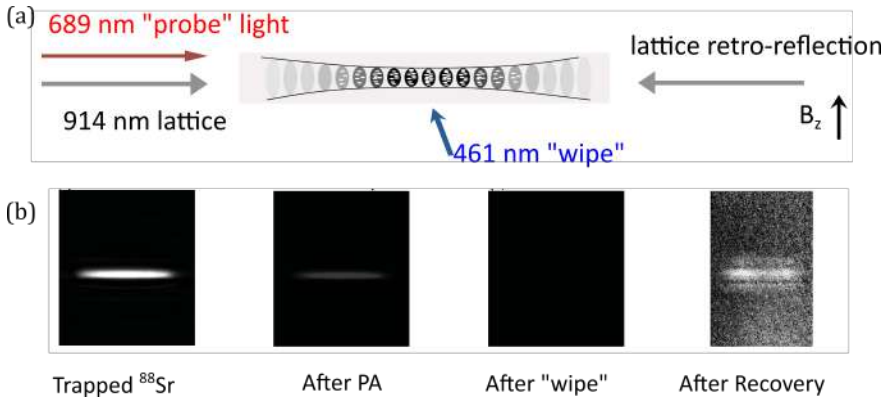

Figure 1.4: (a) Cartoon of Sr atoms in a lattice, probed by 689 nm light. (b) Atomic absorption images taken transverse to the lattice direction at various points along the experimental sequence. Adapted from Ref. [10].

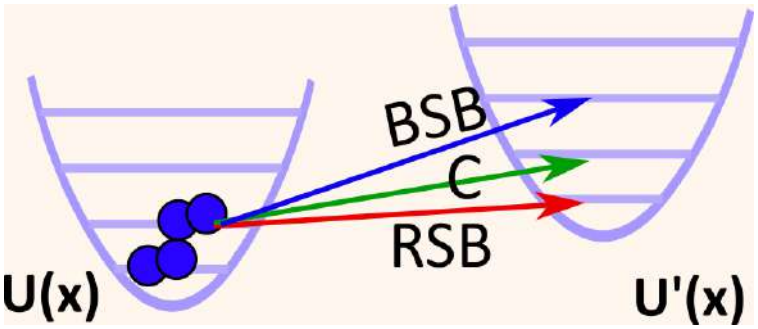

Figure 1.5: Molecules in the resolved sideband regime in a harmonic trap. The carrier (C) and red and blue sideband (RSB, BSB) transitions between molecular states in an approximately harmonic trap are indicated. Adapted from Ref. [83].

Figure 1.6 shows an optical spectrum with carrier and sideband transitions visible, as well as the deformed carrier lineshape with FWHM Γ_C. Also shown is the dependence of the light shifts, axial trap frequency, ω_x, and Γ_C on the lattice light power.

In order to test the this thermometry method, we compared it with the more widely used sideband-area technique [96]. In this alternative method, the temperature is determined from the ratio of the red to blue sideband area,

$$T_x \approx \frac{\hbar\omega_x}{k_B}\left(ln\frac{A_{\text{blue}}}{A_{\text{red}}}\right)^{-1}. \tag{1.4.2}$$

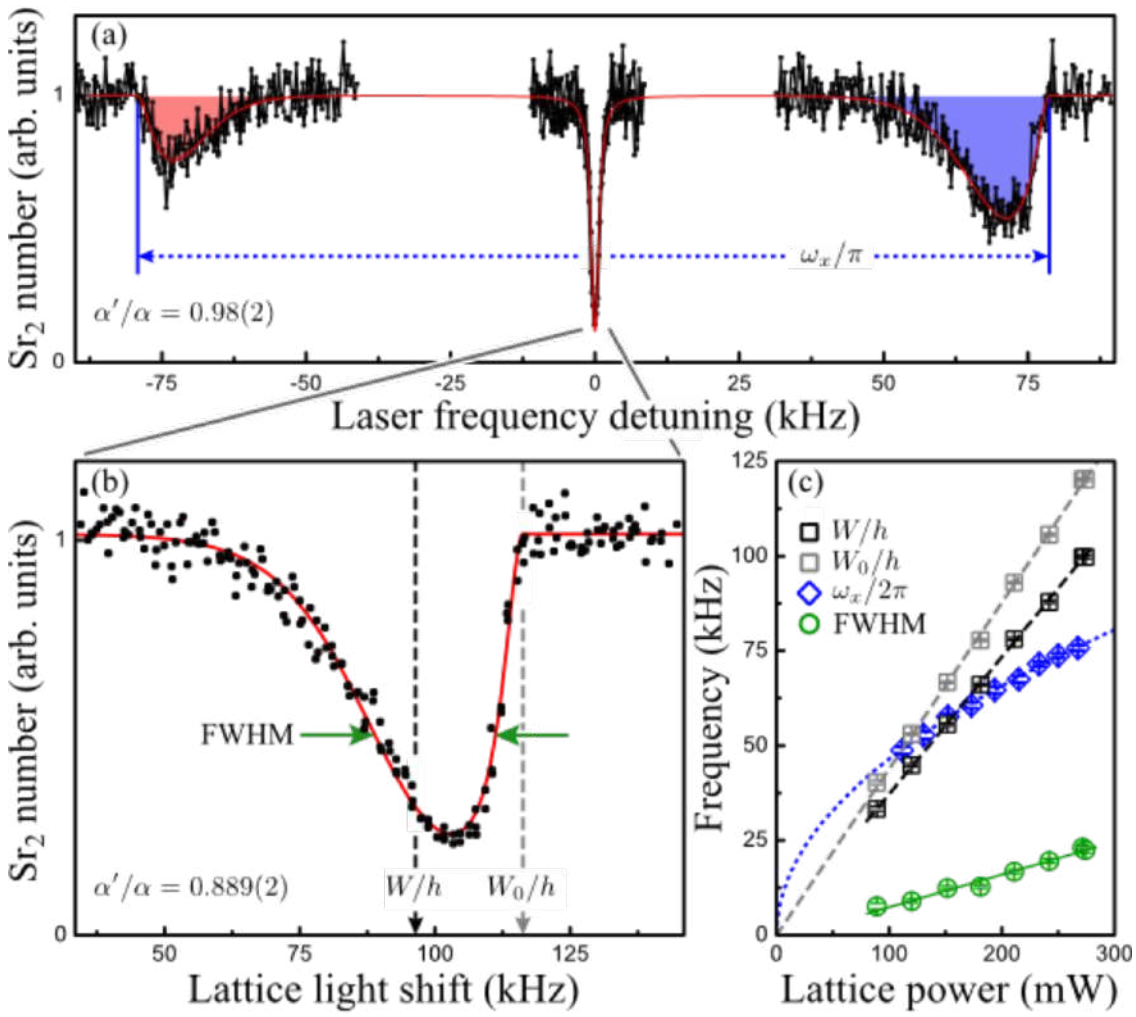

Figure 1.6: From Reference [83]. (a) Spectrum of tightly confined Sr_2 molecules. Depletion corresponds to transitions to other molecular states in a state-insensitive lattice. The central carrier transition and the first-order red and blue sidebands are visible. The axial trap frequency $\omega/2\pi = f_x \approx 80$ kHz is found from the sideband spacing. (b) The carrier line shape in a state-sensitive lattice, including light-induced shift and broadening. The average light shift W/h and the temperature-independent contribution to the light shift W_0/h are indicated. Zero detuning of the probe laser on the horizontal axes in (a) and (b) corresponds to zero lattice light shift. (c) The dependence of W/h, W_0/h, f_x, and Γ_C on the lattice light power. Figure from Ref. [83].

Taking data as a function of lattice power, we compared the two techniques (Figure 1.7) to measure the temperature and found an order of magnitude reduction in the uncertainty by using the carrier thermometry method.

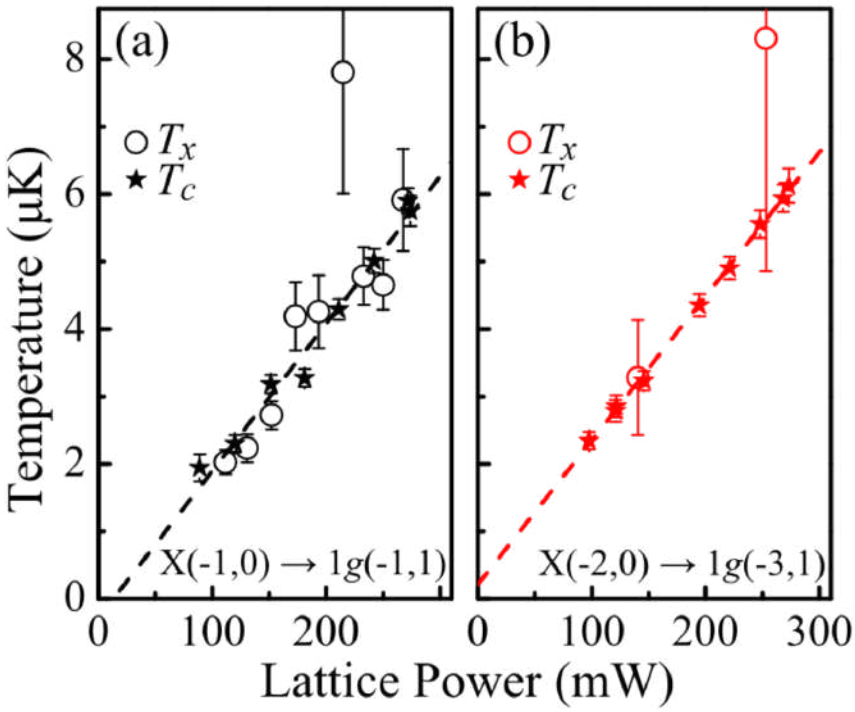

Figure 1.7: Carrier thermometry (stars) compared to sideband-area thermometry (circles) for ultracold molecules in an optical lattice. Data is taken for two ground states: (a) $v = 1$ and (b) v =2. Figure from Ref. [83].

1.4.3 Subradiance in Ultracold Molecules

This section regards work published in Ref. [21]. The molecules discussed here have nuclei separated by large distances (hundreds of Bohr radii), existing at the last few vibrational bound states before dissociation. And yet, while one may expect properties similar to that of two atoms at this range, molecular features without atomic analogues are prominent. One dramatic feature we observed in the Sr_2 dimer was the presence of subradiant states, a feature arising from the internal symmetry of homonuclear molecules [21]. Superradiance and subradiance are coherent phenomena for two or more particles affecting spontaneous radiation processes where the decay probability is amplified or inhibited due to constructive or destructive interference arising from phase-locking of atomic dipoles [97, 98]. While superradiance is readily observed due to the amplified nature of the emitted light (see: lasers), subradiance

is considerably more difficult to observe since the suppressed emission probability results in ultra-narrow or non-existent transitions, and excited states with correspondingly long lifetimes.

In molecules, subradiance arises due to the symmetry properties of the homonuclear molecular wavefunction. In the ground state, all states have even (*gerade*) symmetry in the wavefunction, $|X^1\Sigma_g^+\rangle \approx |^1S_0\rangle|^1S_0\rangle$, allowing E1 (electric dipole) transitions to odd (*ungerade*) excited molecular states, while being forbidden to *gerade* excited states. This is a manifestation of the destructive interference of the decay probability amplitudes between the two Sr atoms in the molecule, resulting in low-lying *gerade* excited states being subradiant with ≈ 0 decay rates. In other words, the symmetry of these wavefunctions arranges the atoms such that they cannot cooperatively emit a photon. In contrast, the excited states with *ungerade* symmetry are superradiant, with a decay rate that is twice the atomic decay rate from $^3P_1$ to $^1S_0$.

However, two factors can limit the lifetimes of the subradiant states. First, M1 (magnetic dipole) and E2 (electric quadrupole) interactions couple states with the same symmetry, even though these amplitudes are very weak. These transitions are schematically illustrated in Figure 1.8. Second, weak predissociation contributes to non radiative decay.

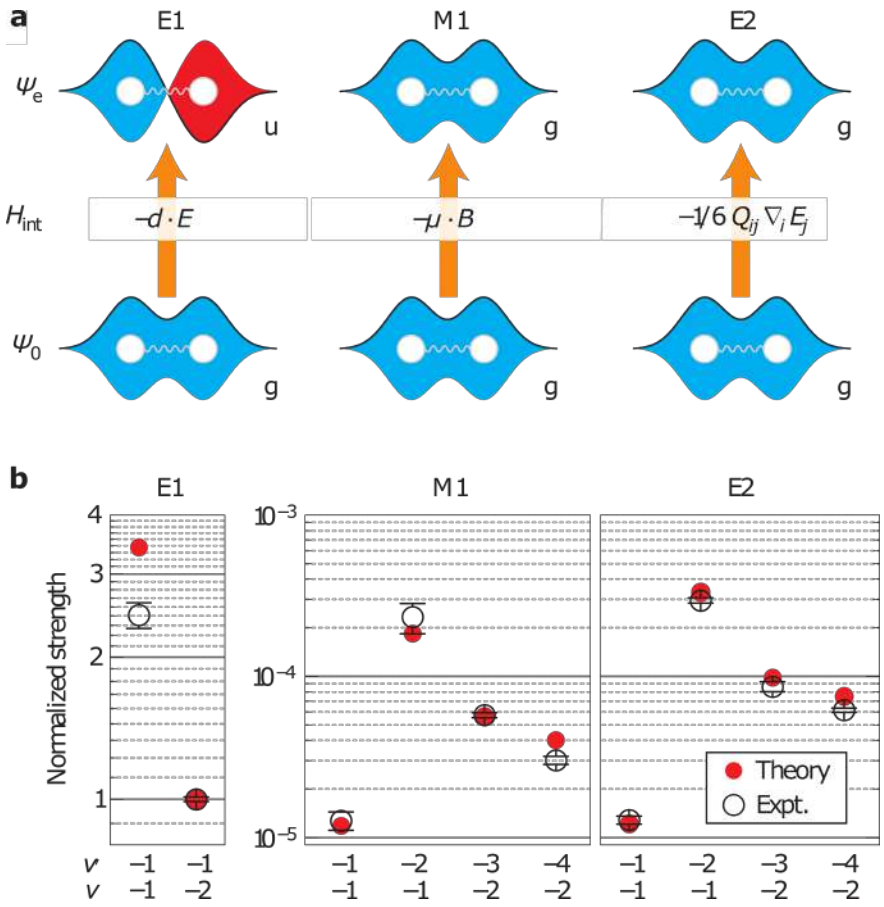

Figure 1.8: (a) Schematic representation of the gerade-ungerade symmetry of homonuclear molecules and the types of transitions, E1, M1, or E2, allowed between them. (b) Measurements and predictions for the transition strengths for allowed and forbidden transitions in the $^{88}Sr_2$ molecule. Values are normalized to the strength of an E1 transition to a superradiant level.

In order to accurately measure the lifetimes of these long-lived states, we developed and performed the measurement schemes shown in Figure 1.9. At first, we drive Rabi oscillations between ground and excited gerade states to measure the length of a π-pulse. Setting this, we apply a π-pulse to the molecules to put them into the excited state, wait a varying amount of time, then bring them back to the ground state to perform recovery and measure the remaining population. This results in the lifetime measurement of Figure 1.9(b), which we convert to linewidth. In Figure 1.9(c), we show how these states' lifetimes can be probed by driving transitions directly to the continuum. The signal is the atomic recovery signal - the

left-hand peak results from driving the $v' = -1$ state to the ${}^1S_0 + {}^1S_0$ continuum, which cuts off sharply as we cross the dissociation threshold. As we increase the laser energy, we become resonant with driving the molecules to the ${}^3P_1 + {}^3P_1$ asymptote, which begins sharply as we increase the laser frequency above the threshold. The lifetime measurement is shown in Figure 1.9(d).

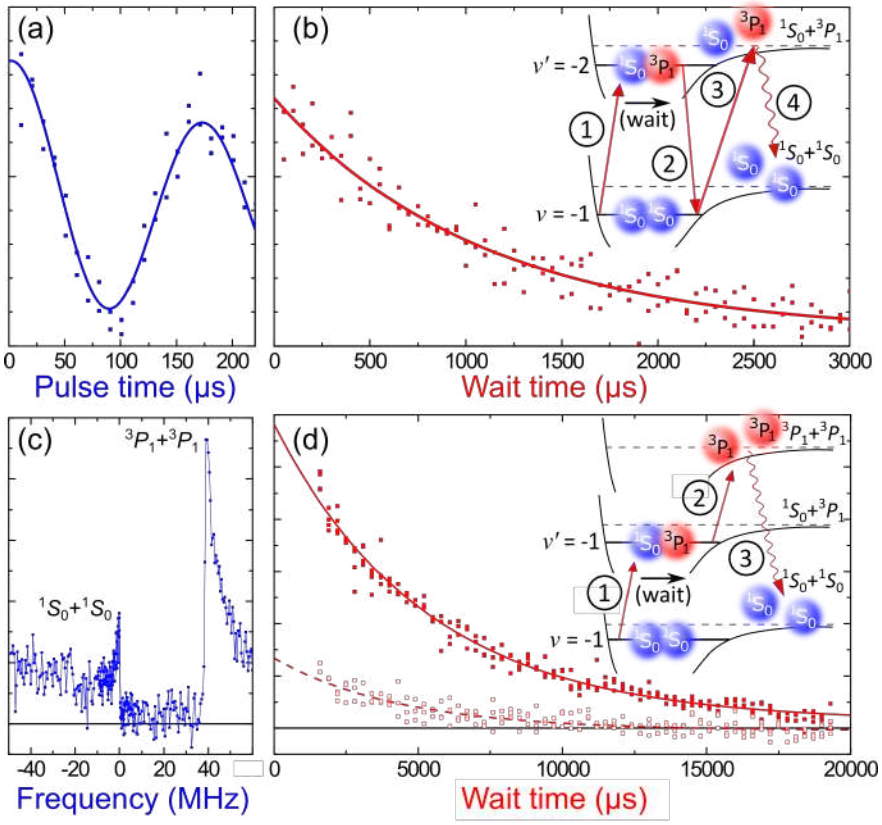

Figure 1.9: Direct measurements of subradiant state lifetimes. (a) Rabi oscillations between gerade states. (b) Decay in the excited state population, measured via π-pulses up and down. Cartoon shows the four-step process from molecule to atomic detection. (c) Atomic signal from coupling the least bound gerade state directly to continuum. (d) Lifetime measurement of the least bound state. Cartoon shows the simplified three-step fragmentation process. Adapted from Ref. [21].

The theory behind the gyroscopic predissociation and higher-order radiative contributions to the linewidth was worked out by collaborators in Poland (R. Moszynski *et al.*) using an *ab initio* model, and in Figure 1.10 we compare to the data. The agreement is excellent, and

we see that the predissociative contribution is the dominant lifetime quenching mechanism.

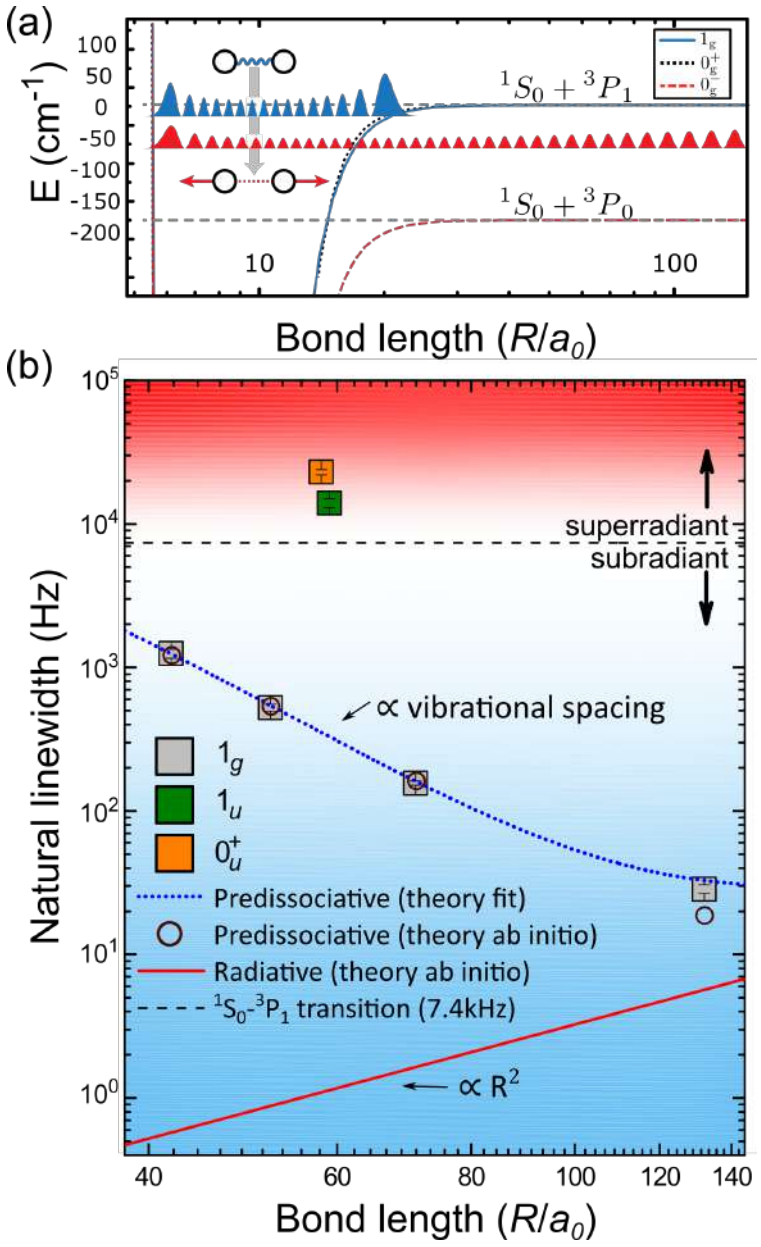

Figure 1.10: (a) Schematic representation of gyroscopic predissociation in Sr_2, where a bound state couples to a lower lying potential via the coriolis interaction, leading to a non radiative fragmentation of the molecule. (b) Measured superradiant and subradiant linewidths as a function of bond length, overlayed with *ab initio* theory predictions. Adapted from Ref. [21].

The Sr_2 state we measured with the narrowest linewidth ($v' = 1$) has a lifetime 300x longer than the atomic state, corresponding to an optical linewidth around 30 Hz, an unprece-

dented precision in molecular physics, and opening the door to ultrahigh-resolution molecular physics, including applications to molecular clocks. Moreover, the direct photofragmentation spectra of coupling the excited subradiant state to the ground state continuum has a width corresponding to excess energies in the nanokelvin range. This demonstrates the possibility of ultracold, near-threshold molecular photodissociation.

1.4.4 Magnetic Control of Transition Strengths

Another feature of the weakly-bound Sr_2 molecules that we explored was the mixing of nearby states by magnetic field. This is enabled by the relatively close spacing that is a general feature of molecules, but an anomaly in atoms. This effect was used in our experiment to control the strengths of forbidden optical transitions by over 5 orders of magnitude, using modest fields up to ± 60 G. This work was published in Ref. [84].

The mixing occurs entirely in the electronically excited state, since spinless Sr_2 molecules in the electronic ground states, $|\gamma\rangle$, interact very weakly with the field. According to perturbation theory, the mixing of a specific excited state, $|\mu\rangle$, with other nearby states, $|\nu\rangle$, can be described to first order in the field strength B as [84]

$$|\mu(B)\rangle \approx |\mu(0)\rangle + \sum_{\nu \neq \mu} \frac{B}{B_{\mu\nu}} |\nu(0)\rangle, \tag{1.4.3}$$

which is characterized by the parameter $B_{\mu\nu} = (E_\mu - E_\nu)/\langle \mu(0)|H_Z/B|\nu(0)\rangle$, giving an admixing per unit B for the Zeeman interaction, $H_Z = \mu_B(g_L \mathbf{L} + g_S \mathbf{S}) \cdot \mathbf{B}$.

The strength of a transition is given by the square of the Rabi frequency, $\Omega_{\gamma\mu} = \langle \gamma | H_e | \mu \rangle$, for the electric dipole Hamiltonian, H_e. As a function of applied field, this strength is

$$|\Omega_{\gamma\mu}(B)|^2 \approx |\Omega_{\gamma\mu}(0)|^2 + B^2 \left| \sum_{\nu \neq \mu} \frac{\Omega_{\gamma\nu}(0)}{B_{\mu\nu}} \right|^2 + B \sum_{\nu \neq \mu} \left(\frac{\Omega_{\gamma\mu}(0) \Omega *_{\gamma\nu}(0)}{B *_{\mu\nu}} + \frac{\Omega *_{\gamma\mu}(0) \Omega_{\gamma\nu}(0)}{B_{\mu\nu}} \right). \tag{1.4.4}$$

For forbidden transitions, the first and last term are zero, so the dependence on the field strength is quadratic, as observed for low fields in Figure 1.11. For allowed transitions, the third term, linear in B, captures the constructive or destructive interference we observe for $m = m' = \pm 1$ components. The field dependence of the $\Delta J = 3$ transition strength in Fig. 1.11(e) comes from higher order admixing not captured by this model.

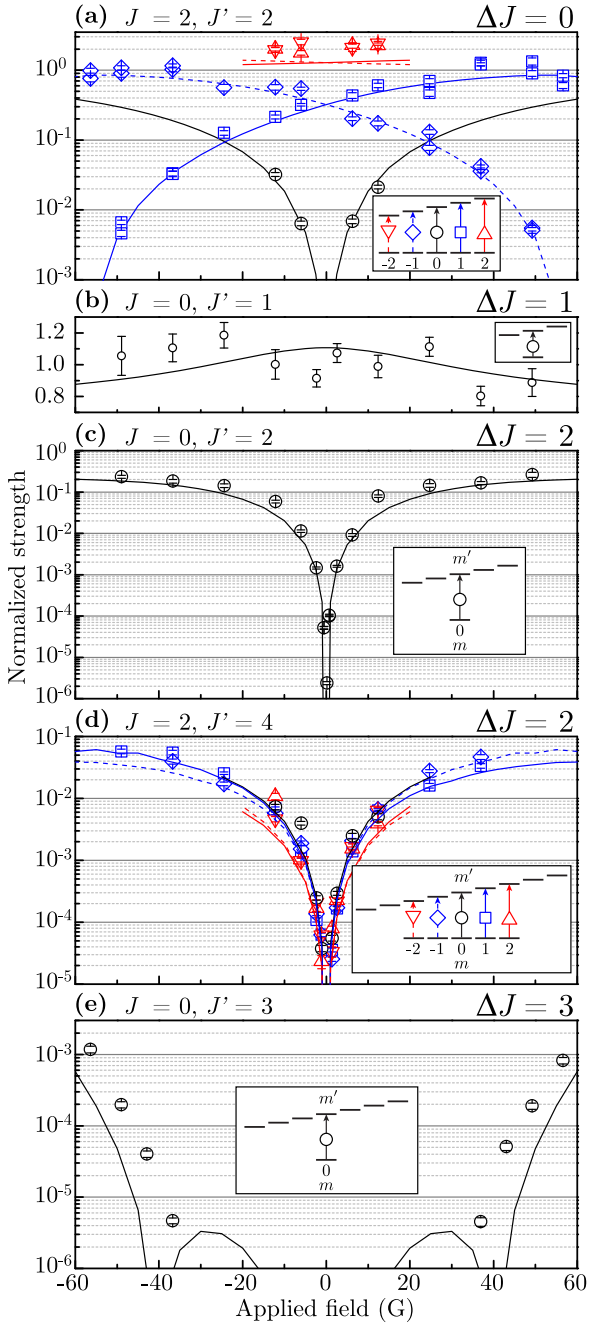

Figure 1.11: Magnetic control of optical π transitions near the Sr_2 intercombination line. Points are experimental data and curves are theoretical calculations. (a) $\Delta J = 0$ transition with forbidden $m = 0 \rightarrow m' = 0$ component becomes allowed with field while the $m = \pm 1 \rightarrow m' = \pm 1$ transitions which are normally allowed become strongly suppressed. (b) A transition with $\Delta J = 1$ is allowed, and is relatively insensitive to applied field. (c),(d) Forbidden transitions with $\Delta J = 2$ which vary in oscillator strength by over five orders of magnitude, becoming comparable to the strengths of allowed transitions. (e) A highly forbidden transition with $\Delta J = 3$ becomes allowed due to second-order admixing. Adapted from Ref. [84].

The Sr_2 experiment has continued to produce cutting-edge science results, keeping the promise of exciting and unique physics that is only accessible from molecules. In particular, McDonald and co-workers imaged photodissociation products from individual quantum states, not only producing beautiful pictures and insight into the pure wavefunction of spherical harmonic components, but also demonstrating a breakdown of the quasiclassical theory and developing a full quantum description of molecular dissociation processes [85]. Moving forward, the research is making significant headway into production of dimers in the rovibrational ground state, and also states in the intermediate depth of the molecular electronic potential. Since bound state energy spacings at different depths of the potential depend differently on the electron-proton mass ratio, measuring the energies of these states is sensitive to variations in this ratio. Furthermore, the large range of bond lengths that can be probed with extreme accuracy opens the door to searches for non-Newtonian contributions to gravity at nanometer-scale distances. Fascinating indeed!

Chapter 2

Dynamics of Buffer Gas Cooling

Buffer gas cooling is the general technique where a molecular or atomic species of interest is cooled via collisions with a cold inert gas. This method is (relatively) simple and works in a wide variety of applications across atomic and molecular physics. Here, we use the buffer gas as a thermalizing bath for molecules. The buffer gas that is used should be chemically inert and stable, and for the temperatures we want to achieve, helium fits the bill quite nicely. It has a large cold scattering cross section with almost any atom or molecule, and there is no risk of freezing up pipes. In general, buffer gas cooling is not limited to using a helium buffer gas, although this is most common. Quite a few species have been cooled with other inert noble gases, such as neon, but since our BaH experiment uses He, I will focus on that.

Buffer gas cooling relies on cold, elastic collisions with He atoms to thermalize the molecules to low temperatures. In these collisions, the molecules lose both translational kinetic energy and internal energy, which means that the resulting products are truly cold in the sense that it is possible to create a molecular beam with a high phase space density and low rovibrational temperature. The method largely relies on inelastic collisions and is general to any atom or molecule regardless of its energy structure, providing an attractive approach for any molecule cooling lab. The significant reduction in thermal velocity of an

atom or molecule means that the number of absorption/emission cycles required for laser cooling is dramatically reduced, which can in turn enhance any laser cooling scheme by a significant percentage.

In practice, buffer gas cooling typically occurs in a cryogenic cell filled with the buffer gas, and molecules are introduced via a fill line or laser ablation. Because the end goal of this specific experiment is a magneto-optical trap, we require high vacuum and good optical access to the molecules. In a buffer gas cell, this is not possible, so it is necessary to create a molecular beam.

The basic ingredients for buffer-gas cooling are: (1) a source of cold He gas, (2) a gas of the molecular species you are trying to cool, and (3) bringing the first two ingredients into contact with each other in a cold environment. Item (1) is fairly straightforward; He gas can be flowed through a 4K heat exchanger, such as a bobbin in two or more stages, where the cold temperatures can be achieved using a pulse tube refrigerator (PTR), or a Gifford-McMahon Cryocooler, for example. Item (2) can be achieved via a few methods including laser ablation or capillary filling. We use laser ablation, where a high energy pulsed laser is focused to a target precursor of the molecule of interest, and the resulting plume of material provides the gas of molecules. Laser ablation is widely applicable, efficient, and fairly straightforward. However, for molecular radicals, the ablation of a solid target typically yields a wide variety of ablation products, but the molecule of interest is typically a sizeable fraction of the ablation products, and if not, additives and target preperation techniques have been used to enhance this fraction. Furthermore, while ablation is a typically violent process, creating unpredictable behavior of the resultant plume and unusual plasma dynamics at tens of thousands of degrees, the fast thermalization time afforded by buffer gas cooling quickly mitigates these problems.

The dynamics of the molecules through a buffer gas can be estimated using some first principles. Here, I'll go through some estimates to guide the design parameters of the cell.

We are looking to find the thermalization time and make it shorter than the extraction time so that the molecules have a good chance to approach the buffer gas temperature by the time they leave the cell through the aperture. At the same time, the extraction time must be shorter than the diffusion time of the molecules to the cell wall. A schematic cartoon drawing of a buffer gas cell is shown in Figure 2.1

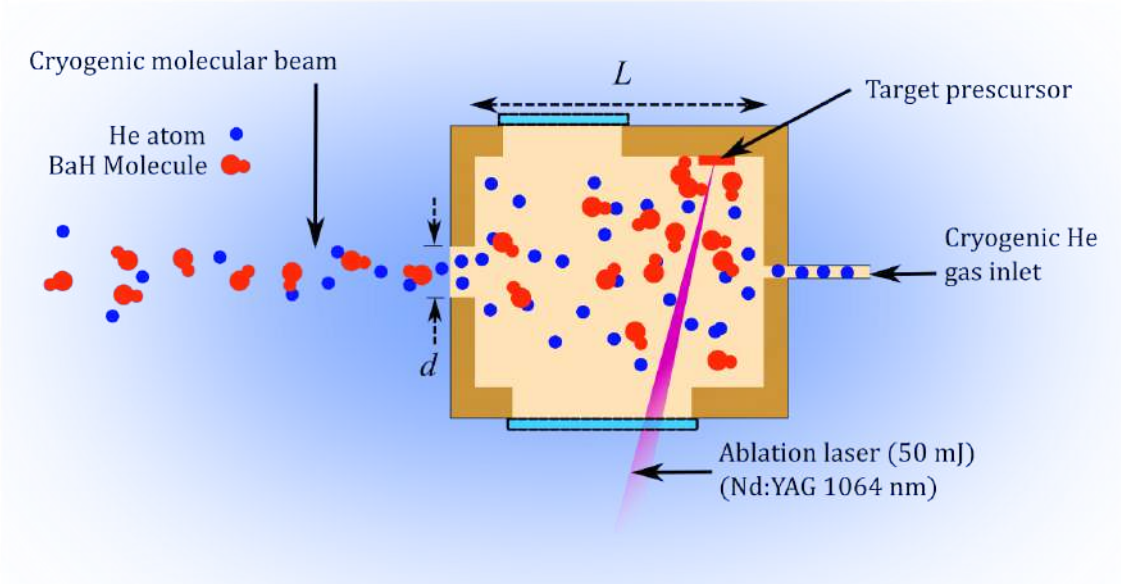

Figure 2.1: Cartoon drawing of the cryogenic buffer gas cell apparatus. The cell is made out of OFHC copper, has windows for optical access and is of length L, with an output aperture of diameter d. The 4 K cell is filled with a helium buffer gas through the inlet line at the right. This He is precooled via a series of bobbins, and enters the cell at around 4 K. While the cell is filled with helium, a strong laser is focused onto a target precursor to produce the molecule of interest via laser ablation, where a surface plasma at 10,000 ° K ejects molecules which thermalize with the buffer gas within about 100 collisions. The molecules leave the cell with the He gas through an output aperture, forming a beam.

2.1 Introduction of Molecular Species

A quick survey into the relatively large body of buffer gas cooling literature reveals that there are three main ways to introduce the molecule of interest into the system [54]. One option is laser ablation of a solid precursor, where a powerful laser is focused onto a sample to

create a surface plasma, which then ejects all types of atom-molecule combinations. Surface temperatures at the target can typically reach thousands or even tens of thousands of degrees (K) [99]. Another option is to flow the molecules of interest into the cell via a pipe, much in the same way helium is flowed into the cell. This requires a relatively stable molecule, and also sets a limit on the final temperature of the buffer gas cell, since the line temperature must be above the freezing point of the molecule [100]. Finally, it is sometimes possible to form the molecules of interest inside the cell by combining the two techniques above. For example, the fluorides are commonly produced via ablation of a solid metal alkaline earth target (perhaps with some additives) in an SF_6 atmosphere [2]. The chemical process appears to work most successfully in a cryogenic environment, which indicates that the SF_6 gas freezes onto the target surface before ablation, and gets ablated together with the metal. Skoff *et. al.* demonstrate production of YbF via ablation of a solid Yb target while flowing SF_6 into the cell via a heated pipe [101]. The hot Yb atoms coming out from the ablation plasma easily break off a fluorine atom from the gas, and form stable YbF. This technique of cold chemistry appears to be most reliable, and works remarkably successfully for fluoride diatomics.

Of the three methods above, the hydrides are generally limited to laser ablation, since their high reactivity makes it difficult to store for any long periods of time, and connecting a 1200^{o}C furnace oven to a 4 K cell may be challenging. For the third, chemical reaction option, ablating barium metal is straightforward, but finding a suitable hydrogen donor gas is challenging. H_2 has an exceptionally high binding energy, lowering the possible reaction rate. Other hydrocarbon gases could be considered, but these are detrimental to vacuum, or may freeze too easily. We attempted to use both H_2 and methane gas, with disappointing results.

Laser ablation is a well-established technique in both scientific and technical fields, with applications from surgery to mass deposition and surface processing. Laser ablation can be

accomplished with either continuous or pulsed lasers, but the energies required usually demand a pulsed laser. The applications are too numerous to list, and there is a corresponding body of literature studying the dynamics of this violent process. However, a fundamental understanding of the complicated physical processes that are involved is elusive, and there are no hard and fast rules for what makes a good ablation target, and what ablation products to expect in what quantities. The coupling between the focused laser light and the sample is necessarily complex since the thermal coupling depends on many minute factors in the target, which in most cases is not homogeneous across the surface. Moreover, these optical and thermal properties change upon the formation of the plasma and it becomes increasingly difficult to track the numerous chemical reactions that are occurring in the rapidly changing environment, under constantly changing initial conditions as the target surface is modified by the laser.

The precursor target properties can strongly influence the ablation yield, shot-to-shot variation, and durability of the target. As a result, it is important to try many variations and combinations in target preparations including sintering, annealing, pressing, additives, and other techniques. The large parameter space here can make this process particularly challenging, and the (almost comically) detailed and expansive literature on each of the possible techniques is testament to this.

In the case of BaH, we attempted a wide variety of techniques to create robust targets. The precursor we use is BaH_2, which conveniently can be purchased commercially in the form of 3-5 mm 'chunks' or as a powder. We attempted many procedures to press the powder into round targets but in the end, the best performance was achieved from the chunks. The ablation yield from the chunks did not increase with annealing. These chunks resemble small, amorphous rocks, are brittle, and have a light grey color. Glued onto a target holder, you may be fortunate to find about 30% of the surface suitable for ablation. Unfortunately, as all hydrides, BaH_2 reacts quickly with oxygen and moisture in the air, and forms $Ba(OH)_2$, at

which point the sample promptly crumbles into a useless pile of whitish powder. Since this process happens within about 15 seconds, it is necessary to perform all sample preparation inside a glovebox. This preparation is a fairly simple process where rocks are selected, mostly based on size, are cleaved in half to expose a clean, flat surface, and then glued onto some type of target holder. We cleave the targets using a small pair of wire cutters, and the rocks break in much the same way you may expect chalk to break. The cleaved rocks are glued with Loctite 414. Once the glue is dried, the sample holder is transferred from the glovebox to the opened cryostat by briskly carrying it across the room whilst flowing Ar gas over it via a flexible hose.

Our buffer gas cells are designed to have a removable, threaded insert as the sample holder, enabling a change of sample without removing the cell. Once the target holder is screwed into place, He or Ar gas can be flowed into the cell via the inlet pipe until the vacuum chamber is sealed. This ensures that the samples remain uncontaminated by oxygen or water. The specific geometry of our cells are described in Section 4.1.3.

2.2 Cryogenic Buffer Gas Cell

The ablation process occurs inside a buffer-gas filled cryogenic cell, which in our design is made of oxygen-free copper and has an internal volume of a few cm^3, given by the cross sectional area $\times$ the length of the cell. The cell is kept at a fixed temperature between 1 and 10 K. Cold He buffer gas flows from the back to front of the cell, entering through a thin pipe, and exiting through an aperture on the end of the insert. Ideally, this buffer gas should be at the same temperature as the cell, so it is typically made to pass through several heat exchangers before entering the cell. The flow of buffer gas into the cell, f_{in}, can be controlled and monitored using a commercial mass flow controller. We found that adding a copper mesh at the end of the inlet pipe, right where the He enters the cell, made

an improvement to the extraction efficiency. This is most likely because the mesh acts as a diffuser for the flow of incoming He, making the He density more homogeneous throughout the cell volume.

A key factor in determining the thermalizing capabilities of a buffer gas in a cell is the density. To know the density of buffer gas in the cell, n_{He}, we need to know the flow rate out of the cell. This can be determined from the molecular conductance through a small aperture. As described in Ref. [102], consider a molecule of mass m in a unit cell of temperature T, with a mean thermal velocity,

$$\overline{v_{TH}} = \sqrt{\frac{8k_bT}{\pi m}},$$

where k_b is the Boltzmann constant. This molecule, with velocity component in the z direction given by $\overline{v_Z}$, will hit the $+z$ face of the cell $\frac{1}{2}\overline{v_Z}$ times per unit time. With n molecules in the cell, the number of particles hitting a unit area per unit time will be $\frac{1}{2}n\overline{v_Z}$. Since for a given molecule, $v_Z = v\cos\theta$, the thermal average is $\overline{v_Z} = \overline{v_{TH}\cos\theta}$. Over just the upper hemisphere we are considering, $\overline{\cos\theta} = \frac{1}{2}$, and therefore

$$\frac{1}{2}n\overline{v_Z} = \frac{1}{4}n\overline{v_{TH}}. \tag{2.2.1}$$

For an aperture of area A_{ap}, as in our buffer gas cell, the flow of particles out of the cell is

$$f_{out} = \frac{1}{4}n\overline{v_{TH}}A_{ap}. \tag{2.2.2}$$

Now, we can balance the flow rates in and out of the system and find solve for n_{He} by setting $f_{out} = f_{in}$, as will be true in the steady state. f_{in} is set by the mass flow controller which is external to the cryostat. We find that

$$n_{He} = \frac{4 f_{in}}{\overline{v_{TH}} A_{ap}}. \tag{2.2.3}$$

In the above, there is no mention of the "nozzle length" of the aperture, that is, the thickness of the aperture, l_N. In principle, both l_N and A_{ap} determine the type of flow that emerges from the cell, mainly due to their effect on the number of collisions that occur in the gas as it exits. The pressure differential and shape of the aperture can also influence this number. A large l_N ensures many collisions near the exit, which changes the beam properties significantly compared to the gas properties in the cell. This defines the supersonic beam, where the many collisions at the exit cause the buffer gas to behave more like a fluid, and since the collisions are primarily in the forward direction, the beam is "boosted" out of the cell, leading to the supersonic forward velocity. This increase in velocity happens during free and adiabatic expansion into the vacuum, so the extra energy in the forward direction is really taken from the transverse motion - hence cooling occurs as the beam expands and accelerates forward, until the density of the beam is low enough to stop the collisions. This is known as "freezing". These supersonic beams have extremely narrow velocity distributions on the order of 50 m/s (FWHM), but the group velocity of the pulse is very high, often around 400 m/s or faster [54, 103].

At the other extreme, when l_N is thin, the output beam is simply a sampling of the thermal properties of the gas inside the cell, and the resulting beam is a one dimensional Maxwell-Boltzman distribution (in the case where molecules are well thermalized). This is known as an effusive beam, resulting in broad velocity distributions (up to 200 m/s FWHM) that spread the molecule number out over a wide range of velocity classes, including some very slow molecules (<30 m/s). Effusive beams are commonly employed in situations where the molecule production method is particularly effective, and molecule number is not going to be an issue. This is unfortunately not the regime that BaH is in!

The goal of the buffer gas cell here is to be in an intermediate regime, where there is a somewhat narrow velocity distribution to manipulate optically, but with a manageable forward velocity. That is, something that can be slowed to near stationary in the lab frame within a few thousand photon cycles.

The cell design should be motivated to optimize the molecule number at the desired forward velocity. In general however, the cell design is constrained in size by the amount of cooling power available. For example, larger cells may be able to handle more buffer gas flow, but this alters the requirements on helium cryopumps, which will ultimately take energy away from the cooling.

To understand how to optimize molecule number, we will consider the diffusion time of the molecule of interest, the pump-out time of that molecule from the cell, and the thermalization time of the molecule with the helium buffer gas. These three time scales depend on combinations of aperture size, cell cross section and length. The length of the cell should be constrained on the lower limit by the minimum thermalization time, τ_{therm}, and therefore, minimum length, l_{therm}, of space a particle needs to thermalize with the buffer gas. On the other hand, it is limited by the time it takes for a particle to stick to a wall, determined by the diffusion time, τ_{diff}, and thus the cell cross sectional area. Finally, the pump-out time, τ_{pump} should describe the amount of time the molecule spends in the cell, and should fit somewhere between the previous two time scales.

2.3 Thermalizing Molecules with a Buffer Gas

Soon after production, the molecules must thermalize with the buffer gas and exit the cell before they diffuse and stick to the walls of the cell. The ablation process produces molecules at fairly extreme temperatures - over 10,000 degrees Kelvin [99], so the buffer gas technique must reduce this thermal temperature by 4 orders of magnitude over the course of a few

hundred microseconds. Therefore, the central issue to keep in mind when designing a cell is the efficiency of the thermalization process. A useful feature of the buffer gas cooling is that the collisions are generally inelastic, which cools the internal rotational temperature of the molecule simultaneously with the translational. This quenching is not as effective for the vibrational motion, but generally, molecules end up in the ground vibrational state as well. To determine design parameters for the cell, we first examine the translational temperature thermalization properties.

Using a hard sphere model, we can estimate the change in temperature for a molecule after an elastic collision with a buffer gas atom as

$$\Delta T = (T' - T)/\kappa, \tag{2.3.1}$$

where T is the temperature of the buffer gas, T' is the temperature of the molecule before a collision, and $\kappa = (M+m)^2/2Mm$. Since this is the temperature change per collision, we can write the differential equation in terms of T_N, the temperature after N collisions as

$$\frac{dT_N}{dN} = -(T_N - T)/\kappa, \tag{2.3.2}$$

which, via separation of variables has the solution,

$$T_N = (T_0 - T)e^{-N/\kappa} + T. \tag{2.3.3}$$

For $T_0 = T'$ before any collisions $\approx 10000K$, $T_N = T = 4K$, and using $m_{^3He} = 4$ amu, $M_{BaH} = 138$ amu, N is about 200 to get within a few percent. To understand how long these 200 collisions would take, we can use the mean free path of the molecule within the buffer gas, defined as

$$\lambda = \frac{1}{\sigma n_{He}} \frac{1}{\sqrt{1 + M/m}} \tag{2.3.4}$$

where σ is the scattering cross section between the molecule and He, and n_{He} is the density of the buffer gas, and say that the time between the $N-1$ and Nth collision is $t_N = \lambda / v_N$, where the velocity before each collision is $v_N \propto \sqrt{T_N}$. We can sum this over the number of collisions to find the total time,

$$t = \sum_{N=0}^{200} \frac{\lambda}{\sqrt{\frac{3k_B}{M}[(T_0 - T)e^{-N/\kappa} + T]}}. \tag{2.3.5}$$

Using a buffer gas density of 1×10^{21} atoms/m^3 and a typical value of $\sigma \approx 10^{-14}$ cm^2 [54], this thermalization time is ≈ 2 ms.

It is important to also consider the internal thermalization of the molecule upon interaction with a buffer gas, that is, how quickly the buffer gas collisions can reduce the rotational and vibrational temperatures of the molecule. Since the relaxation time for the translational temperature is proportional to the mean free path, it is inversely proportional to the collisional cross section. The same picture for thermal relaxation applies to rotational relaxation, and diatomic molecules have measured rotational cross sections of the same order as the collision cross section [104], in that $\sigma_{rot} \approx \sigma$, implying that the rotational time should be on the same order as the translational one.

The translational and rotational thermalization rates of the molecules provide important information about the buffer gas dynamics and the performance of our cell. The rotational thermalization needs to occur fast enough to populate our state of interest, and the translational thermalization needs to make those molecules cold.

2.4 Diffusion Through Cell and Beam Extraction

The continuity equation states a conservation of matter as $\frac{\partial\phi(\mathbf{r},t)}{\partial t} + \nabla \cdot \mathbf{j} = 0$, with the flux of particles, $\mathbf{j}$ diffusing outward from an initial distribution of particles with density $\phi(\mathbf{r}, t)$ [102]. Fick's first law states that the flux of material diffusing outward is proportional to the gradient of the density distribution: $\mathbf{j} = -D(\phi, \mathbf{r})\nabla\phi(\mathbf{r}, t)$, where $D(\phi, \mathbf{r})$ is the constant of proportionality. Together, these two equations form the diffusion equation,

$$\frac{\partial\phi(\mathbf{r}, t)}{\partial t} = \nabla \cdot [D(\phi, \mathbf{r})\nabla\phi(\mathbf{r}, t)]. \tag{2.4.1}$$

In general, $D(\phi, \mathbf{r})$ is not constant. However, following Skoff *et. al.* [101], we can approximate it to first order with the so called Chapman-Enskog approximation for a large density of background gas at temperature T, which relates D to the thermally averaged diffusion cross section, $\bar{\sigma_D}$. This approximation is only valid for a diffusion constant that does not vary with distance and assumes that the temperature of the species is not changing dramatically. This is really only true after the ballistic expansion of the ablation plume, so what we are looking for is the diffusion time after an initial expansion of the plume. This is okay in some sense, since it means we are looking for an upper limit on the diffusion time/length. The result is,

$$D(\phi_{He}, \mathbf{r}) \approx D(\phi_{He}, T) = \frac{3}{16\bar{\sigma_D} n_{He}}\sqrt{\frac{2\pi k_B T}{\mu}}, \tag{2.4.2}$$

where μ is the reduced mass between He and the species of interest. Since this removes the $\mathbf{r}$-dependence from D, we can pull it out of the gradient in Equation 2.4.1. The 1-D solution to the diffusion equation is

$$n_{He}(x, t) = n_{He0}\text{Erfc}\left(\frac{x}{2\sqrt{Dt}}\right). \tag{2.4.3}$$

To first order, the expansion of the error function is $n_{He}(x,t) = n_{He0}\left[1 - 2\left(\frac{x}{2\sqrt{Dt\pi}}\right)\right]$, and the quantity $2\sqrt{Dt\pi}$ is the characteristic diffusion length, describing the distance the particle travels in a diffusion time, t. Therefore, for a cell of cross-sectional diameter L we find,

$$\tau_{diff} = \frac{L^2}{4\pi D} \tag{2.4.4}$$

We now need the effective τ_{pump}, which describes the timescale at which the cell is emptied of the buffer gas, and thus how much time it takes for a particle of interest to be swept from the cell by the helium gas. From Equation 2.2.3 for the density of the buffer gas in the cell, we can divide by the volume of the cell to arrive at the differential equation for the number of particles leaving the cell, $\dot{N}$, given an initial number of particles, N, inside a cell of volume V_{cell}:

$$\dot{N_{He}} = \frac{1}{4} N_{He0} \overline{v_{He0}} \frac{A}{V_{cell}}. \tag{2.4.5}$$

The solution is an exponential with characteristic time

$$t_{pump} = \frac{4V_{cell}}{\overline{v_{He0}} A}. \tag{2.4.6}$$

Note that $V_{cell} = L_{cell}^3$, where L_{cell} is the characteristic length of the cell.

We can now define the dimensionless $\gamma_{cell} = t_{diff}/t_{pump}$, so that $\gamma_{cell} > 1$ corresponds to a good extraction efficiency, where the molecules can be pumped out of the cell faster than they diffuse and stick to the walls. Dropping numerical factors of order unity and using Eq. 2.4.2 for D,

$$\gamma_{cell} = \frac{n_{He0}\sigma_D A}{L_{cell}} = \frac{\sigma_D f_{in}}{L_{cell}\overline{v_{He0}}}. \tag{2.4.7}$$

It is important to note here that despite the lack of any dependence on the aperture size, A, experimentally it has been observed both in our apparatus and others that aperture sizes with characteristic length below 3 mm have very poor efficiency [54].

Therefore, we see that if σ_D is a couple orders of magnitude smaller for BaH than for a proven buffer cell species like Yb, we need to compensate with a lot of flow, a very small cell, and a very low temperature.

The velocity at which molecules leave the cell is somewhere between the thermal velocity and a supersonic velocity. As mentioned before, these regimes are defined by the number of collisions that occur near the cell exit, where no collisions is the effusive, thermal regime, while many collisions will lead to a boosted beam and the supersonic regime.

In general, the forward exit velocity, v_f, of the molecules is characterized by the Reynolds number of the aperture, $\mathcal{R}_A = d/\lambda$, where d is the output aperture diameter. When the mean free path $\lambda \gg d$ and $\mathcal{R}_A \ll 1$, the exit velocity is approximately the thermal velocity, and we have an effusive beam.

At the other end of the spectrum, when $\mathcal{R}_A > 100$, there are collisions occurring near the aperture and transverse momentum is converted into forward momentum, resulting in a boosted beam. Typically, "fully supersonic" beams are defined as those with $\mathcal{R}_A > 1000$. The intermediate regime we are looking for is for $1 < \mathcal{R}_A < 10$.

Since we want $\gamma_{cell} > 1$, we can rearrange Equation 2.4.7, taking $A = \pi d^2/4$ to find that,

$$\mathcal{R}_A > \frac{L}{d}, \tag{2.4.8}$$

which tells us that $\frac{L}{10} < d < L$.

Chapter 3

Preliminary Study of BaH Ablation at Room Temperature

Prior to any major construction and investment into a large experiment to laser cool BaH, it was imperative to explore some basic properties of the molecule. BaH has been studied since the 30s, however the literature is fairly dated, with the most recent studies in the 1990s, and several important papers available only on microfilm...

To understand the ablation product dynamics and spectroscopy better, we constructed a simple chamber system to test out the ablation on a BaH target. This project went through several iterations, as we tried a few different ideas out. The primary goal of the apparatus was to spectroscopically identify the relevant transitions in BaH, and try to measure the He-BaH scattering cross section. The material in this Chapter is published in Reference [69].

The experimental setup is shown in Figures 3.1 and 3.2. Our chamber consisted of a four-way cross with three ports as windows and one port towards a vacuum gauge, argon input valve, and turbo pump. In this configuration, we could glue the target on a small, chair-like target holder in the center of the cross, send an ablation laser pulse though the 'front' window, and probe through the remaining axis. To study collisional cross sections,

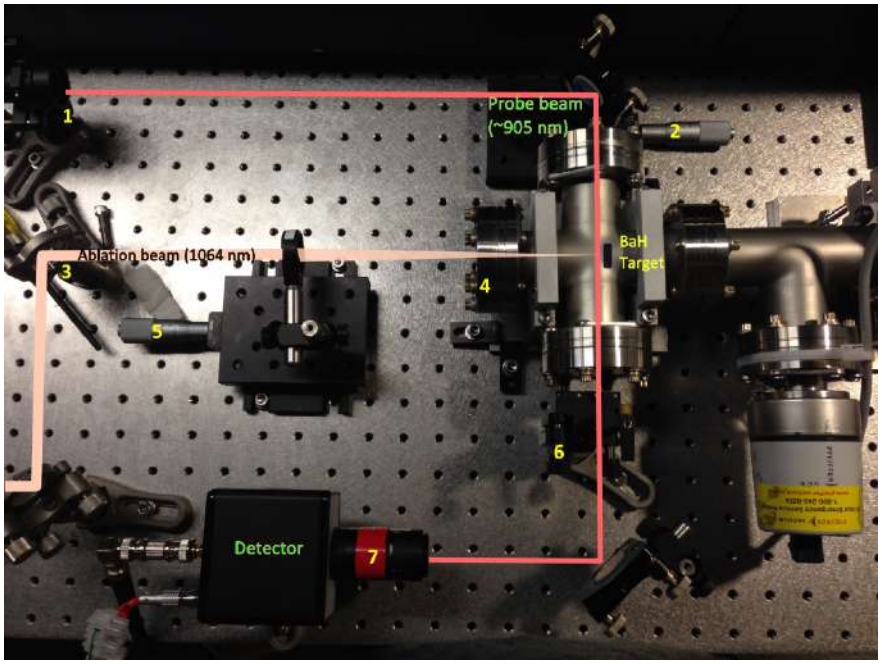

Figure 3.1: Set up for the ablation tests on BaH. This arrangement is for absorption spectroscopy. 1. Beam expander; 2. Translation stage; 3. High damage threshold mirror to steer ablation beam; 4. Front window for ablation; 5. Focusing lens adjustment; 6. Polarizing beam splitter; 7. 910(10) nm filter and lens.

buffer-gas can be introduced to the chamber via an inlet line before the vacuum pump valve. While simple, the apparatus enabled us to perform absorption spectroscopy within a few mm of the target, thus probing the ablation plume.

The ablation laser is a BigSky Nd:YAG laser with 8 ns wide, 50 mJ pulses at 1064 nm. At 100% energy, the focused ablation beam produced a visible ablation plume on the target, an effect which tended to saturate the photodetector, therefore spectral filters at the probe wavelength were used before the photodetector. The local intensity of the ablation beam could be varied by changing the position of the last lens before the chamber. In typical experiments, the ablation beam was focused about 1 cm behind the target, as a direct focusing would burn a hold through the target within 100 shots. The repetition rate of the ablation laser was typically chosen to be 2 Hz, since faster rates would raise the vacuum level inside the chamber more rapidly than the turbopump could remove the ablation products.

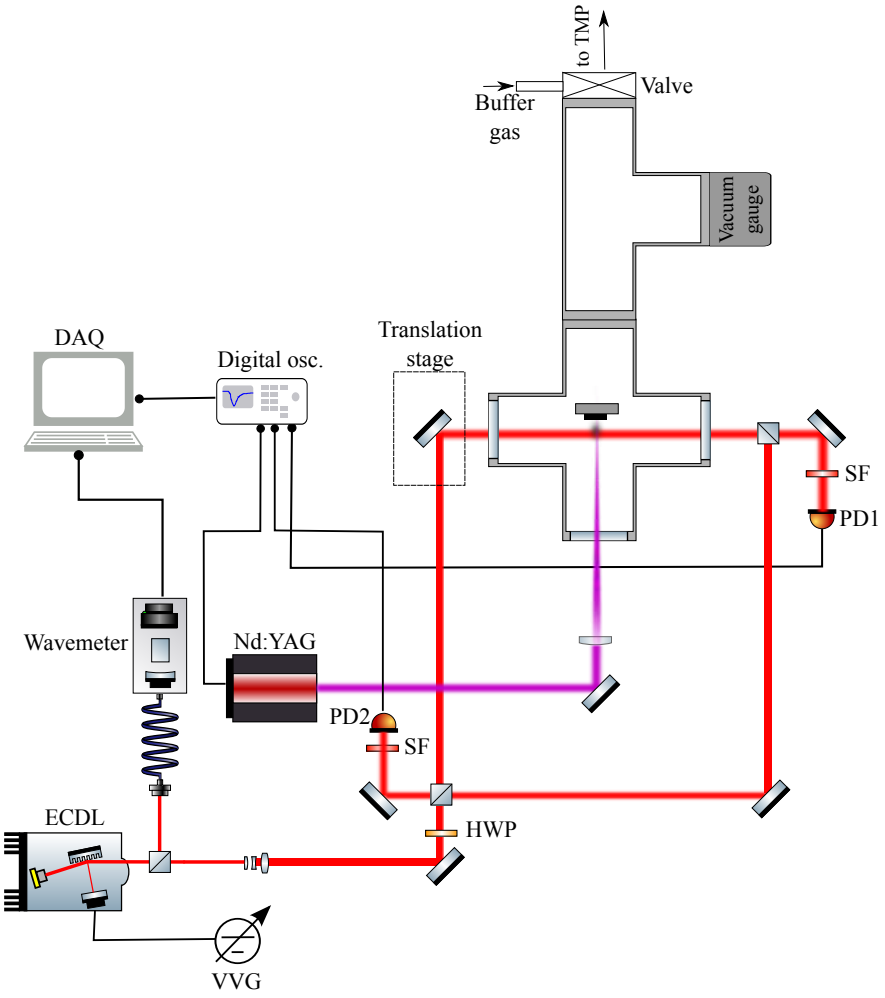

Figure 3.2: Schematic drawing of the experimental apparatud showing the test chamer and spectroscopy setup. HWP: half-wave plate; PD: photodetector; SF: spectral filter; TMP: turbomolecular pump; VVG: variable voltage generator; ECDL: external cavity diode laser. The inset shows the experimental geometry in close proximity to the target in the presence of an ablation plume with forward speed u at time t. The probe beam is normal to the plume. x_w: position of the chamber window; L: distance from the target to the probe beam; t/β : ypical width of the plume.

However, as will be noted below, the repetition rate has a pronounced effect on the resulting ablation plume in this room temperature setup.

The probe beam is a homebuilt, external cavity diode laser (ECDL) in the Littman-Metcalf configuration. A piezoelectric element controlled by a variable voltage source, was used to vary the horizontal alignment of the external cavity, enabling simple wavelength

tuning for spectroscopic measurements. For this preliminary setup, we had two ECDLs, one centered at 905 nm and one at 1060 nm, each with 25 mW of power, to probe the X-A and X-B molecular transitions. Beam splitters as arranged in Figure 3.2 allow counterpropagating probes for precise measurements of the Doppler shift due to any non-transverse alignment of the probe relative to the forward velocity of the ablation plume. This is crucial for non-flat targets such as ours, as each specific spot on the target that is ablated determines a different forward direction. We perform laser spectroscopy by monitoring the probe laser extinction after passing through a plume. The signal from the photodetector was monitored on a 200 MHz digital oscilloscope; a typical absorption feature lasts approximately 10 μs after ablation.

3.1 Time Resolved Resonant Absorption in an Ablation Plume

Ablation was fairly straightforward to achieve in our apparatus, in that we fired the ablation laser at a Barium Hydride target, and were able to perform absorption spectroscopy on the resulting plume with repeatable success. However, we noticed that there were two observable issues with these results.

- Shot-to-shot variation of the absorption signal. While the probe laser was not locked, its frequency drift and linewidth is much smaller than the expected linewidth of the transition. However, we still observed a decay in absorption signal strength as a function of shot number, indicating a loss in ablation efficiency. Figure 3.3 shows this decay and a subsequent mode-hop in the probe laser, which we can easily distinguish.

- BaH could only be detected in the region very close to the target sample <10 mm, and even then the signal was very small. The large temperatures (10,000 K) associated with

ablation meant that the resulting plume would disperse extremely quickly, and we could verify the drop off in density with our absorption measurement. As a result, scanning the laser frequency over a single ablation pulse was not possible as the interaction time between the plume and the probe was limited to about 5 μs. So typical spectroscopic measurements had to be made by stepping the probe wavelength between each pulse.

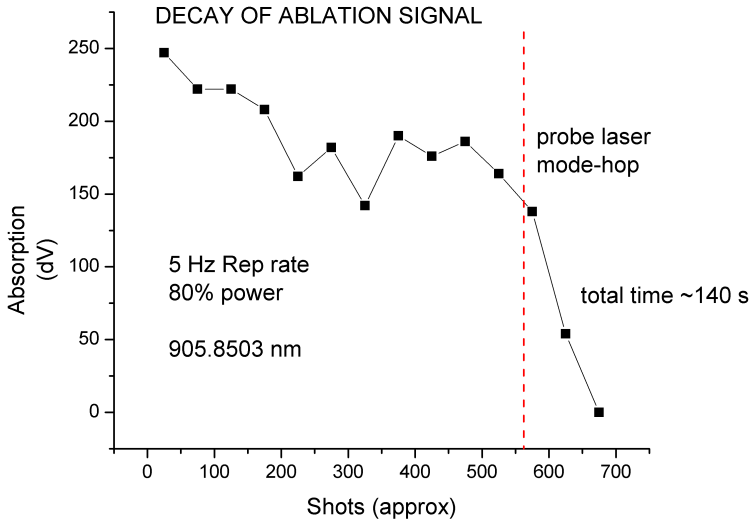

Figure 3.3: Premilinary measurements of BaH ablation via absorption spectroscopy at typical operating conditions showing decay of ablation efficiency and mode-hop issues.

Despite these limitations, modeling time-resolved absorption signals provide a wealth of information about the molecular ablation products, including temperature, forward velocity, and the initial density of the cloud. The function we are looking for will describe the density of the ablation cloud as a function of position and time, which we can then use in a standard AMO model for laser absorption to fit our signal. Ablation generated gas clouds have been studied and modeled for thin-film deposition, and here we adopt a commonly used hydrodynamical model that begins by describing an elliptical cloud with a full Maxwell-Boltzmann distribution that has equilibrated from desorption from a surface plasma. In the coordinate system described in the inset of Figure. 3.2, we can write this initial velocity distribution as,

$$p(\vec{v},T,u)(dv)^3 = \frac{\beta^3}{\sqrt{\pi^3}} \exp\left[-\beta^2(v_x^2+v_y^2+(v_z-u)^2))\right] dv_x dv_y dv_z, \tag{3.1.1}$$

moving with a stream velocity $\vec{u}$ normal to the target surface. $\beta = \sqrt{M/(2k_BT)} \equiv v_{th}^{-1}$ is the inverse of the most probable thermal velocity, M is the molecular mass, and T is the temperature after the equilibration time t_eq. The effective temperature of effusion for a diatomic molecule is $T \sim 0.8\,T_s$ [105], with T_s being the ablation surface temperature.

The evolution of this initial distribution can be described by solving the collisionless Boltzmann equation for the phase-space distribution $f(\vec{x},\vec{v},t) = f_0(\vec{x}-\vec{v}t,\vec{v})$, where f_0 is defined as the phase-space density at t=0, and for a rapidly equilibrating process, $f_0(\vec{x}-\vec{v}t,\vec{v}) = p(\vec{v},T,u)n_0(\vec{x}-\vec{v}t)$, where $n_0(\vec{x})$ is the initial spatial distribution. For this initial spatial distribution, we can assume the same two-dimensional Gaussian profile as that of the ablation laser, with radius $w_{pl} = 4\sqrt{ln(2)}\sigma_{pl}$, which defines the initial width of the plume, where σ_{pl} is the Gaussian RMS width. In the z-direction, we use a Dirac-Delta function, $\delta(z)$, so that,

$$n_0(\vec{x}) = \frac{N_0}{2\pi\sigma_{pl}^2} e^{-\left(\frac{(x)^2+(y)^2}{\sigma_{pl}^2}\right)} \delta(z) \tag{3.1.2}$$

To find the density of molecules after some time, $n(\vec{x},t)$, we integrate $f_0(\vec{x}-\vec{v}t,\vec{v})$ over the 3-dimensional velocity space defined by the differential volume element,$d^3\vec{v} = dv_x\,dv_y\,dv_z$, which yields,

$$n(\vec{x},t) \;=\; \frac{e^{-\beta^2\left(\frac{x^2}{t^2+w_{pl}^2\beta^2}+\frac{y^2}{t^2+w_{pl}^2\beta^2}+\frac{(z-ut)^2}{t^2}\right)} N_0\beta^3}{\pi^{3/2}t^3\left(1+(w_{pl}\beta/t)^2\right)}. \tag{3.1.3}$$

The quantity $w_{pl}\beta$ corresponds to a time scale for when a molecule at the center of the

plume can reach the edge of the ablation surface and vice versa, defining a equilibration time, t_{eq}. For typical ablation parameters, $T = 8000$ K and $w_{pl} = 100\mu$m, $t_{eq} \approx 80$ ns, which is well below the scale at which we observe absorption, as indicated in Figure 3.4. Therefore, we can take Equation 3.1.3 at $t \gg t_{eq}$, which yields a density function,

$$n(\vec{x}, t) \quad \propto \quad t^{-3} \exp\left[-\beta^2(x^2 + y^2 + (z - ut)^2)/t^2)\right]. \tag{3.1.4}$$

Equation 3.1.4 exhibits t^{-3} asymptotic time decay as predicted by Kools et al. [106]. In general, this time dependence does not hold for all models; for instance, in Ref. [107] a TOF distribution proportional to t^{-4} is employed to fit data, based on the theory developed in Ref. [105].

Having found an appropriate expression for the time dependence of the expanding gas-cloud density, we can turn to atomic physics to calculate the absorption of the probe light and expected photodetector signal. The probe is a laser with Gaussian width, w and intensity I, crossing the ablation plume transverse to $\vec{u}$. As a result, the absorption signal is a time-of-flight density measurement that integrates across the x axis of the plume. The expected signal can be modeled with the Beer-Lambert law. For an infinitesimal slice, dx of the plume, the differential change in light intensity is

$$-\frac{\mathrm{d}I}{I} \approx n(\vec{x}, t)\sigma(\omega)\mathrm{d}x, \tag{3.1.5}$$

where $\sigma(\omega)$ is the light-matter absorption cross-section, which is a function of the light frequency, ω. Integrating both sides of this expression over x across the plume diameter yields an equation for the intensity at the detector,

$$I = I_0 e^{OD(y,z,t)}. \tag{3.1.6}$$

The optical density, $OD(y,z,t) = \int_{-\infty}^{\infty} n(\vec{x},t)\sigma(\omega)\mathrm{d}x$, can be evaluated using Eq. 3.1.4 so that,

$$OD(y,z,t) \equiv -\ln\left(\frac{I}{I_0}\right) = \frac{N_0\,\beta^2\sigma(\omega)}{\pi t^2\sqrt{1+(t_{eq}/t)^2}} e^{\left[-\frac{\beta^2}{t^2}\left(\frac{y^2}{(1+t_{eq}/t)^2}+(z-ut)^2\right)\right]}, \tag{3.1.7}$$

which we can plug back into Equation 3.1.6 to give us an expression for the intensity that depends on time and the spatial coordinates, y and z. For small values of $OD(y,z,t)$, and small intensities, we can use a Taylor expansion to get the result for intensities beyond x_w. The intensity is also multiplied by the 2-dimensional Gaussian profile of the probe centered at $y = 0$ and $z = L$, which gives us the result,

$$\begin{aligned} &I(x > x_w, y, z, t) \\ &\quad = I_0 \exp\left[-2((z-L)^2+y^2)/w^2\right]\left(1 - \frac{N_0\,\beta^2\sigma(\omega)}{\pi t^2\sqrt{1+(t_{eq}/t)^2}} e^{\left[-\frac{\beta^2}{t^2}\left(\frac{y^2}{(1+t_{eq}/t)^2}+(z-ut)^2\right)\right]}\right). \end{aligned} \tag{3.1.8}$$

To calculate the photodetector signal, given by the change in probe laser power P_0, we integrate over y and z, which results in the time-resolved fractional absorption,

$$\begin{aligned} \mathcal{A}(t) &\equiv \frac{\Delta P(t)}{P_0} \\ &= 2N_0\sigma(\omega)\frac{e^{-\frac{2(L-tu)^2\beta^2}{2t^2+w^2\beta^2}}\beta^2\left(1+\mathrm{erf}\left[\frac{2Lt+uw^2\beta^2}{w\sqrt{2t^2+w^2\beta^2}}\right]\right)}{\pi t^2 w^2\sqrt{1+(t_{eq}/t)^2}\sqrt{\left(\frac{2}{w^2}+\frac{\beta^2}{t^2}\right)\left(\frac{2}{w^2}+\frac{\beta^2}{t^2+t_{eq}^2}\right)}\left(1+\mathrm{erf}\left[\frac{\sqrt{2}L}{w}\right]\right)} \\ &\simeq N_0\sigma(\omega)\frac{e^{-\frac{(L-tu)^2\beta^2}{t^2}}\beta^2}{\pi t^2} \qquad (\text{for } L > w/\sqrt{2}, t > \beta w). \end{aligned} \tag{3.1.9}$$

We can fit the above expression to our TOF profiles and, at the peak absorption, occuring

at time, t_p, we can estimate the molecular density as,

$$N_0 \simeq \mathcal{A}\frac{e^{\left(1-\frac{t_p u}{2L}\right)}\pi t_p^2}{4\beta^2\sigma(\omega)}. \tag{3.1.10}$$

The absorption cross section, $\sigma(\omega)$ is described by the optical Bloch equations and contains the natural Lorentzian lineshape. However, we must include Doppler broadening in our formulation, given that the thermal velocity spread is very large in our experiment. A molecule with velocity in the x direction, v_x will see counterpropagating probe light, with frequency ω, shifted by $+\omega v_x/c$. As a result, for a molecular transition with resonance frequency ω_0, the molecules will only absorb light that is red-detuned by $\delta = +v_x\omega_0/c$. Using this relation with velocity in the velocity distribution defined by Equation 3.1.1, we can then find the distribution of molecules with absorption frequencies shifted from ω_0 in the interval from ω to $d\omega$, where $dv_x = (c/\omega_0)d\omega$ [108]. Additionally, we want to account for the misalignment of the probe with the x-axis of the problem, which we can characterize with the angle, θ. The result is a molecule distribution given by,

$$p_x(\omega, T)d\omega = \frac{\beta c}{\omega_0\sqrt{\pi}}\exp\left[-\beta^2\left(\frac{c(\omega-\omega_0)+u\,\omega_0\sin\theta}{\omega_0}\right)^2\right]d\omega. \tag{3.1.11}$$

This defines the Gaussian spectral lineshape function for the absorption, which has full-width at half-maximum (FWHM) $\Delta\omega = 2\sqrt{\ln(2)2k_bT\omega_0^2/(mc^2)}$, and a Doppler-shifted center due to the misalignment angle θ. In the two level approximation, conservation of energy requires that the rate at which molecules scatter energy out via spontaneous emission equals the rate at which energy is absorbed. With N_1 and N_2 denoting the populations in the lower and excited states, this means that,

$$(N_1 - N_2)\sigma(\omega)I(\omega) = N_2A_{21}\hbar\omega, \tag{3.1.12}$$

where A_{21} is the spontaneous emission rate from the upper to lower level. Using the

optical Bloch equations, as in Ref. [108], we find that,

$$\sigma(\omega) = \frac{g_u}{g_l}\frac{\pi^2 c^2}{\omega_0^2} A_{21} \times g_L(\omega), \tag{3.1.13}$$

in which g_u and g_l are the upper and lower state degeneracies, respectively, and $g_L(\omega)$ is the lineshape function. Using this result, we see that integration of Equation 3.1.9 over the spectral distribution along the direction of propagation yields the fractional absorption spectrum,

$$\mathcal{A}(\omega) \propto \sigma(\omega) \equiv \frac{g_u}{g_l}\frac{\pi^2 c^2}{\omega_0^2} A_{21} \frac{c\sqrt{\pi}}{\beta\omega_0} e^{-\frac{\beta^2(c(\omega-\omega_0)+u\,\omega_0\sin(\theta)^2)}{\omega_0^2}}. \tag{3.1.14}$$

For a Doppler broadened transition, like that above, $\Delta\omega$ is directly linked to the effective temperature of the gas as,

$$T_K = \frac{mc^2}{8\ln(2)k_b}\left(\frac{\Delta\omega}{\omega_0}\right)^2. \tag{3.1.15}$$

Thus a measurement of a full absorption spectrum provides a direct measurement of the transverse translational temperature of the ablation plume.

In Figure 3.4, you can see sample traces, as well as best-fits to the data. These TOF profiles provide information about the molecular yield as well an estimate for the forward velocity of the plume, by measuring the shift in the peak of absorption.

Equation 3.1.9 can be useful for finding the initial density of the plume given a calculated absorption cross section, but we would also look to glean information about the spontaneous decay process of the excited molecular state through direct measurements of the absorption cross section. However, without independent measurements of the initial ablation plume density, this is not possible with the derived equations. Fortunately, the saturation intensity at which non-linear absorption dominates the transition between ground and excited

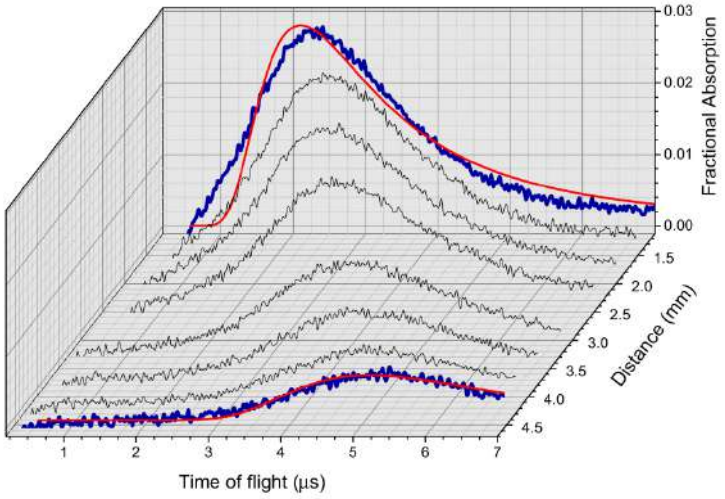

Figure 3.4: Time-of-flight absorption signals of probe laser passing through the BaH ablation plume. Each trace is recorded at a distance L, from the target, showing the clear drop off in signal. Red lines show the best fit of the data according to Eq. 3.1.9. The shift in the peak of absorption as a function of the distance provides an estimate for the center of mass forward velocity.

states also yields information about the strength of the transition. The standard saturation intensity for absorption is,

$$I_s = \frac{g_l}{g_u}\frac{\pi hc}{\lambda^3 \tau}\frac{1}{r(J,N)\, R_{v'v"}} \quad , \tag{3.1.16}$$

where τ is the lifetime of the excited state, $R_{v'v"}$ is the vibrational branching ratio, proportional to the Frank-Condon factor, and $r(J,N)$ is the branching ratio for the dipole transition moment of the excited rotational level $|N', J'\rangle$ to a specific rotational level $|N'', J''\rangle$ of the X state. The rotational branching ratio $r(J,N)$ can be expressed as function of the Höln-London factor $\mathcal{S}_{J'N'JN}$ as, [109]

$$r(J,N) = \frac{\mathcal{S}_{J'N'JN}}{(2J'+1)}. \tag{3.1.17}$$

In order to faithfully capture the lineshape features, we must again include Doppler

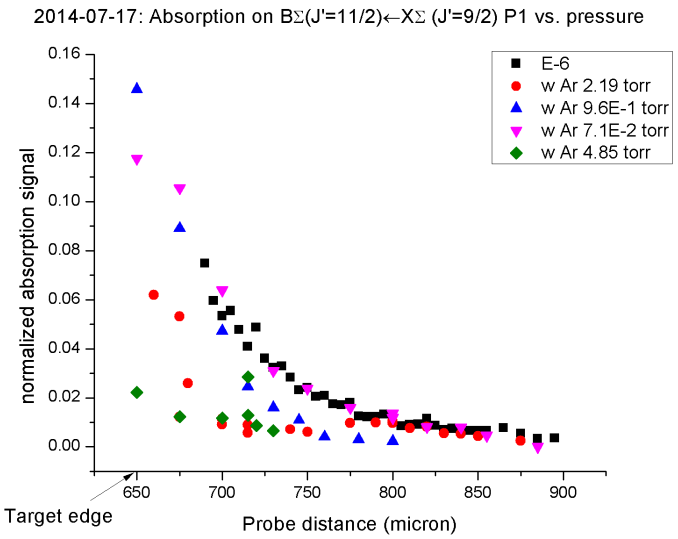

Figure 3.5: BaH absorption as a function of distance from the target with various Argon background pressures. The distances listed on the x-axis are with respect to an arbitrary zero. The target edge is at 650 mils.

broadening, characterized by $\Delta\omega$ as before, as well as transit time broadening, introduced by the finite interaction time of the plume with the probe, and characterized by the transit time, $\tau_t = 1/\Gamma_\tau = 2w/v_p$, which represents the time it takes for the peak density of the plume to pass through the laser beam. For the quasi-closed three level system formed by the two spin rotation states within the $N'' = 1$ ground state, and the $N' = 0$ excited state, the saturation effects can be modeled by solving rate equations for the level populations. The resulting effective saturation intensity is,

$$I_{s(eff)} \approx I_s \frac{1.2\Gamma_\tau \Delta\omega}{\Gamma^2} \frac{\Gamma + \Gamma_\tau}{[1 - r(J'', N'')R_{01}]\Gamma + 3\Gamma_\tau}, \tag{3.1.18}$$

in which $\Gamma = 1/\tau$ is the total radiative relaxation rate, and R_{01} is the vibrational branching ratio from the $B(v = 0)$ excited state to $X(v = 1)$ ground state.

3.2 Molecular Yield and Thermal Properties of the Ablation Plume

We studied the properties of the ablation plume by looking at laser absorption spectra of the probe light. In these experiments, we were limited to observing BaH produced from a solid BaH_2 precursor. For the yields measured in Fig. 3.6, the probe laser wavelength was tuned to the $P_2(4.5)$ transition. The ablation laser power could be varied either by adjusting the settings on the laser controller in increments of 5% of the full power (50 mJ), or by adjusting the distance between the focusing lens and the target. With these parameters, we can estimate the ablation laser fluence, F = (laser energy)/($\pi\times$beam waist^2). There is a clear ablation threshold around 90 J/cm^2 at which the $|N = 5, J = 4.5\rangle$ state population is about 10^7. Below this, there is no molecules observed.

The ablation threshold depends on several physical properties of the target surface such as the hardness, the roughness, and the reflectivity at the ablation laser wavelength. Both the density and the hardness of our BaH_2 chunks are low compared, for instance, to metallic Yb or hot pressed targets. Hence we considered this value to have large potential for improvement by switching to hard targets of BaH_2 as done in Ref. [64] for similar CaH molecules. However, later experiments in cryogenic setting showed little to no improvement for targets that were vacuum pressed out out BaH_2 powder.

We also observed a dependence of the molecular yield both on the pulsed laser repetition rate f_r and on the number of shots on the target. For a laser fluence of 129 J/cm^2, the absorption strength is nearly constant from $f_r = 1$ Hz to 15 Hz, and then reduces, while the shot-to-shot degradation rate depends linearly on f_r, with a characteristic decay constant $\tau(f_r = 2\text{ Hz}) = 2000$ shots. Surprisingly at $f_r = 15$ Hz, after about 100 laser pulses of constant decay of the absorption, the signal began to increase to twice its starting strength. We interpret this as the constant heating of the target due to a weak thermal link to its

environment. At $f_r = 20$ Hz we also observed a two-peak absorption profile due to thermal desorption of the hot surface after the first ablation event.

In a cryogenic setting, it is not realistic to run at repetition rates above 2 Hz, since the energy deposited on the cold cell will exceed the cooling power of the cryocooler used.

There is also a large dependence on target position, with many ablation spots producing orders of magnitude lower molecules. After a spot is exhausted, we must change the alignment of the final mirror to search for a new ablation spot. For a given spot, shot-to-shot fluctuations of up to 25% are observed in the probe absorption, therefore, we average at least 4 ablation pulses for a single data point.

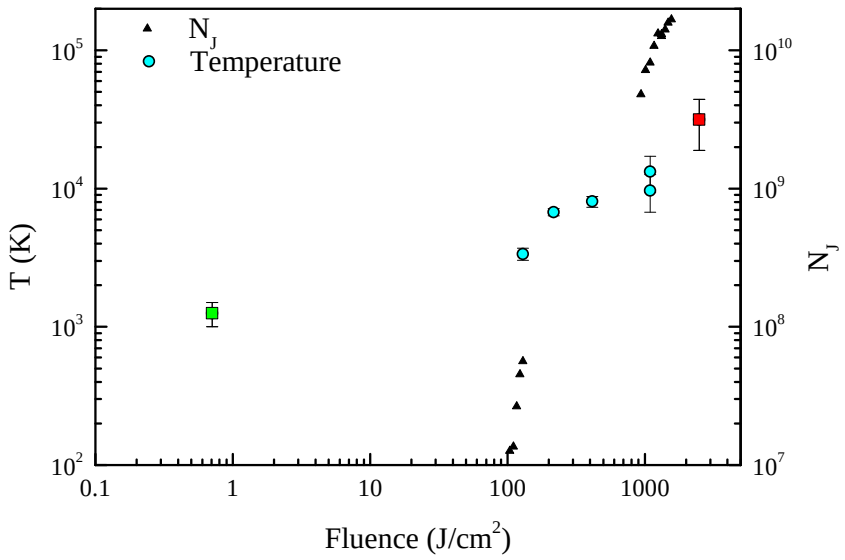

Figure 3.6: Experimental data obtained via laser absorption spectroscopy of ablated BaH and Yb (for comparison). The translational temperature and molecular yield in the J"=4.5 state are shown. For the population measurements, the ablation laser beam waist was set via the distance between the final lens and the target, and then the laser energy was varied between 50-100% of the max (50 mJ). Yb is shown to ablate much more easily, where comparatively little ablation fluence was required to make a significant plume.

The corresponding translational temperatures due to the ablation process were recorded by measuring the FWHM of the absorption spectra, which also depends on the fluence of the ablation beam onto the target. The thermal motion of the molecules results in the

inhomogenous broadening described in Eq. 3.1.11. The temperature was extracted using Eq. 3.1.15.

A minimum temperature of around 1800 K was measured at 16 J/cm^2. At this fluence value, the typical molecular yield is 1.8×10^8, and a forward velocity $u = 910$ m/s. For higher fluence we observed a linear increase of the translational temperature. The extrapolated temperature at the ablation threshold is about 1500 K. This estimate is in fair agreement with previous experiments on BaH gases created in King furnaces which indicated that BaH_2 has a decomposition point near 1300 K [110].

The molecules can also be characterized by their rotational temperature, which is determined by the population distribution within rotational levels. We can find the distribution of the total population among the rotational ground states $|N'', J''\rangle$ by comparing the relative strengths of observed absorption lines. These strengths are related to the population in each state, which in turn is governed by the Maxwell-Boltzmann distribution at some rotational temperature T_r [111]. Measurements of transition branches, which probe successive ground rotational states with the same angular momentum change, provide comparable strength from which to extract the populations. A measurement of the rotational temperature of the P_2 branch is shown in Fig. 3.7. Most of the rotational ground state population distribution measurements show a poor agreement with a pure Maxwell-Boltzmann distribution; with a cut-off rotational number $J = 11.5$, a best fit of the rotational temperature yields about 400 K - one order of magnitude lower than the translational temperature. Discrepancies between translational and rotational temperature in ablation plumes were earlier reported [54] and confirms the non-thermal origin of ablation. By using this rotational temperature, we can estimate the total molecular yield as

$$N_{tot} \simeq N_J \frac{(2S+1)k_b T_r}{(2J+1)\, hcB_X} \exp[\frac{hcF(J)}{k_b T_r}] \sim 3 \cdot 10^9, \tag{3.2.1}$$

where the effective rotational spacing $F(J) = B_X J^2 + (B_X - \gamma_X/2)J - \gamma_X/2$ takes into account the spin splitting of the considered transition branch. B_X and γ_X are the rotational, and spin-rotation equilibrium constants for the X-state.

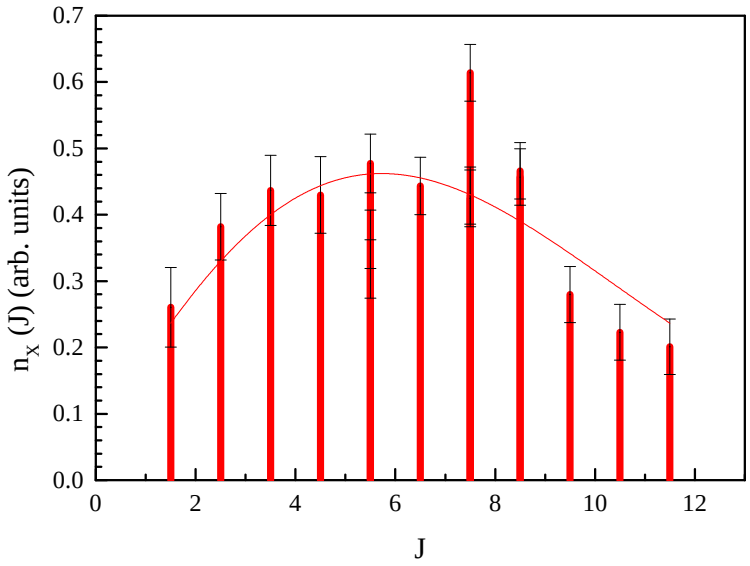

Figure 3.7: Relative populations of the ground rotational levels of BaH, measured in the room temperature apparatus. These measurements correspond to the absorption amplitudes of the first 11 lines within the $P2$ branch. The bar heights represent the measured line absorption,normalized according to Eq. 3.2.1.

3.3 Diffusion and Cooling with Room Temperature Buffer Gas

In order to explore the possibility of buffer gas cooling BaH, we looked to measure the scattering cross section between BaH and He as well as between BaH and Ar. The scattering cross section determines the efficacy of dissipating thermal energy in the molecules, which is crucial to know before embarking on an large investment to make a cryogenic apparatus. The buffer gases introduced were at room temperature (T_{bg} = 297 K), and of 99.999 % purity. As mentioned in previous chapters, buffer gas cooling reduces the temperature of

the species of interest by dissipating the translational energy via elastic collisions and the rotational energy via inelastic scattering. These different mechanisms can explain differences in final rotational and translational temperature below [54].

3.3.1 Translational Cooling

The cooling of the molecule of interest from a 10000 K surface plasma takes place via inelastic collisions that thermalize it with the cooler buffer gas. There are many published studies of ablation plumes expanding into a background buffer gas. Ref [104] showed that it can be divided in two phases: an initial ballistic expansion of the plume away from a surface plasma, followed by a diffusion outwards into the containing volume, which depends inversely on the buffer gas pressure. Thermalization of the ablation plume with the buffer gas occurs in both phases. As derived previously, the solution to the generalized differential equation for the ablation plume temperature as a function of collisions can be written in the form [112]

$$T_n = (T_0 - T)e^{-n/\kappa} + T. \tag{3.3.1}$$

However, our data is taken as time-of-flight measurements, not in terms of the number of collisions, therefore we must parameterize this solution as a function of time. The solution in Chapter 2 can be simplified to this end by taking the thermally averaged relative speed, $\bar{v}$, instead of the instantaneous velocity after each collision, to find an average rate of elastic collisions, $R = \bar{v}/l$, in which l is the mean free path. Then, $R = \rho_{bg}\sigma_{bg,BaH}\bar{v}$ is the product of the buffer gas density $\rho_{bg} = p/(k_b T_{bg})$ with p being the pressure read by the vacuum gauge (corrected for the particular buffer gas used), the collision cross section $\sigma_{bg,BaH}$, and the thermally averaged relative speed

$$\bar{v} = \sqrt{\frac{8k_B}{\pi}\left(\frac{T}{M} + \frac{T_{bg}}{m}\right)} \sim \sqrt{\frac{8k_B T}{\pi\mu}}\,. \tag{3.3.2}$$

As a result, our equation to fit the TOF data is,

$$T_t = (T_0 - T)e^{-Rt/\kappa} + T. \tag{3.3.3}$$

Therefore, in order to measure the cross section, $\sigma_{bg,BaH}$, we can measure the temperature of the gas as a function of buffer gas, which should show an exponential dependence, as in Eq. 3.3.3. The translational temperature can be determined by recording Doppler-broadened spectra of the BaH molecules and using Eq. 3.1.15. Figure 3.8 shows typical Doppler temperatures measured at different time intervals from the ablation pulse. The inset shows two spectra, one without He buffer gas which we use to extract the starting temperature of the molecules, and a second one taken with buffer gas, at a time 1.1 μs after ablation. The temperature evolution follows an exponential decay, as predicted by Eq. 3.3.3, for both He and Ar buffer gasses. The fitted thermalization rates are used to estimate the thermally averaged elastic cross sections $\sigma_{BaH,He} = (0.31 \pm 0.02)\, 10^{-20}$ m^2 and $\sigma_{BaH,Ar} = (8 \pm 3)\, 10^{-20}$ m^2 respectively. These results are similar to the ones reported for YbF [101], which indeed have been found to underestimate the actual cross sections by nearly one order of magnitude.

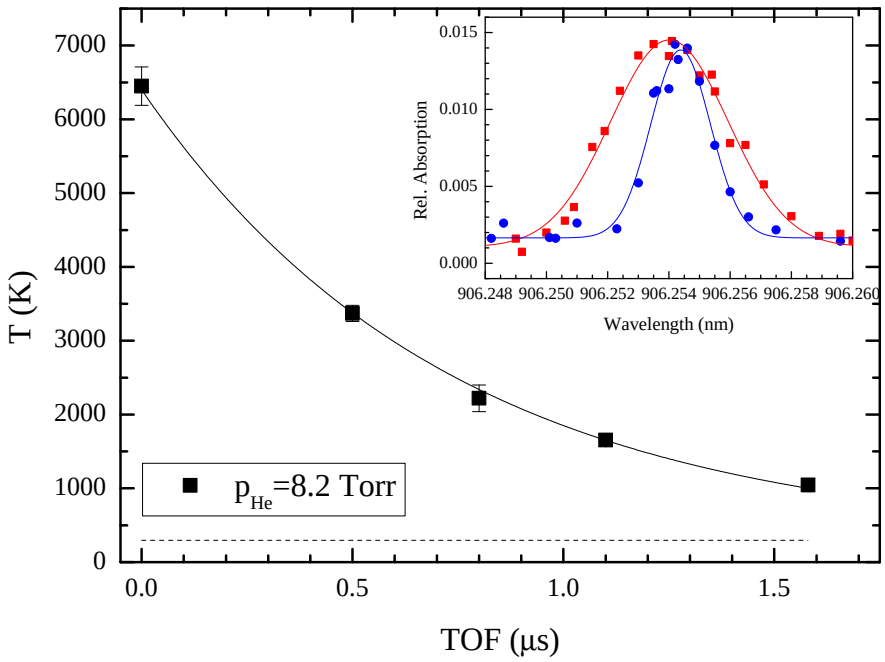

Figure 3.8: BaH Doppler temperatures as a function of time since ablation, measured in the presence of a Helium buffer gas. Doppler temperatures extracted via spectroscopic measurements of a typical P1 transition between the $X\Sigma$ and $B\Sigma$ electronic states. The fit is made with Eq. 3.3.3, and the exponential shows good agreement with the measured data. The inset shows two absorption spectra taken after 1.1 μs after ablation, with and without a Helium buffer gas. The narrower spectrum, taken in the presence of a buffer gas, demonstrates the translational cooling that the BaH molecules undergo during expansion into a buffer gas.

The cross section σ_{BaH-He} can also be found by studying the time dependence of the density of the ablation plume as it diffuses through the buffer gas. Here, we look closely at the tails of the TOF distributions, where molecules are no longer ballistically expanding through the fixed location of the probe beam, but rather diffusing out of the probe beam, lowering the density of the gas and thus the corresponding absorption signal. At these longer times ($t > 7\mu s$), the molecules have already thermalized with the local buffer gas distribution, as evidenced by the data in Fig. 3.8. Therefore, the fall-off in signal should have an exponential dependence governed almost completely by the solution to the diffusion equation.

Fitting the diffusion constant in exponential functions to the tails of TOF distributions in an Argon buffer gas yields $\sigma^{(D)}_{BaH,Ar} = (19 \pm 9)\,10^{-20}$ m^2, where the large technical noise near the end of the TOF data results in the large fractional uncertainty. We do this for a variety of pressures, as those shown in Figure. 3.9. We also repeated this measurement for Yb as a comparison, finding $\sigma^{(D)}_{Yb,Ar} = (1.9 \pm 0.1)\,10^{-17}$ m^2.

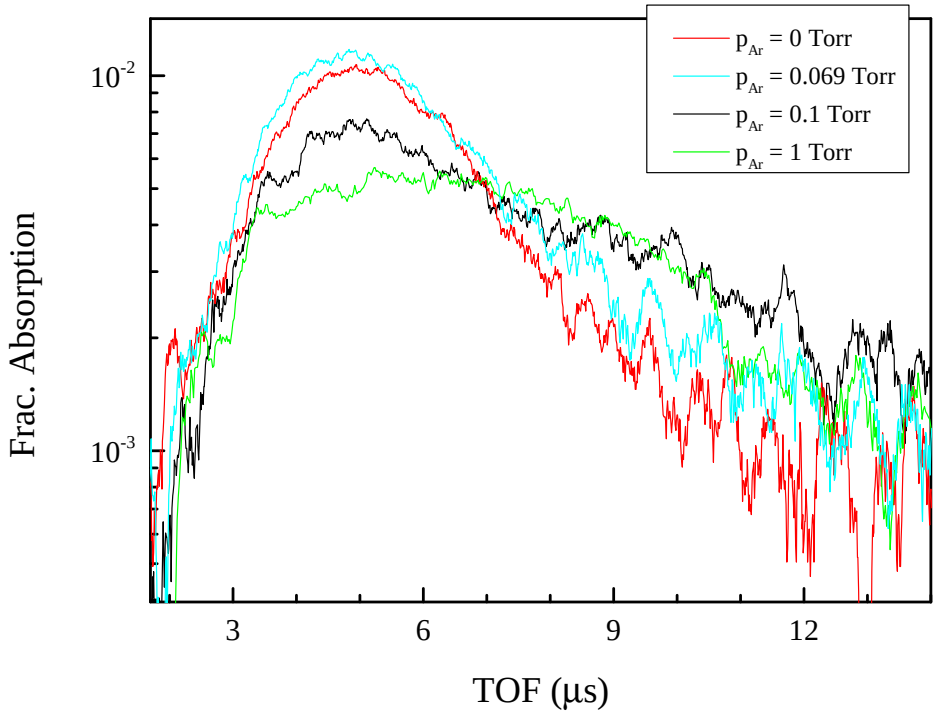

Figure 3.9: TOF profiles for BaH expanding into a Argon buffer gas. Times after 7 μs represent a change from ballistic to diffusive expansion.

The BaH-He elastic cross section, σ_{BaH-He}, found above is a crucial parameter for determining the brightness of a He buffer-gas cooled beam of BaH. The beam extraction efficiency of a molecule from the buffer-gas cell can be characterized by the dimensionless ratio, γ_{cell} of Equation 2.4.7, between the time it takes a diffusing molecule to stick to the cell wall and the He exit time from the cell. The brightest beams (up to 50% extraction efficiency) are achieved with $\gamma_{cell} > 1$. This ratio is directly proportional to σ_{BaH-He} and the buffer-gas density, therefore the comparatively low value of σ_{BaH-He} can be compensated by cell geom-

etry (such as the volume or target positioning) and experimental parameters that optimize the buffer-gas density.

3.3.2 Rotational Cooling

In addition to translational cooling, we studied the evolution of an initial nonthermal rotational distribution of BaH, described above, in the presence of a buffer gas. The rotational temperature T_r is estimated by fitting a Boltzmann distribution to the relative strengths of the P2 absorption lines originating from the lowest 11 ground-state rotational levels ($J = 1.5 - 11.5$), as shown in Fig. 3.10. Collisions of BaH with both Ar and He buffer gases at room temperature lead to absorption enhancement at higher J and a better agreement with a thermalized Maxwell-Boltzmann distribution. For Ar buffer gas, $T_r = 860 \pm 140$ K at p = 0.79 torr after 5 μs TOF, while for He, $T_r = 480 \pm 40$ K at p = 40 torr after 2 μs TOF. This result is in agreement with a thermalization process modeled by an exponential decay with the equilibrium temperature set by the instantaneous translational temperature. In the case of Ar, the rotational thermalization time is measured to be about $7 \pm 2.5\mu$s, which is about twice the estimated translational thermalizaton time. This is in agreement with previous results that report rotational cross sections smaller than or similar to the corresponding elastic cross-section values.

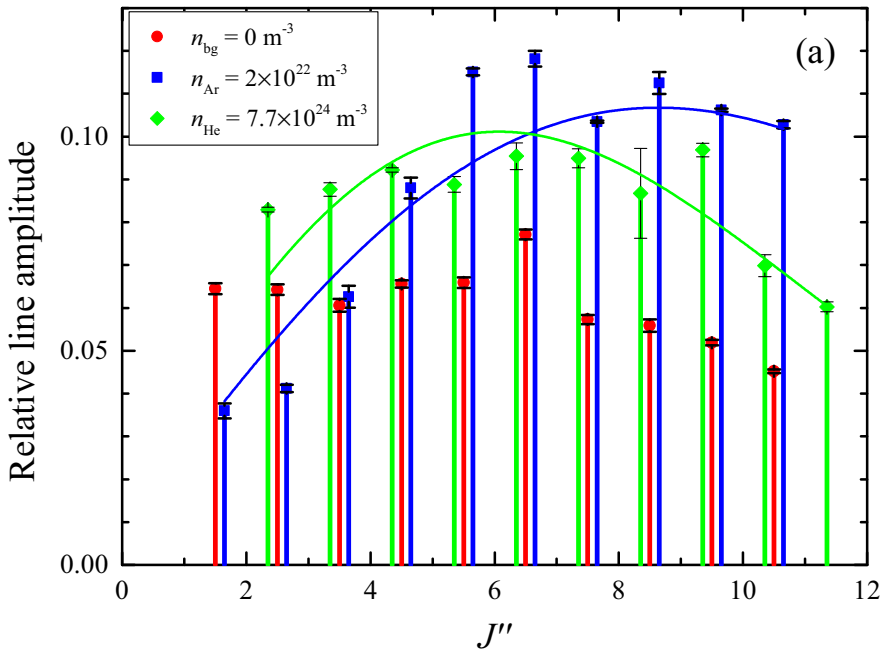

Figure 3.10: Rotational cooling of ablated BaH by Ar and He buffer gases. Here, we show experimentally measured absorption on P2 lines for various ground-state rotational levels, to determine the rotational temperatures with and without a room-temperature buffer gas. When there is no buffer gas, a rotational temperature cannot be reliably fit, since the distribution is not thermal.

3.4 Rovibrational Spectroscopy of the $B \leftarrow X(0,0)$ Transition

The motion of atoms or molecules relative to a probing laser results in a predictable broadening of absorption spectra. For a thermal distribution, there is equal broadening to both higher and lower frequencies, and additionally, any net motion of the atoms or molecules, such as in an ablation plume, results in an overall shift of the line. Thermal broadening can be calculated and extracted from a Gaussian width in the absorption spectra, especially when the broadening is much larger than the natural Lorentzian linewidth of the transition.

This is a formal definition for Doppler broadening, which limits the ultimate resolution of the room temperature apparatus.

We performed precise laser spectroscopy on the rotational levels of the $B^2\Sigma^+(v'=0) \leftarrow X^2\Sigma^+(v=0)$ electronic transition by observing the absorption lines of the two P branches ($\Delta J = \Delta N = -1$) and the satellite ${}^PQ_{12}$ branch ($\Delta J = 0; \Delta N = -1$). The identification of the observed transitions was based on the lines reported in Ref. [113] and on the expected values calculated from the equilibrium constants [72]. The calculated values of the rotational transitions assumed both the ground X and excited B states are pure Hund's case (b), a result of which is the splitting of rotational states via the spin-rotation interaction into two manifolds with angular momentum $J = N \pm S$ that are denoted $F(N)$ [114].

$$\begin{aligned} F_1(N) &= BN(N+1) - DN^2(N+1)^2 + HN^3(N+1)^3 + \frac{\gamma_N}{2}N \\ F_2(N) &= BN(N+1) - DN^2(N+1)^2 + HN^3(N+1)^3 - \frac{\gamma_N}{2}(N+1), \end{aligned} \quad (3.4.1)$$

where $F_1(N)$ and $F_2(N)$ refer to the components with $J = N + 1/2$ and $J = N - 1/2$ respectively, and the effect of centrifugal distortion on the spin-splitting constant is approximated as $\gamma_N = \gamma + \gamma_D N(N+1)$. For details on molecular structure, refer to Chapter 5.

We tuned our ECDL laser over 5 nm by adjusting the cavity mirror angle and monitoring the wavelength on a wavelength meter (HighFinesse WS-6). In this way, we could locate all lines from $J = 1.5$ to $J = 8.5$ for the P_1 branch, from $J = 1.5$ to $J = 11.5$ for the P_2 branch, and from $J = 0.5$ to $J = 3.5$ for the ${}^PQ_{12}$ branch. The values of the corresponding transition wavelengths are listed in Table 3.1. A piezoelectric element on the cavity alignment mirror enabled fine tuning on the wavelength to record complete Doppler broadened spectra from most of the absorption lines. Sample lineshapes are shown in Fig. 3.11, which have been fitted with a Gaussian function fit that yields typical FWHM of 3 pm.

Table 3.1: List of all the transition lines identified by laser absorption spectroscopy and their comparison with previous data. The number in parentheses is one standard deviation representing fit and systematic error. Where no error is present, only the absorption peak has been identified.

Branch	J	This work (nm)	Ref. [113] (nm)	Theory [72] (nm)	Difference (pm)
P_1	1.5	905.31970(3)	–	905.32024	0.54
	2.5	906.09010(8)	906.0991	906.09132	1.22
	3.5	906.88130(5)	906.8896	906.88223	0.93
	4.5	907.69225(6)	907.6947	907.69279	0.54
	5.5	908.5226	908.5375	908.52281	0.21
	6.5	909.3735	909.3769	909.37212	-1.35
	7.5	910.2390	910.2295	910.24055	1.55
	8.5	911.1269	911.1335	911.12796	1.06
P_2	1.5	905.46645(7)	–	905.46699	0.54
	2.5	905.85052(6)	905.8521	905.85112	0.6
	3.5	906.25370(8)	906.2593	906.25420	0.5
	4.5	906.67563(4)	906.6816	906.67614	0.51
	5.5	907.1161	907.1307	907.11690	0.8
	6.5	907.5765	907.5851	907.57642	-0.08
	7.5	908.0541	908.0656	908.05467	0.57
	8.5	908.5510	908.5590	908.55162	-0.52
	9.5	909.0685	909.0777	909.06724	-1.26
	10.5	909.6014	909.6168	909.60153	0.13
	11.5	910.1555	910.1599	910.15449	-1.01
${}^{P}Q_{12}$	0.5	905.29633(1)	–	905.29664	0.31
	1.5	906.05214(3)	–	906.05193	-0.21
	2.5	906.82640(8)	–	906.82702	0.62
	3.5	907.6195	–	907.62171	1.3

These measurements yield a resolution three times higher than the ones measured in a furnace with a Fourier transform spectrometer [72]. The measured values of the absorption lines deviate from the expected wavelengths by about 120 MHz on average with a standard deviation of 280 MHz, which is comparable to the 200 MHz accuracy of the wavemeter.

The ground state spin splitting $\Delta\nu_{ss}$, shown in Figure 3.11 is of particular interest for possible laser cooling of the BaH molecule. The rotational branching in a molecular cooling

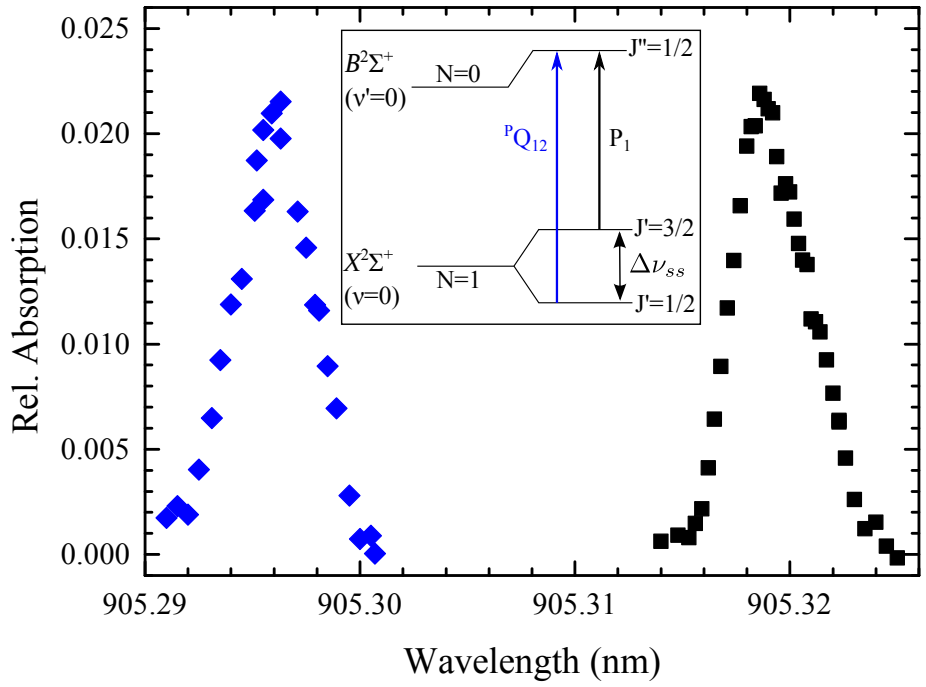

Figure 3.11: Sample lineshapes showing absorption of the $B^2\Sigma^+(N=0) \leftarrow X^2\Sigma^+(N=1)$ transitions. The spacing between the peaks (8.53 GHz) is the spin splitting of the $X^2\Sigma^+(N=1)$ level. Inset shows the rotational energy diagram.

cycle can be limited by driving an $N' = 0 \leftarrow N'' = 1$-type transition (see, for example, [115]), where the single prime indicates the excited state. For the excited state $B^2\Sigma^+(N' = 0, J' = 0.5)$, parity selection rules allow only two possible decay channels (neglecting the hyperfine structure): one through a P_1 transition to $J = 1.5$, and the second through the satellite branch ${}^PQ_{12}$ to $J = 0.5$, both of which have the same rotational line strength [116]. We observed well resolved spectral profiles, measuring a frequency splitting $\Delta\nu_{ss}(N = 1) = 8.53(2)$ GHz centered at about 905.3 nm.

Given their importance, we performed measurements of both the $P_1(1.5)$ and the ${}^PQ_{12}(0.5)$ transition wavelengths with higher accuracy by means of a Doppler-shift free interrogation scheme. Doppler-shifts due to a mismatch between the probe beam and the perpendicular to the ablation plume propagation direction are the principal systematic error in determining the absolute wavelength of these transitions. The misalignment is difficult to track because

the forward velocity vector of the plume is determined by the particular positioning of each BaH_2 sample and its surface properties.

The principal systematic effect on direct spectroscopy on ablated BaH molecules is the Doppler effect due to a non-zero angle of the line-of-sight with the perpendicular direction of the forward velocity, which depends on the particular positioning of each BaH_2 sample and its surface regularity. However, we can introduce a second beam, counter-propagating to the initial laser. If exactly colinear to the first beam, the second beam will be shifted by the overall plume velocity exactly opposite that of the first beam. Therefore, the average measured frequency should be that of the molecular transition. We did exactly this by co-aligning two counter propagating probe beams (with mrad precision) and probing the ablation plume with the two beams, either one after the other or simultaneously, as shown in Fig.3.12. The differential absorption from each beam's respective photodetector is centered on the Doppler-free resonant wavelength, while some common-mode noise sources like the ablation yield and laser frequency cancel out, increasing the detection signal-to-noise ratio leading to an uncertainty as low as 3.6 MHz.

Note that this is separate from the saturated absorption spectroscopy technique, where the thermal motion of the molecules or atoms can also be removed via 'hole-burning' of the velocity distribution. In our set-up, such complete removal of the Doppler effect is not possible because the motion of the molecules transverse to the probe beam propagation direction is too fast.

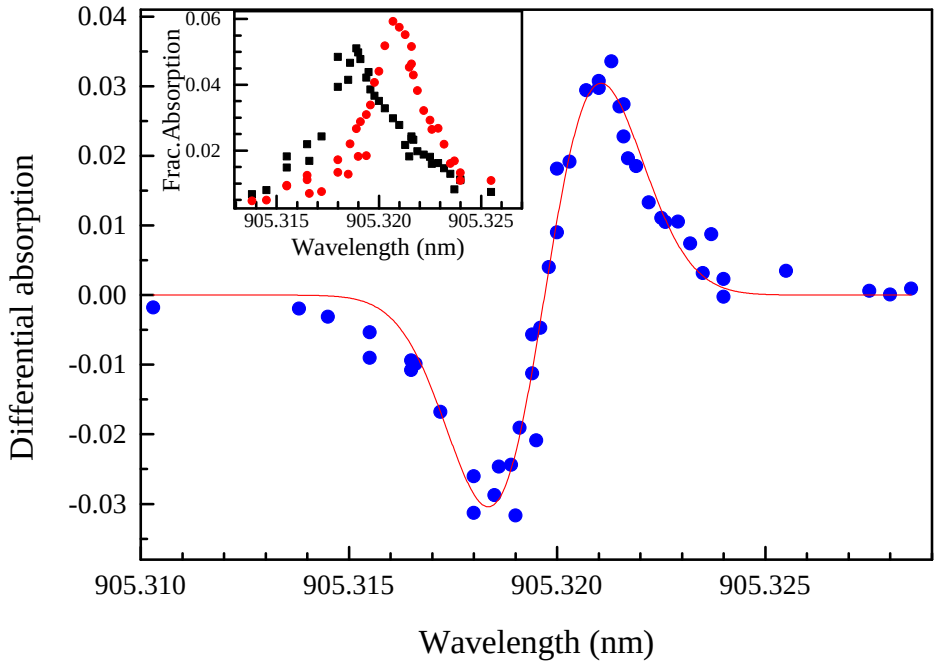

Figure 3.12: Measurement of the Doppler shift for the transverse spectroscopy on the $P_1(1.5)$ cooling transition. The signal shown is the difference in absorption signals between the two photodetectors for counterpropagating beams passing through the ablation plume. The inset shows the two raw photodetector absorption signals

It is possible to increase the accuracy on the ground state $\Delta\nu_{ss}$ by measuring the frequency difference between each P_1 line and its corresponding satellite transition ${}^PQ_{12}$ as a function of N, which depends only on γ_N, as well as the line splitting of the two P branches:

$$\Delta\nu_{12}(P) \equiv P_1(N) - P_2(N) = (\gamma_B - \gamma_X)N - \frac{1}{2}(\gamma_B + \gamma_X). \tag{3.4.2}$$

Here, the γ's are the spin splitting constants for the B and X electronic levels. Both the line splitting and the spin splitting data (10 data points and 4 data points, respectively) were used to determine the spin rotation constants of equation 3.4.2. The resulting values are $\gamma_X = 0.19165(88)$ cm^{-1}, $\gamma_B = 4.7532(12)$ cm^{-1}, and $\gamma_{BD} = 0.0003297(55)$ cm^{-1} for the centrifugal distortion term for the B state, which contributes to the energy as N^2. The uncertainty is limited by the scatter of line-splitting points with higher N where no full

spectrum was recorded. The ground state centrifugal distortion constant γ_{XD} was neglected in this calculation because it is expected to be on the order of 10^{-5} cm^{-1}. The agreement with Ref. [72] (in which the number of transitions recorded is in the hundreds) is at the fourth significant digit for both the linear spin rotation constants.

Chapter 4

Apparatus

The apparatus we have built closely resembles some of the other existing experiments for buffer gas cooling molecules. As discussed previously, at the heart of every apparatus is a small copper chamber, or cell, at 4K. Inside this cell, a molecular precursor must be ablated into a flowing gas of 4K He where it will thermalize, and the resulting flow should be extracted as a beam. Most experiments to date use a Pulse Tube Refrigerator (PTR) to cool the copper cell down to the required temperature. The PTR has two stages of cooling, one at 40K and one at 4K, and it must be contained inside of a vacuum chamber. To reduce heat loads, radiation shields should be implemented, and careful consideration must be taken into the support structure. There are variations in the details, but the above parts are common to pretty much all buffer gas cooling apparatuses. Needless to say, all copper parts should be Oxygen-Free High-Conductivity (OFHC).

4.1 Beam Source Cryostat

4.1.1 Vacuum Chamber

The vacuum chamber was custom designed by ZLab and built by Precision Cryogenic Instruments. The design is based upon a Doyle Group's iteration of a buffer gas cooling apparatus that included options for a 1K He pot. This option can allow pumping on liquid ^{4}He at the 4K stage to further reduce the temperature of the copper cell to 1K. However, quite a bit of extra space is required. Following the advice of the Doyle group, the design was made reasonably large to allow for flexibility in the interior design of the system, as well as to make working inside easier. In the end, it turns out that the $N'' = 1$ rotational state in BaH that we are most interested in is most populated at around 6-7 K, and we had enough power in the PTR to cool the cell to this temperature, so the 1K pot was not necessary for this molecule. As a result, this vacuum chamber is quite oversized as a cryostat for the source. Its large size means that it is harder to pull vacuum, and there is more blackbody radiation. Furthermore, the design places the cell 40 cm from the exit aperture, which limits optical access to the beam. On the plus side, the large size makes repairs and modifications particularly easy, and we can fit a large amount of charcoal cryopump inside the 4 K region.

The chamber design consists of a welded aluminum frame with 6 separable panels for the sides. These are attached via 5/16" socket cap head screws spaced 2" apart around the perimeter of each panel. The vacuum seal is made with a custom made o-ring which fits into a groove cut into the frame. Each of the side panels has an ISO-80 adapter for a custom made window, which provides optical access to the buffer gas cell. The front panel has a KF-50 adapter and the top panel has 4, KF-40 adapters, a custom hole for the PTR, and an ISO-100 adapter for the 170 L/s Pfeiffer-Balzers TPU 170 turbo pump. Since the ultimate pressure of the chamber is limited by the panel seals, we maintain o-ring sealing for all the openings. The KF-40 openings on the top are used for electrical connections, vacuum measurement,

a gas-input line, and a pressure relief valve - which is a necessary safety component of any cryogenic set-up. A port for a residual gas analyzer is also available, which has proved particularly useful for leak detection.

We made the custom made windows by using epotek- epoxy to glue BK-7 glass windows to ISO80 to ISO100 conical adapters. Since the BK-7 glass has an emissivity that is an order of magnitude higher than that of aluminum, and there is, by design, a direct line of sight to the cell, the radiative heat load can be quite significant. Therefore, these windows should be limited in size, as should any optical access apertures on the inner radiation shields.

The procedure for gluing the windows is relatively simple, but requires care. The epoxy must be prepared carefully, following the manufacturer's instructions, using appropriate precision weight scales to proportion the components, and stirring gently to minimize the introduction of air bubbles. Of most importance is pumping on the prepared epoxy with a rough pump for about one hour to remove any bubbles that are inevitably introduced in the mixing process. To actually glue the windows, the surfaces must be well cleaned with acetone, followed by isopropanol, and free of any dust. Ideally, they should be cleaned and glued inside of a fume hood. We found that the seal was best made when we placed just enough epoxy to barely cover the contact surfaces when the pieces were pressed together. Also, we immediately remove any excess epoxy that drips into the inside of the aluminum adapter, as this can outgas into the vacuum. After pressing the two pieces together, visually inspect for any bubbles, and try to remove them by applying pressure to that region. We found that baking the windows did not help their performance. Typical vacuum in our system with a 170 l/s turbo pump before cooldown is $1\text{x}10^{-5}$ torr.

As mentioned before, cooling is achieved with a Pulse Tube Refrigerator, and specifically, we use a Cryomech PT 415. This PTR has 1.5 W of cooling power on the 4K stage, and 40 W of cooling on the 45K stage. Descriptions for how this device operates are readily available elsewhere, and its specific operation only matters to this project if it fails. Each

stage of the PTR is thermally anchored to a radiation shield, which we label respectively as the outer and inner shield. Schematics and drawings can be found in Appendix D.

The entire cryogenic apparatus is built around the geometry of the PTR, however, since the PTR has a limited load bearing weight capacity on it's cold stages, it is not possible to hang the radiation shields and associated machinery directly to it. Instead, the outer shield, which is thermally anchored to the 45K stage of the PTR, is suspended via 6, stainless steel rods from welded support brackets on the top panel of the chamber. Therefore, the upper panel of the chamber supports the entire weight of the experiment. This outer shield, like the outer chamber, is made of aluminum, and consists of 4 corner struts and 6 sides that are all .125" thick, except the top, which is .625" thick. This upper plate is thicker since it must support this shields' weight, as well as the 4K shield assembly. It also contains various holes for feedthrough and temperature sensors, as well as mounting holes for a Helium bobbin and thermal links. All outward facing sides of the aluminum panels for the outer shield are polished using a buffing wheel and some basic polishing grease. This process is arduous, but is vital to maximize the reflectivity in order to minimize the radiative heat load. After polishing, the panels should be sonicated in an acetone bath to remove the polishing grease and then cleaned using isopropanol.

From the outer shield hangs the inner shield - essentially a copper box - by 5 additional stainless steel rods. The design is slightly different from that of the 45K shield. Rather than corner struts, the top and bottom panels are 3/8" thick with tapped holes around the edges, and thin side panels are screwed to these plates with brass screws. The top panel has a large opening for the PTR 4K cold finger, various holes for thermal lugs, electrical connections, and He line, as well as slots to mount the buffer gas cell connector. The design allows for some flexibility in the arrangement of things inside the 4K box, and the side panels can be easily remachined larger to accommodate a 1K pot. Like the outer shield, the panels for the inner shield are polished in a similar manner to ensure good reflectivity.

The PTR and the shields must make good thermal contact to minimize cool-down time and maximize the cooling power of the PTR. However, the PTR stages have a quoted mechanical motion between 1-2mm between room temperature and the minimum temperature, so the thermal links must be flexible to ensure that there is no significant strain on the delicate PTR tubes. We use a thermal link design that is inspired by those used at Harvard in the Doyle group. Each thermal link consists of two 0.625" diameter braided OFHC copper ropes that are threaded through a hole in a copper lug, and welded along the back using spare copper filler material to fill gaps. The weld joint is then milled down to make a smooth surface. These lugs are then cleaned and can be anchored to the PTR and shield with bolts, and using a thin layer of Apiezon N vacuum grease. More thermal links means a better thermal connection, and so we extend each stage of the PTR using copper that is cut to fit our chamber well, and are able to fit 6 thermal links, each with two copper braids on the outer shield, and 4 thermal links to the inner shield.

In order to introduce 4K Helium gas into the cell, we flow ultra-high purity Helium gas through a series of copper and stainless steel tubes to get to the cell. To control the flow, high purity (5-9) Helium is regulated at a standard bottle, and makes its way to an Aera Mass Flow Controller (MFC). The MFC can control the Helium flow rate between 0-20 sccm with 0.5 sccm accuracy using a solenoid valve. Following the MFC is a needle valve to neck down the vacuum conductivity between the MFC and the cryostat, ensuring the pressure differential across the MFC is not too large. From here, the Helium enters the cryostat.

The Helium is cooled through a 2 stage heat exchanger, with each stage connected to a radiation shield. The heat exchangers consist of a copper tube wrapped in a coil around a copper cylinder, and we call this assembly the bobbin. The bobbins are thermally isolated from each other and the outer vacuum chamber by using the stainless steel sections of tube between them. We found that the thermal connection between the copper tube and the copper cylinder is best made by soldering these two pieces together with a low temperature

silver solder (at least 4% Ag). Simply adding a bunch of Apiezon N does not do the trick. (See Appendix B for details).

Introducing a constant flow Helium buffer gas into the chamber is problematic for the vacuum and thus for the heat load on the inner sections (see below). At cryogenic temperatures, every cold surface is a pump at some level, since most molecules will freeze and stick to any surface they touch. Helium, however, does not freeze. The common solution for removing Helium gas loads is to use cryopumping activated charcoal. In granular form at cryogenic temperatures, the charcoal is able to trap and hold the Helium gas in its porous structure. Experimentally, it has been determined [117] that activated coconut charcoal is the most effective at cryopumping Helium gas, and so we coat the inner surfaces of the inner radiation shield with it. In order to make good thermal contact, we use Epotek thermal epoxy which is well rated for strength and thermal conductivity at cryogenic temperatures.

There is a limit to how much Helium can be pumped by the cryopump as it saturates to capacity, and the charcoal must be regenerated which can be achieved simply by warming up the apparatus to approx 40 K. It is important to note that charcoal absorbs and retains both water and oxygen at room temperature, and this is partially released under vacuum our apparatus, which is particularly troublesome since BaH2 is water and oxygen reactive. The water and oxygen can be removed by periodically baking the copper panels that the charcoal is mounted on at 200^{o} C, but this process causes oxidation. In practice, we have found that cycling the temperature of the system between 4K and room temperature improves the charcoal performance. Since an entire cycle takes about 24 hours, we try and do this on the weekends.

4.1.2 Heat Loads and Radiation Shields

The two contributions to the heat load on the shield are conductive and radiative. Here, we estimate the steady state heat load that the PTR will have to remove from the system. The

differential form of Fourier's Law for conduction in materials tells us the heat flux per unit area with the relation [102]:

$$\vec{q} = -k\nabla T$$

Where k is the thermal conductivity of the medium and ∇T is the local temperature gradient. Integrating over the material's total surface area is straightforward, especially for a material with a 1-D temperature gradient, like the support rods we use in our radiation shields, and we find,

$$\frac{\Delta Q}{\Delta t} = -\frac{A}{L}\int_{T_0}^{T_f} k dT$$

Where A is the area and L is the length of the rod in question. k is not a constant over large temperature gradients, which is why it stays in the integral. The rods we use are stainless steel, and we can find data from Brookhaven national lab for the value of the integral for Stainless steel [118]. A rod of length 10 cm and radius 0.4 cm connecting the 45K stage to 300K stage conducts 1.3(3) Watts of energy. Assuming a 20% error in the rough integral value, with 6 such rods, the thermal conductive load to the 45K stage is 0.75(3) Watts.

Between the 45K stage and 4K stage, the rods would be of length 12 cm and same radius. This yields a heat load per rod of 0.19(2) Watts. Given 5 rods to hold up this section, the heat load is 0.94(2) Watts.

We should also be concerned with electrical wires for the silicon diode thermometers we use to measure the temperature of the shields and buffer gas cell. Factoring in the 4 electric copper wires (26Gauge corresponds to r=0.02 cm) for the temperature monitor, the heat load from 4K to 300K (running a distance of 30cm) is 0.27(1) Watts. However, realistically, we could presumably create a thermal contact with the 45K stage, and reduce this heat load. Using a length of 12 cm and the new temperature difference, we find that the heat load from these 4 wires is 0.19(1)Watts.

Between the 45K stage and the 300K stage (distance 18cm), these wires would put an additional heat load of 0.32 Watts.

The radiative component of the heat load is much more significant. Following Reference [119], we can estimate the heat load due to radiation on the 45 K radiation shield as:

$$Q_{rad} = \frac{\sigma A_1 (T_2^4 - T_1^4)}{\frac{1}{\epsilon_1} + \frac{A_1}{A_2}\left(\frac{1}{\epsilon_2} - 1\right)}$$

Where, Q_{rad} is the power radiated to the inner shield from the outer shield in Watts, A_1 is the area of the inner shield (m^2), A_2 is the area of the outer shield (m^2), T_1 is the temperature of the inner shield (K), T_2 is the temperature of the outer shield (K), ϵ_1 is the emissivity of the inner shield(0.05 for polished aluminum, 0.03 for polished copper), ϵ_2 is the emissivity of the outer shield (0.095 for unpolished aluminum), and σ is 5.67x10$^-$8 $(W \cdot m^{-2} \cdot K^{-4})$ [120].

Given the cryostat dimensions, the radiative heat load on the 45K stage is 26 Watts.

For the 4K shield, we use the upper limit of the emissivities to find that the radiative heat load is less than 0.009 Watts.

4.1.3 Buffer Gas Cell Geometry

Figuring out the optimal geometry of the cell is a complicated art. While the basic calculations in earlier sections can guide us, there is a large parameter space to explore, and each physical modification to the cell requires at least 28 hours to test, which includes warmup and cooldown times. There is not a detailed chronicle of failed cell geometries, which makes deviations from the most common designs futher difficult to motivate. In the case of BaH, the relatively small scattering cross section with Helium, combined with a low ablation yield means that we had to spend a great deal of time squeezing every last molecule out of the cell. In this section, I will outline most of the cell geometries that have been explored, but there

are certainly gaps in the possible parameter space, given that it is difficult to change only one parameter, and further difficult to understand which change actually increases the extracted molecular yield. Finally, the cell geometry must be optimized to produce the highest number of molecules with longitudinal velocities that are feasible to slow.

In high flow regimes, the cell temperature increases since the PTR cannot completely cool such a large influx of He before it gets to the cell. Additionally, high flow regimes and thus high densities lead to more supersonic beams and high forward velocities. Therefore, we must limit the aperture size of the cell to maintain a certain buffer gas density. The cell length is limited on the shorter end by the thermalization time of the molecules, since they need to be able to thermalize with the cold Helium gas before exiting the chamber. As we saw above, this is set by the cell aperture. The length is limited in the longer end by the diffusion time of molecules to the wall. Finally, we can only lower the temperature of the cell as low as our PTR can cool.

Designs for the various cells below can be found in Appendix D.2.

The initial cell we installed was designed to offer variability in cell length, which was a fairly mysterious parameter (Figure 4.1). Other buffer gas experiments have cell lengths between 1 and 3 inches, so we attempted to be able to vary this distance by making a long cyclindrical cell with an insertable front piece which would protrude into the cell cavity, shortening it. The cylindrical diameter was 1", and apertures were varied between 3 mm and 7 mm diamter. One drawback of this cell was the lack of internal optical access for short configurations. One side of the cylinder had a hole with window for ablation access, and opposite it, a flat section was milled out to facilitate easy gluing of samples.

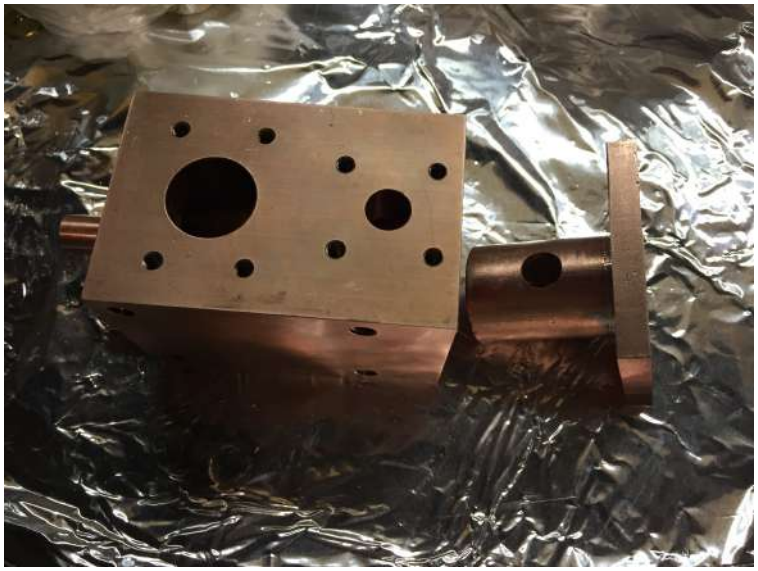

Figure 4.1: Initial cell design with removable insert to vary cell length.

The optical access of this cell only permitted probing the molecules or atoms $\approx$ 1 cm from the output of the cell. Since BaH was expected to be difficult to detect, we initially loaded our cell with Yb metal and were pleasantly surprised to see the signal shown in Fig. 4.2. Here, the effective cell length was maximal at 2.8", and the cell aperture was 3mm.

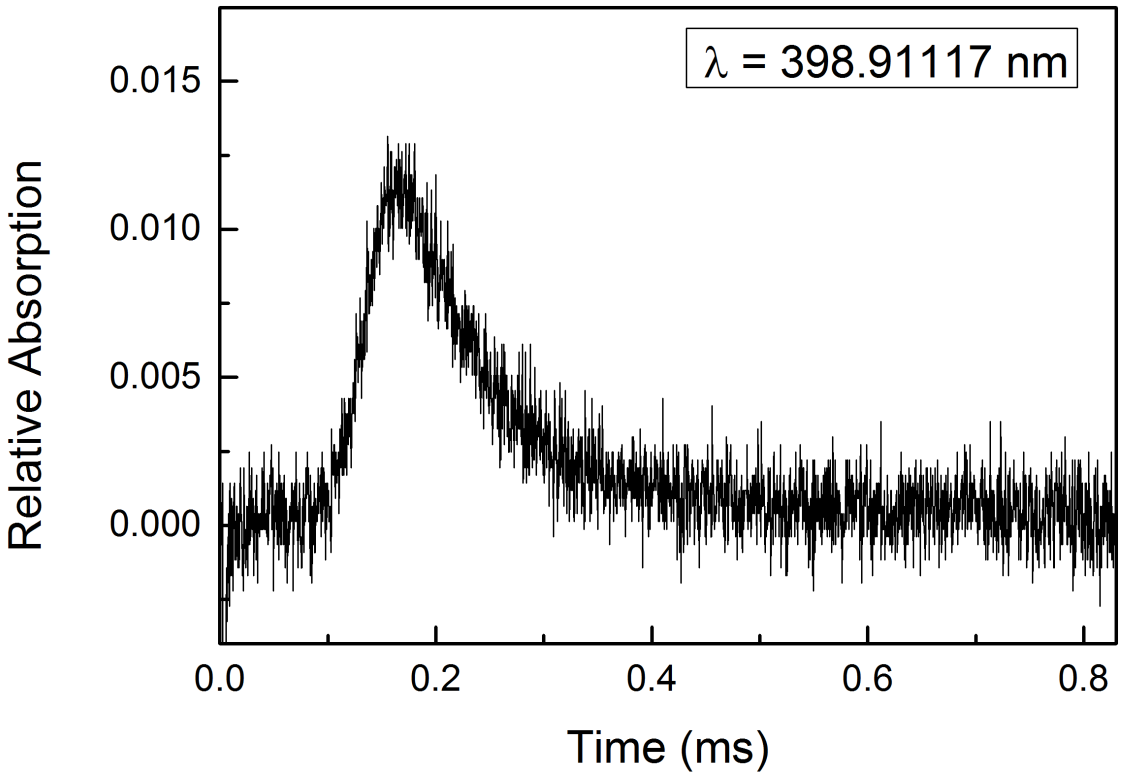

Figure 4.2: First absorption signal of Yb beam in cryogenic set up.

With the 2.8" cell length, no BaH was observable with any amount of flow, so we had to try a shorter cell length of 1". The initial detection of BaH in this cell geometry (Figure 4.3) required a large amount of Helium flow to observe - above 40 sccm, which caused the coconut charcoal to saturate and release Helium gas very rapidly. This situation was difficult to diagnose, since there was such limited optical access, and the probe was very far from the cell exit. But it gave us indication that the cell length of 1" could produce molecules.

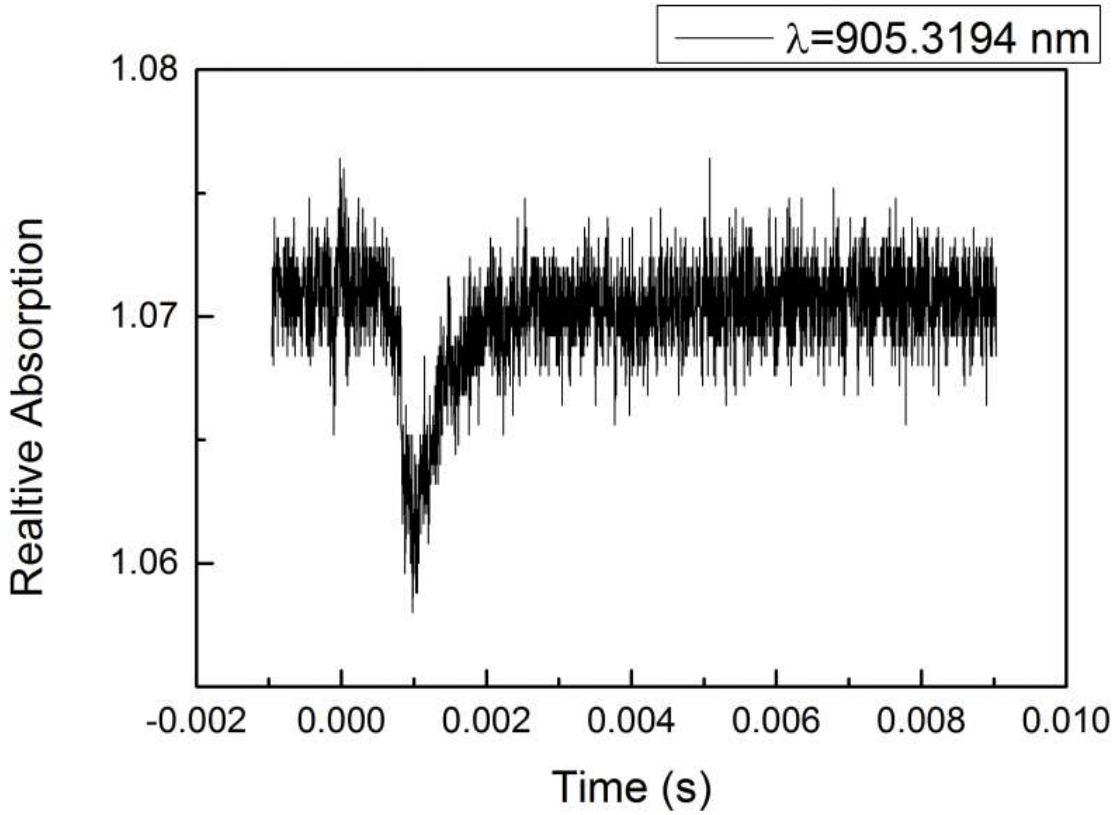

Figure 4.3: First absorption signal of BaH beam in cryogenic set up. Even this small fractional absorption signal (1%) required over 40 sccm of Helium flowing into the chamber, resulting in rapid saturation of the cryopumps.

The next iteration of the cell was to use the long internal space of the cell above to try an intermediate (2") cell length. In this case, we saw only very fast molecules escape the cell, characterized by extremely narrow (time scale $\approx 100\,\mu$s) absorption pulses reminiscent of the room temperature ablation experiments. This was most likely a result of all the buffer gas thermalized molecules diffusing to the cell walls. In other words, the cell was too long.

After this, we machined a shorter cell that allowed for better optical access, called V3, which is still in use today. While the design specifics are listed in the Appendix D, the basic design can be seen in Figures 4.4 and 4.5. One main feature of the design is the threaded target mounting cylinder, which can be easily removed to glue new targets onto, without major removal or disassembling of the cell. In order to maintain a good seal, the threads

are wrapped in Teflon tape prior to screwing in. The removable insert also allows us some freedom in the positioning of the target within the cell volume - either recessed into the cell wall, flush with the wall, or protruding into the chamber. Experimentally, we determined tha protruding into the volume, into the Helium flow was optimal.

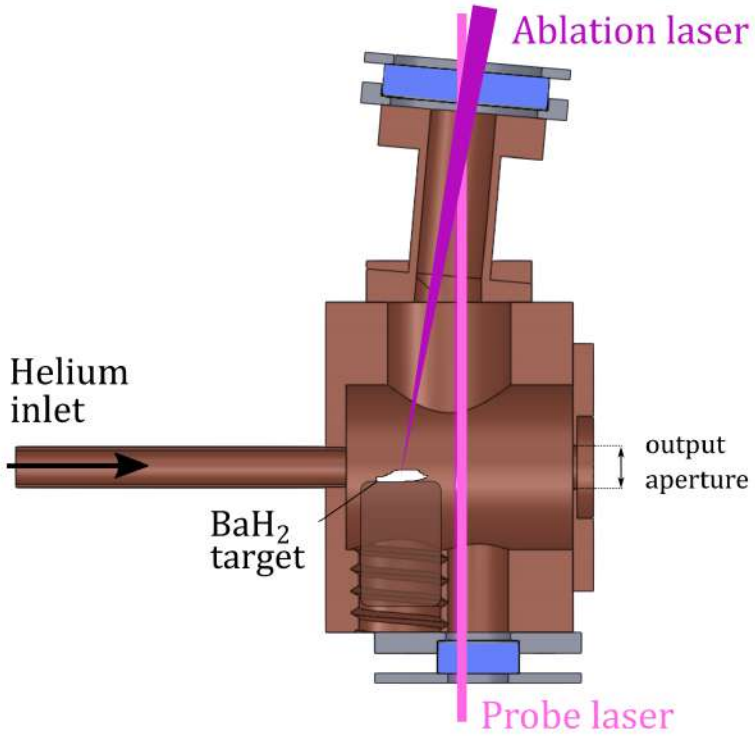

Figure 4.4: Cell V3 schematic, in cross section view from the top. The helium inlet at the left brings in the cryogenic buffer gas, while the ablation laser enters through the protruding window at the end of the snorkel at the top of the figure. A window at the bottom allows optical access for absorption measurements inside the cell. The target is mounted onto a threaded cylinder that screws into the side of the cell, allowing easy target changes.

We quickly found the need to use an protrusion to mount the window that the ablation laser would go through, as the window would crack very quickly. Protruding the window with a 1.5" snorkel also aided with the gradual coating of the ablation window with time. Even with the window further away, the window still becomes coated over time, causing increased absorption of the ablation light, leading to damage. Therefore, it is necessary to

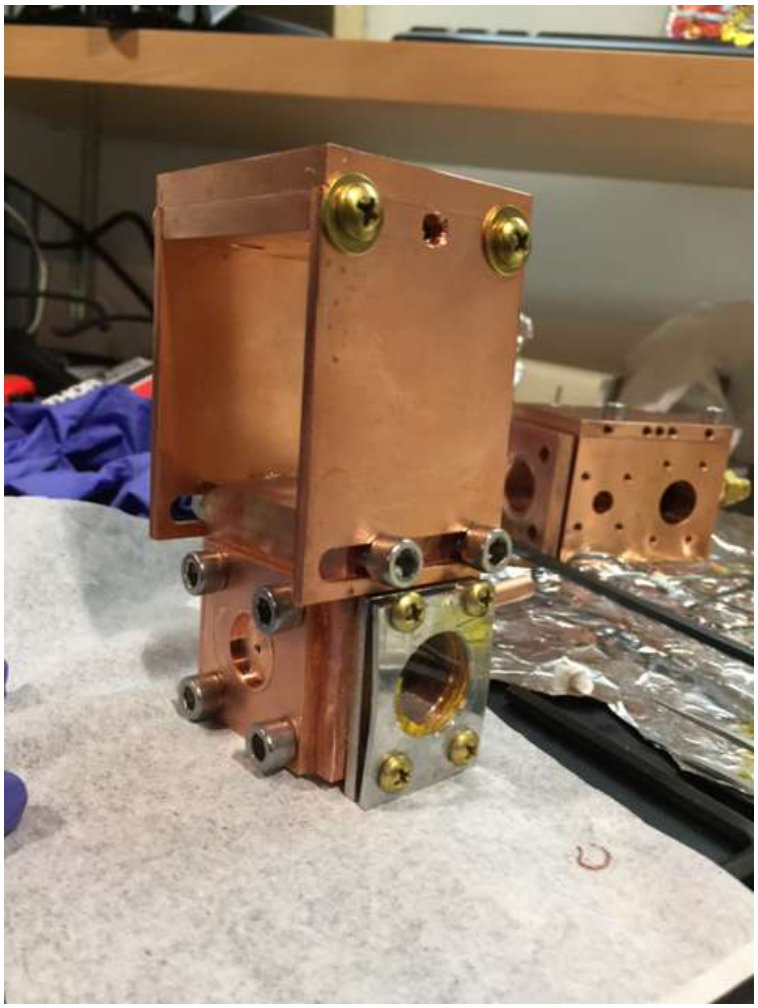

Figure 4.5: Cell V3, shown in foreground. The cell is designed to have an internal length of 1.25", and a cylindrical diameter of 1". The ablation window is shown on the right side before the installation of a snorkel to push it further from the target, mounted on the opposite interior side. The aperture diameter in the photograph is 3 mm.

change this window out every few months to ensure good performance.

A small 0.5" diameter window opposite the ablation window allowed pass-through optical access for absorption measurements. This window also needs periodic cleaning. Opposite the Helium inlet, the cell design is open to allow for different front plates with different aperture sizes. The plates are made to be as flat as possible on the side to mate with the cell, and are secured using 4, 1/4-20 vented socket cap head screws. A small amount of Apiezon N grease ensures a close to airtight seal and good thermal contact.

With this shorter cell, we varied the aperture diameter in a few different iterations from 1.6 mm to 10 mm. While molecules were observable for all the apertures, the variation in ablation efficiencies among and within targets made it difficult to quantify the performance of each specific aperture size. Yet, 1.6 mm was consistently poor, with only very fast molecules coming out, while 10 mm appeared to have very few molecules, barely visible above the signal to noise. As a result, we settled in the middle at 5 mm or 7 mm, since both appeared to work equally consistently. A sample trace showing nearly 50% extraction efficiency for a 5 mm aperture is shown in Figure 4.6. Furthermore, the out-of-cell signal, shown in black, appears to show molecules exiting the cell up to 3 ms after ablation, which is near the estimated time for complete thermalization, indicating the desired operation of the cell.

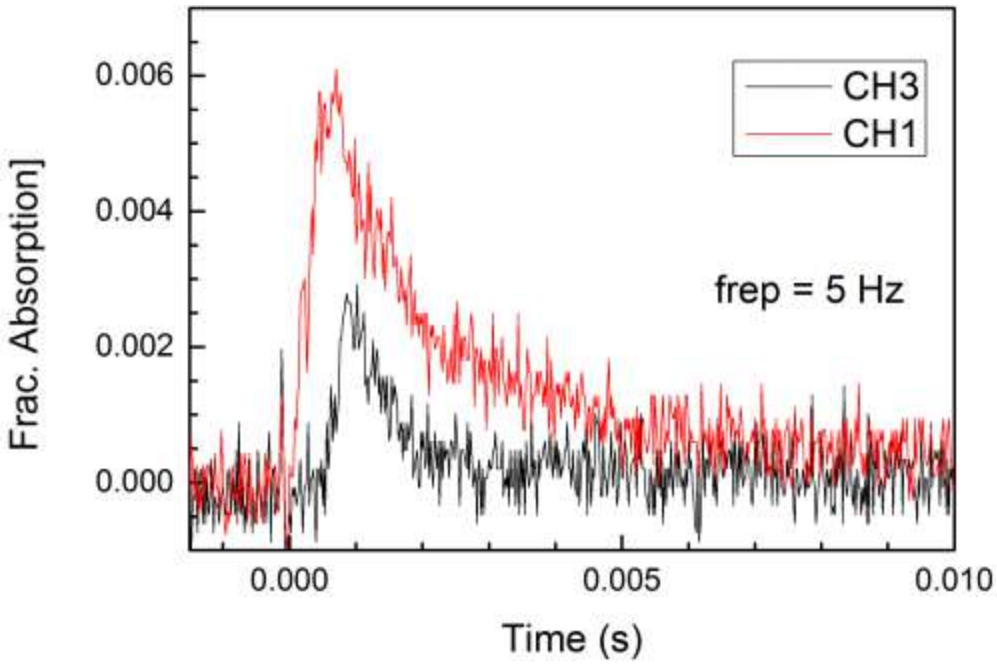

Figure 4.6: Extraction efficiency measurement for Cell V3 with 5 mm aperture for a ablation laser repetition rate (frep) of 5 Hz. Red Ch1 trace corresponds to probe absorption inside the cell, while black Ch3 trace corresponds to probe absorption 2.5 mm outside of the cell. Time axis is triggered off of the ablation laser pulse.

Following the advice of students in Dave DeMille's lab at Yale, we added a coconut charcoal coated copper plate with a 1 cm hole in the center, approximately 10 cm form the

cell exit. This is actually built out as an extension to the cell using 4 copper rods. In practice, we see no discernible improvement with the plate, but it is also not apparently detrimental, and so it remains a part of our experiment. Most likely, geometric cuts are made further downstream by the vacuum system, and this plate serves primarily to pump excess Helium.

We also tried a version of the cell - V4, which had an extreme diameter and was rectangular shaped, while maintaining the length as before. The hope was to increase the diffusion time to the cell walls, while maximizing the thermalization time, but ultimately, there was not so much improvement. We suspect that the molecules do not easily make it back to the cell aperture as they diffused out from the central region too far. In the end, we find that the optimal cell configuration is cell V3, which has a 1" cylindrical diameter, 1.25" length, and a 5 mm aperture. Trial and error shows that a 100x100 copper mesh placed on the Helium inlet helps the signal, and the target should be protruded almost to the center of the cell.

In Figure 4.7, we see the waveform data for both absorption and fluorescence for the 5 mm aperture cell, measured 10 mm outside the cell, and 53 cm downstream.

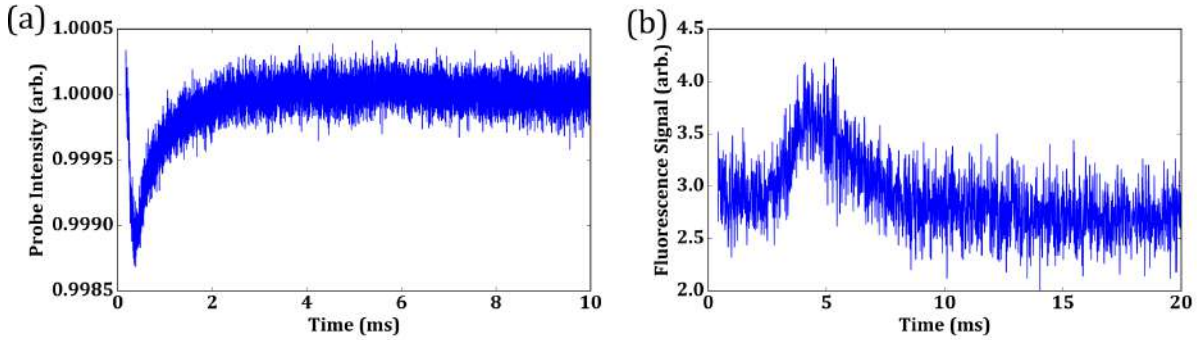

Figure 4.7: Comparison of two probe positions along the molecular beam - out-of-cell, and downstream. (a) Laser absorption measurements on a fast photodiode, taken 1 cm beyond the cell aperture. (b) Time resolved fluorescence raw data from a photomultiplier tube, taken 53 cm downstream from the cell, showing fluorescence up to 8 ms after ablation.

Cell geometry should also be characterized by the velocity profile produced, since our ultimate goal is to make the slowest molecules, and we do not want to have accidentally made a supersonic or effusive source. In Figure 4.8, we can see that for the apertures of 3

mm, 5 mm, and 7 mm diameter, the beam is operating in a desired mode, with a velocity distribution centered around 150 m/s or less, but also with width of the order 50-100 m/s. This also tells us that our choice of aperture was approximately correct, since the 5 mm diameter appears to provide the most molecules at the slowest velocity. Finally, in Figure 4.9, we can see that a thicker aperture, creating a nozzle-like exit to the cell, indeed increases the forward velocity of the beam, as is expected when increasing the number of collisions at the output.

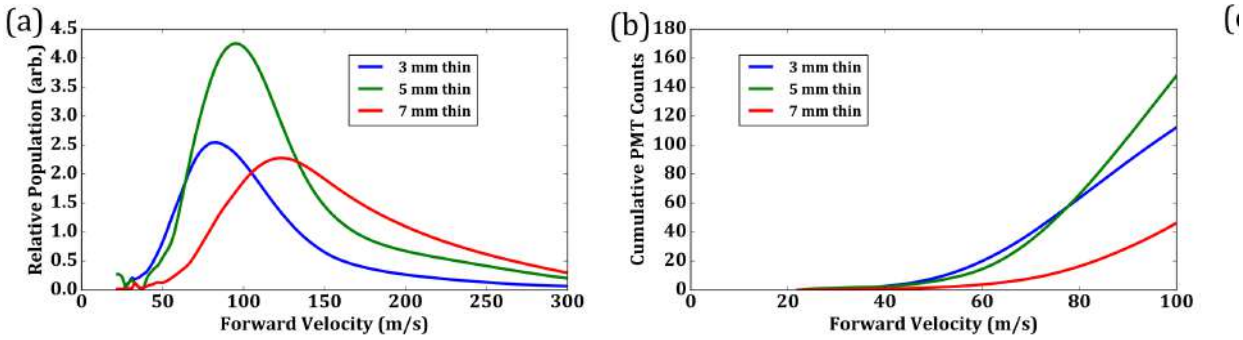

Figure 4.8: Comparison of velocity profiles resulting from aperture size and nozzle length at the cell. (a) Velocity profiles analyzed extracted from comparisons of upstream and downstream data. While the 7 mm has more molecules over the total waveform, the 3 mm and 5 mm apertures are better optimized for slow molecules. (b) Cumulative distribution function for the velocity profiles in (a), for beam velocities <100 m/s. 3 mm and 5 mm are comparable, with 3 mm having slightly more molecules in the slowest velocity class.

The flow dependence of the in-cell signal is shown in Figure 4.10 for two different mass flow controllers which are labeled by their respective brand names. We see that the in-cell performance is very consistent and repeatable, with the absorption signal rising linearly until about 15 sccm where it then levels out. Higher flows are shown in Figure 4.11 for different ablation powers, indicated by faction of full energy (50 mJ). Here we see that there is a peak flow rate for the maximum in-cell absorption. However, this peak is not present for the out-of-cell data.

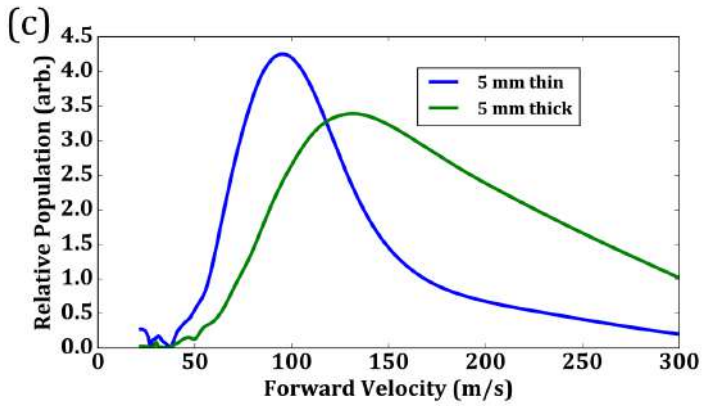

Figure 4.9: Comparison of velocity profiles for 5 mm diameter aperture with either "thin" ($<$ 1 mm) or "thick" ($\approx$ 5 mm) aperture, indicating the nozzle length. While the thick aperture has a higher integrated number of molecules, the long thermal tail is not useful for us. The thin aperture has much better performance for the <100m/s velocity class.

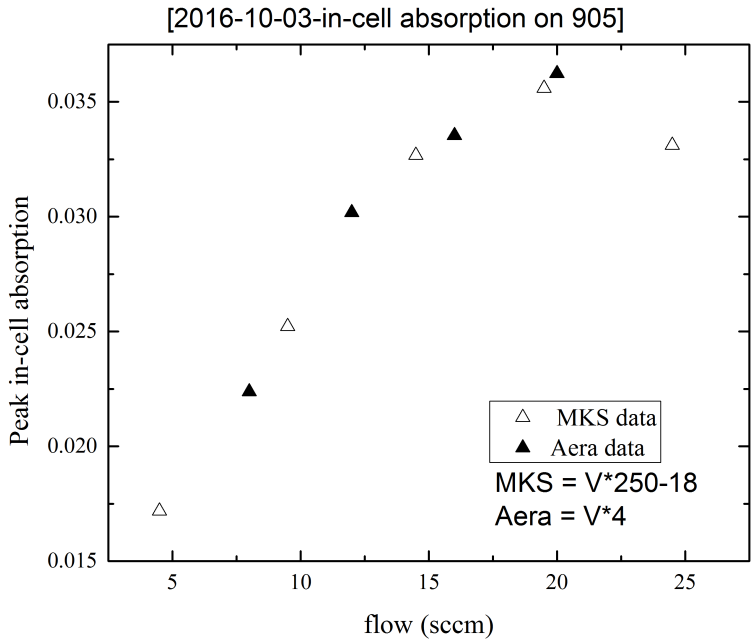

Figure 4.10: In-cell absorption vs helium flow rate into the cell in sccm for two different mass flow controllers labeled by brand name. Each show repeatable and consistent peak absorption. To maximize the in-cell signal, we need to use $>$ 15 sccm.

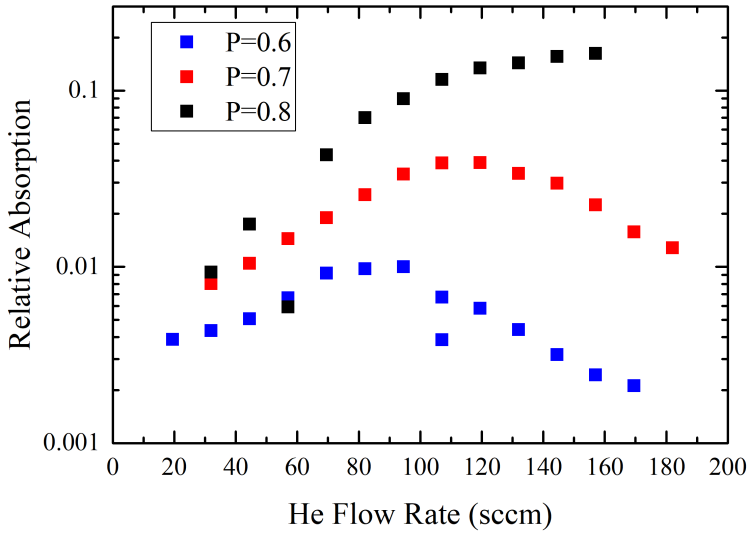

Figure 4.11: In-cell absorption vs helium flow rate into the cell in sccm for 3 different ablation powers corresponding to fraction of full power.

4.2 Fluorescence Detection and Slowing Region

In order to detect molecules downstream of the buffer gas cell where molecule numbers will be fairly small, it is necessary to use fluorescence detection to be sensitive to the relatively small molecular density. One especially challenging aspect of our molecule is that the main cycling transition at 1060 nm is not within the sensitivity range of most commercially available photomultiplier tubes (PMTs). There are, to our knowledge, 2 possible PMTs that have quantum efficiency (QE) around 1% at this wavelength, but these are prohibitively expensive. This is quite unfortunate, as a cycling transition is usually the best way to bump up photon numbers from a fluorescence experiment. The repumping fluorescence transition is another option to detect, since the decay from the $B\Sigma$ excited state at 905 nm can be detected with about 1-2 % QE. Furthermore, detecting fluorescence at a different wavelength than the excitation is advantageous for background rejection with filters. Unfortunately, the expected photon count rate out of the repumpers is far lower since the molecules only fall into the first vibrational ground state with less than 0.6% probability, so the low quantum efficiency is particularly difficult to work with unless the molecules are regularly cycling through the

laser cooling scheme.

As an alternative, we decided to detect the molecules using a higher energy $E\Pi$ state, with an excitation wavelength of 683 nm. PMTs with QE around 6-7% are readily available. This measurement directly detects the ground state molecules, and the excited state has a FCF around 95 %, making cycling a possibility for enhanced detection. Unfortunately, this probe is not a part of the laser cooling scheme, making it a partially destructive measurement. Nevertheless, we have good background rejection from the high power cooling lasers, however, because the excitation is the same wavelength as the collected light, we require the use of light baffles to minimize the probe laser scattering.

There are two main detection regions along the molecular beam path. One of the fluorescence regions is located directly at the output of the buffer gas cryostat, and the system is centered around a Conflat cube, shown in Fig. 4.13, which the molecular beam passes through (hopefully). Along the transverse axis parallel to the optical table, we extend the cube using a singe CF nipple section on each side, using blackened copper gasket/baffles to make the two seals. We have explored two techniques to make light absorbing baffles.

In the first, we use a black foil, cut to fit the copper gasket. This foil is a product from Acktar called Metal Velvet which is designed to reduce light scattering. Below 1000 nm the specular reflectance is limited well below 0.5%. Hemispherical reflectance, which describes reflectance from a diffuse light source, is also quite low, as seen in the plot below. The material has a low-outgassing adhesive, and can be baked at up to 150 C. Each baffle, made by machining an aperture in a solid copper CF gasket, was coated on both sides with a circular cutout of the Acktar MetalVelet, made to fit as close as possible to the exposed region of the gasket. An example gasket is shown in Figure 4.12.

Our second technique to blacken the fluorescence region is via a chemical process to grow Cupric-Oxide directly on the copper gaskets. To make effective light baffles, OFHC copper blanks are first machined in a milling machine to make rectangular slots of 1/4" height and

1.5" length, which allow for a few experimental configurations, including using several passes of a light beam back and forth through the detection region without overlapping, for state preparation and detection with separated beams, or for exploring timescales for the molecule-light interactions. Following the procedure developed by Norrgard *et al.* [121], the gaskets are cleaned in a isopropanol ultrasonic bath, then cleaned in a solution of 1% Citranox in deionized water, and finally rinsed with deionized water. The black cupric oxide is grown by immersing the gaskets into a solution prepared with 50g of NAOH (>90% purity) and 50g of NaClO (>80% purity) in one-half liter of deionized water. The solution is maintained at a temperature just below 100^o by placing the beaker of solution in an outer bath of tap water on a hot plate. After 10 min, the parts are removed and cleaned off with deionized water before being dried with clean N2. The chemical reaction involves several steps, and the final one that makes the CuO is,

$$\mathrm{Cu(OH)_2(s)} \xrightarrow[\text{heat}]{} \mathrm{CuO(s) + H_2O(l)}. \tag{4.2.1}$$

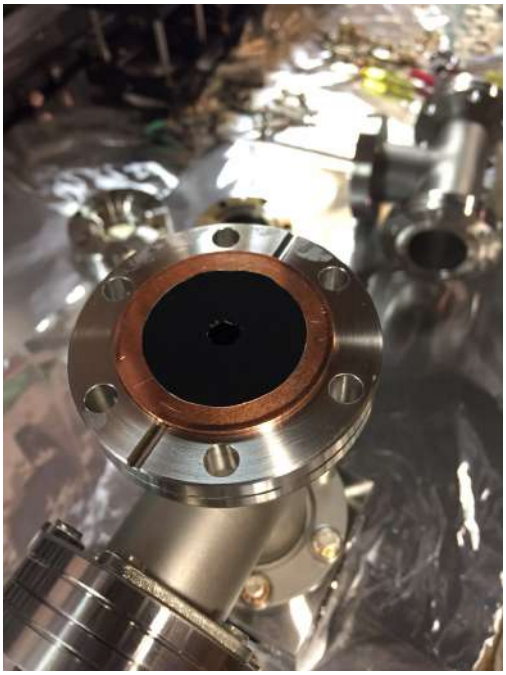

Figure 4.12: Photo of Acktar Metal Velvet coated gasket.

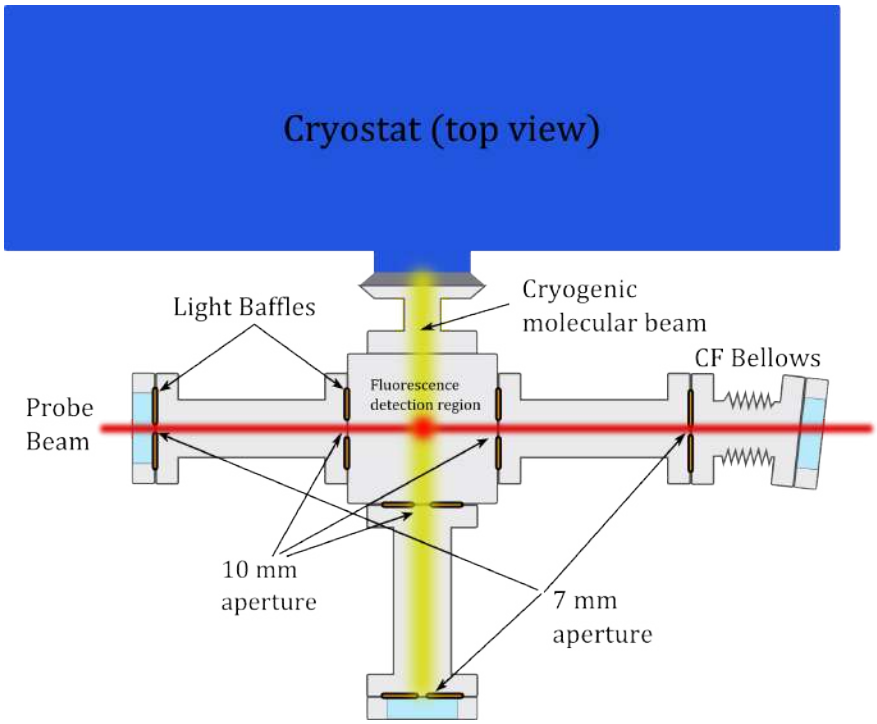

Figure 4.13: Cartoon schematic of fluorescence region.

At the output of the transverse axis, we use a short bellows section to angle the output window in order to minimize back reflections. The windows are (mostly) B-coated Thorlabs windows. The CF nipples can be replaced with vacuum tee sections to be used for attaching a vacuum gauge and separate pump, if necessary later on.

Along the transverse axis perpendicular to the table (shown in Fig 4.14), we put a spherical mirror with radius 10 cm, below the chamber, and a couple lenses and a filter before the PMT above the chamber. This would optimally give us about 10% of the total solid angle for isotropically emitted light.

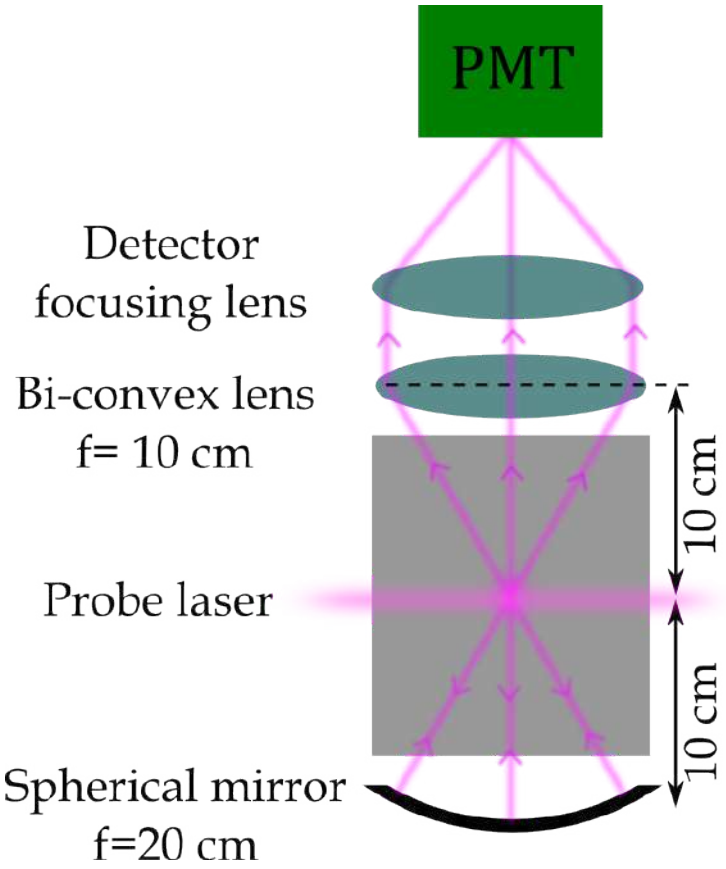

(2).png

Figure 4.14: Cartoon schematic of light collection optics in the fluorescence region.

Further downstream from this cube, we have a second fluorescence region made from an octagonal CF chamber from Kimball Physics. This octagonal chamber allows us to have

optical access from the transverse direction as well as form a 45^o angle to confirm time-of-flight based velocity measurements. Furthermore, its flattened shape means that the PMT window can be placed closer the source. Below this chamber we attach a large capacity, 700l/s turbo pump. This allows us to maintain high vacuum along the entire detection region.

Light baffles are also employed in this octagonal detection region, making use of the 1.33" CF optical access ports to attach nipple sections as shown in Figure 4.15. Here, instead of making baffles out of the copper gaskets used to connect sections together, we machine out OFHC copper pipes that fit into the nipple, with one end open and the other with a cap. The cap is machined on a lathe to make a knife edge hole with the diameter specified by the system configuration. A photo is shown in Figure 4.16. These light baffles are crucial to reducing background laser light scattered from the windows. Without them, the PMT is not operable.

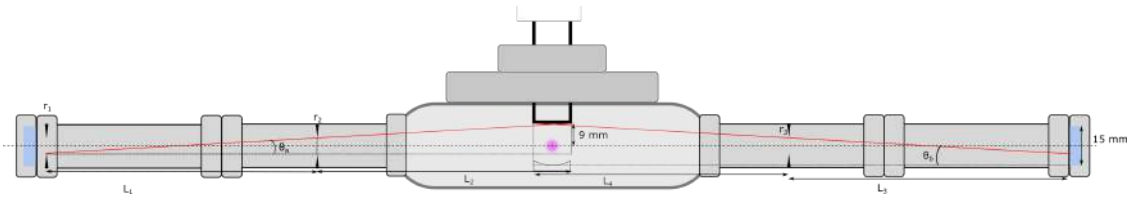

Figure 4.15: Drawing of light baffle system in the octagonal fluorescence region for use with a light pipe. r1 and r2 indicate the baffle diameter.

Figure 4.16: Photo of blackened OFHC copper pipe-baffles used in the octagonal detection region. Here, there are shown just after blackening, being rinsed in deionized water.

4.3 BaH Sources

As mentioned before, in our system we ablate solid precursors of BaH_2 to produce BaH. The fact that we can buy it in small rock form is convenient, since we are not bound to pressing our own pellets. On the other hand, these rocks appear to have very different surface qualities from sample to sample, which makes consistency an ongoing challenge.

The target preparation and loading procedure is quite straightforward. In an Ar filled glovebox, we open the sealed bottles of BaH_2 rocks and select a piece based on the surface smoothness and flatness of sides. Since it is unlikely to find a rock with two parallel surfaces, we usually use cutters to break the rock in half, exposing the inner surface. The brittle

material tends to break cleanly and reveal a relatively flat surface. We then glue this piece onto the removable target holder, then transfer the holder over to the cryostat, while using an Ar hose to blow Ar over the sample while it is outside the glovebox. It is important to do this step quickly, as the hydride will rapidly react with oxygen to form BaOH, which we have shown is an unsuitable ablation precursor.

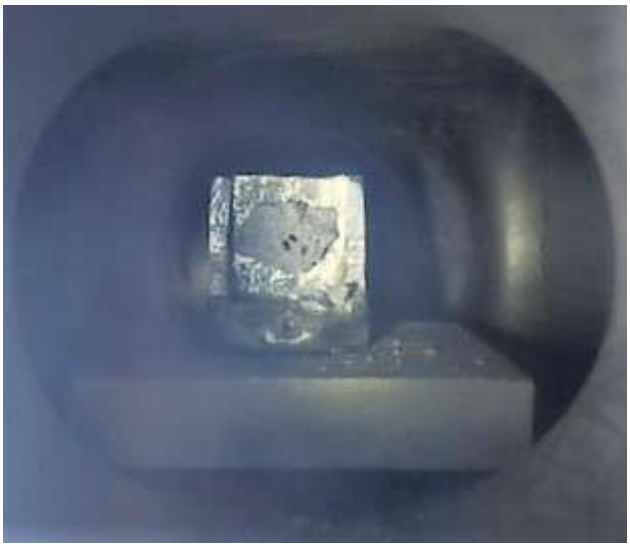

Figure 4.17: Photo of a rock of BaH_2 mounted in the room temperature ablation set up. The rock is glued to an aluminum "chair". This rock is similar to those used in the cryogenic apparatus, but is uncleaved. The dark black spots are locations that have been ablated for several hundred shots. Debris from the target can be seen strewn in front of the chair mount.

While cleaving the rocks during preparation should somewhat homogenize the sample surfaces, we in fact see that very few spots on the targets provide 'good' ablation. That is, stable molecule number over a few 1000 shots. Other parts of the target will either yield no signal at all, or a large molecule number for < 10 shots before a rapid dropoff in signal. It remains unclear what exactly makes a spot 'good'. Observation of used targets show that the spots that have been heavily ablated have deep holes drilled into the material (Figure 4.17).

Pressing a pellet of the precursor material could potentially homogenize the samples and provide more consistent ablation surfaces, but other groups appear to have similar issues to

us in surface consistency.

Experiments that utilize diatomic fluorides have found great success by ablating the metal partner and flowing warm SF_6 into the cell. The SF_6 immediately freezes onto the target, and thus the ablation laser releases both the metal partner and detached fluorine atoms, which can combine into the desired diatomic. We have tried to replicate this technique by using barium metal and flowing gases with H atoms that have fairly low bond energies, such as methane ($C\text{-}H_4$), but unfortunately, had no success. The hydrogen atoms unsurprisingly stay together very tightly, making releasing free H-atoms very unlikely. In the future, we could attempt to use a discharge source near the cryogenic region and pipe in some of the atomic H to the cell.

4.4 Laser System

In order to address the large spin-rotation splitting in our molecule, we decided to bite a bullet and make two lasers for each relevant vibrational ground state. This means two lasers for the main cooling transitions, and 2 lasers for every new repump. Creating 8.6GHz sidebands is possible, but costs about as much as a new laser for the appropriate EOMs and necessary RF equipment. Additionally, efficiencies are not particularly good.

4.4.1 External Cavity Diode Lasers

The main cooling lasers are Littman-Metcalf configured External Cavity Diode Lasers (ECDLs) that follow a simple design from Reference [122] and shown in Fig. 4.18. The design typically results in lasers with linewidths on the order of 100kHz. The optical diode is housed in a TEC controlled mount with a collimating lens tube. In a typical case, the diode is oriented so that the light is polarized vertically, which results in the long axis of the asymmetrical spatial mode of the light to be horizontal. The light emitted from the diode reflects off of

grating such that the zeroth order reflects through an exit hole in the laser housing and the first order reflects onto a mirror. The light hitting the mirror is reflected back along the same path to the grating so that the minus first order is reflected from the grating back into the diode. This path, diode-grating-mirror-grating-diode, forms the external cavity used to narrow and amplify the laser light. The angle of the mirror determines the exact frequency of the light that is resonant with the cavity, allowing for wavelength tunability over about 10 nanometers in a typical setup. In our design, a piezoelectric element is placed on the horizontal control axis of the mirror, enabling external electrical control of the wavelength.

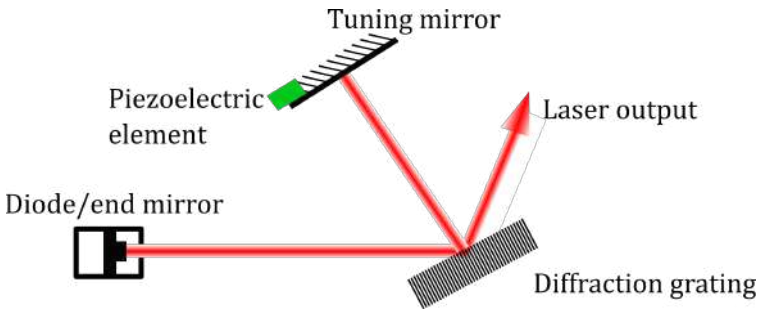

Figure 4.18: Cavity configuration for a Littman-Metcalf ECDL. The 1st diffracted order is retroreflected off of a tuning mirror and the resulting -1 order provides feedback to the diode. The tuning mirror can be coarsly adjusted by hand, or more finely with a piezoelectric element.

4.4.2 Laser Lock

While atomic experiments can typically find a straightforward way to lock lasers to spectroscopic features in some atomic vapor cell, such a scheme is typically not possible in experiments with molecular radicals. Fortunately, wavelength meters can offer precision and accuracy suitable for ultracold molecule trapping and cooling at tenable prices, and in combination with a software lock, can provide the necessary laser control. In our experiment, we use a WS-7 from Toptica with an 8 channel multiplexer, which quotes 10 MHz precision and 60 MHz absolute accuracy. The meter provides many more digits than this, and can be further stabilized by using one of the channels to monitor a stabilized HeNe laser, and

correcting any other lasers through monitored changes in the wavemater reading.

Our software lock is built in Labview, and offers 8 channel PID control limited only by the speed of the wavemeter exposure time. It would of course be ideal to make a hardware lock based on spectroscopic features in BaH, however, the only reliable way we could find to implement such a scheme would be in using a BaH furnace, which in principle is very similar to a heat pipe, such as those used for Strontium or Sodium, but requires temperatures above 700^o C. This presents some significant technical challenges. Moreover, using a stabilized He-Ne to calibrate the wavemeter can reduce the uncertainty of the lock to below 1 MHz, which is below the linewidths of the molecular transitions we use.

4.4.3 Broadening for White-Light Slowing

In order to slow the molecular beam, we need to scatter photons in the longitudinal direction at the resonant frequency of the molecules, while compensating for the Doppler shift arising from the molecules' velocity. As they are slowed, the Doppler shift changes, requiring some compensation. One approach is to use chirped light, as in Ref. [123], where the laser frequency is directly swept. In Ref. [68], the technique of 'white light' slowing is employed, where the slowing light is broadened out to match the width of the velocity distribution, ensuring that there is some light at every Doppler shifted velocity class. This has the advantage of addressing more molecules at once, but in practice, both techniques are shown to be of comparable efficacy [123].

Our initial approach is to try 'white light' slowing, and to do so, we take 3 electro-optical modulators in series to successively add sidebands to the laser, and sidebands to the sidebands. Using a 30 MHz, 13 MHz, then 8 MHz, we can achieve a span of sidebands spaced more or less 1 MHz apart, with approximately 100 MHz width.

Chapter 5

Molecular Energy Structure

5.1 Molecular Structure and Notation

The energy structure of BaH is complicated, to say the least. It is a molecule after all. However, laser cooling requires a complete understanding of all the involved states, and given the brevity of literature studying BaH in much detail, much of the groundwork for this project involves precision measurement of the energy levels. But before we get into that, I'll try and clarify a little on molecular notation, which has a simplicity commensurate with that of the molecules we try and describe!

The challenge is to identify the different possible quantized motions of the molecule. The electronic, vibrational, and rotational degrees of freedom are ideally separate. I'll restrain myself to classifying properties of diatomics only, as anything more would be quite masochistic.

The electronic state, determined by the valence electrons of the constituent nuclei, is denoted by a term symbol, much like in atoms. These states are labeled with capital letters, with X indicating the ground state, and $A, B, C...$ labeling excited states from there. Within each electronic state, the vibrational and rotational motion is quantized, with vibrational

level spacings typically 2 orders of magnitude larger than that of the rotational levels. The vibrational and rotational motion is specified by quantum numbers. Since we deal with diatomic molecules, vibrations are straightforward, and should only require one label, v. Rotations are necessarily more complicated.

There are a few different sources of angular momentum in a molecule and how they couple together depends on the type of molecule.

The electrons of an atom move in a spherically symmetric electric field, which means that the orbital angular momentum $\vec{L}$ of these electrons is a constant of their motion. In a diatomic molecule, the spherical symmetry of the field is reduced to axial symmetry along the internuclear axis. As a consequence, we can only reliably say that the projection of $\vec{L}$ along the internuclear axis is a constant of motion, similar to how one would quantize the angular momentum of an atom in the presence of a strong electric field. This projection, denoted as $\vec{\Lambda}$ is the number that is quantized and can take any of the values, $\vec{M}_\Lambda = \Lambda, \Lambda-1, \Lambda-2, ..., -\Lambda$. While in atoms, different electron orbitals with increasing $|\vec{L}|$ are labeled as $S, P, D, ...$, in molecules, states with electrons in orbitals of increasing Λ are labeled with the Greek analogues, $\Sigma, \Pi, \Delta, ...$

The electrons also contribute their spin, $\vec{S}$ to the total angular momentum, and it is convenient to call the projection of $\vec{S}$ onto the internuclear axis as $\vec{\Sigma}$. Note that $\vec{S}$ refers to the total spin due to any unpaired electrons belonging to either atom in the molecule. If the nuclear motion couples weakly to the electronic orbital or spin motion, while the electronic motion is coupled very strongly to the internuclear axis, then the convenient term $\Omega = \Lambda + \Sigma$ is well defined.

The last contribution to the angular momentum comes from the rotation of the nuclei about their center of mass. We call this quantity $\vec{R}$, though in the absence of orbital angular momentum ($\vec{\Lambda} = 0$), $\vec{R} = \vec{N}$.

All the quantities above must add together to build up the total angular momentum of

the molecule, which, excluding the nuclear spin, is denoted $\vec{J}$. Building up $\vec{J}$ depends heavily on the type of molecule to determine the order in which to couple the different sources of angular momentum. The different cases are called Hund's cases, and will be discussed later. In addition to the terms above, the nuclear angular momentum , $\vec{I}$ couples, to $\vec{J}$ above to form $\vec{F}$.

Finally, the eigenfunction of the valence electron in the molecule can be either symmetric or antisymmetric with respect to a reflections through any plane that intersects the internuclear axis. This distinction is made in the term symbol with either a + or − sign.

The labels above are used to denote the term symbols in a molecule as

$$^{2S+1}\Lambda^{\pm}_{\Omega}$$

One final detail in classifying the states comes out of the inversion symmetry when the molecular potential itself is centro-symmetric, i.e. homonuclear molecules. This 3-d inversion property classifies orbitals as *gerade*, *g* or *ungerade*, *u*, using the German words for even and odd to denote the parity. BaH does not require this label.

5.2 Energy levels

The energy levels of a molecule in principal should be found by solving the Schrodinger equation for i electrons moving around k nuclei with a Hamiltonian that accounts for the electronic energy, the vibrational energy, and the rotational energy. This quickly gets complicated, since the Coulomb potential that the electrons are moving in is dependent on the internuclear distance, which varies in time for each vibrational level. As a result, the electron energy eigenvalues, E_{el}, depend on the internuclear distance, while the energies for the nuclei depend on the eigenfunctions for the electrons - yikes! Luckily, the Born-Oppenhiemer ap-

proximation tells us that the variation of internuclear distance is sufficiently slow enough to ignore the first and second derivatives of the eigenfunctions with respect to nuclear distance. If so, then any additional energy above the minimum energy from the electronic motion must be due to vibrational energy, E_v or rotational energy, E_r. The result is that the total eigenenergies can be well approximated by the decoupled sums of the energies corresponding to each degree of motion, specifically,

$$E_{tot} = E_{el} + E_v + E_r \tag{5.2.1}$$

In line with convention (which must be followed!), the energy can be expressed in wavenumber (cm^{-1}) symbols corresponding to the terms above, represented by so-called "term values",

$$T = T_e + G + F. \tag{5.2.2}$$

The electronic energy term, T_e is the eigenenergy for the Hamiltonian describing the interaction for BaH between the two nuclei and the 2 free electrons. It would be best left to other references to describe the models, *ab initio* or otherwise, that consider the electronic energy, T_e.

5.2.1 Vibrational energy

Near their minimum, molecular potentials are well approximated by a harmonic oscillator [111]. Adding just one order of anharmonicity, the cubic term, gives very accurate representations of observed vibrational spectra of diatomic molecules. The term values for the vibrational quantum number, v are given by the solution to the anharmonic oscillator,

$$G(v) = \omega_e(v + \tfrac{1}{2}) - \omega_e x_e(v + \tfrac{1}{2})^2 + \omega_e y_e(v + \tfrac{1}{2})^3 + ... \tag{5.2.3}$$

Ignoring cubic terms and above, $G(v) = \frac{E(v)}{hc}$, where $E(v) = h\nu(v + \frac{1}{2})$ are the eigenenergies of the harmonic oscillator, therefore, ω_e is the vibrational frequency of the molecule in cm^{-1} divided by the speed of light.

5.2.2 Rotational Energy

To begin an appropriate description of the rotational energy in a diatomic molecule, we can model it as a non-rigid rotator, that is, two masses with reduced mass, μ, connected by a massless spring with constant k, and rotating with angular speed ω [111]. As the molecule rotates with magnitude of angular momentum, $R = I\omega$, the internuclear distance stretches from the equilibrium distance r_e of the spring to a distance r_c. At this configuration, the moment of inertia is $I = \mu r_c^2$. The total energy of this system is then

$$\begin{aligned} E &= E_{kinetic} + E_{potential} \\ &= \frac{1}{2} I\omega^2 + \frac{1}{2} k(r_c - r_e)^2 \\ &= \frac{N^2}{2\mu r_c^2} + \frac{1}{2} k(r_c - r_e)^2. \end{aligned} \tag{5.2.4}$$

At this distance, the centripetal forces are balanced so that,

$$-k(r_c - r_e) = \mu\omega^2 r_c = \frac{R^2}{\mu r_c} \approx \frac{R^2}{\mu r_e}, \tag{5.2.5}$$

where the approximation is true to first order for small values of R. Using the value of $k(r_c - r_e)$ from Eq. 5.2.5 in Eq. 5.2.4,

$$E = \frac{R^2}{2\mu r_e^2} - \frac{R^4}{2\mu^2 r_e^6 k} + ... \tag{5.2.6}$$

where higher order terms would enter due to larger differences between r_c and r_e. In a

quantum system, the angular momentum has total magnitude $\sqrt{R(R+1)}\hbar$, and therefore,

$$E = \frac{\hbar^2}{2\mu r_e^2} R(R+1) - \frac{\hbar^4}{2\mu^2 r_e^6 k} R^2(R+1)^2 + ... \tag{5.2.7}$$

The constant terms above are labeled B and D respectively, and so the term symbol for rotational energy is written,

$$F(R) = BR(R+1) - DR^2(R+1)^2 + ... \tag{5.2.8}$$

In the above, the constants B and D are proportional to $\left[\frac{1}{r_e}\right]^2$. For more exact calculations, these equilibrium constants can be replaced with vibrational level specific ones, denoted by B_ν, and D_ν, which account for the coupling between the vibration and rotation.

We need to extend our model a bit more to take into account the motion of the electrons flying about the nuclei. This is best treated in a quantum mechanical approach, discussed in section 5.6.

5.3 Hund's Cases

In order to understand the possible transitions in BaH, or any molecule, we need to first make sense of the different ways the angular momentum can couple together, depending on the electronic state of the molecule. In the ground state, the electronic angular momentum tends to strongly couple to the internuclear axis because of the electric field between the nuclei, however, in excited states, the nuclear motion begins to move at a rate where the Born-Oppenheimer approximation breaks down and the electron can no longer follow the motion of the internuclear axis. This process is known as decoupling, and keeping track of the different possible situations are a series of orderings known as Hund's cases, which are described below. In both the cases we ignore the nuclear spin $\vec{I}$, but it is only required to

add this to the total angular momentum $\vec{J}$ to form $\vec{F}$.

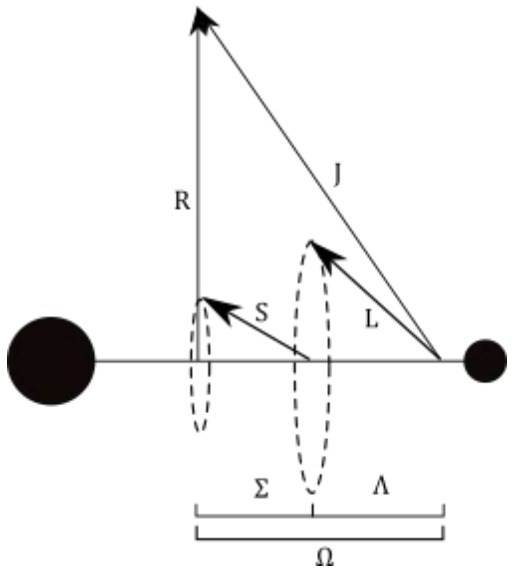

Figure 5.1: Angular momenta coupling for a Hund's case (a) molecule.

5.3.1 Hund's case (a)

A common situation for diatomic molecules in their electronic ground state is Hund's case (a) (Figure 5.1. Here, the orbital angular momentum of the electron $\vec{L}$ is strongly coupled to the internuclear axis as Λ, since the most prominent feature the electron sees is the cylindrically symmetric electric field formed by the nuclei. The spin-orbit coupling is strong in this case, and so the electron spin $\vec{S}$ is also projected onto the internuclear axis as Σ. These two angular momenta add together to form the good quantum number, $\Omega = \Lambda + \Sigma$, oriented along the internuclear axis. Ω then couples to the angular momentum due to the rotation of the molecule, $\vec{R}$, to form $\vec{J} = \vec{\Omega} + \vec{R}$ with magnitude $\sqrt{J(J+1)}\hbar$. Each of the precessions of $\vec{L}$ and $\vec{S}$ can occur in equal and opposite directions, which manifest as positive or negative axial components, $\pm\Lambda, \pm\Sigma$, resulting in the possible $\pm\Omega$. To fully define a molecular state in *ket* notation, we have $|\eta, \Lambda, S, \Sigma, J, \Omega, M_J\rangle$, where η is a stand in for all the other quantum numbers that are not explicitly stated.

5.3.2 Hund's case (b)

The other most common case for ground states is Hund's case (b) (Figure 5.2), which is a good description for the ground state of BaH. In this case, the spin-orbit coupling is weak or non-existent (i.e. $\Lambda = 0$), and $\vec{S}$ is no longer coupled to the internuclear axis, and therefore neither Σ nor Ω are defined. In this case, $\vec{L}$ precesses rapidly about the internuclear axis, and Λ, if present, is well defined. $\vec{\Lambda}$ couples to the nuclear motion, $\vec{R}$ to form $\vec{N}$, and then the total angular momentum is $\vec{J} = \vec{N} + \vec{S}$. The basis function can be written, $|\eta, \Lambda, N, S, J, M_J\rangle$.

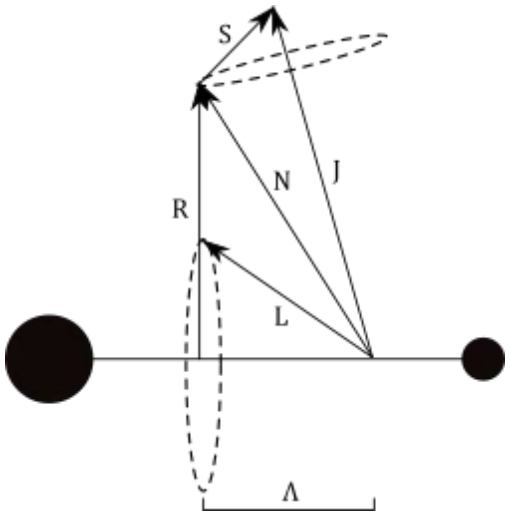

Figure 5.2: Angular momenta for a Hund's case (b) molecule where $\Lambda \neq 0$.

Most often, molecular states are some intermediate coupling between cases (a) and (b), and of course, basis states for one case can be written as a linear combination of basis states of another case. In practice, you should choose the case that minimizes off diagonal elements in the effective Hamiltonian.

5.3.3 Other Hund's cases

The other cases, (c), (d), and (e) are not relevant for the molecular states at hand, so I will refer the reader to the excellent reference, Chapter 6 of [114].

5.4 Rovibratational Structure of Electronic Transitions

In a somewhat coarse picture, when a molecule undergoes a transition between two electronic states, it does so between specific rotational and vibrational level within those states. The electronic transition is governed by selection rules as follows [111]:

$\Sigma^+ \leftrightarrow \Sigma^+$ and $\Sigma^- \leftrightarrow \Sigma^-$ but not $\Sigma^+ \leftrightarrow \Sigma^-$,

$\Delta\Lambda = 0, \pm 1$, $\Delta\Omega = 0, \pm 1$,

$\Delta J = 0, \pm 1$, but not $J = 0 \rightarrow J = 0$, and for $\Omega = 0 \rightarrow \Omega = 0, \Delta J \neq 0$

The energy difference between those two states can be described as the difference between the energies from equation 5.2.2, and is given by,

$$\Delta E = T' - T'' = (T'_e - T''_e) + (G' - G'') + (F' - F''). \tag{5.4.1}$$

Convention dictates that two primes ($''$) indicates the lower energy state, and a single prime ($'$) denotes the higher one.

The vibrational motion is not goverened by a specific conservation law, and therefore, there are no strict selection rules to govern which vibrational state in the upper electronic potential with couple with any in the lower one. Instead, the governing physics is determined by the *Frank-Condon principle*, which, in broad terms, assumes that the electronic energy transition happens on a timescale much shorter than that of the nuclear vibrational motion. As a result, the nuclei in the molecule are in very nearly the same place they were before the electron made the transition. Transitions to other vibrational states very different from the starting one would require an appreciable change in either position or relative velocities of the nuclei. This leads to the conclusion that vibrational transitions will be most energetically favorable, or probable, between those states having a high degree of overlap in their spatial wavefunctions.

After the molecule chooses a vibrational level that it would like to go to, it may also undergo changes to its rotational state. For these diatomic molecules, the angular part of the wavefunction are the eigenfunctions of the angular momentum operators, $\hat{\mathrm{N}}^2, \hat{\mathrm{N}}_Z$, in the z laboratory axis. These are given by the spherical harmonics, $Y_{N,M_N}(\theta, \phi)$, and a rotational transition is determined by the evaluation of the transition dipole operator, $\hat{d}$ between initial and final states. Since the $\hat{d}$ can be written in the same irreducible representation of the rotation group SO(3), the symmetry properties of the spherical harmonics make it easy to find out which terms of the integral are zero. In particular, the transition matrix element is nonzero only if, $\Delta N = 0, \pm 1$.

5.5 The *5d* States of BaH: $A^2\Pi_{1/2}$, $A^2\Pi_{3/2}$, $B^2\Sigma^+$, $H^2\Delta_{3/2}$, $H^2\Delta_{5/2}$

While the exact details of the electronic structure is left for other texts, it is important to review which electronic states are present around the ones we want to use, since they all interact. The lowest excited state in BaH is the $H^2\Delta$ state, which has two projections of $\Omega = 3/2$ and $\Omega = 5/2$, arranged in that order [78, 124]. Above, lies the two states, $A^2\Pi_{1/2}$ and $A^2\Pi_{3/2}$, and finally, the $B^2\Sigma^+$ state above those. These 5 electronic states are all formed form the $5d$ state of the barium atom, and share similar spectroscopic properties with the $X^2\Sigma^+$ ground state, which is a main reason the FCFs happen to be favorable for our purposes [70].

To first order, the interactions between these states can be described by a 5x5 interaction Hamiltonian that deals only with the (v=0 states), with matrix elements arising from a series of 4 parameters: $\alpha_{vv'}, \beta_{vv'}, \eta_{vv'}, \zeta_{vv'}$ describing terms from the effective Hamiltonian [125]. For BaH, this matrix is calculated in Reference [124], and the mixing coefficients are listed in Table 5.1.

State	$^2\Delta_{5/2}$	$^2\Delta_{3/2}$	$^2\Pi_{3/2}$	$^2\Pi_{1/2}$	$^2\Sigma^+$
$^2\Delta_{5/2}$	0.999745			0.0000	0.0000
$^2\Delta_{3/2}$		0.9762	0.2167	0.0000	0.0000
$^2\Pi_{3/2}$		-0.2169	0.9760	0.0000	0.0000
$^2\Pi_{1/2}$	0.0000	0.0000	0.0000	0.9688	0.2480
$^2\Sigma^+$	0.0000	0.0000	0.0000	-0.2480	0.9688

Table 5.1: Mixing coefficients of the d-states of BaH for J=1/2.

Molecular constant	Value for (v=0) (cm^{-1})
T_v	0
B_v	3.3495907(28)
$D_v \times 10^4$	1.127057(64)
$H_v \times 10^9$	2.9837(39)
γ_v	0.192063(30)

Table 5.2: Spectroscopic constants for the $X^2\Sigma^+$ state in BaH, measured by Ram *et. al.* [126]

5.6 Fine and Hyperfine Structure

For the ground state, the relevant fine and hyperfine structure are given by perturbations to the molecular Hamiltonian given by,

$$\mathbf{H_{Fine}} = \gamma_\nu \mathbf{N} \cdot \mathbf{S}, \qquad \mathbf{H_{HyperFine}} = b_\nu \mathbf{I} \cdot \mathbf{S}. \tag{5.6.1}$$

There are other nuclear hyperfine terms that arise due to various interactions, but in BaH, experimental results [127] show that only the Fermi-Contact interaction, arising from effects when the electron and nucleus are found in the same location, has a significant effect. These two interactions are best dealt with together using degenerate perturbation theory, and diagonalizing the subspace of states in the Hund's case (b) coupling scheme [128]. The basis states for Hund's case (b) molecules are written as $|\eta, \Lambda; N, S, J, I, F, m_F\rangle$, in which η describes the electronic state of the molecule, $\mathbf{N}$ is the rotation and $\mathbf{S}$,the electronic spin couple together to form $\mathbf{J}$, which in turn couples with $\mathbf{I}$ to form $\mathbf{F}$, which has its magnetic

sublevels labeled by m_F. in the following, I will go through each term in detail to calculate the matrix elements of the fine and hyperfine parts of the effective Hamiltonian.

Fine Structure

The fine structure in diatomic molecules arises due to the interaction between the electron spin, $\mathbf{S}$ and rotation of the molecule, $\mathbf{N}$, and can be considered a perturbation of the form $\mathbf{N}\cdot\mathbf{S}$. Each rotational state has 2-fold degeneracy, with quantum number $\mathbf{J} = \mathbf{N} \pm \mathbf{S}$, and we look to diagonalize the subspace spanned by these two states, therefore, we need to calculate the matrix elements given by,

$$\langle \eta, \Lambda; N, S, J, I, F, m_F | \gamma_\nu \mathrm{T}^1(\mathbf{N}) \cdot \mathrm{T}^1(\mathbf{S}) | \eta', \Lambda'; N', S', J', I', F', m'_F \rangle, \tag{5.6.2}$$

where γ_ν is the spin-rotation coupling constant. Since, these quantities are defined in different coordinate systems - $\mathbf{N}$ in the 3-D lab frame, and $\mathbf{S}$ in the molecule frame - we have used spherical tensor notation. This term can be evaluated using result (5.173) in Ref. [114], which yields,

$$\begin{aligned}
&\langle \eta, \Lambda; N, S, J, I, F, m_F | \gamma_\nu \mathrm{T}^1(\mathbf{N}) \cdot \mathrm{T}^1(\mathbf{S}) | \eta', \Lambda'; N', S', J', I', F', m'_F \rangle \\
&\quad = \gamma_\nu (-1)^{S+N+J} \delta_{J,J'} \begin{Bmatrix} S' & N' & J \\ N & S & 1 \end{Bmatrix} \langle N || \mathrm{T}^1(\mathbf{N}) || N \rangle \langle S || \mathrm{T}^1(\mathbf{S}) || S \rangle \delta_{\eta,\eta'} \delta_{\Lambda,\Lambda'} \delta_{I,I'} \delta_{F,F'} \delta_{m_F,m'_F}.
\end{aligned} \tag{5.6.3}$$

The reduced matrix elements for **N** and **S** can be evaluated with the Wigner-Eckart theorem so that the RHS is

$$= \gamma_\nu (-1)^{S+N+J} \begin{Bmatrix} S' & N' & J \\ N & S & 1 \end{Bmatrix} \delta_{N,N'} [N(N+1)(2N+1)]^{1/2} \delta_{S,S'} [S(S+1)(2S+1)]^{1/2}, \tag{5.6.4}$$

$$= \gamma_\nu (-1)^{S+N+J} \begin{Bmatrix} S & N & J \\ N & S & 1 \end{Bmatrix} [N(N+1)(2N+1)]^{1/2} [S(S+1)(2S+1)]^{1/2}. \tag{5.6.5}$$

For $N = 1$, the 2 possible J levels are $J = 3/2$ and $J = 1/2$, each with $S = 1/2$. By evaluating the $6-j$ symbols, we find that the perturbation is already diagonal in our chosen basis, and the degeneracy is lifted so that for $J = 3/2$, the spin splitting is $\frac{1}{2}\gamma_\nu$, and for $J = 1/2$, the spin splitting is $-1\gamma_\nu$. The $6-j$ symbol for N=0, J=1/2 is 0.

For the value of $\gamma_{nu} = 0.192062\text{cm}^{-1}$ in Reference [126] listed in Table 5.2, we find that the spin rotation splitting for the first rotational level is predicted to be 8.64 GHz. Using Equation, 5.2.8, we can calculate the rotational splitting for $N'' = 1$ as 201 GHz, and now we have the course rotational structure of the ground state,shown in Figure 5.3.

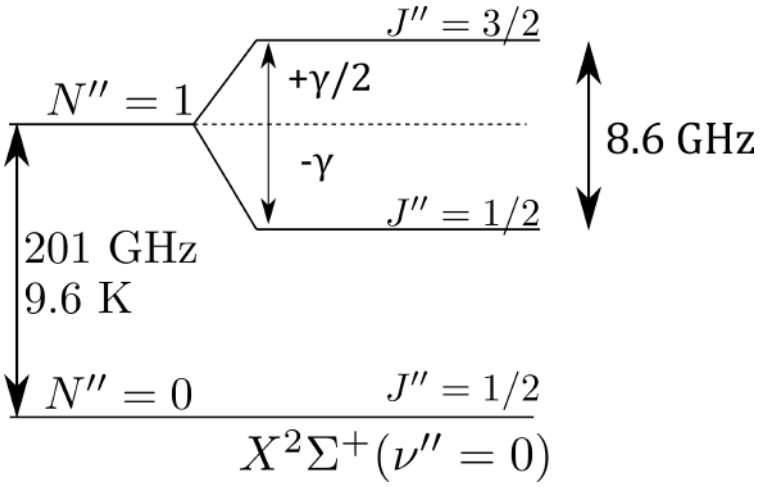

Figure 5.3: Rotational energies of relevant ground states, including spin-rotation coupling. Values for energy are predicted based on constants provided in Ref. [126]].

Hyperfine structure

The hyperfine structure can also be calculated in a similar manner. Here, the perturbation arises due to the interaction between the electronic and nuclear spins (**S**, and **I**). We now have a 4-dimensional subspace spanned by the degenerate states labeled by $\mathbf{F} = \mathbf{J} + \mathbf{I}$. Using the same basis states as before we write,

$$\langle \eta, \Lambda; N, S, J, I, F, m_F | b_F \mathrm{T}^1(\mathbf{S}) \cdot \mathrm{T}^1(\mathbf{I}) | \eta', \Lambda'; N', S', J', I', F', m'_F \rangle, \tag{5.6.6}$$

where b_F is the relevant hyperfine constant. As before, we can use result (5.173) in Ref. [114], keeping in mind that $\mathbf{F} = \mathbf{J} + \mathbf{I}$, to get,

$$\begin{aligned}
&\langle \eta, \Lambda; N, S, J, I, F, m_F | b_F \mathrm{T}^1(\mathbf{S}) \cdot \mathrm{T}^1(\mathbf{I}) | \eta', \Lambda'; N', S', J', I', F', m'_F \rangle \\
&= (-1)^{J'+I+F} \delta_{F,F'} \delta_{M_F,M'_F} \begin{Bmatrix} I' & J' & F \\ J & I & 1 \end{Bmatrix} \langle N, S, J || \mathrm{T}^1(\mathbf{S}) || N', S', J' \rangle \times \\
&\langle I || \mathrm{T}^1(\mathbf{I}) || I' \rangle \delta_{\eta,\eta'} \delta_{\Lambda,\Lambda'} \\
&= (-1)^{J'+I+F} \begin{Bmatrix} I' & J' & F \\ J & I & 1 \end{Bmatrix} [I(I+1)(2I'+1)]^{1/2} \delta_{\eta,\eta'} \delta_{I,I'} \times \\
&\langle N, S, J || \mathrm{T}^1(\mathbf{S}) || N', S', J' \rangle.
\end{aligned} \tag{5.6.7}$$

Focusing just on the $\mathrm{T}^1(\mathbf{S})$ term for a moment, and taking full, unabashed advantage of the Wigner-Eckart Theorem,

$$\begin{aligned}
&\langle N, S, J || \mathrm{T}^1(\mathbf{S}) || N', S', J' \rangle \\
&= \delta_{N,N'} (-1)^{N+S+J+1} [(2J+1)(2J'+1)]^{1/2} \begin{Bmatrix} S' & J' & N \\ J & S & 1 \end{Bmatrix} \langle S || \mathrm{T}^1(\mathbf{S}) || S' \rangle \\
&= (-1)^{N+S'+J+1} [(2J+1)(2J'+1)]^{1/2} [S(S+1)(2S'+1)]^{1/2} \begin{Bmatrix} S' & J' & N \\ J & S & 1 \end{Bmatrix} \delta_{S,S'}.
\end{aligned} \tag{5.6.8}$$

Which leaves us with the full form of the matrix elements for the hyperfine structure as,

$$\begin{aligned}
&\langle \eta, \Lambda; N, S, J, I, F, m_F | b_F \mathrm{T}^1(\mathbf{S}) \cdot \mathrm{T}^1(\mathbf{I}) | \eta, \Lambda; N, S, J', I, F, m'_F \rangle \\
&= (-1)^{J'+I+F} (-1)^{N+S+J+1} \begin{Bmatrix} I & J' & F \\ J & I & 1 \end{Bmatrix} \begin{Bmatrix} S & J' & N \\ J & S & 1 \end{Bmatrix} \times \\
&[(2J+1)(2J'+1)]^{1/2} [S(S+1)(2S'+1)]^{1/2} [I(I+1)(2I+1)]^{1/2}
\end{aligned} \tag{5.6.9}$$

State	Total shift relative to rotational level (MHz)
$\|N=1, J=3/2, F=2\rangle$	2892.75
$\|N=1, J=3/2, F=1\rangle$	2861.47
$\|N=1, J=1/2, F=1\rangle$	-5765.97
$\|N=1, J=1/2, F=0\rangle$	-5750.25
$\|N=0, J=1/2, F=1\rangle$	11.75
$\|N=0, J=1/2, F=0\rangle$	-35.25

Table 5.3: Energy shift due to fine and hyperfine perturbations to the $X^2\Sigma^+$ ground state, $N=1$ and $N=0$ rotational levels.

To find the total splitting, we combine the fine-structure and hyperfine Hamiltonians and diagonalize them together, so the total Hamiltonian to diagonalize for $N=1$ looks like,

$$H_{\mathbf{S}\cdot\mathbf{N}+\mathbf{S}\cdot\mathbf{I}} = \begin{pmatrix} \gamma_\nu/2 + b_F/4 & 0 & 0 & 0 \\ 0 & \gamma_\nu/2 - b_F 5/12 & b_F\sqrt{2}/3 & 0 \\ 0 & b_F\sqrt{2}/3 & -\gamma_\nu - b_F/12 & 0 \\ 0 & 0 & 0 & -\gamma_\nu + b_F/4 \end{pmatrix}.$$

The eigenvalues and thus energy shifts are listed in Table 5.3, and schematically shown in Figure 5.4. The off diagonal elements in the above matrix indicate the mixing between J states sharing the same F quantum number, namely, $F=1$. In BaH, the large size of γ_ν relative to b_F means that this mixing is small as compared to other diatomic molecules that have been cooled. The eigenstates of this Hamiltonian are given in Table 5.4

Ideal J State labels	Superposition of pure states
$\|N=1, J=3/2, F=2\rangle$	$\|J=3/2, F=2\rangle$
$\|N=1, J=3/2, F=1\rangle$	$\alpha\|J=3/2, F=1\rangle - \beta\|J=1/2, F=1\rangle$
$\|N=1, J=1/2, F=1\rangle$	$\alpha\|J=1/2, F=1\rangle + \beta\|J=3/2, F=1\rangle$
$\|N=1, J=1/2, F=0\rangle$	$\|J=1/2, F=0\rangle$

Table 5.4: Eigenstates of the effective Hamiltonian of the ground state $X\Sigma$ in the first rotational state $N = 1$. Ideal J state labels are used throughout this document with the understanding that the $F = 1$ levels have, in reality, small admixtures of the opposite spin rotation state contributing. The mixing coefficients are, $\alpha = 0.9999$, and $\beta = 0.0026$.

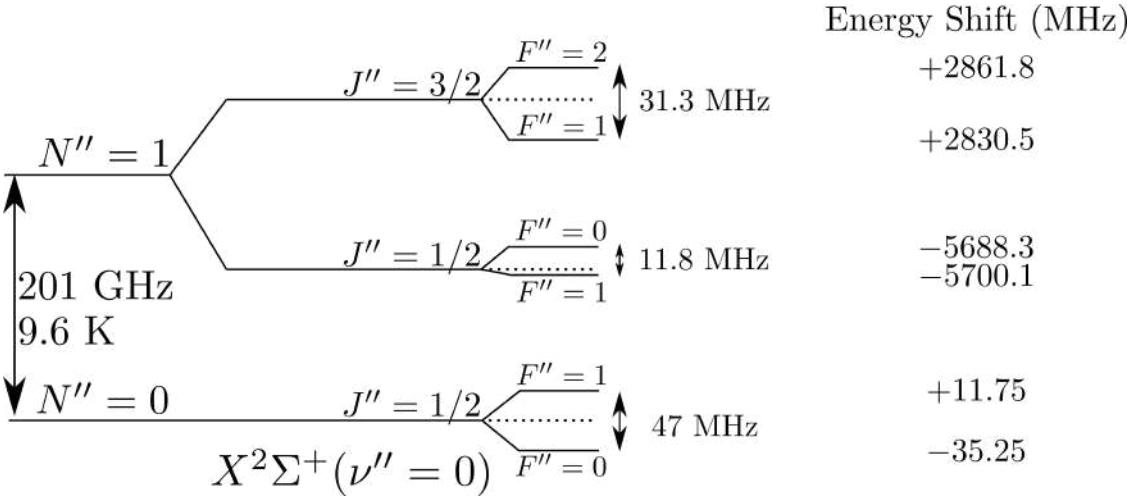

Figure 5.4: Energy shifts due to fine and hyperfine perturbations to the $X^2\Sigma^+$ ground state, $N = 1$ and $N = 0$ rotational levels.

5.7 The Molecular Zeeman Effect

Just as in atoms, the Zeeman effect in molecules arises from the interaction between a non-zero magnetic moment of the molecule with an external magnetic field, $\vec{B}$. In a diatomic molecule, there are three contributions to the molecular magnetic moment. The orbital and spin parts of the angular momentum ($\vec{L}$ and $\vec{S}$) of unpaired electrons are the primary sources of the magnetic moment, $\mu = \mu_B(|\vec{L}| + 2|\vec{S}|)$, where 2 is the electron g-factor. The rotational motion of the nuclei and and moments associated with the spins in the nuclei

form the remaining two parts of the net magnetic moment and these two are on the order of the nuclear magnetic moment, μ_N. In general, the first contribution from the orbital and spin angular momenta of the electrons dominates. Interaction of μ with an external field manifests as a splitting of degenerate energy levels,

$$\Delta E = g\mu|B|, \tag{5.7.1}$$

where g characterizes the strength of the interaction.

For our goals in creating a MOT of BaH, understanding the Zeeman interaction is crucial to forming the appropriate trapping and cooling forces. The $B^2\Sigma - X^2\Sigma$ and $A\Pi_{1/2} - X^2\Sigma$ systems are expected to be favorable for creating a MOT since the molecular g-factors of the upper and lower state are comparable, which leads to sufficient trapping forces [129]. In this section, we aim to make a prediction for the molecular g-factors.

The Zeeman shifts for the Hund's case (a), $^2\Pi$ states are most strongly influenced by the parity dependent terms, g_l' and $g_r^{e'}$. The matrix elements for this Zeeman Hamiltonian are expressed in Eq. 9.71 of [114], and the typically dominant parity dependent term can be described with a single effective g factor as,

$$g_{eff} = \frac{1}{3}(g_l' - g_r^{e'}), \tag{5.7.2}$$

where the approximations $g_l' \approx \frac{p}{2B}$ and $g_r^{e'} \approx \frac{q}{B}$ can be used with the λ-doubling constants, p and q, and rotational constant B [130].

In Hund's case (b), describing both the$B^2\Sigma$ and $X^2\Sigma$ states, we can calculate the g factors in a semiclassical way as follows. The overall g-factor for each state must account for the spin-rotation and hyperfine interactions, and so in the presence of a small magnetic field **B** along the z-axis, the Zeeman Hamiltonian for a molecule with total magnetic moment

$\mu_{\mathbf{H}} = \mu_B g_F \mathbf{F}$ is approximately,

$$H_Z = -\mu_{\mathbf{H}} \cdot \mathbf{B} \tag{5.7.3}$$

$$= -(\mu_{\mathbf{J}} + \mu_{\mathbf{I}}) \cdot \mathbf{B} \tag{5.7.4}$$

$$= g_J \mu_B \mathbf{J} \cdot \mathbf{B} - g_I \mu_N \mathbf{I} \cdot \mathbf{B} \tag{5.7.5}$$

$$= \mu_B \left[g_J J_z - g_I \left(\frac{\mu_N}{\mu_B} \right) I_z \right] B_z. \tag{5.7.6}$$

Here, μ_B is the Bohr magneton, and μ_N is the nuclear magneton. $\mathbf{J}$ is the resultant vector sum of the rotation of the molecule $\mathbf{N}$ and the free electron spin $\mathbf{S}$. The effective spin-rotation Landé g-factor is g_J, and the nuclear g-factor is g_I.[1] In the BaH isotope of interest, $\mathbf{I} = 1/2$. What is necessary, though, is finding g_F, defined as the total effective g-factor for a given hyperfine level with total angular momentum F and Zeeman sublevel M_F. In other words, the same Zeeman Hamiltonian above, but written as,

$$H_Z = \mu_B g_F M_F B_z. \tag{5.7.7}$$

The procedure involves carefully evaluating how each of the magnetic moments above couple to the magnetic field axis. And in order to evaluate that, we will need g_J and g_I individually. As we will see shortly, finding g_I is not necessary since the nuclear moment is so small.

Finding g_J amounts to finding the projection of $\mu_{\mathbf{J}} = \mu_B g_J \mathbf{J} = \mu_B (g_L \Lambda + g_s S_J) \frac{\mathbf{J}}{|\mathbf{J}|}$ in the direction of the field (Figure 5.5). Note that while $\mathbf{J} = \mathbf{N} + \mathbf{S}$, there is no magnetic moment associated with $\mathbf{N}$. Both states of interest here have no orbital angular momentum (Λ), so the contribution to $\mu_{\mathbf{H}}$ arises solely via how the electronic spin angular momentum and

[1] Since nuclear magnetic moments can be parallel or anti-parallel to $\mathbf{I}$, the convention is to make the nuclear magnetic moment, $\mu_{\mathbf{I}} = g_I \mu_N \mathbf{I}$ positive.

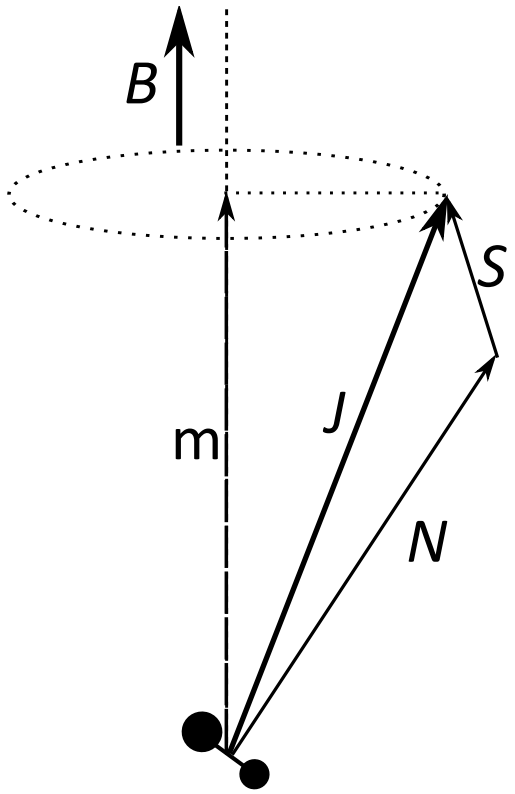

Figure 5.5: Angular momenta for a Hund's case (b) $^2\Sigma$ molecule where $\Lambda = 0$.

rotation of the molecule couple to the field axis $\hat{z}$ through $\mathbf{J}$. This can be found by taking,

$$\mu_{\mathbf{J}} \cdot \hat{\mathbf{z}} = g_s |\mathbf{S}| \cos(\mathbf{S}, \mathbf{J}) \cos(\mathbf{J}, \hat{\mathbf{z}}),$$

where,

$$\cos(\mathbf{S}, \mathbf{J}) = \frac{J(J+1) + S(S+1) - N(N+1)}{2\sqrt{J(J+1)}\sqrt{S(S+1)}}, \qquad \text{and} \qquad \cos(\mathbf{J}, \hat{\mathbf{z}}) = \frac{J_z}{\sqrt{J(J+1)}}.$$

If $H_Z = -\mu_{\mathbf{H}} \cdot \mathbf{B} = \mu_B g_J J_z B_z$, then it is clear that,

$$g_J = g_s \frac{J(J+1) + S(S+1) - N(N+1)}{2J(J+1)}. \tag{5.7.8}$$

For the $X^2\Sigma^+(N = 1, J = 3/2)$ and $X^2\Sigma^+(N = 1, J = 1/2)$ states, this yields 2/3 and

-2/3, respectively. For the $B^2\Sigma^+(N=0, J=1/2)$ state, $g_J = 2$, which is in contrast to the $A^2\Pi_{1/2} \leftarrow X^2\Sigma^+$ system, where the fine structure g-factor of the upper state is ≈ 0, and type-II MOT forces are minimized for any light polarization condition [129]. In reality, all the excited states are mixed so that in each case, a particular Hund's case is not completely applicable, but our value for g_J still is approximately true.

To find the molecular g_F for these states, we must repeat the procedure above for the spin-spin interaction, and couple the nuclear moment, $\mu_{\mathbf{I}} = g_I \mu_N \mathbf{I}$, to the lab z-axis via $\mathbf{F} = \mathbf{J} + \mathbf{I}$, the total angular momentum. The effective g-factor is then,

$$g_F = g_J \frac{F(F+1) + J(J+1) - I(I+1)}{2F(F+1)} + g_I \left(\frac{\mu_N}{\mu_B}\right) \frac{F(F+1) + I(I+1) - J(J+1)}{2F(F+1)} \tag{5.7.9}$$

$$\approx g_J \frac{F(F+1) + J(J+1) - I(I+1)}{2F(F+1)}. \tag{5.7.10}$$

In the second step we neglect the second term proportional to $\frac{\mu_N}{\mu_B} \approx \frac{1}{1836}$. The results for the relevant levels are listed in Table 5.5. In the preceeding, we have neglected mixing between different J states, which is valid only for small fields where the spin-rotation interaction is the dominant effect. It is reassuring that the above semi-classical result is reproduced exactly in Ref. [114] as the first order prediction for the g-factor using a fully quantum mechanical approach.

As we saw in the previous section, however, the quantum number J is not particularly good in this basis, and the F=1 hyperfine states for the $X^2\Sigma^+$ ground state are mixed. As a result, a more reliable way to predict the g-factors is to add in the Zeeman Hamiltonian to the effective Hamiltonian and see how the energies change with a small magnetic field. The matrix elements to calculate can be found in Ref. [114] with equations 8.183 and 8.185, which give the total electronic and nuclear Zeeman Hamiltonian as,

$$
\begin{aligned}
&\langle \eta, \Lambda; N, S, J, I, F, m_F | \mu_{\mathbf{H}} \cdot \mathbf{B} | \eta, \Lambda; N, S, J', I, F', m_F \rangle \\
&= B_z \mu_B g_s (-1)^{F-m_f} \begin{pmatrix} F & 1 & F' \\ -m_F & 0 & m_F \end{pmatrix} (-1)^{F'+J+1+I} [(2F'+1)(2F+1)]^{1/2} \\
&\times \begin{Bmatrix} F & J & I \\ J' & F' & 1 \end{Bmatrix} (-1)^{J+N+1+S} [(2J'+1)(2J+1)]^{1/2} \begin{Bmatrix} J & S & N \\ S & J' & 1 \end{Bmatrix} \\
&\times [S(S+1)(2S+1)]^{1/2} - g_I B_z \mu_B (-1)^{F-m_f} \begin{pmatrix} F & 1 & F' \\ -m_F & 0 & m_F \end{pmatrix} (-1)^{F+J+1+I} \\
&\times [(2F'+1)(2F+1)]^{1/2} \begin{Bmatrix} F & I & J \\ I & F' & 1 \end{Bmatrix} [I(I+1)(2I+1)]^{1/2}.
\end{aligned}
\tag{5.7.11}
$$

Therefore, for a small magnetic field, B_z, the Hamiltonian in the subspace of ground state hyperfine levels ends up looking like,

$$
H_{Zeeman} = B_z \begin{pmatrix} 0.49924 & 0 & 0 & 0 \\ 0 & 0.834094 & 0.469884 & 0 \\ 0 & 0.469884 & -0.334854 & 0 \\ 0 & 0 & 0 & 0 \end{pmatrix}
$$

which we can diagonalize together with the rest of the effective Hamiltonian and consider the coefficients for energy corrections proportional to B as effective g-factors. We can do this for the ground state since we have the hyperfine and spin-rotation constants available, but we cannot do the same effective Hamiltonian approach for the excited $B^2\Sigma^+$, since the constants are unknown. Given that we are only interested in the N=0 rotational level of this electronic state, and there are only 2 hyperfine levels to consider in this manifold, we can expect that the off-diagonal elements are zero.

State	Ideal case g-factor	Including State Mixing
$X^2\Sigma^+(N=1, J=3/2, F=2)$	0.500	0.500
$X^2\Sigma^+(N=1, J=3/2, F=1)$	0.833	0.836
$X^2\Sigma^+(N=1, J=1/2, F=1)$	-0.333	-0.336
$X^2\Sigma^+(N=1, J=1/2, F=0)$	0.000	0.000
$B^2\Sigma^+(N=0, J=1/2, F=1)$	1.000	.9388
$B^2\Sigma^+(N=0, J=1/2, F=0)$	0.000	0.000

Table 5.5: Tabulated g-factors for total hyperfine interaction, with and without assuming mixing between states.

However, the excited $B^2\Sigma^+$ state is mixed with several other excited states, most importantly the $A^2\Pi_{1/2}$ state for given values of J [124]. This mixing affects the g-factor of the F=1 state in the $B^2\Sigma^+$ state. The fact that these states are unpure introduces a small reduction to the $B^2\Sigma^+$ state g-factor.

To exactly calculate the g-factors then, one must solve the effective Hamiltonian describing the interaction between the 5 d-states of BaH ($A^2\Delta_{5/2}$, $A^2\Delta_{3/2}$, $A^2\Pi_{3/2}$, $A^2\Pi_{1/2}$, and $B^2\Sigma^+$) to see what compositions of unperturbed states form the observed states. Diagonalizing the interaction Hamiltonian given in Ref. [124], which spans the states above, we find the mixing coefficients as the components of the eigenstates, and the values are listed in Table 5.1. The correction due to electronic state mixing is negligible (order 10^{-5}) for the ground states, but is relevant for the excited $B^2\Sigma^+$ state.

5.8 Branching Ratios

In order to properly model the distribution of the molecules in different states as they are laser cooled, we need to understand the rotational branching ratios from each possible excited magnetic sublevel to those in the ground state. Both the $A\Pi$ and $B\Sigma$ cooling schemes comprise of 4 hyperfine magnetic sublevels in the excited state, and use all 12 of the ground state hyperfine sublevels in the $X\Sigma$ ground state. Calculating the branching ratios amounts

to evaluating the transition matrix dipole element between each of the possible states, and will tell us how the intensity of the transition is distributed among each of the possible decay paths. Furthermore, we can use this to understand how quickly dark states will be populated, and compare these results to experimentally observed rates.

The first step to calculating the branching ratios is to correctly write all the relevant basis states. For the $A\Pi$ state branching ratios, the ground states are all written in Hund's case (b), $|\eta; N, J, F, m_F\rangle$, in which $\eta \rightarrow \Lambda = 0, \Sigma = 1/2$, whereas the excited states are labeled using the Hund's case (a) notation, $|\eta, S, \Sigma, \Omega, J, I, F, m_F\rangle$. In this notation, η refers to all quantum numbers that are clearly defined and common to all the relevant states. For the calculation of the transition matrix element, we must work in all the same basis. It is easier to convert case (b) to (a), so we will do that. In the $A\Pi$ state, the angular momentum of the electron is strongly coupled to the internuclear axis as it moves through the cylindrically symmetric electric field between the two nuclei. The strong spin-orbit coupling means that the electron spin is also strongly coupled to this axis. The projection of the electron angular momentum, Λ, and the projection of the electron spin, Σ, add in two possible configurations to form $|\Omega| = 1/2 = |\Lambda + \Sigma|$, resulting in the possibility in being either $\Lambda = +1$ and $\Sigma = -1/2$, or $\Lambda = -1$ and $\Sigma = +1/2$. The energy eigenstates are formed by the symmetric and antisymmetric combinations of these two possible configurations with opposite parity [131]. Using the notation, $|\Lambda, \Sigma, \Omega, J\rangle$, These levels are:

$$\left|J = \frac{1}{2}, +\right\rangle = \frac{1}{\sqrt{2}}\left|1, -\frac{1}{2}, \frac{1}{2}, \frac{1}{2}\right\rangle + \frac{1}{\sqrt{2}}\left|-1, +\frac{1}{2}, -\frac{1}{2}, \frac{1}{2}\right\rangle, \tag{5.8.1}$$

$$\left|J = \frac{1}{2}, -\right\rangle = \frac{1}{\sqrt{2}}\left|1, -\frac{1}{2}, \frac{1}{2}, \frac{1}{2}\right\rangle - \frac{1}{\sqrt{2}}\left|-1, +\frac{1}{2}, -\frac{1}{2}, \frac{1}{2}\right\rangle. \tag{5.8.2}$$

From the $N = 1$ ground state with $-$ parity, we can only access the $+$-parity $J = 1/2$, $A\Pi$ state. For the $X\Sigma$, ground states, each Hund's case (b) state can be written as a linear

superposition of Hund's case (a) basis states as [82],

$$|N, J, F, m_F\rangle = \sum_{\Omega}\sum_{\Sigma}(-1)^{J+\Omega}\sqrt{2N+1} \times \begin{pmatrix} S & \Sigma & N \\ \Lambda & J & -\Omega \end{pmatrix} |\Lambda, S, \Sigma, \Omega, J, F\rangle. \tag{5.8.3}$$

When calculating this, it is important to remember that the ground state levels with $F = 1$ are mixed between the spin rotation states as in Table 5.4. However, this contribution can be accounted for at the end of the calculation by taking linear combinations of resulting states using the relevant the mixing coefficients.

The matrix element for the electric dipole transition operator $\hat{d}$, between the initial and final Zeeman sublevels, labeled $|A\rangle$ and $|X\rangle$, respectively, is

$$m_{AX} = \langle A|T_p^{(1)}(\hat{d})|X\rangle, \tag{5.8.4}$$

Can be evaluated as,

$$\begin{aligned} m_{AX} &= \langle A|T_p^{(1)}(\hat{d})|X\rangle, \\ &= \langle \eta', S', \Sigma', \Omega', J', I', F', m'_F|T_p^{(1)}(\hat{d})|\eta, S, \Sigma, \Omega, J, I, F, m_F\rangle \\ &= \sum_{p=-1}^{+1}(-1)^{F'-m'_F+F+J+I+1}\sqrt{2F'+1}\sqrt{2F+1} \\ &\times \begin{pmatrix} F' & 1 & F \\ -m'_F & p & m_F \end{pmatrix} \begin{Bmatrix} J & F' & F \\ J' & I & 1 \end{Bmatrix} \\ &\times \langle \eta', S', \Sigma', \Omega', J'|T_p^{(1)}(\hat{d})|\eta, S, \Sigma, \Omega, J, \rangle. \end{aligned} \tag{5.8.5}$$

State	(1/2,0,0)	(1/2,1,-1)	(1/2,1,0)	(1/2,1,+1)
(1/2,0,0)	0	2/9	2/9	2/9
(1/2,1,-1)	0.2213	0.2218	0.2218	0
(1/2,1,0)	0.2213	0.2218	0	0.2218
(1/2,1,+1)	0.2213	0	0.2218	0.2218
(3/2,1,-1)	0.1102	0.0282	0.0282	0
(3/2,1,0)	0.1102	0.0282	0	0.0282
(3/2,1,+1)	0.1102	0	0.0282	0.0282
(3/2,2,-2)	0	1/6	0	0
(3/2,2,1)	0	1/12	1/12	0
(3/2,2,0)	0	1/36	1/9	1/36
(3/2,2,+1)	0	0	1/12	1/12
(3/2,2,+2)	0	0	0	1/6

Table 5.6: Branching Ratios for A-X. Columns are labeled (J', F', M'_F) corresponding to the upper state. Rows are labeled (J, F, M_F) for the lower state. Non-integer numbers are due to J-mixing between $F = 1$ hyperfine ground state levels.

As before in calculating hyperfine structure, we can evaluate the J in the last term in the above equation using the Wigner-Eckart theorem so that,

$$\begin{aligned}
&\langle \eta', S', \Sigma', \Omega', J' || T_p^{(1)}(\hat{d}) || \eta, S, \Sigma, \Omega, J, \rangle \\
&= \sum_{q=-1}^{1} (-1)^{J'-\Omega'} \sqrt{2J'+1}\sqrt{2J+1} \begin{pmatrix} J' & 1 & J \\ -\Omega' & q & \Omega \end{pmatrix} \\
&\times \langle \Lambda', S', \Sigma', \Omega' || T_p^{(1)}(\hat{d}) || \Lambda, S, \Sigma, \Omega, \rangle
\end{aligned} \tag{5.8.6}$$

The final reduced matrix element is now common to all relevant terms, since $\Sigma' = \Sigma$ needs to be satisfied by parity constraints. As such, we don't need to calculate it.

State	(1/2,0,0)	(1/2,1,-1)	(1/2,1,0)	(1/2,1,+1)
(1/2,0,0)	0	1/9	1/9	1/9
(1/2,1,-1)	1/9	1/9	1/9	0
(1/2,1,0)	1/9	1/9	0	1/9
(1/2,1,+1)	1/9	0	1/9	1/9
(3/2,1,-1)	2/9	1/18	1/18	0
(3/2,1,0)	2/9	1/18	0	1/18
(3/2,1,+1)	2/9	0	1/18	1/18
(3/2,2,-2)	0	1/3	0	0
(3/2,2,1)	0	1/6	1/6	0
(3/2,2,0)	0	1/18	2/9	1/18
(3/2,2,+1)	0	0	1/6	1/6
(3/2,2,+2)	0	0	0	1/3

Table 5.7: Branching Ratios for B-X. Columns are labeled (J, F, M_F) corresponding to the upper state. Rows are labeled (J', F', M'_F) for the lower state.

Chapter 6

Measurements on Cryogenic Buffer Gas Cooled Molecular Beam

The cryogenic buffer gas beam apparatus here is optimized for the creation of ultracold molecules. In this context, the most important parameters to consider are the flux, forward velocity distribution, angular divergence and transverse temperature. These parameters must all be taken into consideration when determining whether the molecules can be optically manipulated to where a significant number can be loaded into a MOT. The results of this section are published in Reference [80].

6.1 Molecule Number

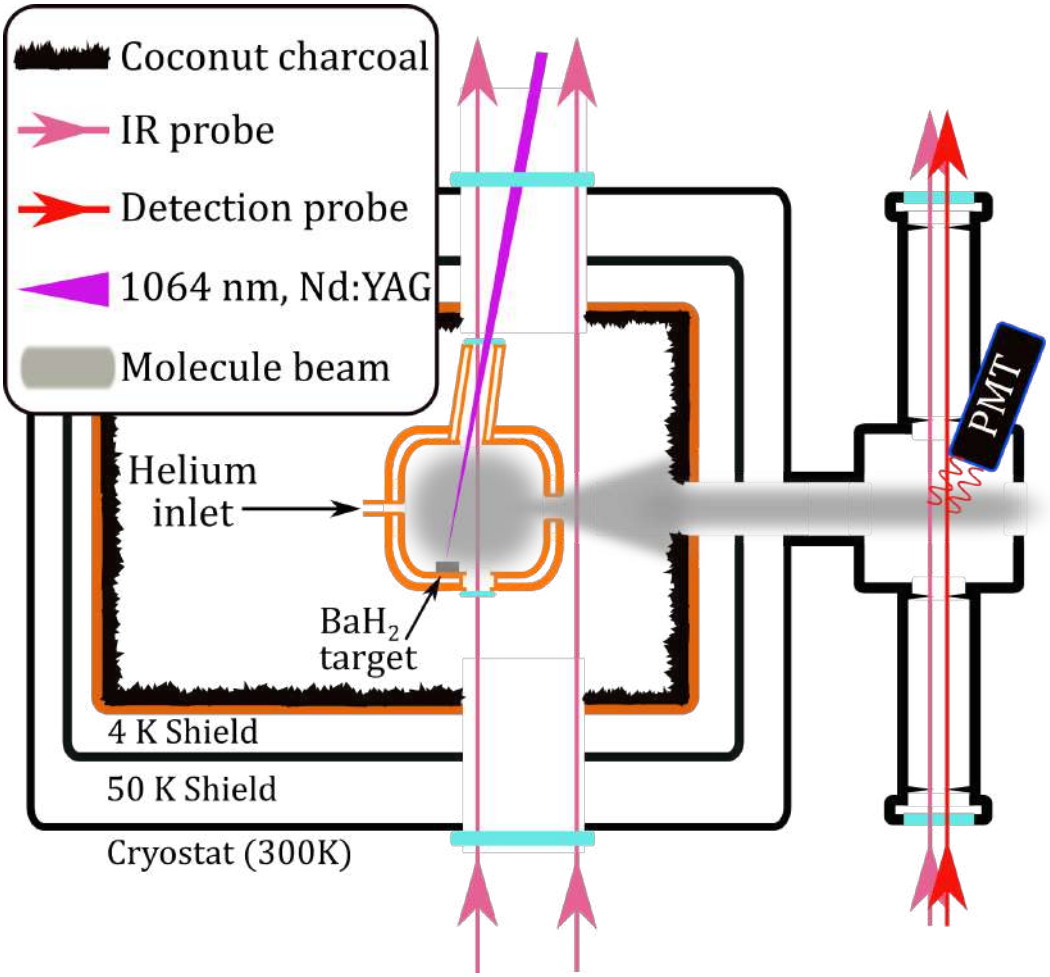

Figure 6.1: Diagram of the buffer-gas-cooled beam source of BaH for flux, and forward velocity measurements. The diatomic molecules are created through pulsed laser ablation of a BaH_2 rock inside a cryogenic copper cell filled with flowing He gas. As the molecules are swept out of the cell, they can be optically probed at various locations along the beam: in the cell and just after the cell via absorption, and in the downstream science region which is furnished with a PMT for fluorescence detection using visible light. Coconut charcoal coating on the inner shield as well as on additional copper fins (not shown) acts as a fast cryopump for excess He. The inner copper shield is nominally at 4 K and is surrounded by a 50 K aluminum shield. The entire assembly is enclosed in a vacuum-tight aluminum chamber with large optical windows on both sides.

The molecular flux downstream from the source is detected via fluorescence with a PMT as shown in Fig. 6.1. For characterizing the molecular beam we use a single-frequency

laser resonantly driving the $N'' = 1, J'' = 1/2$ spin-rotation level of the electronic ground state to the $N' = 0, J' = 1/2$ level of the $E^2\Pi_{1/2}$ excited state. Because of the approximately equal branching ratios between the two spin rotation levels, molecules are pumped out of the detection state with approx 1 photon. Assuming that the molecules are equally distributed in each hyperfine magnetic sublevel, we detect one third of the total molecules present in the N" = 1 rotational state. In addition, the probe laser intersects slightly less than a tenth of the molecular beam cross-sectional area. The detection efficiency of the system is the product of the 2% PMT quantum efficiency at 684 nm and the 2.5% geometric collection efficiency of the detection optics.

Each of these factors combined with the signal size of around 500 PMT counts in the detection region per ablation pulse yields approximately 4×10^7 molecules in the $X^2\Sigma^+(v'' = 0, N'' = 1)$ state per pulse. Some of our ablation targets yield up to three times as many molecules.

This number represents the number of molecules in a given rovibrational state. To get a more comprehensive view of the molecule number across all rotational states, we can use the formula,

$$\frac{Number_N}{TotalNumber} = \frac{(2N+1)}{Q} e^{-BN(N+1)/kT} \tag{6.1.1}$$

where Q is the sum of rotational state partition function:

$$Q = 1 + 3e^{-2Bhc/kT} + 5e^{-6Bhc/kT} + 7e^{-20Bhc/kT} + ...$$

For the low temperatures that we are concerned with, we can take the first 3 or 4 terms of this sum, checking that indeed, at T=6 K, the 5th term is already of the order 10^{-4}. The cell temperature of 6 K should be an approximate proxy for the rotational temperature, and at this temperature, we see that Equation 6.1.1 yields a total population of 1.1×10^8

molecules.

6.2 Forward Velocity and Velocity Spread

To determine the forward velocity distribution of the molecules, we make time-resolved molecular density measurements 2 cm away from the cell exit via absorption spectroscopy and, simultaneously, downstream in the fluorescence detection region, using the $X^2\Sigma^+(v''=0, N''=1)$ ground state. These two measurements of beam density as a function of time give waveforms that provide detailed information about the instantaneous distribution of molecules. The forward velocity distribution results from deconvolving these two waveforms in a process analogous to spatial time-of-flight analysis in quantum gas experiments. Rees McNally is responsible for figuring out this analysis for us.

In this analysis, we are looking to find the function that evolves an initial temporal distribution into another one measured later. In other words, we are looking for the Green's function between two time of flight (TOF) distributions, $n_f(x,t)$ and $n_i(x',t')$, separated by a parameter, Δx that is the difference between the initial position x', and final position x. For each molecule, the time at which it crosses the initial position, x' is given by the variable, t', and the time at the final position is denoted by t, so that $\partial t = t - t' = \Delta x/v$, where v is the velocity of that molecule. The instantaneous values for initial and final times as t_i and t_f. The Green's function is the velocity distribution, $V(t-t')$, such that,

$$n_f(x,t) = n_i(x',t') * V(t-t') \tag{6.2.1}$$

$$= \int_{t'}^{t} n_i(x',t')V(t-t')\,dt' \tag{6.2.2}$$

$$= \int_{t'}^{t} n_i(x',t')V(\frac{\Delta x}{v})\,dt'. \tag{6.2.3}$$

We can drop some formality for convenience and simply write from here on out that $V(t-t') = V(v)$, understanding that $V(v)$ is the connecting function of the velocity operator, between the variables t and t'. From the convolution theorem,

$$\mathcal{F}\{n_f(x,t)\} = \mathcal{F}\{n_i(x',t')\}\mathcal{F}\{V(v)\}, \tag{6.2.4}$$

where $\mathcal{F}\{x\}$ denotes the Fourier Transform of x. This makes finding the velocity distribution simple, and we have,

$$V(v) = \mathcal{F}^{-1}\left\{\frac{\mathcal{F}\{n_f(x,t)\}}{\mathcal{F}\{n_i(x',t')\}}\right\}. \tag{6.2.5}$$

We can test out Equation 6.2.5 with a couple simple examples. In the first, we can imagine the initial and final distributions are simple Dirac Delta functions such that $n_i(x',t') = \delta(t'-t_i)$ where t_i is when molecules cross x', and $n_f(x,t) = \delta(t-t_f)$ where t_f is when all the molecules reach position x. Plugging into Equation 6.2.5,

$$V(v) = \mathcal{F}^{-1}\left(\frac{e^{it_f\omega}}{e^{it_i\omega}}\right) \tag{6.2.6}$$

$$= \sqrt{2\pi}\,\delta(\partial t - \Delta t) \tag{6.2.7}$$

$$= \sqrt{2\pi}\,\delta(\frac{\Delta x}{v} - \Delta t), \tag{6.2.8}$$

$$\tag{6.2.9}$$

Where in the last step we have used the fact that $\partial t = t - t' = \Delta x/v$, and $\Delta t = t_f - t_i$. The result tells us that $V(v)$ is a delta function centered at $v = \frac{\Delta x}{\Delta t}$, which is expected - all it did was move our initial distribution along in time and space. This example is shown in Figure 6.2.

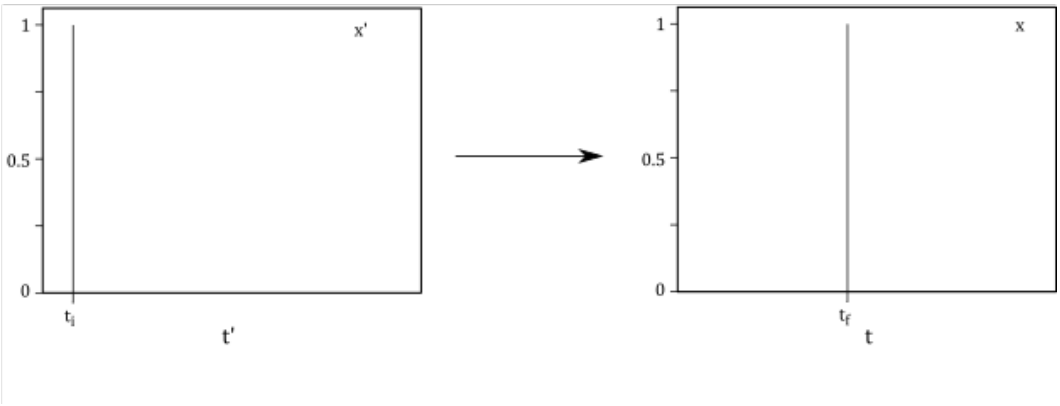

Figure 6.2: The simplest case of deconvolving a TOF distribution, where an infinitely short pulse of molecules cross x' at t_i, which is understood to be the time shortly after molecules leave the cell. Downstream, we measure the molecules crossing x at a later time t_f, again measured as an infinitely short pulse. The connecting function for these two waveforms is a constant velocity function, where the each molecule has velocity $v = \Delta x/\Delta t$

.

We can test it out for a more complicated example where, again, all the molecules start at x' at t', making the initial distribution a delta function at t', $n_i(x', t) = \delta(t - t')$ (Figure 6.2). This time, we can imagine that the final waveform is a Gaussian in time of the form,

$$n_f(x,t) = \frac{1}{\sqrt{2\sigma^2\pi}} e^{\frac{-(t-t_f)^2}{2\sigma^2}}, \tag{6.2.10}$$

where σ is the Gaussian variance of the waveform. Then we find,

$$\mathcal{F}\{n_i\} = \frac{e^{i\omega t_i}}{\sqrt{2\pi}}$$
$$\mathcal{F}\{n_f\} = \frac{e^{i\omega t_f - \frac{\omega^2\sigma^2}{2}}}{\sqrt{2\pi}}$$

And therefore, Equation 6.2.5 gives us,

$$V(v) = \frac{e^{(\frac{x}{v}-(t_f-t_i))}}{\sigma}, \tag{6.2.11}$$

which yields a velocity distribution as that shown in Fig. 6.3, exhibiting a high velocity tail and a steep, low-velocity rise. This distribution qualitatively resembles the Maxwell-Boltzmann distribution from ablation studies done on the room temperature experiment.

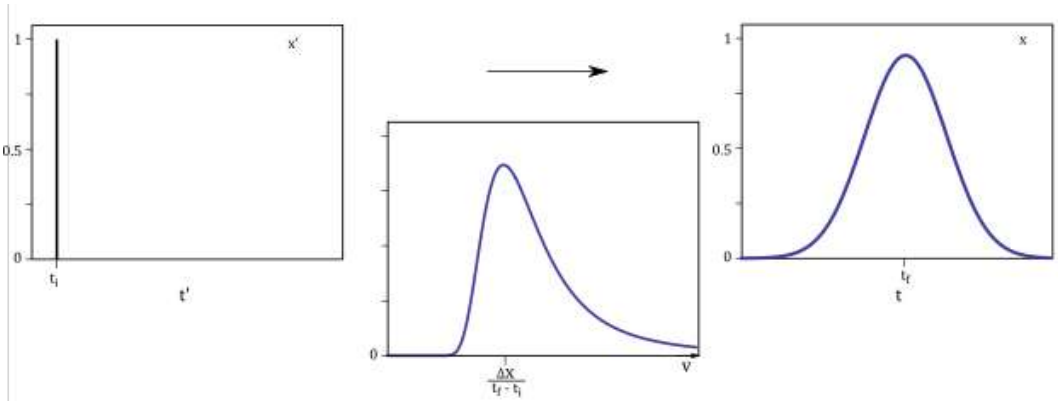

Figure 6.3: Another simple case of deconvolving a TOF distribution, where an infinitely short pulse of molecules cross x' at t_i, which is understood to be the time shortly after molecules leave the cell. Downstream, we measure the molecules crossing x at a later time t_f, this time measured as an Gaussian pulse in time. The connecting function for these two waveforms is a velocity function with a high velocity tail and a fairly steep low-velocity rise. The most peak velocity, that which the most molecules have, is $v_p = \Delta x/(t_f - t_i)$, the same as for the previous simple case.

From these two examples we can be fairly convinced that Equation 6.2.5 does what we expect. For numerical data, we should take the Fast Fourier Transform algorithm (FFT), and add a scaling constant, λ, in the denominator of the Inverse FFT to reduce noise by supressing the high-frequency noise. The value of λ is tuned according to the level of noise in the data set. The resulting algorithm on the data is,

$$V(v) = FFT^{-1}\left\{\frac{FFT\{n_f(x,t)\}}{FFT\{n_i(x',t')\}+\lambda}\right\}. \tag{6.2.12}$$

The resulting distribution will be in the time variable, so we can directly substitute the coordinate with $v = \Delta x/t$, where Δx is the distance between the two measurement points. The results of this analysis are given in Fig. 6.4 for various He flow rates from 4.4 to 22 sccm.

These waveforms, averaged over approximately 30 shots and smoothed with a 2 point window, are normalized to the peak molecule flux, but the data do not show significant variation in the number integrated molecules over the range of flow rates. Fig. 6.4 and its inset show that the fraction of slow molecules with forward velocities below 100 m/s doubles as the He flow is reduced from 22 to 4.4 sccm, reaching over 10%. At even lower flow rates the molecular flux begins to degrade. The distributions in the figure are not all taken with the same ablation spot, and this accounts for some of the qualitative discrepancy in the high velocity behavior. For example, the velocity distributions taken at 22, 13.2, and 4.4 sccm were taken without moving the ablation laser alignment, but the 17.6 sccm trace required an adjustment of the ablation spot to increase the molecule flux. Yet, it is evident from the data in Fig. 6.4 that the low-velocity behavior is stable and systematic in its dependence on the flow rate.

That the overall shape of the velocity distribution can be affected by the particular choice of target or ablation spot, as is the case for the 17 sccm trace, is indicative of the incomplete thermalization of molecules in the cell. The molecules that are ejected form the target with the highest velocities leave the cell before they completely thermalize with the buffer gas, imprinting the source dependent phase space distribution onto the high-velocity tail of the measured distributions, which results in the relatively broad and asymmetric nature of the velocity distributions.

This dependence indicates that we may be able to further improve the relative number of low velocity molecules through further refinements to the buffer gas cell geometry.

Further complicating this tail, the velocity distributions above 250 m/s are slightly less reliable than those for lower velocities since this signal comes from faster molecules arriving in the detection region very shortly after ablation, while there is a minimum waiting time after ablation to begin detecting in order to avoid the stray fluorescence.

In the fluorescence detection region we can limit the transverse temperature of the molecules to 0.1 K by comparing the expected natural linewidth of the $B^2\Sigma^+$ state to the measured spectra. This cold transverse temperature is consistent with geometric constraints on the beam and allows us to characterize the relevant properties of BaH at a higher optical resolution than was previously possible, enabling direct measurements of hyperfine structure and molecular g-factors.

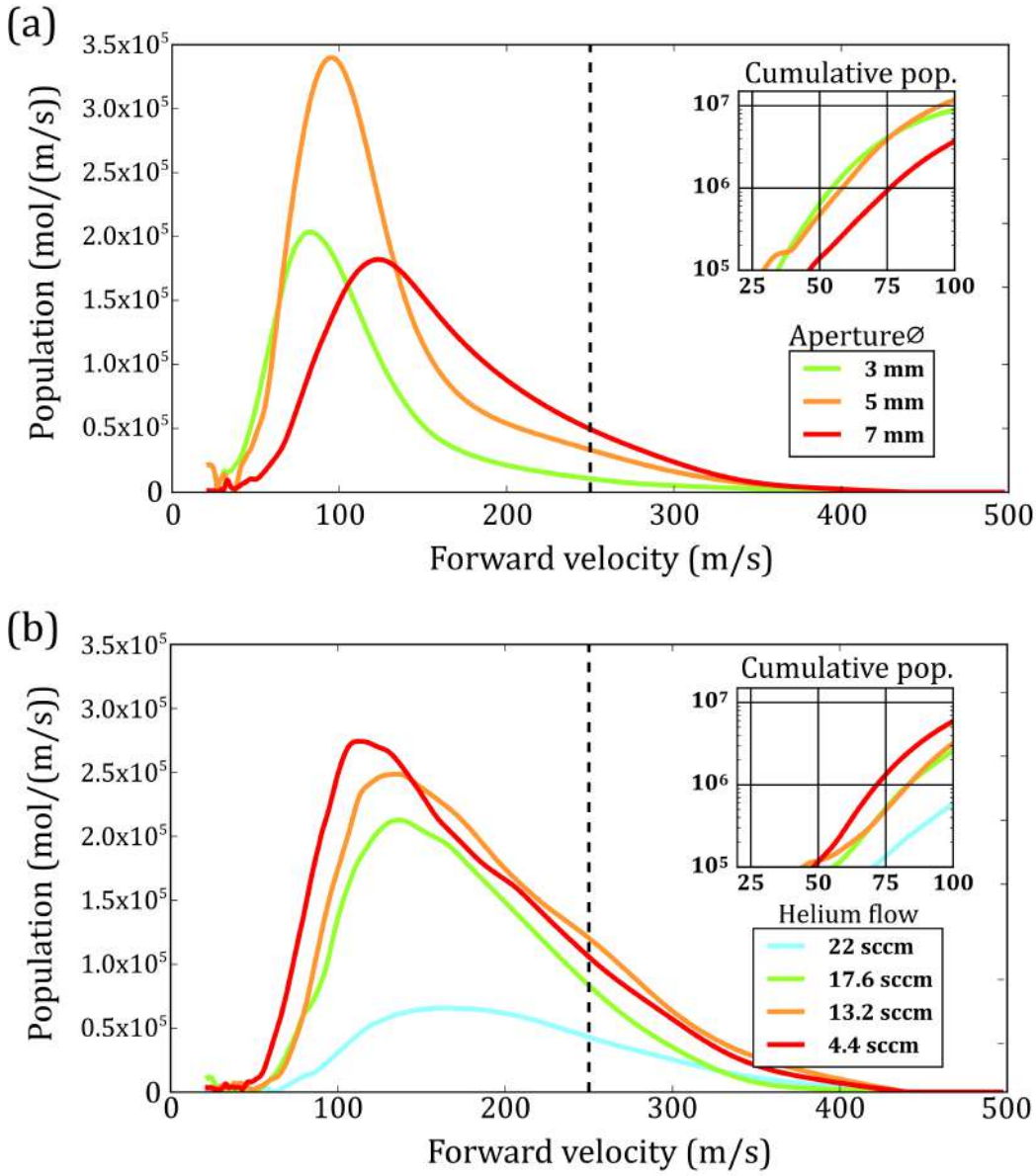

Figure 6.4: Measured forward velocity distributions of BaH molecules at a range of buffer gas flow rates. Each distribution is normalized to its peak value. The total molecule number does not significantly vary in this range of flow rates. Velocity distributions above 250 m/s (dashed line) are slightly less reliable due to a moderate sensitivity on specific data cuts made to reject fluorescence noise from ablation light. The small-scale structure at low velocities is an artifact of deconvolution. The distributions show little variation with He flow rate for high velocities, but there is a clear enhancement of the slow molecule number for lower flow rates. Some variation is seen for different ablation samples or spots, as in the 17.6 sccm trace, indicating incomplete translational thermalization. The inset shows the percentages of molecules below a given velocity under 100 m/s.

6.3 Measured Molecular Properties of BaH

6.3.1 Hyperfine Constants

As previously noted, a crucial parameter for MOT trapping is the hyperfine splitting of both the ground and excited states. MOT lasers must be detuned from the zero-field transition frequency by a value on the order of $2\pi \times \Gamma$, where Γ is the natural linewidth of the transition. In the case of BaH, this corresponds to about 8 MHz. If the excited state hyperfine splitting is of this order, then MOT trapping becomes impossible, since lasers that are red detuned for molecules in one transition are blue detuned for those in the other, driving anti restoring transitions.

The hyperfine structure in BaH has been studied in only one previous paper [127], where electron spin resonance spectra were obtained for the $X^2\Sigma^+$ state of BaH trapped in solid argon matricies at 4K. Knight and Walker measured the Fermi Contact interaction constant $b_F = 47(2)$ MHz, from spectra of the $N = 0$ ground state, and a negligible dipolar interaction term. However, their measurements were insensitive to the centrifugal distortion hyperfine term, C, and furthermore, argon matrix measurements are expected to lower the free space value of these constants [132]. Our experiment provides a cold sample with which to measure the hyperfine structure with high resolution spectroscopy.

Geometric constraints on the molecular beam as it exits the cryogenic region limit the transverse temperature of the molecules to ≈100 mK. Combined with our signal to noise, this allows us to perform precision laser spectroscopy and resolve the hyperfine structure at the 4 MHz level. While spectroscopy would typically be done via fluorescence, directly detecting fluorescence from the $A^2\Pi$ or $B^2\Sigma$ states is challenging because of wavelength limitations of PMTs. However, these states can be probed by optically pumping molecules between the ground state spin-rotation levels ($X^2\Sigma^+(J'' = 1/2)$ and $X^2\Sigma^+(J'' = 3/2)$), via $B^2\Sigma^+$ or $A^2\Pi_{1/2}$ excited states, and then detecting the remaining populations in one of them via

fluorescence transitions to the $E^2\Pi_{1/2}$ state which lies some 680 nm above the ground state. The highly favorable branching ratios to the original vibrational level for the $5d$ states of BaH make this possible. That the hyperfine splitting in the $J'' = 1/2$ ground state is small is especially helpful for this measurement, since we can simultaneously monitor the population in both levels.

The set up for this experiment can be seen in Figure 6.1. In each measurement, the $X^2\Sigma^+(J'' = 1/2)$ population is monitored by sending a 683.7268 nm laser beam through the detection region and recording fluorescence from the spontaneous decay of the $E^2\Pi_{1/2}$ state. Several beam waists upstream, a probe laser drives transitions from one of the ground electronic spin-rotation levels through the $B^2\Sigma^+$ or $A^2\Pi_{1/2}$ excited state. Depending on which ground state spin-rotation level is pumped, the detected fluorescence is either enhanced or reduced because of the increase or decrease in population. The pump laser is scanned across the transition, resulting in hyperfine resolved spectra. These different measurements are shown in Figure 6.5, and are labeled, A, B, C, and D.

The A and C transitions (905.3197 nm and 1060.8191 nm) enhance the detected fluorescence as the molecules get pumped from the $J'' = 3/2$ ground state level to $J'' = 1/2$, while the B and D transitions (905.2962 nm and 1060.7868 nm) decrease the fluorescence as the molecules are pumped out of the $J'' = 1/2$ level. Each data point in the spectra of Fig. 6.5 is an average of 5 ablation shots.

Since the hyperfine constant for the excited states are unknown, the assignment of individual hyperifne transitions in each spectra requires a bit of thinking. In particular, the ordering of the excited state hyperfine levels could be "flipped", where the $F' = 1$ state lies lower in energy than the $F' = 0$ state. For each configuration, there are two possible spectra, depending on whether the excited state splitting or ground state hyperfine splitting is greater in magnitude.

With no a priori knowledge of the hyperfine splitting (magnitude or orientation) of the

excited state of interest, all we can say is that there will be 3 spectroscopic peaks for both the enhancement and depletion measurements (1→1, 1→0, 0→1 for depletion and 1→1, 1→0, 2→1 for enhancement). For each experiment there are 4 possibilities for the relative arrangement of the peaks. For the 'normal' orientation of excited hyperfine states ($F' = 1$ above $F' = 0$), the 1→1 transition will be of highest energy. For the 'flipped' orientation of excited hyperfine states ($F' = 0$ above $F' = 1$), the 1→0 transition will be of highest energy.

Both the enhancement and depletion measurements for a given excited state share the excited state hyperfine splitting, which we can then use to identify common spacings in the measurements, as schematically shown in Figure 6.6, which shows the possible configurations for pumping through the $A^2\Pi_{1/2}$ state.

The peaks and their spacings in the spectra can be correctly identified by assuming an ordering for the excited-state hyperfine structure and fitting the peak positions for measurements that both deplete and enhance the $J'' = 1/2$ ground spin rotation state. If the initial assumption was correct, there will be no discrepancies in the spacings.

Another consistency check can be done by comparing the relative peak amplitudes for each allowed hyperfine transition. The amount of measured fluorescence depends on the population in the initial state. Assuming an equal population in each Zeeman sublevel, the relative peak amplitudes are then given by the hyperfine level degeneracies. A correctly chosen ordering yields peak spacings and heights that are consistent for all four data sets in Fig. 6.5. The shown fits to the fluorescence spectra are constrained only by the expected peak height ratios. The correctly identified hyperfine spacings are thus tabulated in Table 6.1.

The data is analyzed using an effective Hamiltonian model to extract molecular hyperfine constants, which for the electronic ground state, we can compare to those previously measured in a 4K Argon matrix [127]. As described in detail in Chapter 5, the $X^2\Sigma^+$ ground

Table 6.1: Measured hyperfine spacings for states relevant to laser cooling.

State	Measured hyperfine spacing (MHz)
$X^2\Sigma^+(J''=3/2)$	39(4)
$X^2\Sigma^+(J''=1/2)$	0(4)
$B^2\Sigma^+(J'=1/2)$	52(5)
$A^2\Pi_{1/2}(J'=1/2)$	0(4)

state energy level structure is described with the effective Hamiltonian,

$$\mathbf{H}_{eff} = \gamma_\nu \mathbf{S}\cdot\mathbf{N} + b_F \mathbf{S}\cdot\mathbf{I} + cI_z\cdot S_z, \tag{6.3.1}$$

which ignores negligible terms. Evaluating each term, the resulting hyperfine interaction matrix elements for $^2\Sigma^+$ states are,

$$H_{hf} = \begin{pmatrix} \frac{b_F}{4}+\frac{c}{20} & 0 & 0 & 0 \\ 0 & -\frac{b_F 5}{12}-\frac{c}{12} & \frac{b_F\sqrt{2}}{3}+\frac{c\sqrt{2}}{6} & 0 \\ 0 & \frac{b_F\sqrt{2}}{3}+\frac{c\sqrt{2}}{6} & -\frac{b_F}{12}+\frac{c}{12} & 0 \\ 0 & 0 & 0 & \frac{b_F}{4}-\frac{c}{4} \end{pmatrix}. \tag{6.3.2}$$

Solving the eigenvalue equations for the measured hyperfine splittings yield $b_F = 50(7)$ MHz, and $c = 39(8)$ MHz. The value for b_F is consistent with previous measurements of 47(2) MHz [127]. The value for c, while lacking previous reliable measurements, is consistent with those for other alkaline-earth-metal monohydrides [127].

The hyperfine-structure results in these measurements show manageable splittings that can be addressed using standard electro-optical techniques, and, at first examination, do not present a major obstacle to laser-cooling schemes. In particular, the small $A^2\Pi_{1/2}$ excited state splitting, a common feature for comparable diatomic molecules, allows all excited-state sublevels to participate in optical cycling, maximizing radiation pressure forces. The 52(5)

MHz $B^2\Sigma^+$ splitting is uniquely large among diatomics investigated for laser cooling.

6.3.2 Zeeman Shifts

Introducing a magnetic field across the molecular beam, transverse to both the beam propagation direction and the probe light direction allows for a straightforward determination of the magnitude of the g-factor for each state.

Molecular effective g-factors are crucial parameters for understanding the magneto-optical trapping forces given molecular cooling transition. In particular, the trapping forces depend strongly on the ratio of ground to excited state g-factors [129]. As in Chapter 5, predictions can be made for the three relevant levels in BaH by diagonalizing the effective Zeeman Hamiltonian for each state.

For $^2\Sigma^+$ states, the electronic and nuclear Zeeman interaction Hamiltonian is expressed in Eq. 8.185 of Ref. [114]; in BaH, this corresponds to a Zeeman Hamiltonian with 12 hyperfine

ground m_F states for $X^2\Sigma^+$ and 4 hyperfine m_F states in $B^2\Sigma^+$ as,

$$\begin{aligned}
&\langle \eta, \Lambda; N, S, J, I, F, m_F | \mu_{\mathbf{H}} \cdot \mathbf{B} | \eta, \Lambda; N, S, J', I, F', m_F \rangle \\
&= B_z \mu_B g_s (-1)^{F-m_f} \begin{pmatrix} F & 1 & F' \\ -m_F & 0 & m_F \end{pmatrix} (-1)^{F'+J+1+I} \\
&\times [(2F'+1)(2F+1)]^{1/2} \begin{Bmatrix} F & J & I \\ J' & F' & 1 \end{Bmatrix} (-1)^{J+N+1+S} \\
&\times [(2J'+1)(2J+1)]^{1/2} \begin{Bmatrix} J & S & N \\ S & J' & 1 \end{Bmatrix} \\
&\times [S(S+1)(2S+1)]^{1/2} - g_I B_z \mu_B (-1)^{F-m_f} \\
&\times \begin{pmatrix} F & 1 & F' \\ -m_F & 0 & m_F \end{pmatrix} (-1)^{F+J+1+I} \\
&\times [(2F'+1)(2F+1)]^{1/2} \begin{Bmatrix} F & I & J \\ I & F' & 1 \end{Bmatrix} \\
&\times [I(I+1)(2I+1)]^{1/2}.
\end{aligned} \tag{6.3.3}$$

The Zeeman shifts for the $^2\Pi$ states can be described with a single effective g factor as,

$$g_{eff} = \frac{1}{3}(g_l' - g_r^{e'}), \tag{6.3.4}$$

where the approximations $g_l' \approx \frac{p}{2B}$ and $g_r^{e'} \approx \frac{q}{B}$ can be used with the λ-doubling constants, p and q, and rotational constant B [130]. These constants have been measured in BaH for $A^2\Pi_{1/2}$ by Kopp *et al.* [71], and for $E^2\Pi_{1/2}$ by Fabre *et al.* [77].

Additional contributions to the effective g-factor result from interactions between electronic states. In BaH, the lowest 5-d excited states form an interacting complex [124]. Of these, the $B^2\Sigma^+$ and $A^2\Pi_{1/2}$ states mix strongly, resulting in enhancement of the $A^2\Pi_{1/2}$

state g-factor and slight reduction in that of the $B^2\Sigma^+$ state.

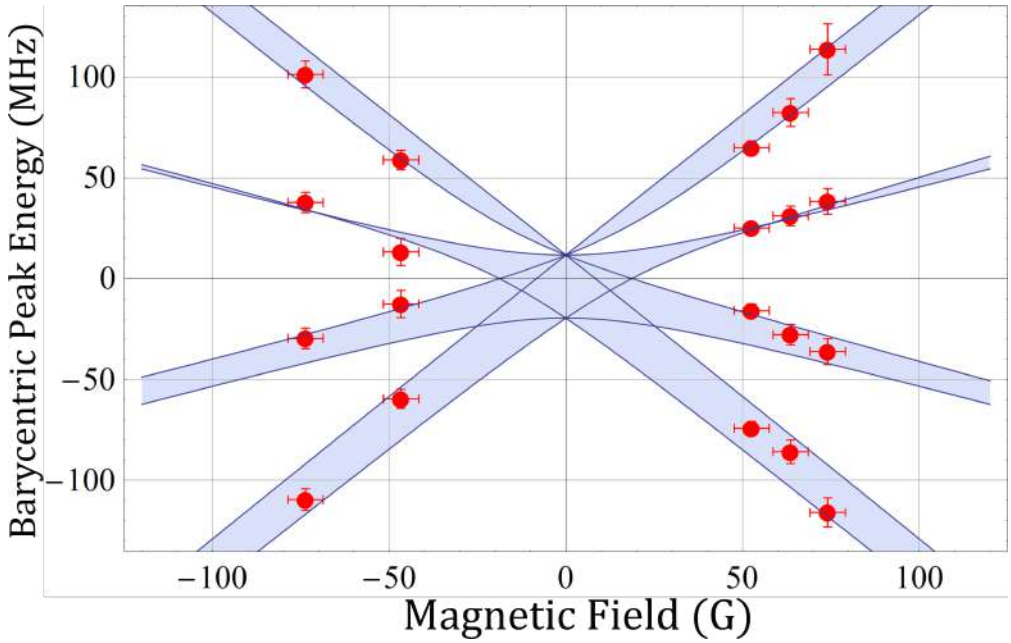

Figure 6.7: Measured Zeeman shifts of the $X^2\Sigma^+(J'' = 3/2)$ ground state sublevels, overlayed on model prediction from diagonalizing the effective Zeeman Hamiltonian. Solid lines represent energies of the m_F sublevels with applied magnetic field. Areas between interacting sublevels are shaded to emphasize unresolved structure.

While the effective Hamiltonian is written in the F basis for these three electronic levels, the large off-diagonal terms in the Zeeman Hamiltonian lead to strong interactions between these hyperfine sublevels even at modest fields. These states quickly rearrange into states best described by m_J basis, for example in Fig. 6.7. As a result, the reported effective g-factors, g_{eff} correspond with the Zeeman energy shifts,

$$\Delta E = g_{eff}\mu_0 B_{app} m_J, \tag{6.3.5}$$

where μ_0 is the Bohr magneton and B_{app} is the applied field.

Zeeman spectra were measured and recorded for the relevant ground and excited states, and the results as well as model predictions are tabulated in Table 6.2. For all experiments, B-field was applied perpendicular to the laser propagation direction, calibrated with

a commercial gaussmeter (Meda). Measurements of the BaH ground state splittings were done through the $X^2\Sigma^+ \leftarrow E^2\Pi_{1/2}$ transition, where by switching between π and $\sigma^\pm$ transitions, we could identify the ground and excited state splitting separately. Measurements of the $B^2\Sigma^+$ and $A^2\Pi_{1/2}$ states were performed through fluorescence reduction measurements, as in the hyperfine measurement, and polarization was again switched to drive π and $\sigma^\pm$ transitions in order to determine the relative signs of each g-factor.

Table 6.2: Measured and predicted effective g-factors for total hyperfine interaction. Strong mixing between Hund's cases makes J the correct basis even for moderate fields.

State	Measured g_{eff}	Prediction
$X^2\Sigma^+(N''=1, J''=3/2)$	+0.56(19)	+0.50
$X^2\Sigma^+(N''=1, J''=1/2)$	-1.37(10)	-1.4
$B^2\Sigma^+(N'=0, J'=1/2)$	+2.76(10)	+2.86
$A^2\Pi_{1/2}(N'=0, J'=1/2)$	-0.56(1)	-0.44
$E^2\Pi_{1/2}(N'=0, J'=1/2)$	-0.16(10)	-0.04

6.3.3 Determination of State g-factor Signs

While we can develop relative assignments of the sign of the g-factors for all the Zeeman shift data, we needed to make an explicit measurement of at least one g-factor. The most straightforward transition for this is with the $X^2\Sigma^+ \rightarrow E^2\Pi_{1/2}$ transition, using circularly polarized light that is propagating co-linear with an applied magnetic field. This setup is shown in the Fig. 6.8.

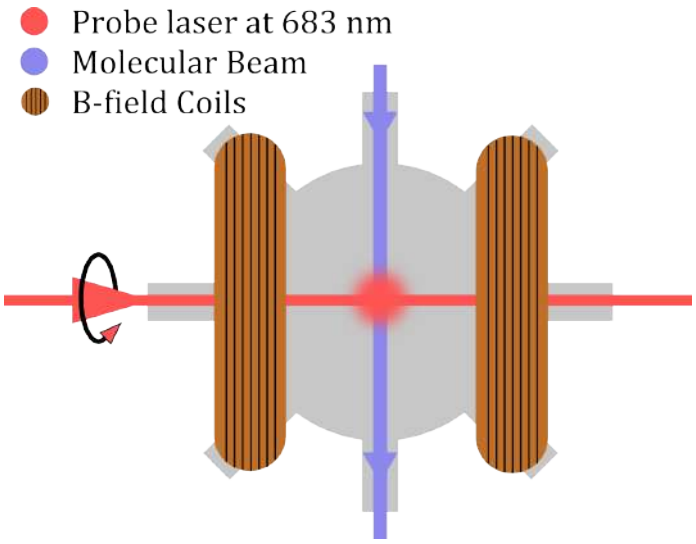

Figure 6.8: Cartoon drawing of the detection region set up for g-factor sign determination.

$X^2\Sigma^+$ ground state

With the setup shown we can look to see how an observed peak can be shifted relative to the 0 field configuration, and this will give us two different results depending on the sign of the g-factor. In Fig. 6.9 are the two experiments we did (though it is technically redundant) to show that the data we took corresponds to a negative g-factor for the $X^2\Sigma^+$ ground state. This works with the following assumptions:

- The $E^2\Pi_{1/2}$ g-factor is small compared to the ground state. (This is confirmed by data taken on 2017-02-07, where we found that it shifts by only 0.05 MHz/Gauss compared to the ground state which is closer to 1 MHz/Gauss)

- That our probe light is indeed right-circularly polarized. We took horizontally polarized light and put it through a $\lambda/4$ plate with a angle of $+45^o$ to the fast axis. This is checked by a circular analyzer.

- That the field direction is correct. Based on the coil winding and current measured, we believe that positive B-field points in the direction of the probe propagation.

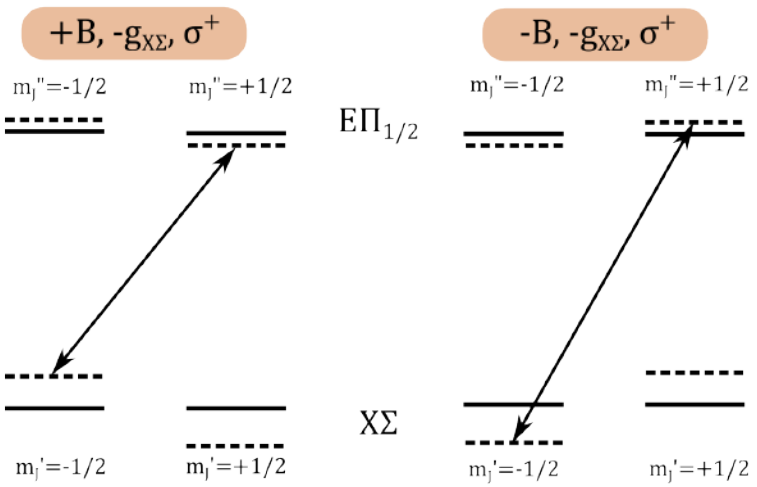

Figure 6.9: Predicted transitions to be observed with an assumed negative g-factor. This indeed corresponds to our measurements.

The data show that the positive field configuration led to a negative shift in energy, whereas a negative applied field led to a positive shift in energy. Therefore the $X^2\Sigma^+$ ground state has a negative g-factor.

$E^2\Pi_{1/2}$ excited state

The $E^2\Pi_{1/2}$ g-factor can be found from the data we took for Zeeman shifts on the $X^2\Sigma^+ \rightarrow E^2\Pi_{1/2}$ transition, varying the linear polarization. The level scheme below assumes that the $E^2\Pi_{1/2}$ state has a negative g-factor, and we look for how the resulting calculation relates to what we observe.

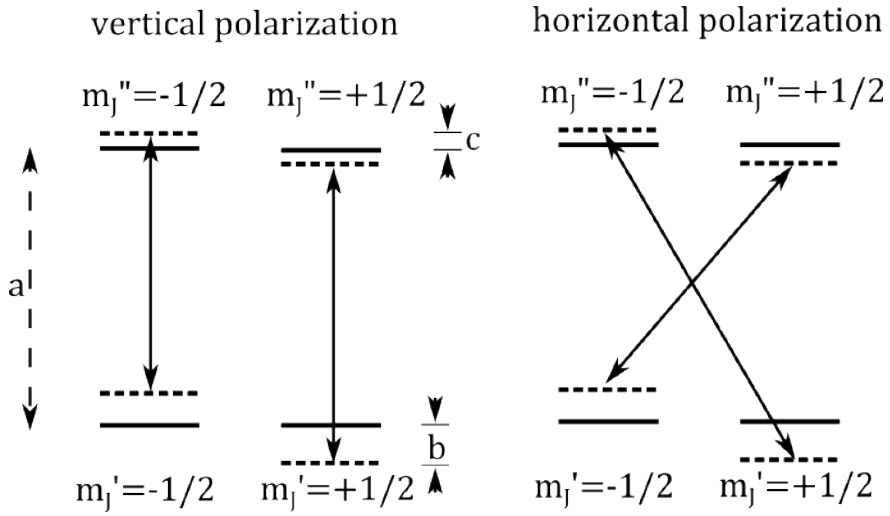

Figure 6.10: Predicted transitions to be observed with assumed negative g-factors in both the $X^2\Sigma^+$ and $E^2\Pi_{1/2}$ states for different polarizations . This indeed corresponds to our measurements.

Referencing the labels in Fig. 6.10, for a vertical polarization, when we park on the we should get that the first peak (P1) is shifted $a - b + c$, and peak 2 (P2) is shifted $a + b - c$ from the no field position. Therefore the splitting between the observed peaks, $\Delta_v = P2_v - P1_v = 2(b - c)$.

For a horizontal polarization, we should get that the first peak (P1) is shifted $a - b - c$, and peak 2 (P2) is shifted $a+b+c$ from the no field position. Therefore the splitting between the observed peaks, $\Delta_h = P2_h - P1_h = 2(b - c)$.

Now,

$$\Delta_v - \Delta_h = -4c,$$

From the data, we find that the difference in peak splittings for vertical or horizontal light is about -17 MHz. This means that c is indeed positive, indicating that our choice of g-factor was correct. Therefore we conclude that the $E^2\Pi_{1/2}$ g-factor is negative.

$A^2\Pi_{1/2}$ excited state

From our Zeeman shift measurements, outlined in Fig. 6.11 for positive applied B-field, we see the two possible level schemes for either a positive or negative g-factor, taken for either horizontally or vertically polarized light. For all these measurements, we were observing depletion while sitting on the $E^2\Pi_{1/2}$ with higher energy. With our knowledge of the $X^2\Sigma^+$ g-factor, we now now that this higher energy peak (with vertical polarization) corresponds to the $m_J = +1/2$ Zeeman sublevel.

The inset data clearly shows that for positive fields, the observed transition for vertically polarized light (red) has lower energy than that observed with horizontally polarized light (black). This corresponds to the level diagram circled in green on the left, indicating that the $A^2\Pi_{1/2}$ state has a negative g-factor.

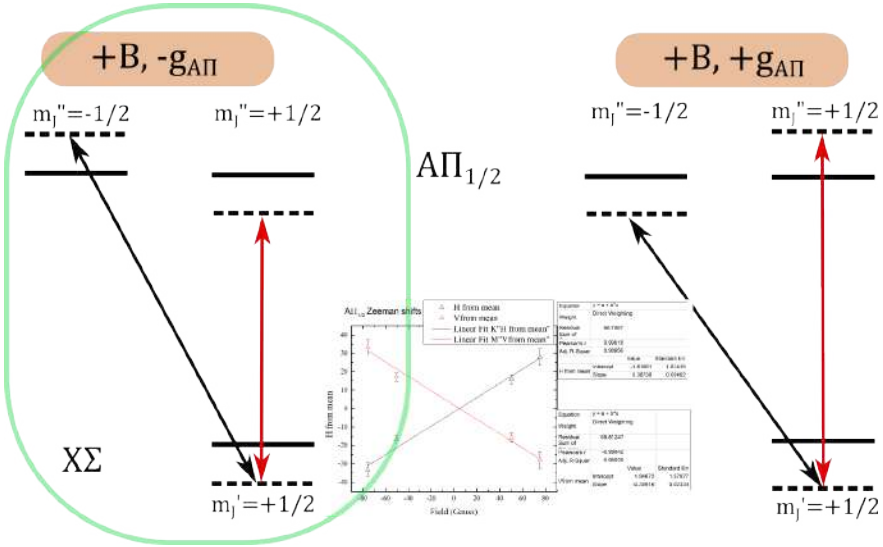

Figure 6.11: Possible g-factor assignments for experiments done with the $A^2\Pi_{1/2}$ state.

$B^2\Sigma^+$ Excited state

We assign the $B^2\Sigma^+$ g-factor very similarly to the $A^2\Pi_{1/2}$, using a similar measurement that involves measuring Zeeman shifts for different polarizations. In this case, the inset data in

Fig. 6.12 shows that for positive fields, the vertically polarized light (red) has higher energy than the horizontally polarized light (black). As a result, we see that the level diagram on the right is correct. Therefore we conclude that the $B^2\Sigma^+$ g-factor is positive.

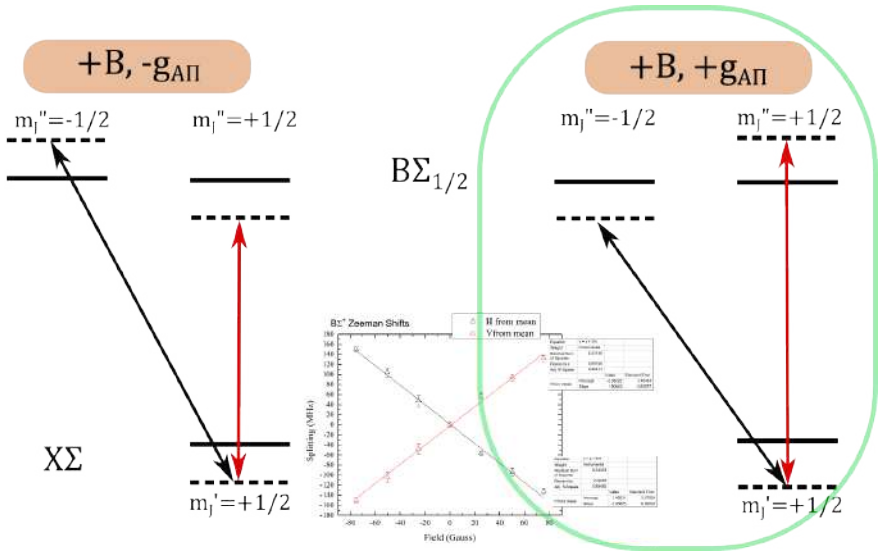

Figure 6.12: Possible g-factor assignments for experiments done with the $B^2\Sigma^+$ state.

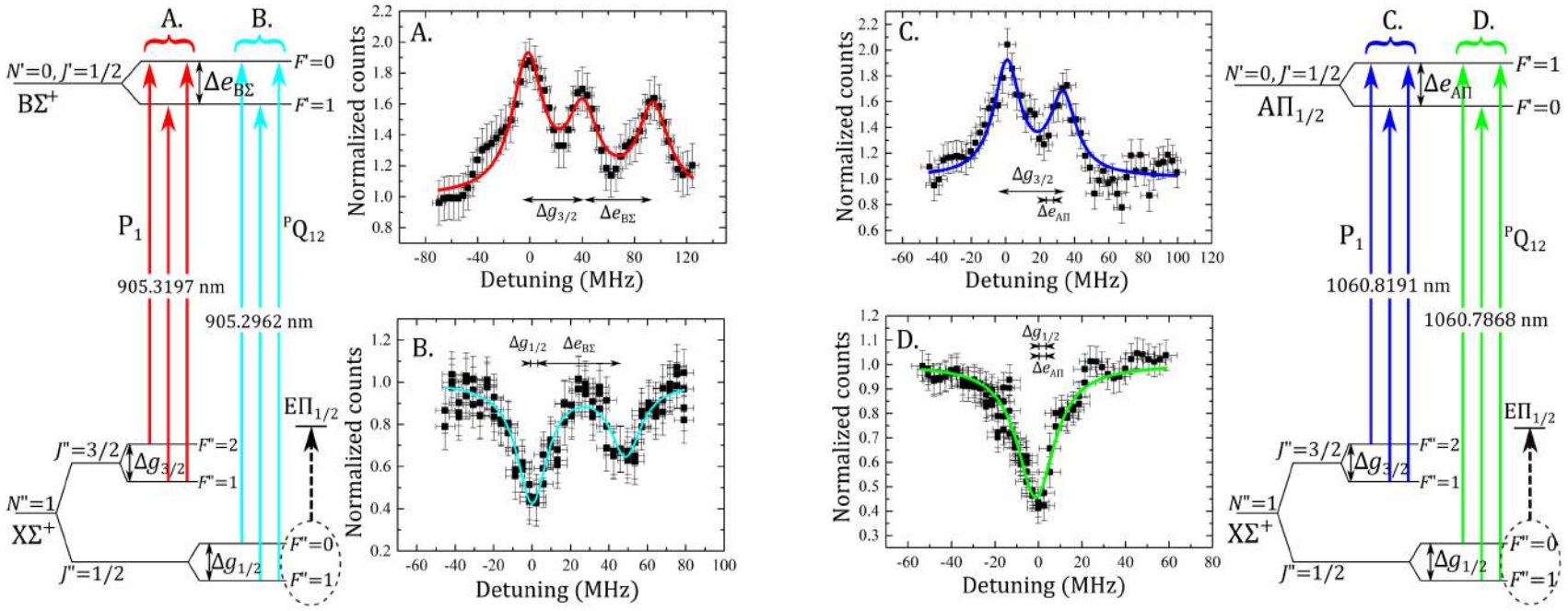

Figure 6.5: Hyperfine-structure-resolved energy levels and measurements for BaH electronic states relevant to laser cooling. Four types of spectra are collected (labeled A, B, C, and D). In all cases, detection is made by monitoring the fluorescence of molecules excited from the $X^2\Sigma^+(N" = 1, J" = 1/2)$ ground state to the $E^2\Pi_{1/2}$ excited state, indicated by the dashed arrows. Transitions labeled A and C show population enhancement due to pumping from the $X^2\Sigma^+(N" = 1, J" = 3/2)$ state via $B^2\Sigma^+$ or $A^2\Pi_{1/2}$. Transitions labeled B and D show population depletion due to pumping out of the $X^2\Sigma^+(N" = 1, J" = 1/2)$ state. The studied ground-state and excited-state hyperfine intervals are marked as Δg or Δe in the diagrams and in the spectra.

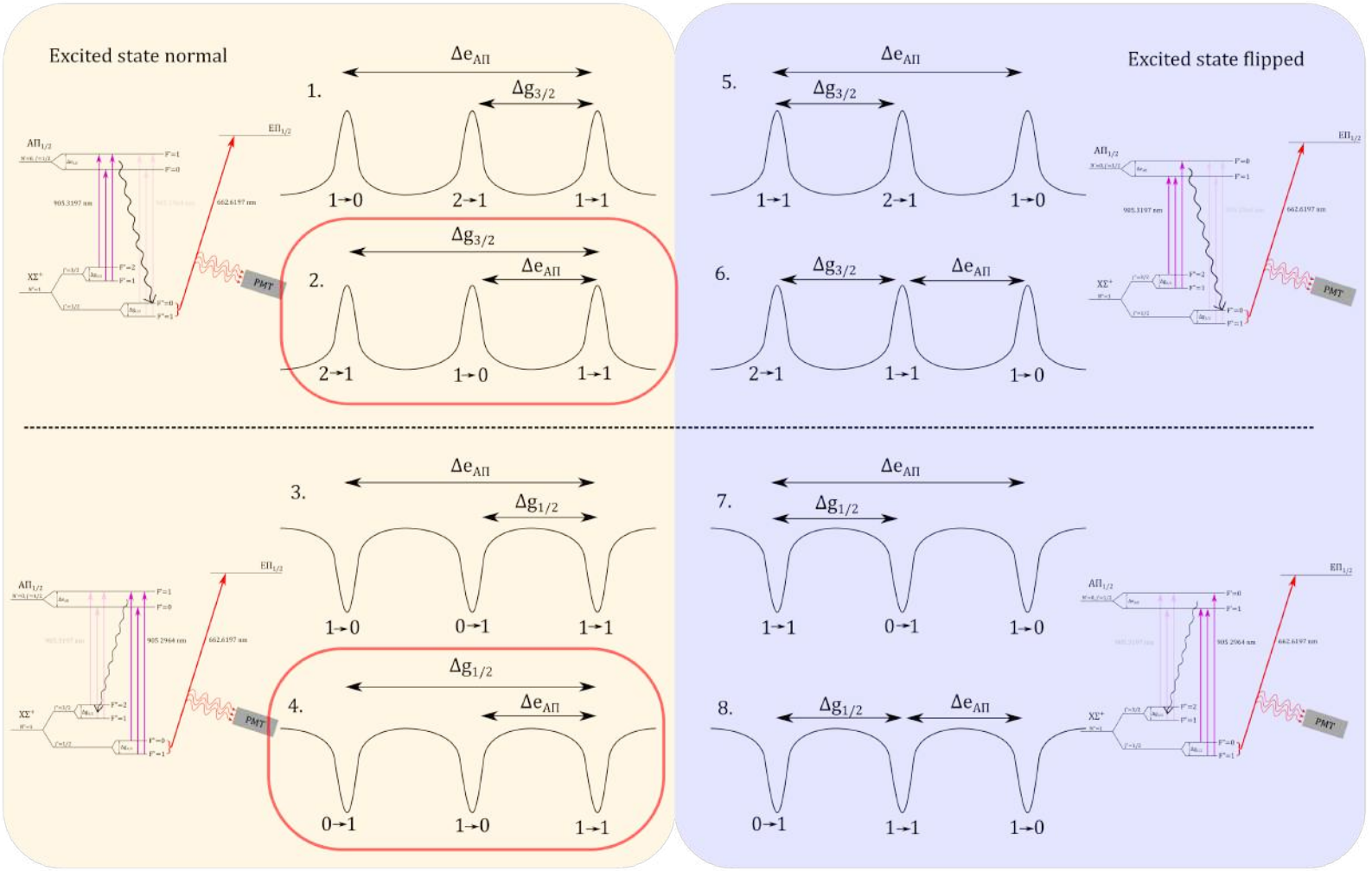

Figure 6.6: Possible hyperfine spectral identification depending on the orientation of the excited hyperfine state. On the left, we see possible spectra for the "normal" configuration, where the $F' = 1$ state lies higher in energy than the $F' = 0$ state. On the right is the "flipped" configuration, where the $F' = 1$ state lies lower in energy than the $F' = 0$ state. Shown for each measurement are possible orderings of the 3 allowed hyperfine transitions depending on the relative size of the ground vs excited hyperfine splitting. Circled in red are the correctly identified spacings that are fully internally consistent with the data. Here, the detection laser is shown at 662 nm, which excites molecules to the $E^2\Pi_{3/2}$ state - an equaivalent measurement as that described in the text.

Chapter 7

Toward Laser Slowing, Cooling and Trapping

The ingredients above are all important pieces in the puzzle of figuring out how to trap the molecule. Ultimately, the molecular properties will determine the feasibility of creating a MOT out of BaH, and in this section, we will explore some of those crucial properties.

The use of optical forces to manipulate atoms has been wildly successful, evidenced by the breadth and number of laser cooling experiments, touching almost every field of physics. The key principle behind laser cooling originates from the momentum, $\hbar k$ that each photon carries, in addition to its energy, $\hbar\omega$, and angular momentum, $\hbar$. When an atom or molecule absorbs a photon, the energy goes into pushing an electron to an excited state, whereas the momentum is transferred to the motion of the atom or molecule, and it recoils from the light source with momentum $\hbar k$. The angular momentum is transferred to the internal motion of the electron.

The opposite process occurs when the atom or molecule emits a photon. The emission process may be stimulated or spontaneous, but the ejected photon in either case carries away $\hbar\omega$ energy, and $\hbar$ angular momentum from the electron, and $\hbar k$ momentum, with the atom

or molecule receiving a kick of $-\hbar k$. For each of the two processes, absorption and emission, the corresponding change in velocity of the atom is $v_r = \hbar k/M$, where M is the mass of the atom. This is a terribly small change in velocity, but many absorption and emission cycles, controlled so that each Δv is in the same direction, will lead to a large velocity change, which is what is used to decelerate or cool atoms.

In the case of cooling, it is necessary to have a velocity dependent, dissipative force. That atomic or molecular absorption is strongly frequency dependent near a resonance, and that there can be a velocity dependent Doppler shift, satisfies the velocity dependence requirement. To be dissipative, the kinetic energy of the molecule should be carried off out of the system and the process of spontaneous emission takes care of this (though optical cooling without spontaneous emission is also possible [133]).

There are two important limits to consider for laser cooling. One is the scattering rate, which tells us how quickly the atom or molecule can undergo an absorption and emission cycle. The excitation rate is, in principle, only limited by how powerful a laser you can buy. The emission rate depends on whether the photon is emitted spontaneously or was stimulated. In the spontaneous case, the rate is limited by the natural lifetime, $\tau = 1/\gamma$ of the excited state. At the saturation intensity of a 2-level transition, the molecule or atom is spending half its time in each state, and the resulting acceleration is $a_{max} = \hbar k\gamma/2M$ [55]. This scattering rate is further modified when more levels are involved in the cooling process, as will be the case for molecules, shown below. When cooling a beam of molecules, as in BaH, we need to be as close to the maximum scattering rate as possible in order to stop the beam in a reasonable distance so that transverse losses are minimized. In atoms, transverse cooling can be effective, but the photon budget of molecules (number of cycles before a molecules falls into an irrecoverable dark state) is quite limited, so it's not worth implementing transverse cooling.

For stimulated emission, the rate is again dependent on the laser power. However, using

stimulated emission to cool atoms or molecules is tricky, since the direction of emission causes the particle to recoil in the direction of the light source, canceling out any deceleration.

The second limit to laser cooling is the Doppler temperature, describing the temperature associated with the natural linewidth of the transition[1]. This temperature characterizes the random nature of spontaneous emission, which in fact adds heat to an atom or molecule during the emission of a photon, and is given as [55],

$$T_D = \frac{\hbar\gamma}{2k_b}. \tag{7.0.1}$$

The Doppler temperature, of typical value in the 100s of μK, is by no means the final limit of cooling, and subdoppler cooling through optical processes can regularly reach about two orders of magnitude lower where we reach the recoil limit, defined by the amount of energy associated with a single photon recoil [55]. This temperature is,

$$T_r = \frac{\hbar^2 k^2}{M k_b}, \tag{7.0.2}$$

which has no dependence on the linewidth of the transition. While this temperature, typically a few μK, is usually seen as the lower limit for optical cooling, many experiments have since surpassed this limit using a variety of techniques.

These 'end goals' are important to keep in mind, but at this early stage in our molecule cooling experiment, there are a few pressing matters to consider from the outset.

Any laser cooling scheme is crucially dependent on a good cycling transition, where the atom or molecule to be cooled is not 'pumped out' of the cooling scheme into some state that is dark to the cooling laser. In atoms, finding a closed, two-level system, much like the ideal

[1]In principle, the concept of temperature is not well defined for the isolated systems that are typically present in laser cooling experiments. In thermodynamics, thermal contact is required between a closed system and its environment to achieve a thermal equilibrium, a state which can then be parameterized with some temperature. Still, it is useful to use the concept of temperature informally defined through the kinetic energy relation, $\langle E_k \rangle = \frac{1}{2} k_b T$, where k_b is the Boltzmann constant

cases found in quantum mechanics textbooks, is fairly easy. In molecules, the additional vibrational and rotational degrees of freedom make a two-level cycling transition difficult to find. We have already seen in the preceeding sections, the complexity of the involved states. Still, there are clever choices to make to get close to a 2-level system. Specifically, we look to transitions that limit both the rotational and vibrational branching for any quasi-cycling transition.

7.1 Limiting Rotational Branching

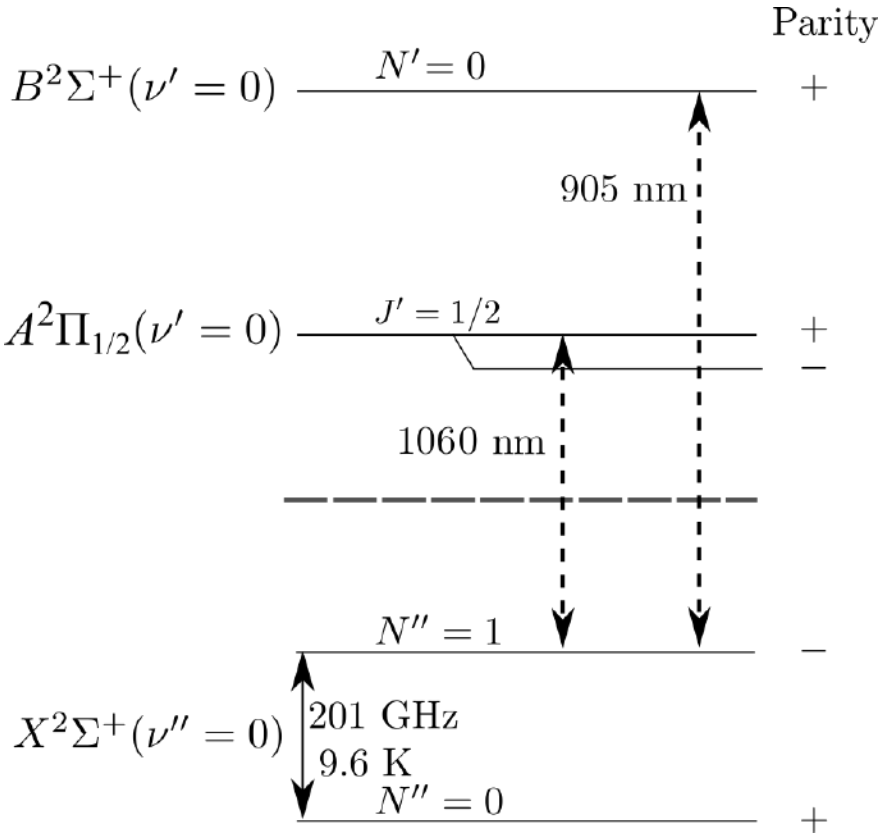

Figure 7.1: Coarse rotational structure for the two possible laser cooling transitions in BaH. By using the transition that removes $\hbar$ angular momentum from $N''=1$, rotational branching back to the ground state is limited.

In a simple atom, exciting to the first excited state with angular momentum $L' = L'' + 1$, in principle limits rotational branching since decay to the $L'' = L'$ is electric dipole forbidden, and there are not additional higher angular momentum ground states with $L' = L' + 2$. However, the introduction of the rotational degree of freedom means that there is a manifold of ground angular momentum states, and further, the addition of $\vec{N} + \vec{S}$ in Hund's case (b) molecules means that we need to consider both the N and J quantum numbers. If we excite, for example, the $J'' = 1/2$ ground state of the $N'' = 0$ rotational state, to the $J' = 3/2$, $N' = 1$ excited state, the molecule is allowed to decay back to the original state, and the $N'' = 2, J'' = 3/2$ ground state.

We can limit the rotational branching by instead driving transitions where $N' = N'' - 1$, as in $N'' = 1 \rightarrow N' = 0$. Therefore we probe and measure laser absorption between the $N'' = 1$ ground rotational state and $N' = 0$ (lowest) excited rotational state, as shown in Figure 7.1. These states have opposite plus/minus parity, so the excited $N' = 0$ state has limited branching to only $N'' = 1$ ground states, across any vibrational level in the $X^2\Sigma^+$ manifold.

The spin-rotation splitting, forming the two $J'' = 1/2$ and $J'' = 3/2$ fine structure states in $X^2\Sigma^+$, are both accessible via decay from either excited state.

7.1.1 Closing Spin-Rotation Structure

The large, 8.6 GHz spin-rotation splitting in BaH is somewhat unique among buffer gas cooled molecule experiments, and it cannot be easily addressed using laser sidebands. In particular, the large splitting makes it so that we are dealing with a 3-level lambda' system, as opposed to a 2-level system with internal structure. While many of the experiments to study BaH can be done using only one leg or the other, we must properly close both in order to achieve cycling.

In order to accomplish this, we used two separate External Cavity Diode Lasers tuned

8.6 GHz apart, as described in an earlier chapter. The lasers are combined via a polarizing beam cube and amplified through a Tapered amplifier before being sent to the experimental table.

Each of these lasers is tuned to drive the $P_1(J'' = 1.5)$ and ${}^{P}Q_{12}(J'' = 0.5)$ transitions respectively to a given excited state (Figure 7.2). If we don't have both correctly tuned, then molecules will simply be pushed to one spin rotation state or the other, much as we did for the hyperfine measurements in Chapter 6.

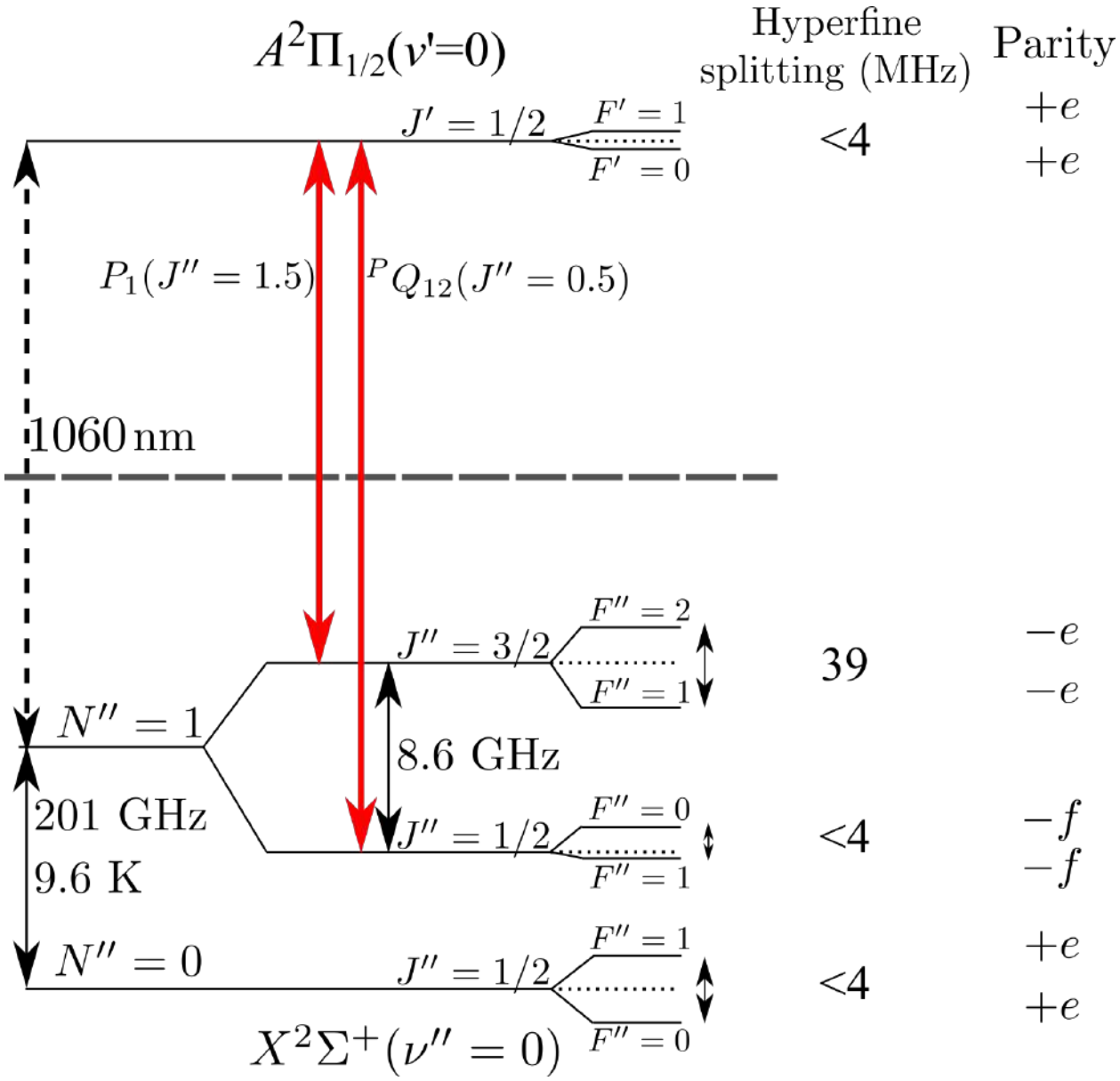

Figure 7.2: Closing the spin rotation structure of BaH. Hyperfine splittings are those measured in Ref. [80].

Within the fine structure, there is still hyperfine branching, which we need to ensure we address with laser sidebands. Recapping a bit, whichever excited state we use, $A^2\Pi$ (Hund's case (a)) or $B^2\Sigma^+$ (Hund's case (b)), the hyperfine coupling is similarly made with $\vec{J}$, so there are 4 hyperfine sublevels in the excited state. The ground state has the 12 sublevels

previously described, making a 16 level system to work with. That's a pretty far cry from the 2-level system we are trying to find! The hyperfine transitions are governed by the rules, $\Delta F = 0, \pm 1$, but not $F' = 0 \leftrightarrow F'' = 0$, and $\Delta M_F = 0, \pm 1$. Therefore, there are 3 possible transitions per spin rotation level, as seen in the data. To address these levels, we use EOMs to apply sidebands onto the light.

The simplest way to confirm the closure of the spin rotation structure is to look directly at the fluorescence from the $A^2\Pi_{1/2}$ excited state. We have made a point that technologically, most PMTs do not typically have the quantum efficiency to detect NIR wavelength, however, we were able to find that Hamamatsu sells a (particularly expensive!) InGaAsP PMT active from 950-1200 nm. The QE is expected to be 1%.

We decided to test it out by borrowing a demo model from the company, performing a simple experiment where we probe the molecular beam, 53 cm downstream from the cell with transverse beams that address one or both spin rotation states. The result of the measurement is shown in Figure 7.3. Direct fluorescence from only the PQ_{12} branch of the spin rotation pair, gives a signal that corresponds to about 2 photons per molecule as they are rapidly pumped into the $J'' = 3/2$ state. A 15x enhancement of the signal is seen for when both spin rotation branches are addressed simultaneously. In fact, we should expect that there would be about 50x enhancement here, given the scattering rate can be a maximum of 1.8 MHz which could give up to 90 photons per molecule in the interaction time. The interaction time for a transverse beam of width 0.5 cm is 50 μs for a molecule moving at 100 m/s. However, the probe beam is likely not saturating the transition as it would for the single spin rotation branch case, as we will see below. In fact, the beam profile could leave only a small portion of the molecular beam scattering at the max rate, so an average scattering rate one fourth of that is believable, and in fact, corresponds to the enhancement factor we see.

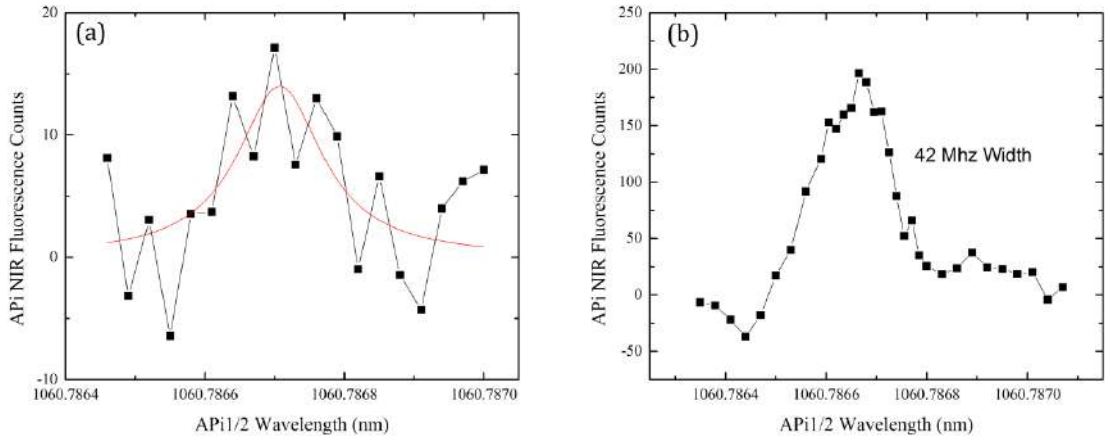

Figure 7.3: Enhancement in direct fluorescence measured from $X^2\Sigma^+(v" = 1) \rightarrow A^2\Pi_{1/2}$ across a 0.6 cm probe laser. (a) Direct fluorescence from only the PQ_{12} branch of the spin rotation pair, corresponding to about 2 photons per molecule as they are rapidly pumped into the $J'' = 3/2$ state. (b) Direct fluorescence is enhanced by a factor of 15.

While we don't see the maximum enhancement in this measurement, the large enhancement demonstrates closure of the spin-rotation state with the $X^2\Sigma^+(v'' = 1) \rightarrow A^2\Pi_{1/2}$ transition.

7.2 Frank-Condon Factors and Number of Cycles

While the rotational branching can be addressed as shown above, we still need to content with vibrational losses which are ultimately what make molecules so difficult to manipulate with optical techniques. Even small losses here can be a non-starter for laser cooling. Specifically, the small momentum associated with scattering a single photon means that an enormous number of scattering events (10s of thousands) are required to meaningfully manipulate a molecule, and so not having a nearly perfectly closed transition will cause the molecule to be lost to some dark state. Ultimately, the lack of selection rules over the vibrational states is what makes this it so difficult to close a molecular transition. Often, we say we

Excited State	Lifetime, τ (ns)	Final State	v''	Branching Ratio	Wavelength
$A^2\Pi_{1/2}$	136.2	$X^2\Sigma^+_{1/2}$	0	0.99461	1060 nm
		$X^2\Sigma^+_{1/2}$	1	0.0535	
		$X^2\Sigma^+_{1/2}$	2	0.00001	
		$H^2\Delta_{3/2}$	0	0.00003	
$B^2\Sigma^+_{1/2}$	120.3	$X^2\Sigma^+_{1/2}$	0	0.98709	905 nm
		$X^2\Sigma^+_{1/2}$	1	0.01189	
		$X^2\Sigma^+_{1/2}$	2	0.00005	
		$A^2\Pi^{1/2}$	0	0.00032	
		$A^2\Pi^{3/2}$	0	0.00012	
		$H^2\Delta_{3/2}$	0	0.00053	
$H^2\Delta_{3/2}$	5791	$X^2\Sigma^+_{1/2}$	0	0.98260	1110 nm
		$X^2\Sigma^+_{1/2}$	1	0.01730	
		$X^2\Sigma^+_{1/2}$	2	0.00010	

Table 7.1: Decay ratios between the relevant states for laser cooling BaH. Values were calculated and listed in [70]

simply have to "Choose the right molecule", meaning that we have to choose molecules which serendipitously have ≈100% branching ratios between the $v = 0$ states of electronic states. These branching ratios are directly related to the Frank-Condon factors between two states, and is a measure of the wavefunction overlap. Lane and co-workers [70] have calculated the expected relevant branching ratios in BaH, as well as lifetimes. This information is listed in Table 7.1.

These decay ratios are important because they set a budget for how many photons can be scattered by our molecules before they are lost to dark states, and these numbers also inform the most effective cooling scheme. Immediately from looking at the branching ratios, we see that the $A^2\Pi_{1/2}$ state is the most closed, and importantly, has limited additional non-negligible decays. This means that repumping can be achieved with few lasers to achieve a quasi-closed situation. Just considering the main, $A^2\Pi_{1/2}$ transition, we can get a quick estimate for the number of photon scatters, N that will leave us with just 10% of the initial population with the formula,

$$N = \frac{\mathrm{Log}(0.1)}{\mathrm{Log}(0.99461)} = 426. \tag{7.2.1}$$

On the other hand, we need to know how many photons we need to slow down a molecular beam from an initial velocity of 50 m/s (the lower end of a buffer gas distribution) to 1 m/s (the capture velocity of a BaH MOT), which for light at 1060 nm is,

$$N_{needed} = \frac{\Delta p}{\mathrm{d}p} = \ 18000, \tag{7.2.2}$$

where Δp is the total change in momentum from the starting to final velocity, and $\mathrm{d}p = -h/\lambda$ is the average change in momentum due to a single photon absorption and emission cycle. Clearly, using just a single transition is not quite enough for us.

7.2.1 Closing Vibrational Losses

Once the main cooling transition is closed, we just found that a molecule can undergo approximately 400 cycles before it is lost to the first vibrational level ($v'' = 1$) of the $X^2\Sigma^+$ state. Within this vibrational level, the molecules are again distributed among both of the spin rotation states, and must be pumped back to the ground vibrational state. One obvious way to do this is by driving the molecule back along the path it came from, i.e. the transition from $X^2\Sigma^+(v'' = 1) \rightarrow A^2\Pi_{1/2}$, and letting the good FCF take it back to $X^2\Sigma^+(v'' = 1)$. Unfortunately, this simple scheme actually limits the scattering rate of the main cycle, since it connects a larger total number of states to a single excited state, and at saturation, the scattering rate goes as $1/N_{tot}$ (see section 7.3).

A better scheme involves using the $B^2\Sigma^+$ state that has almost as good FCFs. This scheme is demonstrated in Figure 7.4. Here, the repump is totally decoupled from the main cooling transitions and only repopulates the ground state via spontaneous decay, which leaves the scattering rate for cooling unaffected.

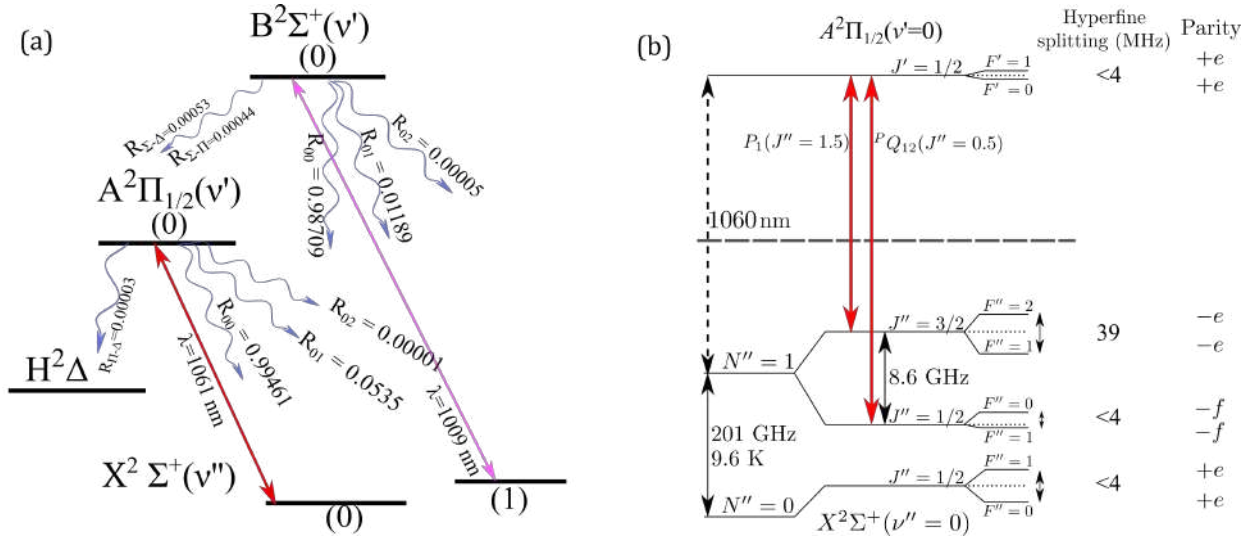

Figure 7.4: Laser cooling scheme for BaH using the $A^2\Pi_{1/2}$ excited state for the main cycling transition and the $B^2\Sigma^+$ excited state for repumping. (a) Electronic and vibrational level structure is shown. Decay branching ratios are those calculated by Lane et. al. [70]. The main cycling transition at 1060 nm is shown in red, while the repump is shown in pink. Both the main transition and the repump require two lasers to close the spin-rotation splitting. (b) Rotational structure of the main cycling transition for laser cooling BaH. The 8.6 GHz splitting in the ground state is present for all vibrational states, and is difficult to span with a single laser modulated, for example, with an electro-optical element.

The actual wavelength for the repump transition has not been experimentally measured before, so we had to predict what the transition would be. Using the molecular constants in Table 7.2, we can find the line by taking the difference in energies according to the energy formulas given in Chapter 5. The resulting predicted wavelengths are 1009.4216 nm and 1009.3930 nm.

If we want to consider the effect of adding a repumping laser, say to connect the $X^2\Sigma^+_{1/2}(v'' = 1) \rightarrow A^2\Pi_{1/2}(v' = 0)$ transition, we can use the approximate approach in Equation 7.2.1 to find that we get up to 58000 cycles before reducing the population down to 10% of its initial value. In order to more properly find the number of cycles in this case, we can model the molecule as it undergoes the cycles in a Markov chain. The result is in Figure 7.5, and shows that 57000 photon absorption and emission cycles are possible before reducing the molecule

State	$X^2\Sigma^+$	$A^2\Pi_{1/2}$	$B^2\Sigma^+$
T_e	0	9457.45	11092.5926
ω_e	1168.42509	1110.55	1088.898
$\omega_e \times x_e$	14.61366	15.29	15.4712
$\omega_e \times y_e$	0.028253	0.0	0.0237
B_e	3.3824355	3.278	3.268795
α_e	0.06565865	0.07283	0.070609
D_e	1.124169×10^{-4}	1.21×10^{-4}	1.15855×10^{-4}
γ_ν	0.192063	nd	-4.75396
γ_1	0.187039	nd	-4.63433
H	3.0061×10^{-9}	nd	2.6267×10^{-9}
Source	[126]	[111]	[72]

Table 7.2: Molecular constants for the relevant electronic states of BaH. All values given in cm^{-1}.

number to just 10% of its initial value.

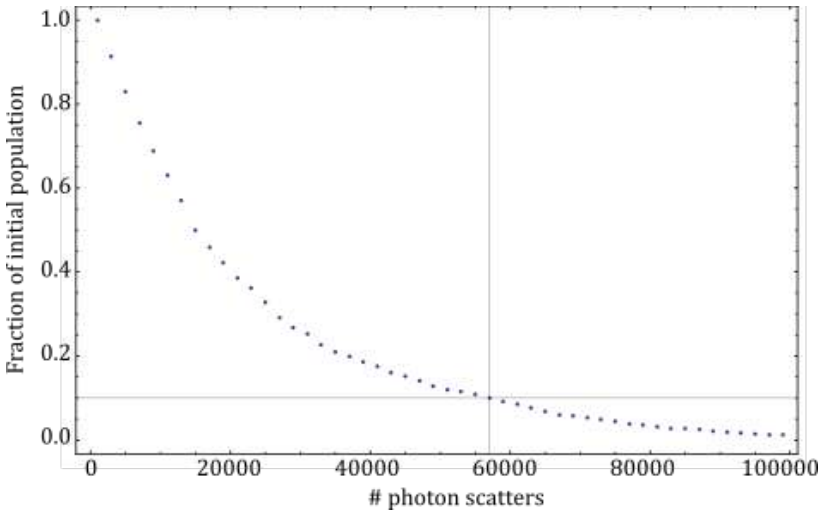

Figure 7.5: Fraction of initial population vs the number of cycles when closing the $X^2\Sigma^+_{1/2} \rightarrow A^2\Pi_{1/2}$ main cycling transition with the $X^2\Sigma^+_{1/2}(v=1) \rightarrow B^2\Sigma^+_{1/2}$ repump. In this case, up to 57000 photon absorption and emission cycles are possible before reducing the molecule number to just 10% of its initial value.

Therefore we see that closing these two transitions is sufficient to slow down the molecular beam and have enough photon cycles left over in our budget for a MOT.

7.3 Scattering Rate

The other important parameter to consider when planning for slowing a molecular beam is the maximum acceleration achievable. This is set by both the change in momentum per photon scattered, $\mathrm{d}p = -h/\lambda$, and the scattering rate, R_{sc}. The scattering rate must be sufficiently high to allow for the beam to be slowed within a reasonable distance. If the slowing section is much longer than 1 meter, the divergence of the molecular beam will lead to unacceptable losses by the time the molecules reach the science chamber. Moreover, the random kicks that accompany radiation pressure slowing necessarily add transverse velocity components to the molecule, further highlighting the need to get things slow as quickly as possible. Focusing again on the $X^2\Sigma^+_{1/2} \rightarrow A^2\Pi_{1/2}$ cycling transition, we see from Table 7.1 that the lifetime of the excited state $\tau_{A\Pi} = 136.2ns$. This corresponds to a scattering rate $R_{sc-A\Pi} = \frac{1}{\tau_{A\Pi}} = 7.3 \times 10^6$ photons per second.

There is a further reduction due to the large multiplicities of levels, since in the fully saturated case of the $X^2\Sigma^+_{12} \leftrightarrow A^2\Pi_{1/2}$ transition, the molecules will be equally distributed over the 16 ground and excited hyperfine states, resulting in only 1/4 of the molecules in the excited state, as opposed to the usual 1/2 factor given in a 2-level system [134].

To understand this a little more rigorously, we want to try and model the fluorescence by considering the occupation probability for a particular excited state, n_e or a given ground state, n_{gi} out of a total of N total ground states. While the excitation rate is unlimited (given technical constraints on laser power), the excited state probability tells us the limit to the scattering rate. The rate equation for that probability is,

$$\frac{\partial n_{gi}}{\partial t} = \Gamma_{gi} n_e + R_{gi}(n_e - n_{gi}), \tag{7.3.1}$$

where Γ_{gi} is the partial spontaneous decay rate between the two hyperfine states of interest and R_{gi} is the excitation rate for those states. Because these are probabilities,

$n_e + n_{gi} = 1$. In the steady state, this normalization condition and Equation 7.3.1 have the solution,

$$n_e = \frac{1}{(N+1) + \sum_{i=1}^{N} \Gamma / R_{gi}}. \tag{7.3.2}$$

When the laser is on resonance with intensity, I_i driving the ith transition, the partial excitation rate is,

$$R_{gi} = \frac{\Omega_i^2}{\Gamma_{gi}} = \frac{\Gamma_{gi} I}{2 I_{sat}}, \tag{7.3.3}$$

with the Rabi frequency of the transition, and $I_{sat} = \pi h c \Gamma / (3\lambda_i^3)$ is the saturation intensity of the transition, defined by the relation $\Omega_i^2 = \Gamma^2 \frac{I}{2I_{sat}}$, where Γ is the total decay rate. Since λ is basically the same for all the transitions in the problem, we can use a common NI_{sat}. Furthermore, we can assume that each partial intensity, I_i is an equal fraction of the total intensity, I_{tot} to drive each transition equally, simplifying the sum to N/I_{tot}. Therefore we can simplify Eq. 7.3.2 as,

$$n_e = \frac{1}{(N+1) + 2N^2 I_{sat} / I_{tot}}. \tag{7.3.4}$$

For a system with N_e excited states and N_g ground states, the situation is a bit more complicated to derive, but the end result is similar, with an excited state probability given as [134],

$$n_e = \frac{N_e}{(N_g + Ne) + 2N_g^2 I_{sat} / I_{tot}}. \tag{7.3.5}$$

In BaH, there are 4 excited hyperfine levels in the excited $A\Pi$ state and 12 $X\Sigma$ ground state levels. As long as we use a very high power (well above the saturation intensity), the reduction in intensity will be 1/4.

This factor of 1/4 leads to $R_{sc-A\Pi} = \frac{1}{\tau_{A\Pi}} = 1.8 \times 10^6$.

This is quite a bit smaller than other cooled diatomics, and, compounding with the heavy mass, makes BaH a challenging molecule to cool in a short distance. In the best case scenario, where the slowing light can fully saturate the entirety of the molecular beam, the acceleration of the molecule is,

$$a = \frac{R_{sc}\mathrm{d}p}{2M}, \tag{7.3.6}$$

where M is the mass of the molecule. Rearranging a simple kinematic equation, the distance, x to slow a molecule from an initial velocity, v_0 to a final velocity, v_f is,

$$x = \frac{v_f^2 - v_0^2}{2a}. \tag{7.3.7}$$

For $v_0 = 70\mathrm{m/s}$ and $v_f = 1\mathrm{m/s}$, and using the numbers above for a, the distance to slow is $x = 1m$.

7.4 Optical Cycling in a Quasi-Closed System

In order to laser cool BaH from 4 K to the Doppler temperature, we must be able to achieve at least 40,000 cycles on the main, $X^2\Sigma^+ \leftrightarrow A^2\Pi_{1/2}$ cooling transition. This requires closing the spin-rotation structure and vibrational losses as above. In order to do so effectively, we need to understand the power requirements, as evidenced by the measurement of closing the spin-rotation state. Second, we must make sure there are no dark states in which molecules no longer see the cooling light, and that losses to states that we cannot address are minimal.

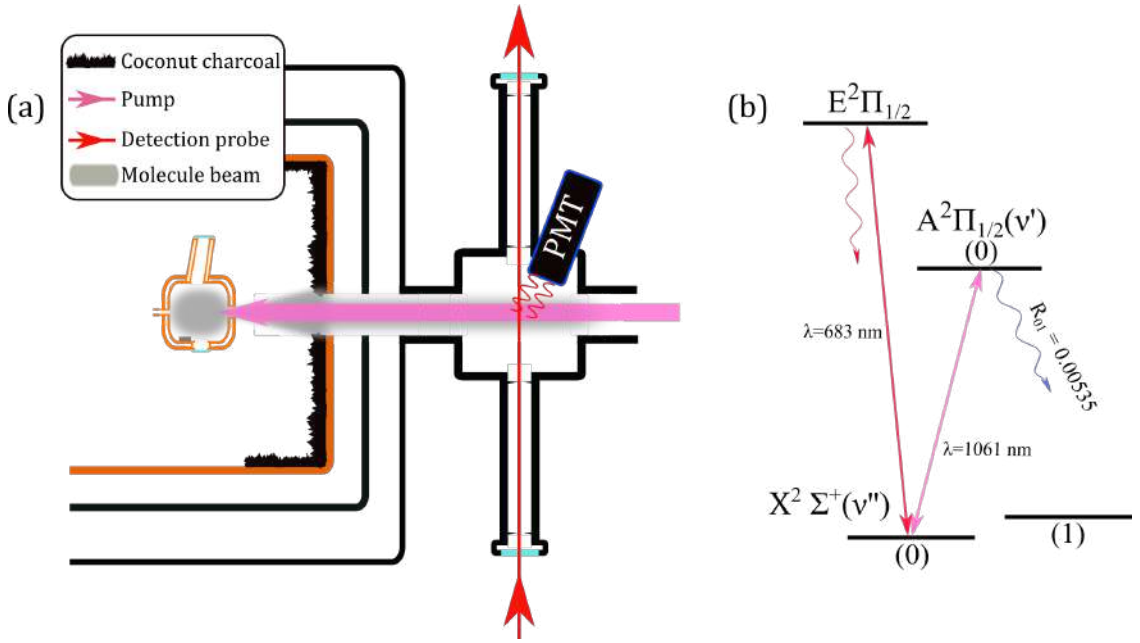

Figure 7.6: Experimental setup to pump out the $v = 0$ vibrational ground state using the $X^2\Sigma^+ \leftrightarrow A^2\Pi_{1/2}$ cooling transition. (a) Cartoon of experimental arrangement. 1061 nm light, corresponding to the $X^2\Sigma^+ \leftrightarrow A^2\Pi_{1/2}$ transition is sent counter-propagating to the molecular beam as soon as molecules leave the cell. The remaining population is probed via the detection probe at 683 nm, driving the $X^2\Sigma^+ \leftrightarrow E^2\Pi_{1/2}$ transition. Between leaving the cell and being probed, molecules have about 53 cm to interact with the 1061 nm light, corresponding to approx 6 ms of interaction time for the peak velocity.

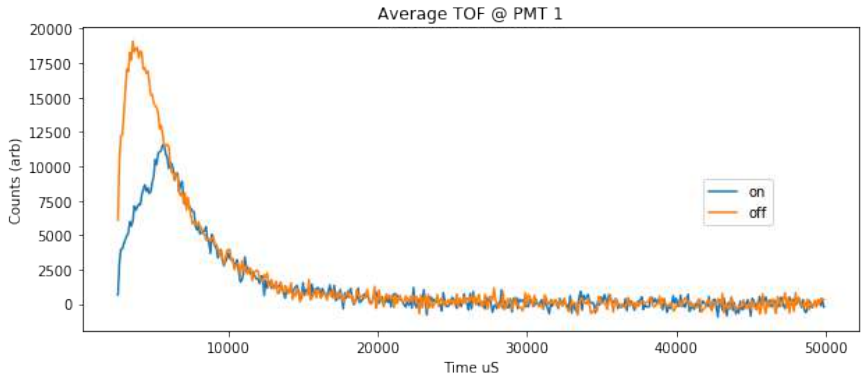

Figure 7.7: Experimental data corresponding to the experiment shown in Figure 7.6 for the 1061 nm light on and off. When the light is on, the population in the ground state is reduced because of the 0.5% loss rate into $(v = 1)$ vibrational ground state.

7.4.1 Power Requirements

Understanding the power requirements of a two-level transition is straightforward and can be found in most introductory atomic physics texts. However, for an open transition the situation is less clear - what does it mean to saturate a transition when molecules are constantly being lost to some other states not addressed by the laser?

In the end, population losses will affect the measured absorption or fluorescence rate (significantly in some cases), since adding more power will mean that this loss rate is faster. However, we can try and address this loss in a rate equation model.

We start with rate equations for the two levels driven by a laser with intensity, I, which leads to a single molecule transition rate, $W = \sigma I \lambda / hc$, where σ is the absorption cross section per molecule at wavelength, λ:

$$\frac{\mathrm{d}N_1}{\mathrm{d}t} = W(N2 - N1) + R_{21} N_2 R \tag{7.4.1}$$

$$\frac{\mathrm{d}N_2}{\mathrm{d}t} = W(N1 - N2) - R_{21} N_2, \tag{7.4.2}$$

where R_{21} is the decay rate from the upper state, while R is the fractional amount of the decay that goes to the original ground state. We care about the population difference, so we can define the difference in population, ΔN and the total population, N_T as,

$$\Delta N = N_1 - N_2, \tag{7.4.3}$$

$$N_T = N_1 + N_2, \tag{7.4.4}$$

$$N_2 = \frac{1}{2}(N_T - \Delta N). \tag{7.4.5}$$

Since R is the branching ratio of molecules that we keep, the total population in the

system goes as,

$$\frac{\mathrm{d}N_T}{\mathrm{d}t} = -R_{21}N_2(1-R). \tag{7.4.6}$$

Now,

$$\frac{\mathrm{d}N_2}{\mathrm{d}t} = \frac{1}{2}\left[\frac{\mathrm{d}N_T}{\mathrm{d}t} - \frac{\mathrm{d}\Delta N}{\mathrm{d}t}\right], \tag{7.4.7}$$

in which we can substitute Equation 7.4.1 on the left hand side, Equation 7.4.6 on the right hand side, and rearrange to put everything in terms of N_T and ΔN to find,

$$\frac{\mathrm{d}\Delta N}{\mathrm{d}t} = R_{21}\frac{(1+R)}{2}(N_T - \Delta N)2W\Delta N - 2W\Delta N. \tag{7.4.8}$$

Taking $\frac{\mathrm{d}\Delta N}{\mathrm{d}t} = 0$,

$$\Delta N = \frac{N_T}{\frac{2}{1+R}\frac{2W}{R_{21}} + 1}, \tag{7.4.9}$$

from which we can recognize a modified saturation intensity,

$$I'_{sat} = \frac{1+R}{2}\frac{hcR_{21}}{2\sigma\lambda}, \tag{7.4.10}$$

which gives us a familiar form for the population difference,

$$\frac{\Delta N}{N_T} = \frac{1}{\frac{I}{I'_{sat}} + 1}. \tag{7.4.11}$$

We can see quickly that I'_{sat} for a lossy system, say with $R = 0.5$, has a saturation intensity that is only 75% of that for a closed two level system.

To get a value for the saturation intensity for the $A^2\Pi_{1/2}$ transition, we can use the 2-level approximation for the absorption cross section where $\sigma = \frac{g_u}{g_l} 3\frac{\lambda^2}{2\pi} \approx \frac{\lambda^2}{3*2}$[2], so that,

$$I'_{sat} = \frac{1+R}{2}\frac{2\pi hc\Gamma_p}{\lambda^3}, \tag{7.4.12}$$

where we have used the substitution, $R_{21} = \Gamma_p$, and Γ_p is the partial decay rate given by Γ/r, for the branching ratio r [131]. This tells us that for a probe beam of radius 0.005 m, we should use at least 5 mW of power to reach the saturation intensity on the main cooling transition. However, to ensure the maximum scattering rate, we should be at least 10x that value.

To get a look at what this looks like, we plug Equations 7.4.1 into Mathematica with some typical parameters: $W = 10 \times 10^6$ Hz, $R_{12} = 10 \times 10^6$ Hz, and $R = 0.5$. The result is plotted in Figure 7.8. In (a), there is a clear decay in the signal after the initial equilibrium that arises. In (b), we can see the expected number of scattered photons, found by integrating the excited state population on a time scale approximately that of the transit time of molecules in the beam.

[2]The factor $\frac{g_u}{g_l}$ accounts for the degeneracies of the sublevels in the upper and lower states.

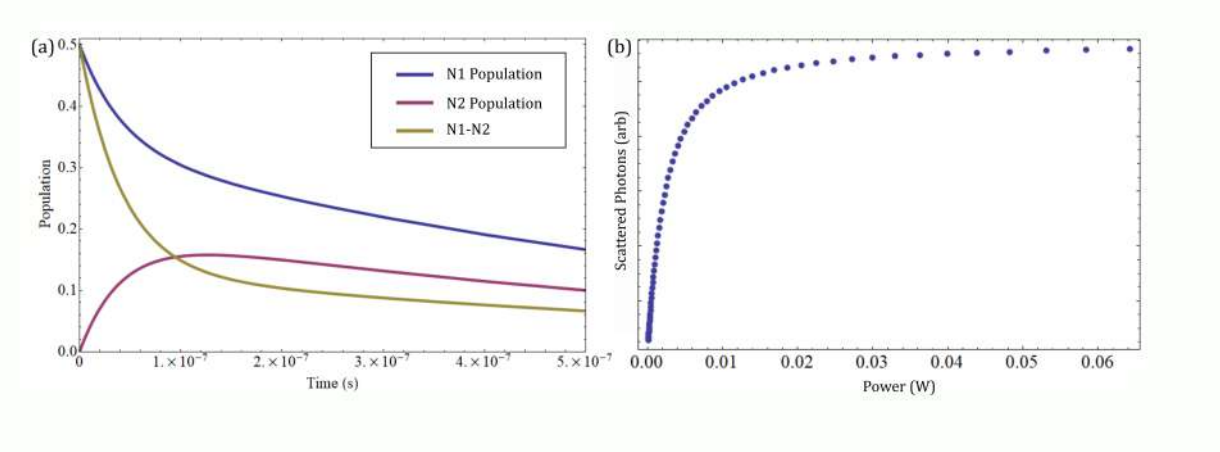

Figure 7.8: Model results for populations in ground and excited state for a leaky upper state. Experimental parameters: $W = 10 \times 10^6$ Hz, $R_{12} = 10 \times 10^6$ Hz, and $R = 0.5$. (a) Populations over a time scale that shows the decaying total population, demonstrating the equilibrium. (b) Expected number of photons, showing a saturation intensity around the expected value of 5 mW.

7.4.2 Dark States and How to Destabilize Them

Typical laser cooling experiments use transitions in which $J'' \rightarrow J'' + 1$, that is, the excited state has a greater angular momentum than the ground state. However, we saw that closing the rotational branching of BaH requires using $J'' \rightarrow J'' - 1$ transitions, which, as we will see, presents complications in fully addressing all of the ground states. Specifically, certain directions of light polarization cannot address all of the ground states simultaneously. Additionally, the light can coherently couple ground states together, causing destructive interference in their transition probability amplitudes. Ground states that are not excited by resonant light in these situations are called dark states, in which a molecule is optically pumped into a state that cannot be addressed by the laser because the coupling to the excited state vanishes [135, 136]. We want to understand carefully which Zeeman sublevels are addressed when driving such a transition with a laser field,

$$E(t) = \frac{1}{2}\mathcal{E}_0\hat{\epsilon}e^{-i\omega t} + c.c., \tag{7.4.13}$$

where the time-varying polarization vector of the electric field, $\hat{\epsilon}$ will be expressed in terms of the irreducible spherical components, E_0, E_{+1}, and E_{-1}, corresponding to π, σ^+, and σ^- polarization. These spherical components are related to the Cartesian components as,

$$E_x = -\frac{1}{\sqrt{2}}(E_{+1} + iE_{-1}) \tag{7.4.14}$$

$$E_y = +\frac{1}{\sqrt{2}}(E_{+1} - iE_{-1}) \tag{7.4.15}$$

$$E_z = E_0. \tag{7.4.16}$$

An intuitive way to understand where the dark states arise from is with the simple, but relevant cases of the $J'' = 0 \rightarrow J' = 1$ transition, shown in Figure 7.9, and the $J'' = 1 \rightarrow J' = 0$ transition, shown in Figure 7.10. In the case shown in Figure 7.9, both light polarizations address, and will continue to address the single ground state magnetic sublevel. On the other hand, in Figure, 7.10, the linear π polarization pumps molecules into the $m'' = \pm 1$ states, where they no longer are addressed, and transverse polarized light (e.g., $\hat{x}$), consisting of both σ^+ and σ^- polarizations, pumps molecules into the $m'' = 0$ state.

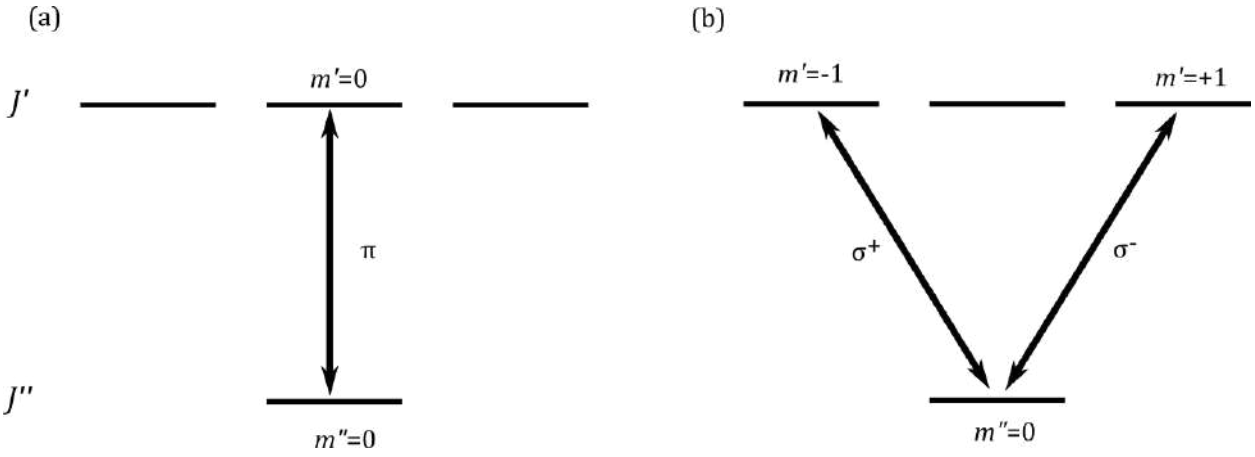

Figure 7.9: Excitation of $J'' = 0 \rightarrow J' = 1$ transition with (a) linearly, and (b) transverse polarized light. Both cases excite the ground state sublevel.

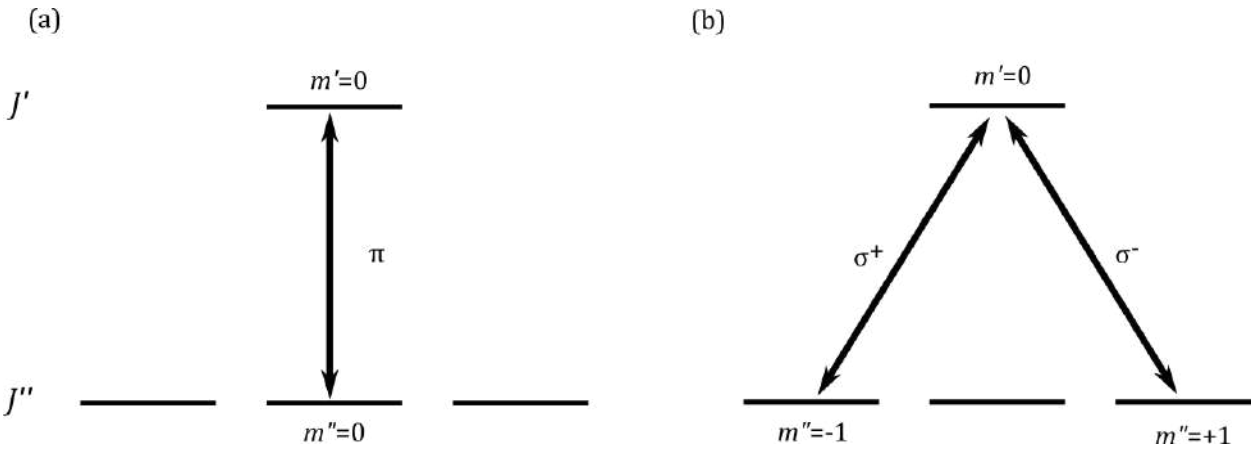

Figure 7.10: Excitation of $J'' = 1 \rightarrow J' = 0$ transition with (a) linearly, and (b) transverse polarized light. In both cases, either the $m'' = \pm 1$ or $m'' = 0$ sublevels are dark to the excitation light.

Here, the situation is clear, but the light field can also create coherent superpositions of ground states, whose transition amplitudes can destructively interfere to create a dark state. Such a condition is not so intuitive from the simple polarization picture above. Therefore, we need to look for a general superposition of dark states,

$$|\psi_{J''}\rangle = \sum_{m''} c_{m''} |J'', m''\rangle, \tag{7.4.17}$$

that satisfies the condition,

$$\langle \psi_{J''}| - \hat{\epsilon} \cdot \hat{\mathbf{d}} | J', m' \rangle = 0, \tag{7.4.18}$$

for all final states, $|J', m'\rangle$.

Using the Wigner-Eckart theorem, the reduced matrix elements for each individual transition are given as,

$$\begin{aligned} &\langle J'', m''| - \hat{\epsilon} \cdot \hat{\mathbf{d}} | J', m' \rangle \\ &\qquad = (-1)^{J''-m''} \sum_{p=-1}^{+1} (-1)^p E_{-p} \\ &\qquad \times \begin{pmatrix} J'' & 1 & J' \\ -m'' & p & m' \end{pmatrix} \langle J''||d||J' \rangle. \end{aligned} \tag{7.4.19}$$

For the simple example from Figure 7.9, with $J'' = 0 \rightarrow J' = 1$, $|\psi_{J''}\rangle = c_0|0, 0\rangle$, and equation 7.4.18 yields,

$$c_0(E_{+1} + E_0 + E_{-1}) = 0. \tag{7.4.20}$$

For any laser polarization, $\hat{\epsilon} = \hat{\mathbf{x}}$ or $\hat{\epsilon} = \hat{\mathbf{y}}$, the solution is always the trivial one where $c_0 = 0$, indicating that there is no dark state except that where there was no molecules to begin with. This is as we expected.

In the other example above, where $J'' = 1 \rightarrow J' = 0$, equations 7.4.17 and 7.4.18 yield,

$$c_{-1}E_{+1} + c_0E_0 + c_{+1}E_{-1}) = 0, \tag{7.4.21}$$

which has non-trivial solutions for both of the polarizations described above. From

Berkeland *et. al.*, the solution space is spanned by,

$$\begin{pmatrix} c_{-1} \\ c_0 \\ c_{+1} \end{pmatrix} = \frac{1}{\sqrt{E_{-1}^2 + E_{+1}^2}} \begin{pmatrix} -E_{-1} \\ 0 \\ E_{+1} \end{pmatrix}, \tag{7.4.22}$$

$$\begin{pmatrix} c_{-1} \\ c_0 \\ c_{+1} \end{pmatrix} = \frac{1}{\sqrt{(E_{-1}^2 + E_{+1}^2)(E_{-1}^2 + E_0^2 + E_{+1}^2)}} \begin{pmatrix} -E_0 E_{+1} \\ E_{-1}^2 + E_{+1}^2 \\ E_0 E_{-1} \end{pmatrix}, \tag{7.4.23}$$

except for the when the light is π polarized, in which case we have,

$$\begin{pmatrix} c_{-1} \\ c_0 \\ c_{+1} \end{pmatrix} = \begin{pmatrix} 1 \\ 0 \\ 0 \end{pmatrix}, \text{and} \begin{pmatrix} c_{-1} \\ c_0 \\ c_{+1} \end{pmatrix} = \begin{pmatrix} 0 \\ 0 \\ 1 \end{pmatrix} \tag{7.4.24}$$

Equation 7.4.22 represents the dark state created by the coherent superposition of molecules in the $m'' = \pm 1$ ground states, present for transverse polarized light. We did not predict this dark state from the simple picture above. Equation 7.4.23 shows the dark states that are created for when both polarizations are present, showing that one cannot solve the issue simply by adding two polarizations into the system. Additionally, if we take $E_0 = 0$, as is the case for transverse polarized light, we recover one of the originally predicted dark states at $m'' = 0$. Finally, when the equations are solved with $E_{\pm 1} = 0$, as in Equation 7.4.24, we find the other predicted dark state from Figure 7.10, where $m'' = \pm 1$ do not interact with the light.

This simple example shows us that drawing level diagrams and analyzing polarization situations is insufficient to understand the possible dark states in the system. It also tells us that dark states arising from $J'' \rightarrow J'' - 1$ transitions cannot be destablized with any static polarization. Berkeland *et.al.* have also made a useful table, recreated here in Table

7.3 with their analysis which summarizes conditions under which dark states may arise.

Table 7.3: Number of dark states for any laser polarization for different angular momentum systems under zero magnetic field. Sourced from Ref [136].

J'	Integer J''	Half-integer J''
J''+1	No dark state	No dark state
J''	One dark state for any polarization	One dark state for circular polarization
J''-1	Two dark states for any polarization	Two dark states for any polarization

For BaH, in the unresolved hyper-fine level case, we will be using the transition, $J'' = 3/2 \rightarrow J' = 1/2$, which in Figure 7.11 appears to have no dark states, yet we know that there will be two dark states for any polarization used. For the hyperfine resolved case, relevant for discussion of a MOT, we will have $F'' = 0 \rightarrow F' = 1$, $F'' = 1 \rightarrow F' = 1$, and $F'' = 1 \rightarrow F' = 2$, which we see will have dark states as well.

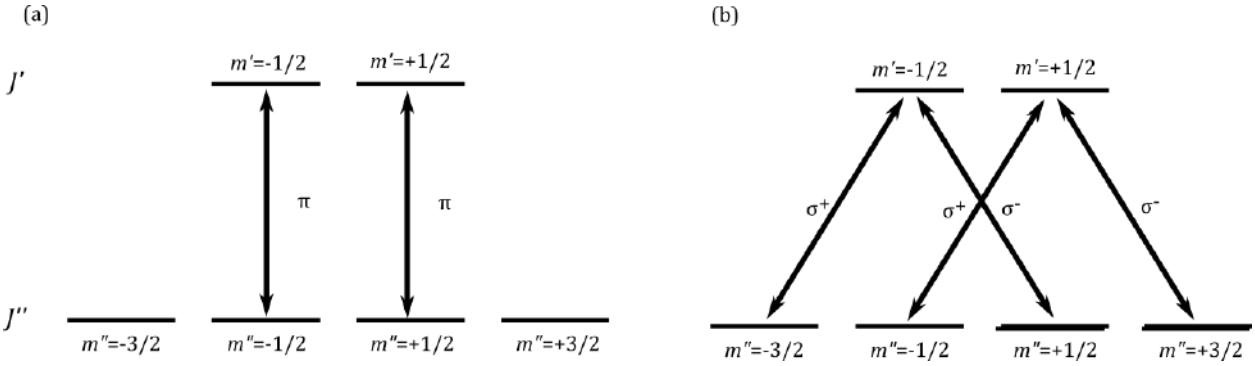

Figure 7.11: Excitation of $J'' = 3/2 \rightarrow J' = 1/2$ transition with (a) linearly, and (b) transverse polarized light. Both cases excite the ground state sublevel.

Destablizing the dark states can either be accomplished by remixing the ground states to redistribute the population to 'bright states' (those accessible by the laser), or by switching the polarization rapidly to change which states are dark. In either case, to achieve the maximum scattering rate, these processes must be done on a timescale that is at least at the spontaneous decay rate Γ of the excited state.

One method commonly employed in molecular beam experiments is magnetic field remixing. In this technique, a remixing magnetic field of magnitude B_r is applied at an angle θ_B to the light polarization, and the coherent superposition of states will undergo Larmor precession. The dark state solutions in Equations 7.4.22 through 7.4.24 are in fact orthogonal to bright state solutions in the Zeeman basis, therefore, this precession should evolve dark states into bright states at a rate,

$$\omega_B = \frac{\mu_B g_J m'' B_r \sin\theta_B}{\hbar}. \tag{7.4.25}$$

Berkeland *et. al.* has studied destabilizing dark states using a static magnetic field as described, specifically for the case of $J'' = 1 \rightarrow J' = 0$. By computing the evolution of the atomic density matrix using the Liouville equation, they have found that the maximum excited state population (which corresponds to the minimized time spent in dark states) occurs for $\omega_B = \Omega/4$, where Ω is the usual Rabi frequency. They also predict $\theta_B = 60^o$ to be optimal, since it equalizes the three transition Rabi frequencies. At the saturation intensity of the transition, the Rabi frequency is defined in such that $\Omega \approx \Gamma$.

Another possible technique to address the dark states is by rapidly modulating the polarization of the laser. Here, the polarization components, E_0, E_{+1}, and E_{-1} should be linearly independently time dependent to ensure that there is no solution for Equation 7.4.21. Reference [136] suggests using AOMs to modulate three different light beams at different frequencies.

A more direct way to remix the ground states is by using microwave fields to couple all the states together via some nearby microwave transition. In molecules such as BaH, this is most convenient to do using the $X^2\Sigma_{1/2}, N'' = 0$ state. In this scheme, all 12 of the relevant hyperfine sublevels originating from $F'' = 0, F'' = 1, F'' = 1$ and $F'' = 2$, are coupled together via the $(N'' = 0, J'' = 1/2, F'' = 1)$ ground state.

7.5 Rate Equation Modeling of Photon Scattering in BaH

In order to understand the cycling of a molecule in a quasi-closed system such as ours, we develop a multi-level rate-equation based model which takes into account as many relevant states as possible. Such a model which considers the probe laser intensity profiles of cooling and repump lasers, branching ratios to different hyperfine levels among the first three vibrational ground states, and detunings from fixed laser frequencies, keeps track of the population balances among states as a function of molecule time spent in the probe beam. This provides us with a few observable results, such as the scattered photon number, saturation intensity, and power broadening profiles. This model is similar to that presented in the earlier section on power requirements, but is based more off of that used in Reference [131]. The reader is encouraged to look there for details.

Since the model tracks populations within each of the many hyperfine sublevels throughout the experiment, we can use it to track the scattered photon number by integrating the number of molecules in the excited state over the time of the model. Since the model is parameterized in terms of distance, we change the variables with the velocity and multiply by Γ to get the photon number.

In a typical fluorescence experiment, the number of photons that are emitted from a probed molecule depends on the probe laser intensity, since this intensity modifies the excitation rate. However, in, for example, a two level system, this increase in fluorescence saturates when the excitation rate R, is larger than the rate at which molecules decay back down to the initial state, since the number of molecules available in the ground state decreases. This is the common saturation mechanism observed in atomic experiments, where everything looks like a two-level system. In molecules, where there are only quasi-closed transitions, every photon absorbed results in a possible loss of that molecule from the cycle,

resulting in a ground state depletion for any probe laser intensity. As pointed out in [131], the average number of photons per molecule is always less than $1/(1\text{-}p)$, where p is the probability of returning to the initial state. So, for example, if the probability of returning to the vibrational ground state is 0.99, as in the vibrational branching ratio for BaH, each molecule can absorb on average 100 photons before it is lost. In a beam experiment like ours, saturation occurs when $1/(1\text{-}p)$ is surpassed by RT, where T is the time for which the molecule interacts with the probe beam. In other words, the transition saturates when you try and hit the molecule with more photons than it takes to pump it into a dark state during its transit time through the probe. We can look to model such a saturation effect in the beam and compare the results to our experiment. Furthermore, we can also examine what the saturation intensity is to a molecule in a quasi-closed transition. After many cycles, the fluorescence can saturate due to the usual saturation mechanism involving a balance of excitation and decay rates, or can "saturate" because the ground state population is decreasing rapidly. Of course, this does not describe a steady state situation, but it is still useful to try and model.

Additionally, we can use the multi-level rate equation model to simulate spectra for different powers to guide our data analysis. In principle, we could fit our power broadening curves to it, and the free parameters of the model are the natural linewidth, Γ and the excited state hyperfine splitting Δ_e. The Franck-Condon factor (Z) from either the $A\Pi$ or the $B\Sigma^+$ state is also a free parameter, but for now we can say we trust the calculation by Ian Lane. Unfortunately, the technical limitations of PMTs mean that we cannot record fluorescence at the required wavelengths to obtain the power broadened spectra, and our measurements via the detection $E\Pi$ state probe only the relative hyperfine populations. Nevertheless, this model still serves use to understand our experiment better.

So the model is as follows: we have a ground state, $X\Sigma$, with two spin-rotation states: $|N'' = 1, J'' = 1/2\rangle$ with two hyperfine levels $|F'' = 1\rangle$ and $|F'' = 0\rangle$, and$|N'' = 1, J" = 3/2\rangle$

with two hyperfine levels $|F'' = 2\rangle$ and $|F'' = 1\rangle$. We are driving a transition to an excited state, $|A\Pi, J' = 1/2\rangle$ or $|B\Sigma, N' = 0, J' = 1/2\rangle$, each similarly with two hyperfine levels $|F' = 1\rangle$ and $|F' = 0\rangle$. The excitation rate between ground and excited levels is

$$R = \frac{\Gamma/2}{1 + 4\delta^2/\Gamma^2} \frac{I}{I_{sat}},$$

where δ is the laser detuning, I is the probe laser intensity, and I_{sat} is the saturation intensity, defined as

$$I_{sat} = \frac{\pi hc\Gamma}{\lambda^3} \frac{g_l}{g_u} \frac{1}{r}.$$

Here, λ is the probe laser wavelength, g_l and g_u refer respectivley to the lower and upper state degeneracies, and r is the branching ratio from the excited state. I assume that the two spin rotation states are addressed by two lasers with identical parameters except for the frequency, which has $\delta = 0$ tuned to the uppermost hyperfine ground state to the uppermost hyperfine excited state. These lasers can be turned 'off' or 'on' in the model.

As a molecule traveling with velocity v along $\hat{z}$ enters the probe beam, it experiences excitation light with an intensity profile equal to that of the laser. Here, we use a top hat-ish distribution given by,

$$I = I_0 \frac{\tanh[z/d + L/d] - \tanh[z/d - L/d]}{(2\tanh[L/d])}.$$

L and d parameterize the shape of the beam, which for $L = 0.001$ and $d = 0.0004$, the beam profile along z looks like,

The populations in each of the 16 hyperfine sublevels with a single vibrational system are denoted as follows, with g or e indicating ground or excited states: $|N'' = 1, J'' = 1/2\rangle$ (F, m_F) = (0,0) = $Ng0$, (1,0) = $Ng1$, and (1,±1) = $Ng2a$,$Ng2b$. $|N'' = 1, J'' = 3/2\rangle$ (F, m_F) = (1,0) = $jNg0$; (1,±1) = $jNg0a$,$jNg0a$; (2,0) = $jNg1$; (2,±1) = $jNg2a$,$jNg2b$;

(2,±2) = $jNg3a$,$jNg3b$. —$N' = 1, J' = 1/2\rangle$ (F, m_F) = (0,0) = $Ne0$, (1,0) = $Ne1$, and (1,±1) = $Ne2a$,$Ne2b$. A prefix vi indicates the population in the same labeled state for the ith vibrational level. In the following equations, the ground and excited state hyperfine splittings are denoted Δg and Δe respectively, with $\Delta g12$ indicating the $J'' = 1/2$ hyperfine splitting and $\Delta g32$ indicating the $J'' = 3/2$ hyperfine splitting. r_{if} indicates the vibrational branching ratios between an initial and final vibrational state. Rif refers to the scattering rate of a laser tuned to each of the possible ground and excited vibrational state transitions. At saturation in a 2-level system, the effective scattering rate, is reduced from the value of $\frac{1}{\tau}$ because the population distribution among states limits the excited state population to only 1/2 of the total population. In a multilevel system, this rate is further reduced by the factor, $\frac{N_e}{N_e+N_g}$, where N_e and N_g are the number of excited(4) and ground(12) state levels. We do not include this factor *a priori* because the model should account for this in the redistribution of population. The fact that we use the $B\Sigma$ state for our repump helps mitigate this reduction in scattering rate, since it decouples the first vibrational ground state. Therefore, the measured rate we should expect out of the model will be $\Gamma_{eff} = \frac{1}{\tau}\left(\frac{4}{16}\right)$. For details on this, see Section 7.3. In order to not pump immediately into the dark $m_F = \pm 2$ dark states, we assume horizontal polarization. This of course does not work in the real experiment, due to the presence of coherent dark states among the ground state levels, but this choice of polarization works for the model. There is assumed to be no magnetic field, even though in practice, a small one is introduced to remix coherent dark states.

Each equation is of the form shown below, where the derivative of the population in each state, multiplied by the molecule velocity, is equal to positive stimulated emission rates from possible excited states and a negative absorption rate proportional to the number of excited states. Then, we add the filling rates due to spontaneous decay from each possible excited state, scaled by the vibrational branching ratio, and a fraction, BR(i, j) based on the calculated branching ratios from a given excited state, j to a ground state i. Because of the

large number of rate equations in the model, only shown are those for the $J'' = 1/2, v = 0$ ground state and those referring to the $v = 0$ excited state.

$$
\begin{aligned}
v\frac{dNg0}{dz} =& R00(\delta)(Ne2a + Ne2b - 2Ng0) + r00\Gamma(\mathrm{BR}(0,0)Ne1 + \mathrm{BR}(0,2)Ne2a + \mathrm{BR}(0,3)Ne2b) \\
&+ r10\Gamma(\mathrm{BR}(0,0)v1Ne1 + \mathrm{BR}(0,2)v1Ne2a + \mathrm{BR}(0,3)v1Ne2b) \\
v\frac{dNg1}{dz} =& R00(\delta + \Delta g12)(Ne2a + Ne2b - 2Ng1) + r_{00}\Gamma(\mathrm{BR}(1,0)Ne0 + \mathrm{BR}(1,2)Ne2a \\
&+ \mathrm{BR}(1,3)Ne2b) + r_{10}\Gamma\mathrm{BR}(1,0)(v1Ne0 + \mathrm{BR}(1,2)v1Ne2a + \mathrm{BR}(1,3)v1Ne2b) \\
v\frac{dNg2a}{dz} =& R00(\delta + \Delta g12)(Ne1 - Ng2a) + R00(\delta + \Delta g12 - \Delta e)(Ne0 - Ng2a) \\
&+ r_{00}\Gamma(\mathrm{BR}(2,0)Ne0 + \mathrm{BR}(2,1)Ne1 + \mathrm{BR}(2,2)Ne2a) + r_{10}\Gamma(\mathrm{BR}(2,0)v1Ne0 \\
&+ \mathrm{BR}(2,1)v1Ne1 + \mathrm{BR}(2,2)v1Ne2a) \\
v\frac{dNg2b}{dz} =& R00(\delta + \Delta g12)(Ne1 - Ng2b) + R00(\delta + \Delta g12 - \Delta e)(Ne0 - Ng2b) \\
&+ r_{00}\Gamma(\mathrm{BR}(3,0)Ne0 + \mathrm{BR}(3,1)Ne1 + \mathrm{BR}(3,3)Ne2b) + r_{10}\Gamma(\mathrm{BR}(3,0)v1Ne0 \\
&+ \mathrm{BR}(3,1)v1Ne1 + \mathrm{BR}(3,3)v1Ne2b)
\end{aligned}
$$

$$
\begin{aligned}
v\frac{dNe0}{dz} =& R00(\delta + \Delta g12 - \Delta e)(Ng2a + Ng2b - 2Ne0) \\
&+ R00(\delta + \Delta g32 - \Delta e)(jNg0a + jNg0b - 2Ne0) \\
&+ R10(\delta + \Delta g12 - \Delta e)(v1Ng2a + v1Ng2b - 2Ne0) \\
&+ R10(\delta + \Delta g32 - \Delta e)(v1jNg0a + v1jNg0b - 2Ne0) \\
&- \Gamma Ne0 \\
v\frac{dNe1}{dz} =& R00(\delta + \Delta g12)(Ng2a + Ng2b - 2Ne1) + R00(\delta + \Delta g32)(jNg0a + jNg0b - 2Ne1) \\
&+ R00(\delta)(jNg2a + jNg2b - 2Ne1) + R10(\delta + \Delta g12)(v1Ng2a + v1Ng2b - 2Ne1) \\
&+ R10(\delta + \Delta g32)(v1jNg0a + v1jNg0b - 2Ne0) \\
&+ R10(\delta)(v1jNg2a + v1jNg2b - 2Ne1) \\
&- \Gamma Ne0 \\
v\frac{dNe2a}{dz} =& R00(\delta + \Delta g12)(Ng1 - Ne2a) + R00(\delta + \Delta g32)(jNg0 - Ne2a) \\
&+ R00(\delta)(Ng0 - Ne2a) + R00(\delta)(jNg1 + jNg3a - 2Ne2a) \\
&+ R10(\delta + \Delta g12)(v1Ng1 - Ne2a) + R10(\delta + \Delta g32)(v1jNg0 - Ne2a) \\
&+ R10(\delta)(v1Ng0 - Ne2a) + R10(\delta)(v1jNg1 + v1jNg3a - 2Ne2a) \\
&- \Gamma Ne2a \\
v\frac{dNe2b}{dz} =& R00(\delta + \Delta g12)(Ng1 - Ne2b) + R00(\delta + \Delta g32)(jNg0 - Ne2b) \\
&+ R00(\delta)(Ng0 - Ne2b) + R00(\delta)(jNg1 + jNg3b - 2Ne2b) \\
&+ R10(\delta + \Delta g12)(v1Ng1 - Ne2b) + R10(\delta + \Delta g32)(v1jNg0 - Ne2b) \\
&+ R10(\delta)(v1Ng0 - Ne2b) + R10(\delta)(v1jNg1 + v1jNg3b - 2Ne2b) \\
&- \Gamma Ne2b
\end{aligned}
$$

We can track the populations in each level as the molecules pass through the laser, made to be resonant with the transition from $J'' = 1/2, F'' = 0$ and $J'' = 3/2, F'' = 2$. For a simple case that resembles our beam experiments, we can apply just the laser that addresses the $J'' = 1/2$ spin rotation state and watch molecules get pumped into the $J'' = 3/2$ state, as is demonstrated in Figure 7.12 (a). This result was found with the probe laser at the classically defined saturation intensity, and shows the rapid depopulation of the $J'' = 1/2$ ground state and corresponding increase in population to the unaddressed $J'' = 3/2$ states. In Figure 7.12 (b), the excited states are shown for the same experiment. Not shown is the slight population increase in the first vibrational state at the 0.1% level.

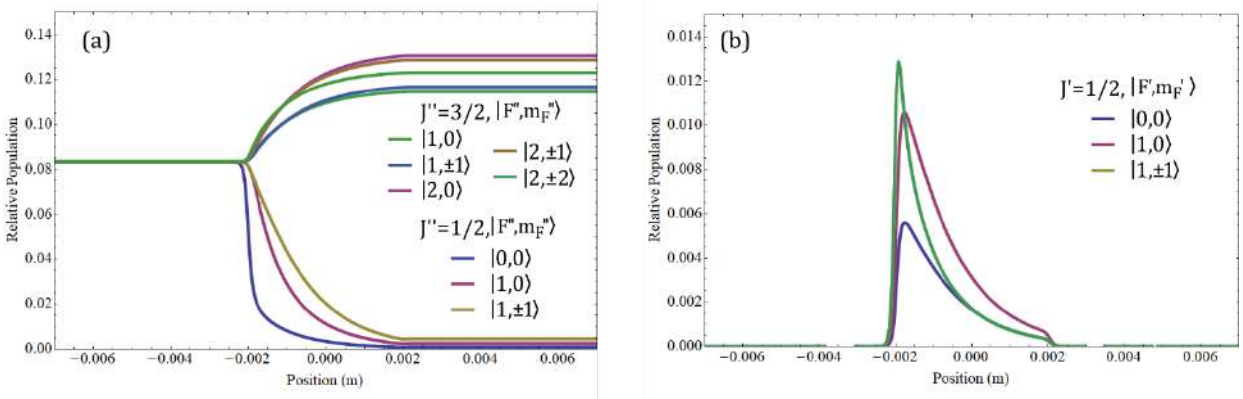

Figure 7.12: Population in (a) ground and (b) excited hyperfine sublevels as a function of distance with only the $J'' = 1/2$ spin-rotation level addressed. The laser is on between -0.002 and 0.002 m. The 4 $J'' = 1/2$ sublevels depopulate quickly as the molecules are pumped into the 8, $J'' = 3/2$ sublevels. The excited state populations in (b) reflect the emptying out of the states accessible by the laser.

Adding in the additional spin-rotation laser resonant with $J'' = 3/2, F'' = 2$, also has a readily understandable effect, seen in Figure 7.13. Since there is a 39 MHz splitting between $J'' = 3/2, F'' = 2$ and $J'' = 3/2, F'' = 1$, the $J'' = 3/2, F'' = 1$ sublevels are essentially dark, causing almost all the molecules to go over to them. In the excited states, we see similar behavior as to the first, but with several times higher peak population.

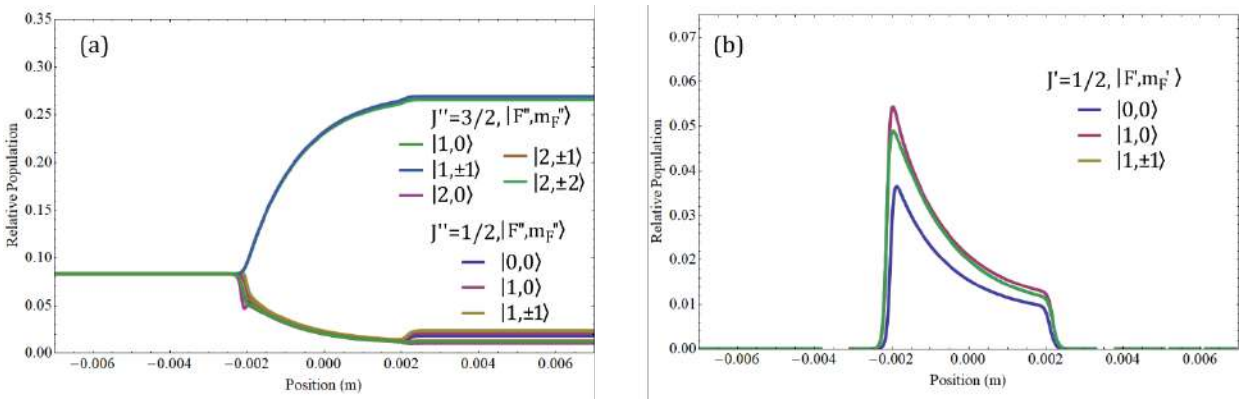

Figure 7.13: Population in (a) ground and (b) excited hyperfine sublevels as a function of distance with both the $J'' = 1/2, 3/2$ spin-rotation levels addressed, but not addressing hyperfine splitting.The laser is on between -0.002 and 0.002 m. All but two sublevels depopulate quickly as the molecules are pumped into the 3, $J'' = 3/2, F'' = 1$ sublevels sublevels. The excited state populations in (b) again reflect the emptying out of the states accessible by the laser. The small increase in ground state populations after the molecules leave the laser probe region is due to the remaining moleucles in the excited state decaying down.

In our experiments to close the spin rotation splitting, we therefore must use sidebands to address the ground state hyperfine splitting. Adding in the effect of the sideband is the same as there being unresolved hyperfine splitting, and we find the results in Figure 7.14, which shows the case for $I = 2I_{sat}$. Here, the populations balance themselves after some initial rapid redistribution process, and we can see the slight downward slope in all the levels as molecules are gradually pumped into $v = 1$. During the laser interaction region, the system is in a steady state, with the most molecules in the $J'' = 1/2, F'' = 1, M_F'' = \pm 1$ sublevels. This is because these states are each only addressed by a single handedness of polarization, and are also each filled by 3 excited states, which means their steady state population is higher than all the others. The $F'' = 2, M_F'' = \pm 1$ and $F'' = 2, M_F'' = \pm 2$ states also are addressed by a single handedness of polarization, but are populated by less states. For $M_F'' = \pm 1$, it can be populated by $F' = 1, M_F' = 0$ and either of the $F' = 1, M_F' = \pm 1$ states. The ground $M_F'' = \pm 2$ can be populated only by either $F' = 1, M_F' = \pm 1$ states. This is why they are not very high in population relative to the others. After the laser stops

interacting with the molecules, we see the populations increase as the molecules that were in the excited state decay back down. Even in this short interaction region corresponding to 40 μs, almost 10% of the initial molecule population is pumped into other vibrational states, and each molecule has scattered on average 14 photons.

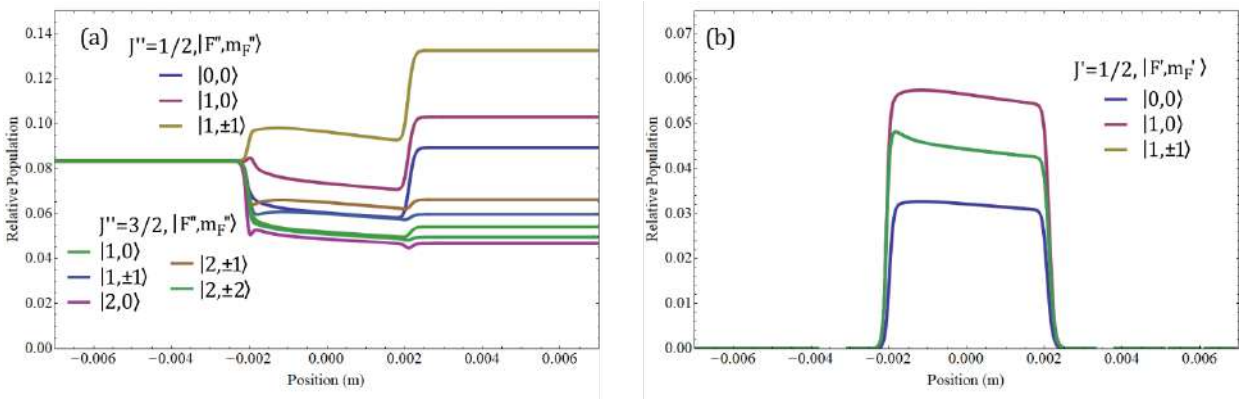

Figure 7.14: Population in (a) ground and (b) excited hyperfine sublevels as a function of distance with both the $J'' = 1/2, 3/2$ spin-rotation levels addressed, as well as the effect of laser sidebands to address hyperfine splittings.The laser is on between -0.002 and 0.002 m. After a quick redistribution of states, the system reaches a steady state, with the most molecules in the $J'' = 1/2, F'' = 1, M_F'' = \pm 1$ sublevels. This is because these states are only addressed by a single handed polarization, and are also each filled by 3 excited states. The $F'' = 2, M_F'' = \pm 1$ and $F'' = 2, M_F'' = \pm 2$ states also are addressed by a single handedness of polarization, but are only populated by a two (for $M_F'' = \pm 1$) or one (for $M_F'' = \pm 2$) excited state each, which is why they are not very high in population relative to the others. Even though the system is in a steady state, there is a slight overall decrease in population in the laser interaction region due to the small loss to the other vibrational states. The increase in ground state populations after the molecules leave the laser probe region is due to the remaining molecules in the excited state decaying down.

By running these experiments above while varying the detuning of the probe laser, we can monitor the scattered photons as a proxy for the expected signal. As mentioned, this does not accurately reflect the experiment we actually perform since we probe the optically pumped populations via a separate state. In fact, the relative heights of the peaks will be quite different and would be better reflected by the sum of ground state populations in plots like Figure 7.12. Nevertheless, the spacings and power broadened widths of peaks we be

useful to compare to experimental data. Simulated spectra are shown for transitions to the $A^2\Pi_{1/2}$ (Figure 7.15) and $B^2\Sigma^+$ (Figure 7.16), using measured hyperfine splittings and with power at the saturation intensity.

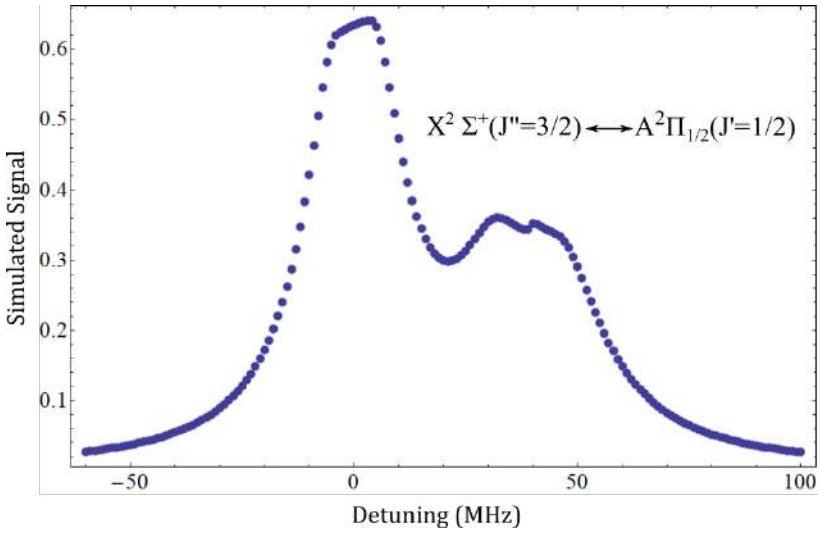

Figure 7.15: Simulated fluorescence from driving hyperfine transitions: $X^2\Sigma^+(J'' = 3/2, F'' = 1, 2) \leftrightarrow A^2\Pi_{1/2}(F' = 0, 1)$. While the molecules are quickly pumped into the $X^2\Sigma^+(J'' = 1/2)$ state, some extra cycling happens between $F'' = 2 \leftrightarrow F' = 1$ due to branching ratios - evidenced by the larger relative size of this fluorescence peak.

Finally, we can vary the power used in the model, and measure the scattered photons as a function of this power to see if the saturation intensity matches with data taken in the experiment. These results are shown in Figure 7.17, along with saturation intensity measurements taken on 11-17-2017. While the data here is quite noisy (shot noise not yet reduced!), the qualitative agreement is good. The only tunable parameter in the model for this was the excitation rate, which affects the overall shape of the curve. Here, we find that an scattering rate of $\approx$100,000 s^{-1} (tuned by hand) matches the data. This is in line with what is expected for our molecule.

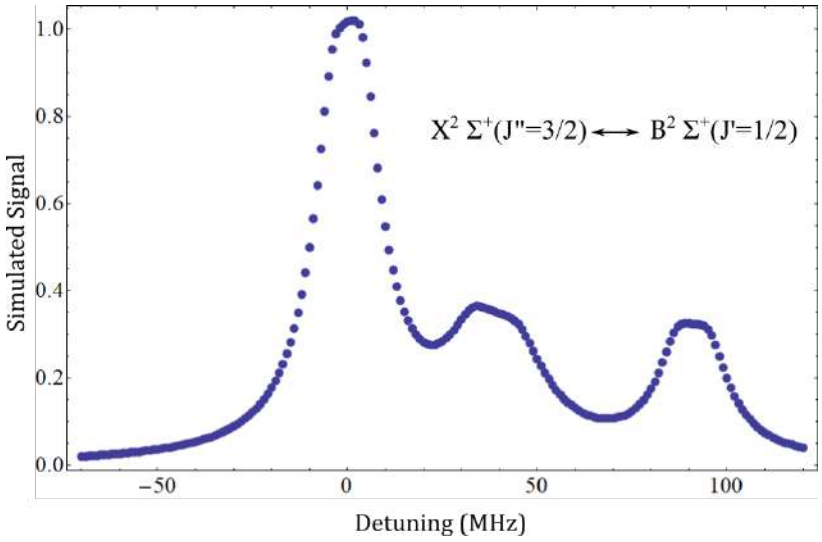

Figure 7.16: Simulated fluorescence from driving hyperfine transitions: $X^2\Sigma^+(J''=3/2, F=1,2) \leftrightarrow B^2\Sigma^+(J'=1/2, F'=0,1)$. While the molecules are again quickly pumped into the $X^2\Sigma^+(J''=1/2)$ state, some extra cycling happens between $F''=2 \leftrightarrow F'=1$ due to branching ratios - evidenced by the larger relative size of this fluorescence peak.

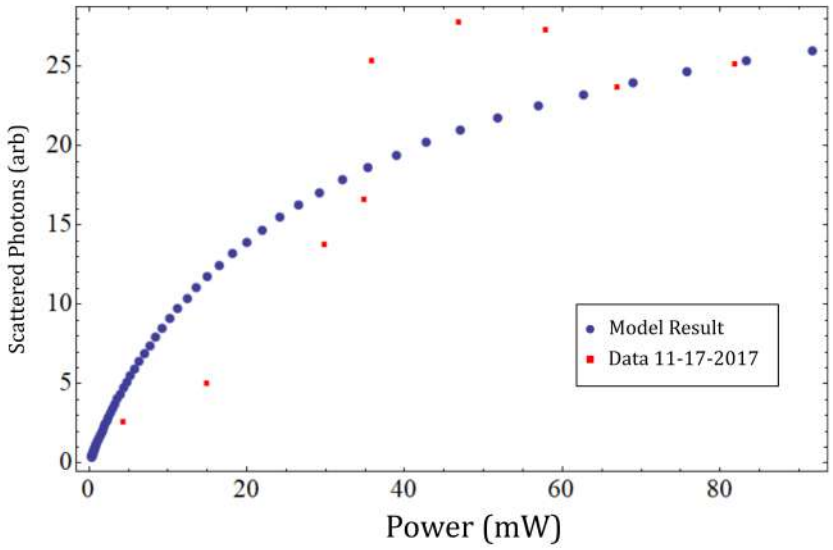

Figure 7.17: MLRE Model compared to experiment for fluorescence vs. probe power. In both the model and the experiment, the probe laser is transverse to the molecular beam. For each power, the model outputs the number of photons scattered by the excited state, which is scaled by an arbitrary factor, set in reality by the molecular density. To achieve agreement with the data, the scattering rate should be ≈100,000 s^{-1}.

7.6 Type II MOT

In order to trap molecules in a Magneto-Optical Trap (MOT), there are some requirements on the energy structure of the molecule we are interested in. In particular, the method by which we limit rotational branching, driving from $N'' = 1 \rightarrow N' = 0$, is unconventional for creating optical trapping forces on the molecules, and, moreover, those forces are strongly dependent on the molecular g-factors of these states. Here, we look to explore this a bit further to understand the requirements to make a BaH MOT. From our Zeeman shift measurements, we found that the sublevels in BaH quickly rearrange themselves under modest fields to be best described in the M_J basis, so we will try and understand the best configurations for both bases, F and J. To guide our analysis, the g-factors for BaH are listed in table 7.4. Much of the analysis below was done in a general fashion by Tarbutt in an illuminating and informative paper with guidance and details of a full MOT model [129].

Table 7.4: Measured and predicted effective g-factors for total hyperfine interaction. Strong mixing between Hund's cases makes J the correct basis even for moderate fields.

State	Measured g_{eff}	Prediction
$X^2\Sigma^+(N'' = 1, J'' = 3/2)$	+0.56(19)	+0.50
$X^2\Sigma^+(N'' = 1, J'' = 1/2)$	-1.37(10)	-1.4
$B^2\Sigma^+(N' = 0, J' = 1/2)$	+2.76(10)	+2.86
$A^2\Pi_{1/2}(N' = 0, J' = 1/2)$	-0.56(1)	-0.44
$E^2\Pi_{1/2}(N' = 0, J' = 1/2)$	-0.16(10)	-0.04

7.6.1 F-basis

In a BaH MOT which we plan to operate on the $X^2\Sigma^+ \leftrightarrow A^2\Pi_{1/2}$ transition, there are 4 hyperfine ground states with $F'' = 0, F'' = 1, F'' = 1$, and $F'' = 2$, and two hyperfine excited states, $F' = 0$, and $F' = 1$. The hyperfine splitting in the excited state is 47 MHz, which is serveral times the natural linewidth. There are a few different combinations of angular

momenta here, so we can go through each possibility to determine the best polarizations for the beams.

In a conventional MOT, atoms are cycled between 2 levels repeatedly in a spatially depending magnetic field in an optical molasses. These two ingredients generate a velocity and position dependent restoring force that both cools and confines. In those two levels, the excited state typically has higher angular momentum than the ground state. For example, a transition from $F'' = 0$ to $F' = 1$, where F'' and F' denote the ground and excited state respectively. This is advantageous because there are naturally no dark states possible, and no leaks by which atoms might get lost. As an atom moves away form the center of the trap and into higher field regions, the degeneracy among hyperfine sublevels is lifted by an amount proportional to the field and the state g-factor, as we have seen in previous section. The restoring and anti-restoring beams should be polarized with either left or right circularly polarized light, σ^- or σ^+ , so that when the light is red detuned from the zero field transition frequency, the atomic states are shifted into resonance in a way that optically pumps the population so that the they are brought back towards the MOT. The choice of polarization depends on the sign and magnitude of the g-factors of the excited state.

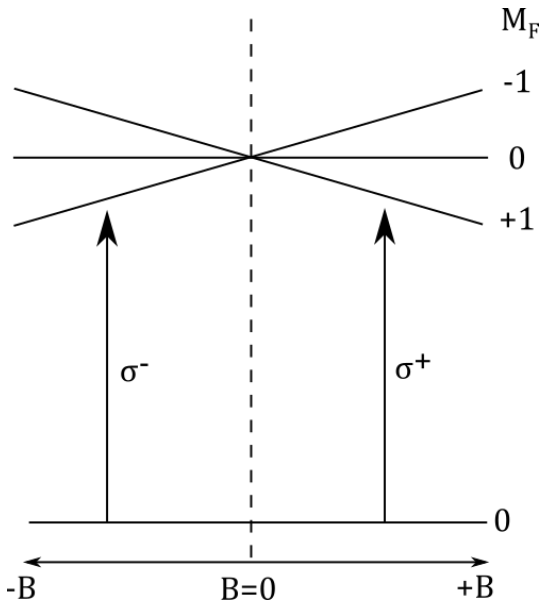

Figure 7.18

$F' = F'' + 1$

The relevant case we will need to examine for BaH is for a negative excited state g-factor for the $A^2\Pi_{1/2}$ state, roughly equal in magnitude to the ground state g-factor. The first situation we examine is for $F'' = 0, F' = 1$, as in Figure 7.18. In this case the restoring beam should be σ^+, so that a molecule moving into the positive field region finds the $M'_F = +1$ state in resonance with that beam, and can be optically pumped to that state. The contribution for the restoring beams is the strongest, so there is a net trapping force.

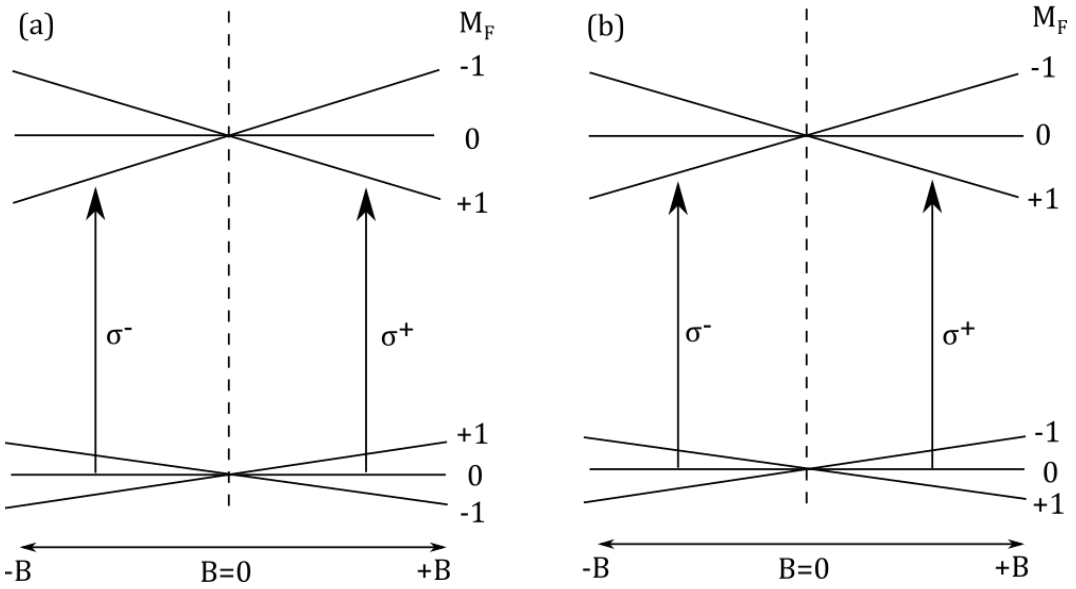

Figure 7.19

$F' = F''$

We also are interested in the case when $F'' = F'$, specifically for the transition from $F'' = 1$ to $F' = 1$. If the g-factors in both states are positive, but larger in the upper state, as in Figure 7.19a, we can choose the restoring beam for molecules moving in the positive field region to be σ^+. In this case, a molecule in the $M_F'' = 0$ can be driven by either the restoring or anti-restoring beams, but is driven most strongly to $M_F' = -1$ via the restoring beam, because it is closer to resonance. Meanwhile the $M_F'' = +1$ state is driven most strongly to $M_F' = 0$. The $M_F'' = -1$ only interacts with the anti-restoring beam to $M_F' = 0$, albeit weakly because it is off resonance. We might worry that molecules will pile up in the $M_F'' = -1$ state, but we must keep in mind that there are orthogonal beams that also interact with the molecules. These orthogonal beams will drive to the $M_F' = -1, 0$ states, and are closest to resonance so they dominate, resulting in a net restoring force.

If the g-factor in the excited state is large and positive but is negative in the lower state, as in Figure 7.19b, we can try and choose the restoring beam for molecules moving in the

positive B direction to have polarization σ^+. Here, the situation is much the same as for (a), and we find a net restoring force for the same reasons, with the orthogonal beams preventing a build up in $M_F'' = +1$.

$F' = F'' - 1$

Finally, we examine the case for which $F'' = 2$ and $F' = 1$, which is shown in Figure 7.20. Here the excited state g-factor is positive and large as before, while the ground state g-factor is positive and small. The restoring laser is chosen to have polarization σ^-, which at first seems counterintuitive. For the ground state sublevels, $M_F'' = 0, +1, +2$, the anti-restoring beam dominates. However, the molecules are always driven most strongly into the $M_F' = -1$ excited state, which decays with 60% probability to $M_F'' = -2$, and 40% probability to $M_F'' = -1$. From these two sublevels, only the restoring beam acts. Since the molecules tend to spend the most time in those two ground state sublevels, there ends up being a restoring force.

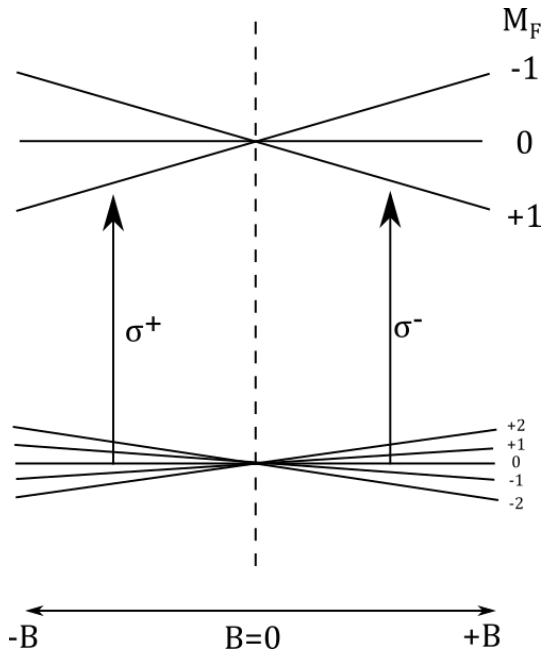

Figure 7.20

7.6.2 J-basis

We will see later that at very modest fields (<10 G) the effective Hamiltonian in BaH becomes much better described by the J basis, instead of the F basis. It will be useful then, to understand how the MOT can work in this other description, so we will go through the relevant cases. For this analysis, we will examine possibilities for either excited state, $B^2\Sigma^+$ or $A^2\Pi_{1/2}$.

$J' = J''$

The first situation we look at is when $J' = J'' = 1/2$. In Figure 7.21a, we see the case for a MOT on $A^2\Pi_{1/2}$. Here, we choose the laser polarization to be σ^+ for the restoring beam for molecules traveling in the positive B direction, and see that the $M_J'' = -1/2$ will be quickly pumped into $M_J'' = +1/2$ by the restoring beam. Molecules in the $M_J'' = +1/2$ state will get pumped out only with the orthogonal or anti-restoring beam, and so the net force is zero.

The same is true for Figure 7.21b, showing the scheme for $B^2\Sigma^+$. While the restoring beam polarization is switched to address the reversed g-factor, the net force still vanishes as molecules pumped into the $M_J'' = +1/2$ only talk to the anti-restoring and orthogonal beams.

We can still achieve a restoring force in two ways. As suggested by Tarbutt, the excitation rate out of $M_J'' = +1/2$ is slow in both cases, so one could imagine rapidly switching the B-field and polarization in an "RF-MOT" configuration. This is a challenging premise, but has been demonstrated in several groups already. In BaH, there is another possibility. Due to the large spin rotation splitting. Blue-detuned lasers can be added to address the $M_J'' = +1/2$ level without affecting nearby transitions. This is schematically shown in Figure 7.22. The additional restoring lasers added here allow the $M_J'' = +1/2$ level to be addressed by the appropriate trapping beams, and there are no nearby transitions to affect.

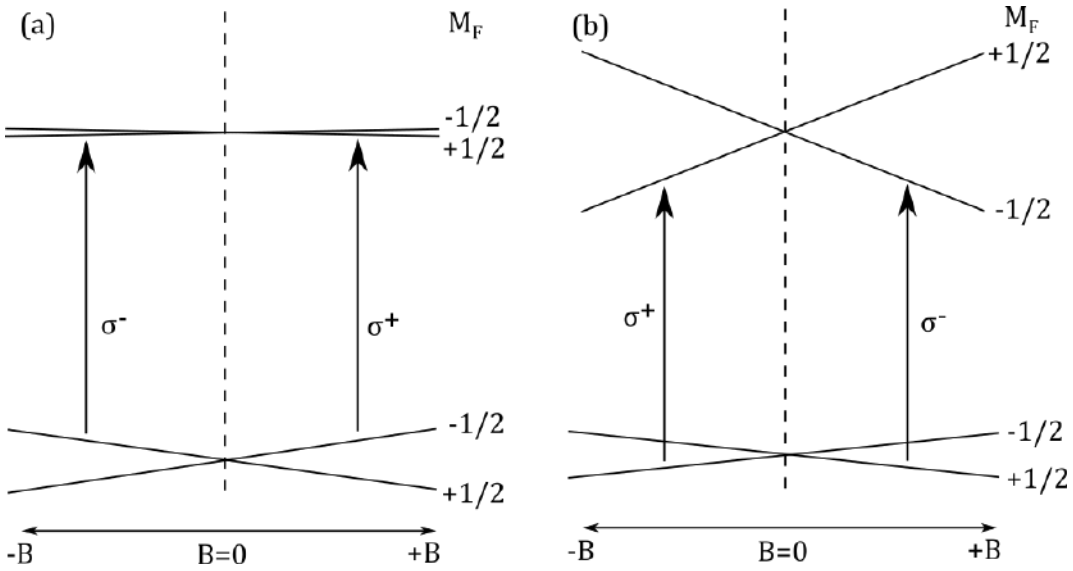

Figure 7.21: Scheme to make a MOT when $J' = J = 1/2$, for two situations. (a) g-factor is small and negative in the excited state as would be true for a MOT made with the $X^2\Sigma^+ \leftrightarrow A^2\Pi_{1/2}$ transition. ba) g-factor is large and positive in the excited state as would be true for a MOT made with the $X^2\Sigma^+ \leftrightarrow B^2\Sigma^+$ transition.

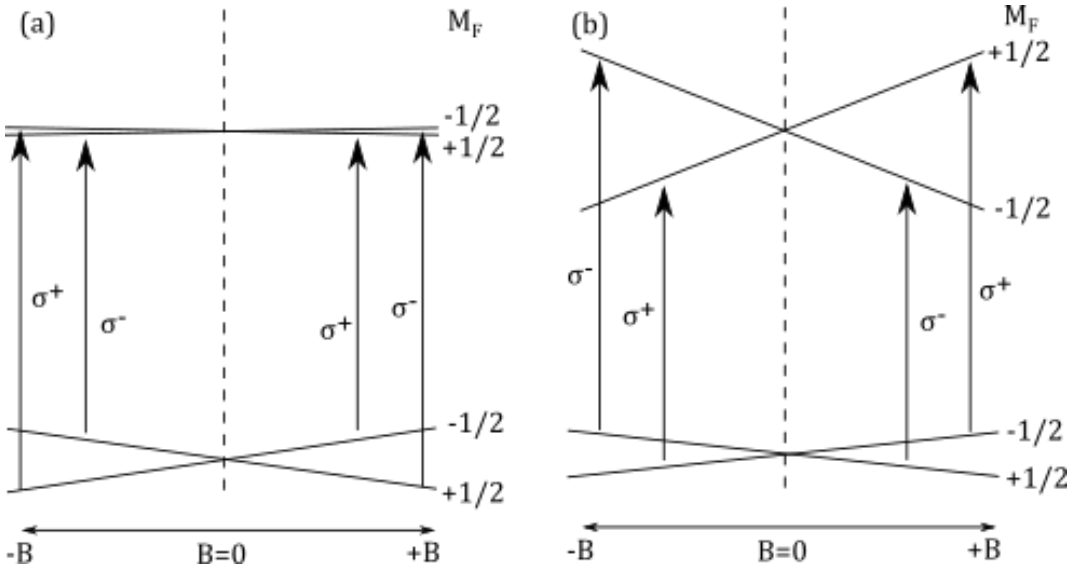

Figure 7.22: Proposed scheme to address a lack of restoring force when only one frequency of restoring light is used. The level structure is the same as Figure 7.21, for (a) and (b).

$J' = J'' - 1$

The other important case is for $J' = J'' - 1$, as is the case for the upper spin rotation ground state. In BaH, the relative sizes of the ground state are shown for two possible laser cooling schemes in Figure 7.23. Here, we have a similar issue as above for both configurations. Molecules that start in the $M_J'' = +3/2$ state for positive B-field, first interact with the restoring σ^- beam, since it is on resonance and has the correct polarization. From the excited, $M_J' = +1/2$ state, they can decay back to $M_J'' = +3/2$ (50%), or $M_J'' = \pm 1/2$ (50%) [55].

If they fall into either $M_J'' = \pm 1/2$, the situation depends on the scheme used. In the $X^2\Sigma^+ \leftrightarrow A^2\Pi_{1/2}$ scheme of Figure 7.23(a), $M_J'' = +1/2$ is accessible by the restoring beam or orthogonal beams. $M_J'' = -1/2$ can interact with the anti-restoring, or orthogonal beams. For the $X^2\Sigma^+ \leftrightarrow B^2\Sigma^+$ scheme of Figure 7.23(b), $M_J'' = \pm 1/2$ are unlikely to interact with either restoring or anti-restoring beam, since they are both far from resonance due to the large excited state splitting. Instead, orthogonal beams will likely dominate. In both cases, the restoring force is greatly reduced.

Eventually, they will make their way to $M_J'' = +3/2$ where they only interact with the anti-restoring beam, which is far off resonance, leaving orthogonal beams to pump them up. All this amounts to a net restoring force, mostly due only to the time molecules spend in $M_J'' = +3/2$, the only state that properly applies a restoring force.

We can try and improve the restoring force by using additional lasers, as shown in Figure 7.24 for both laser cooling transitions. Now, molecules in both the $M_J'' = \pm 3/2$ states interact most strongly with the restoring beams, while the $M_J'' = \pm 1/2$ are again dominated by the orthogonal beams. In this case, the restoring force is active for all of the ground state sublevels.

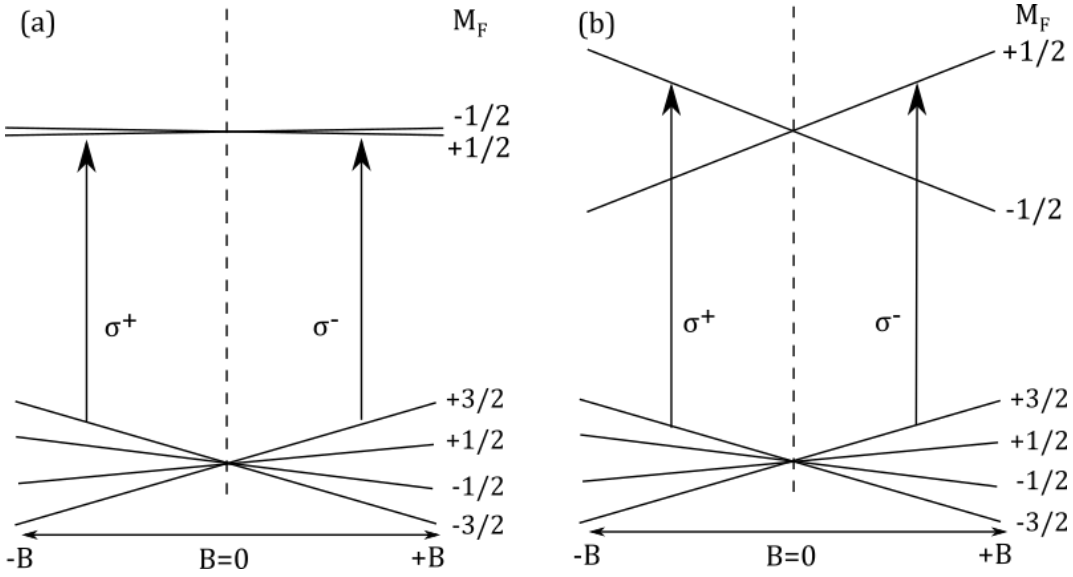

Figure 7.23: Scheme to make a MOT when $J' = J + 1/2$, for two situations. (a) g-factor is small and negative in the excited state as would be true for a MOT made with the $X^2\Sigma^+ \leftrightarrow A^2\Pi_{1/2}$ transition. ba) g-factor is large and positive in the excited state as would be true for a MOT made with the $X^2\Sigma^+ \leftrightarrow B^2\Sigma^+$ transition. The net restoring force here is small or zero.

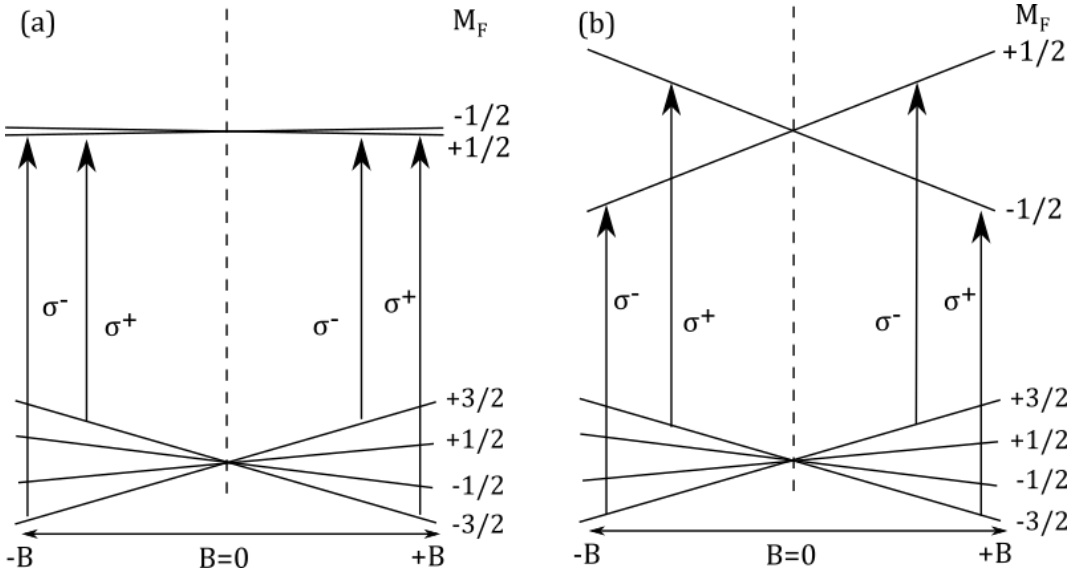

Figure 7.24: Proposed scheme to address a lack of restoring force when only one frequency of restoring light is used. The level structure is the same as Figure **??**, for (a) and (b).

Chapter 8

Outlook

The task of creating an ultracold sample of diatomic molecules is a tall order, and in itself is a challenging technical goal. But the real question is: what do you do with it? In the opening chapters I gave some directions that the field is taking. In particular, studying long-range dipolar interactions between these trapped molecules is a popular physics goal. Additionally, studies of fundamental physics in the form of searches for deviations from the standard model appear to be fruitful and exciting endeavors. In our experiment, we look to take advantage of a somewhat thorny problem in AMO physics, in the study of ultracold hydrogen.

8.1 Prospects for Ultracold Hydrogen

Hydrogen's role in precision science has been particularly special. The chemical properties of hydrogen were identified by Lavoisier in the 18th century, through his definitive experiments to prove that water was not in itself an element, but a product of oxygen and hydrogen [137]. A century later, Johann Balmer discovered a series of hydrogen lines which had spacings that could be predicted by an empirical formula, giving rise to atomic theory [138]. Hydrogen's

simplicity made it possible for Bohr to develop a quantum atomic theory that had startling predictive power for hydrogen. Precision experiments that revealed the fine structure confounded the theory until Dirac's relativistic quantum mechanics. The experiments of Rabi and Lamb were motivations to the development of quantum electrodynamics. So it goes with hydrogen, where precision measurements revealing deviations from theory are true tests of our understanding of the quantum world.

In developing new technologies for scientists, hydrogen has also played a vital role, from the importance of the 21-cm line in radio astronomy and as the first coherent EM radiation source in the maser, leading to the laser, which has undoubtedly transformed AMO physics. Perhaps the most transformative technology to emerge from hydrogen spectroscopy is the optical frequency comb. Theodore Hansch's study of the two-photon spectroscopic $1S-2S$ transition in hydrogen has resulted in over a million-fold increase in the precision of that measurement, resulting from the development of the frequency comb [139].

So then, it seems natural to suggest that ever more precise measurements of hydrogen are fruitful and worthy endeavors. For these measurements, ultracold gases of hydrogen would have experimental advantages over other techniques. A sub millikelvin gas of hydrogen would primarily provide reduced inhomogenous broadening effects, increasing the possible spectroscopic resolution. Furthermore, a trapped, ultracold gas would enable long interaction times, which further increases the possible precision through averaging. Importantly, a dilute gas, as is most commonly found in laser trapping and cooling experiments, offers freedom from density and hyperfine state dependent collisional shifts which are the primary limiting factor behind current efforts in ultracold hydrogen spectroscopy.

Despite the obvious advantages, hydrogen remains elusive as a viable atom for laser cooling and trapping. The main reason is technical: the cycling transition in hydrogen lies in the ultraviolet (121.6 nm), and it is simply too challenging to find enough laser power there. Nevertheless, a heroic experiment led by Dan Kleppner at MIT led to the

formation and study of a BEC of hydrogen, using a combination of advanced cryogenic and magnetic trapping techniques developed over 20 years [140]. In that experiment, the walls of a cryogenic cell are cooled to below 1K and coated with a slim of superfluid ^{4}He. Hydrogen is produced via RF discharge (in that cryogenic environment), and thermalize with the superfluid film via collisions. (If this all sounds vaguely familiar to the preceding thesis, you're quite right). The hydrogen is polarized into a paramagnetic low-field seeking state, which is subsequently trapped within a super-conducting magnetic trap in which the cell is residing. As a final step, the magnetic trap is slowly dialed down to evaporatively cool down the trapped atoms into a BEC. While the experimenters reached the condensate, the optical density was ultimately too high, leading to intractable collisional shifts in the spectroscopy that limited the ultimate precision. Moreover, the optical access was limited by the nature of the cryogenic experiment, creating significant challenges for advanced optical spectroscopy.

Of course, hydrogen spectroscopy remains an active field with many experiments to improve spectroscopic measurements of many lines. A state of the art experiment from the group of Thomas Udem was able to perform the most precise spectroscopy of the 2S-4P transition in H, with the goal of reducing uncertainty of the proton charge radius, r_p [141]. Yet the remaining systematic effects are the first-order Doppler shift from the hydrogen beam temperature of 5.8 K, accounting for over 90% of the error budget. Therefore, the need for an ultracold trapped, H sample is apparent.

This is a situation in which cooling a molecule is a palatable alternative to cooling an atom, in that a molecule containing hydrogen can be cooled, trapped and photo-dissociated, in a rather roundabout way to get a hold of that ultracold hydrogen. This proposal was first developed by Lane *et. al.* [73]. Moreover, the technique described can achieve temperatures several orders of magnitude below the Doppler recoil temperature. This is precisely the motivating reason behind choosing to pursue a hydride radical as our chosen cooling partner.

After all, with CaF, SrF, YO and a few other species along the way, there really isn't all that much room for yet another 'proof of principle' experiment. Here, our science goal is to demonstrate the versatility and feasibility of using molecules as alternative cooling paths to getting at an atom or compound of interest.

How exactly would this work? The key idea is to have zero-energy fragmentation of a molecule. This means that when a molecule (ab) is broken apart into constituent atoms (a and b), the constituent velocities, v_a and v_b, are the same as that of the parent v_{ab}. If this is true, then the temperature of constituent a, via the kinetic energy relation, is,

$$T_a = \frac{\mathrm{m}_a v_a^2}{3k_B}, \tag{8.1.1}$$

where m_a is the mass of atom a, and k_B is the Boltzmann constant. Using the similar relation for the parent atom, and the fact that $v_a \approx v_{ab}$, the ratio between the temperatures of atom a and the parent is,

$$\frac{T_a}{T_{ab}} = \frac{\mathrm{m}_a}{\mathrm{m}_{ab}}. \tag{8.1.2}$$

Therefore we see that if the mass of the parent is very large compared to the constituent atom, and we can achieve the zero-energy fragmentation, the final temperature of the constituent will be lower than the parent. For BaH, and focusing on the H, of course,

$$T_H = \frac{T_{BaH}}{138}. \tag{8.1.3}$$

So the key questions are, (1) how do we achieve zero-energy fragmentation? (2) How cold can we make the BaH?

8.1.1 Zero-Energy Fragmentation

In the normal course of photofragmentation, a molecule is excited up to some excited state via a photon, and before decaying safely back down to the ground state, it dissociates, wither through coupling to some repulsive state through predissociation, or because the excited state it was driven to was within a repulsive potential. Either way, these excited states have elevated energies, resulting in a large constituent velocity, and as a result, the light atoms would go speeding off, never to be seen again. To ensure that there is no excess energy, the dissociation of the molecule must happen precisely at the dissociation limit of the molecular electronic potential.

There are two possible routes to dissociate the molecule at the dissociation limit. Both methods are the reverse of commonly employed molecule formation methods: via Feshbach resonances and photoassociation. To use a Feshbach resonance, the molecular population must be coherently transferred adiabatically through a Feshbach resonance. This could be accomplished by coherently transferring the molecular population from the $N'' = 1$ ground state into the highest vibrational state within the $X^2\Sigma^+$ electronic ground state potential via the stimulated Raman adiabatic passage (STIRAP) technique [142]. STIRAP has been demonstrated in a variety of ultracold molecular experiments to be a highly efficient way to move molecules back and forth between rovibrational states within a molecular potential [13, 143]. From there, an external magnetic field can be used to move that last rovibrational level across the dissociation limit of the potential, which adiabatically converts the molecule into atoms [41]. Importantly, we need to consider the energy scale of the Feshbach fragmentation technique, with is set by the Feshbach linewidth [41, 73], $\Gamma(E)$, which is related to the width of the Feshbach resonance, $\Delta(B)$ as,

$$\Delta(B) = \frac{\Gamma(E)}{2ka_{bg}\delta\mu}, \tag{8.1.4}$$

where k is the wave vector describing the outgoing bodies, a_{bg} is the background scattering length, set by the ground state potential, and $\delta\mu$ is the difference in molecular and atomic dipole moments. As found in Ref. [73], to ensure that the laboratory frame velocity of the hydrogen fragment is perturbed as little as possible, the fragmentation of a parent molecule with thermal energy E_{BaH} should be constrained as,

$$\Gamma(E) \leq \frac{m_H}{m_{Ba}} E_{BaH}. \tag{8.1.5}$$

For a BaH gas at sub mK temperatures, the Feshbach width must be <100 mG, which based on estimates from Ref. [73], is perfectly feasible.

An alternative to Feshbach fragmentation is photodissociation, where molecules are moved via a 2-photon process directly to the dissociation limit of the molecular ground state [47]. Figure 8.1 illustrates this process via the excited $A^2\Pi_{1/2}$ state, which dissociates into a ground state hydrogen and $^3D_1$ excited barium atom [144, 145]. The first leg would require a laser with wavelength $\approx$ 330nm and the second leg requires $\approx$ 1000nm. The Sr_2 experiment in this same lab has studied in great detail the process of molecular photodissociation, showing that such a two photon process can be achieved with excess energies corresponding to order 10s of nK temperatures (Figure 8.2) [87]. This process could potentially be much easier and more straightforward than the Feshbach technique.

After dissociation, the excellent optical access provided by the nature of the MOT enables the possibility to load optical dipole or lattice traps in which to hold the H atoms for precision spectroscopy.

The $A^2\Pi_{1/2}$ state in BaH has a predicted lifetime of 136 ns, corresponding to a Doppler temperature of 28 μK [70]. From Equation 8.1.3, we see that the final hydrogen temperature is $\approx$ 200 nK, well below the Doppler temperature of H (1mK). Recent experiments with CaF have shown cooling below the Doppler limit for that molecule using a combination of

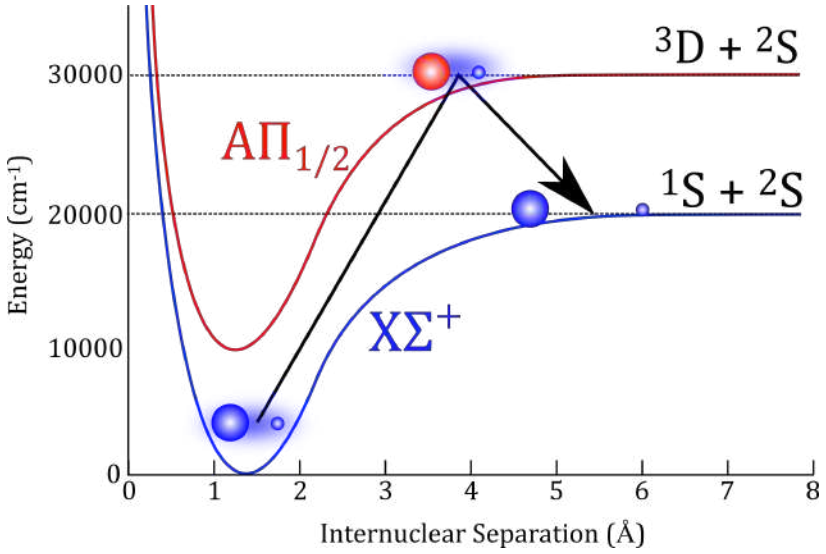

Figure 8.1: Photodissociation scheme to fragment BaH via 2-photon process to the ground state potential continuum. Energy separation and internuclear distance from Ref. [73].

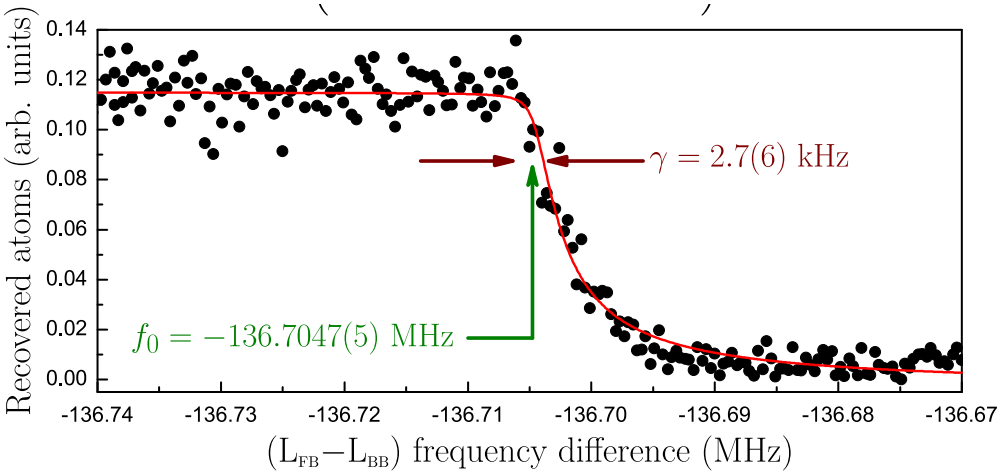

Figure 8.2: From Mickey McDonald's Thesis (Ref. [87]). Demonstration of high resolution 2-photon dissociation with a linewidth corresponding to ≈ 14 nK excess energy deposited onto the atoms. This falls well within the constraints of the dissociation scheme described.

AMO techniques [146].

8.2 Final Remarks

The field of precision measurement with ultracold molecules is in its early stages, but shows much promise as a future direction in AMO physics. In this thesis, I have detailed the design and construction of a buffer-gas cooled beam source and the surrounding apparatus for laser cooling a single diatomic species. It is important to extend the techniques here and in other molecule cooling experiments to new diatomic molecules. Doing so will expand the toolbox available for new experiments and could uncover other molecules to work with.

In this thesis we demonstrated that high density molecular beams are possible with hydrides, which was not evident from previous attempts with LiH or CaH. Continuing this work to creating a magneto-optical trap would provide theorists a new class of molecule to test the precision of *ab initio* calculations. We saw in the preceding section how BaH offers a novel route towards trapped samples of ultracold hydrogen.

The work in this thesis took over 3 years from conception to date, and remains at least a year from a magneto-optical trap. The long timescale is indicative of the breadth of expertise and practical know-how needed to work with molecules. It points to the complex challenges presented in working with molecules - even just holding onto them; each experiment like trying to hold water in your hands.

It has been 30 years since Raab and co-workers published in PRL a magneto-optical trap of sodium atoms [147]. In that time, the atomic MOT has become the workhorse of atomic physics, now so ubiquitous that complete educational kits are available for purchase. So while it is easy to turn a jealous eye towards atomic experiments, a quick look at the possible uses of ultracold molecules is reassuring - ultracold chemistry, dipolar physics, variation of unmonitored fundamental constants, tests of nano-scale gravity, searches for electron electric dipole moment, precision molecular clocks...the list is as long as it is exciting.

Appendix

Appendix A

Relevant Properties of BaH

State	$A^2\Pi_{1/2}$	$B^2\Sigma^+$	H(1S-2P)
λ (nm)	1060.8	905.3	121
τ (ns)	136.2	120.3	1.6
N_2	53794	2258	∞
$T_D(\mu\text{K})$	28.0	31.7	2349
$T_r(\mu\text{K})$	0.124	0.170	1285
a_{max} (m/s^2)	9932	131166	10^9
v_c(m/s)	14	16	1211

Table A.1: Adapted from Ref. [70]. Table of relevant laser cooling parameters as predicted by *ab initio* models. A comparison with direct laser cooling in H atoms is shown in the last column. N_2 is the number of cycles possible before population falls by 90%, with 2 lasers to close vibrational losses in BaH, and an additional repump in H. T_D and T_r are the Doppler and recoil temperatures; $a_{max} = \frac{\hbar k\gamma}{2M}$ is the maximum acceleration due to optical forces; $v_c = \sqrt{2a_{max}x}$ is the capture velocity for a MOT, for a beam diameter of 1 cm.

State	$X^2\Sigma^+$	$A^2\Pi_{1/2}$	$B^2\Sigma^+$	$E^2\Pi_{1/2}$
T_e	0.0	9457.45	11092.5926	14856.63369
ω_e	1168.42509	1110.55	1088.898	1221.912
$\omega_e \times x_e$	14.61366	15.29	15.4712	15.6682
$\omega_e \times y_e$	0.028253	0.0	0.0237	-
B_e	3.3824355	3.278	3.268795	3.520609
α_e	0.06565865	0.07283	0.070609	0.065973
D_e	1.124169×10^{-4}	1.21×10^{-4}	1.15855×10^{-4}	1.167801×10^{-4}
γ_ν	0.192063	nd	-4.75396	-
H	3.0061×10^{-9}	nd	2.6267×10^{-9}	2.8399×10^{-9}
q_v	-		-	0.003475
q_{Dv}	-		-	-0.01552×10^{-4}
q_{Hv}	-		-	0.369×10^{-9}
p_v	-	-5.307	-	0.872460
p_{Dv}	-	13.8×10^{-4}	-	-1.88222×10^{-4}
p_{Hv}	-	-4.9×10^{-9}	-	12.73×10^{-9}
Source	[126]	[71, 111]	[72]	[126]

Table A.2: Molecular constants for the relevant electronic states of BaH. All values given in cm^{-1}.

Appendix B

Soldering Helium Bobbins

The helium bobbins are sections of the helium line that are wrapped around a copper rod that is thermally anchored to a cold part of the experiment. They are a crucial element to ensure that the helium gas going into the cell is as cold as possible. To this end, the bobbins must have good thermal contact across the whole area between the pipe and the rod, and they should be close to the PTR cold finger. the best way to meet the first condition is to use silver solder to affix the copper pipe to the copper rod. Some tips we accumulated are:

- It seems that smaller diameter pipe is better. Anecdotally, the higher impedance in the line corresponds to a better thermalization of the Helium gas as it approaches the cell. Our latest iteration uses a 3/16" diameter OFHC copper pipe.
- To make the coil, wind around an object that is slightly smaller in diameter than the core you will use. So for a 1" core, coil around a 7/8" cylinder.
- The problem with smaller pipe sizes is that it is prone to kinking and collapsing when you try and bend it, in which case you need to cut off that piece and start again. Our method is to first use the tube bender to create a half turn of the coil, then use this as the starting point to wrap around the cylinder.

- Thoroughly clean the parts before soldering.
- Use a lower temperature flame to heat the parts evenly - no need to go crazy hot with the low temperature silver solder.
- To begin with, heat evenly, trying to get the whole rod-coil assembly hot before using any solder.
- Use a solid amount of flux - remember, all the oxidized crap, not to mention the dirt that you didn't clean off, will cause bad solder connections and eventually outgas into the cryostat. We found the brand, 'Stay-Clean' works pretty well.
- Your solder works as a fixed point thermometer. Touch the solder directly to the copper-if it is hot enough, it will melt.
- If you've heated things evenly, the solder should run down the bobbin and start pooling near the bottom. If a lot starts pooling, it means that there are a lot of gaps between the coil and core.

Appendix C

Yb Characterization

Ytterbium is an excellent ablation source, producing so much output from each shot that it is not even necessary to flow Helium in order to see an absorption signal. While this can be useful for initial diagnostics, it is not ideal for optimizing the system for BaH. Nevertheless, the strong signal allowed us to characterize the cell performance. Initial spectroscopy (Figure C.1) of the $^1S_0 - ^1P_1$ line at 399 nm shows good agreement with the isotopic distribution measured by Das *et al.* in Figure C.3 [148], and elsewhere. Additionally, we can examine the time resolved behavior of atoms (Figure C.2) to check the plume length and a sense for the temperature distribution in different parts of the beam.

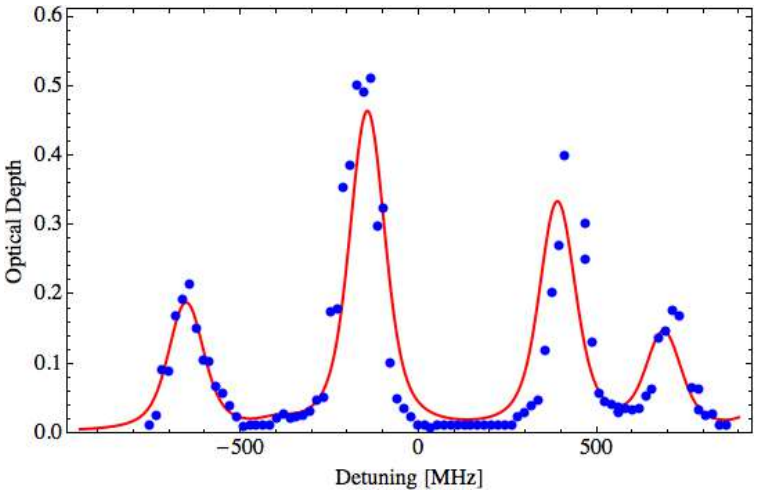

Figure C.1: Spectroscopy of buffer-gas cooled ablated Yb inside of the cryogenic cell. The fit takes into account the natural abundances, transition strengths and inhomogenous Doppler broadening. The temperature is fit to 7.3 K.

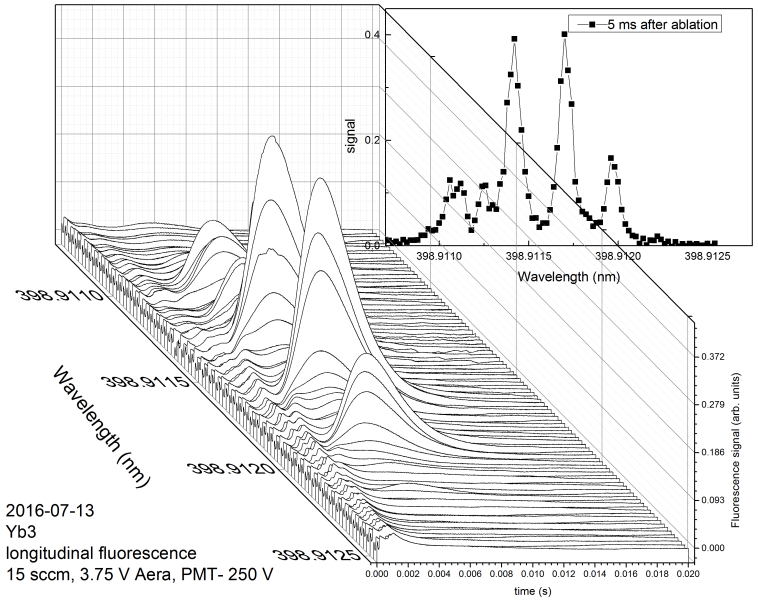

Figure C.2: Time-resovled spectroscopy of buffer-gas cooled ablated Yb inside of the cryogenic cell.

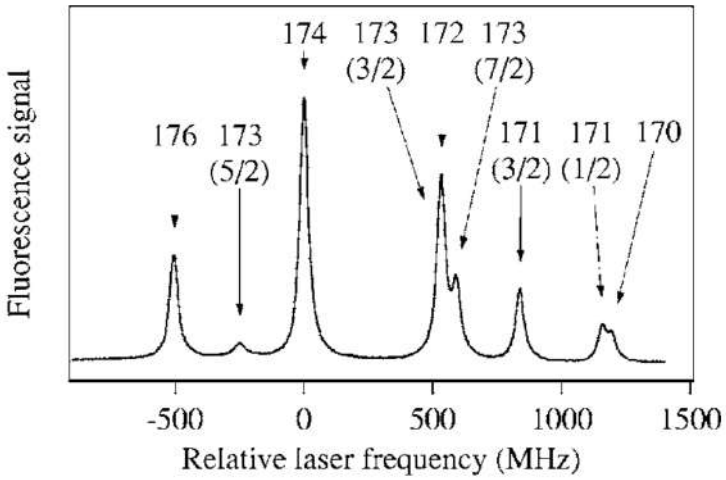

Figure C.3: Doppler free measurements of the isotopic distribution of Yb on the ${}^1S_0 - {}^1P_1$ line [148].

The fit function in Figure C.1 accounts for the natural linewidth and for the inhomogenous Doppler broadening via the Voigt function,

$$\text{Voigt}[x,\delta,\sigma] = \frac{\exp\left[\frac{(-ix+\delta)^2}{2\sigma^2}\right]\text{Erfc}\left[\frac{(-ix+\delta)}{\sqrt{2}\sigma}\right] + \text{Exp}\left[\frac{(Ix+\delta)^2}{2\sigma^2}\right]\text{Erfc}\left[\frac{ix+\delta}{\sqrt{2}\sigma}\right]}{2\sqrt{2\pi}\sigma} \tag{C.0.1}$$

where δ is the HWHM of the Lorentzian function, and σ^2 is the variance of the Gaussian distribution. The ${}^1S_0 - {}^1P_1$ has natural linewidth, Γ= 30.5 MHz according to NIST's database, and so $\delta = \Gamma/2$. The value of σ for a Gaussian frequency response comes from the expression for the typical Doppler broadening due to the Maxwell-Boltzmann distribution and is defined, $\sigma_\nu = \sqrt{k_B T/(m\lambda_0^2)}$.

The resulting fit function is found by taking a weighted sum of the Voigt functions for each isotope and hyperfine transition, with a detuning defined arbitrarily from the larger ^{174}Yb isotope. Compactly, each weight w_A is given by,

$$w_A = W(F') \cdot N_A, \tag{C.0.2}$$

Isotope	Natural Abundance (%)	Hyperfine Transition	Transition Strength
^{168}Yb	0.13		1
^{170}Yb	3.05		1
^{171}Yb	14.3	1/2→3/2	2/3
		1/2→1/2	1/3
^{172}Yb	21.9		1
^{173}Yb	16.1	5/2→3/2	2/9
		5/2→5/2	1/3
		5/2→7/2	4/9
^{174}Yb	31.8		1
^{176}Yb	12.7		1

Table C.1: Isotopes of Yb and strengths of components of the $^1S_0 \rightarrow ^1 P_1$ line.

where N_A is natural abundance of the isotope A, and W is a rotational transition strength factor which depends on the initial and final hyperfine states. This factor is 1 for all the bosonic isotopes [Metcalf eq (4.33)]. The values of N_A, W and the detunings are listed in Table C.1 , with data taken form values sourced from the NIST Handbook of Basic Atomic Spectroscopic Data (NIST-HoBASD) and from [Phys Rev A 72, 032506 (2005)]:

Yb beams typically exhibited some unusual features in the TOF absorption spectra; an example is shown for the tri-modal absorption trace of ^{174}Yb shown in Figure. C.4, which is typical of Yb data taken at high fluence. In this trace, the three 'peaks' occur at different timescales, most likely resulting from different stages of the ablation process. The first peak is around 0.29 ms and it is very narrow, the second is at about 0.56 ms and the third at about 1 ms. Taking a spectrum across the transition, we reanalyze the absorption data by integrating the signal of the three colored areas.

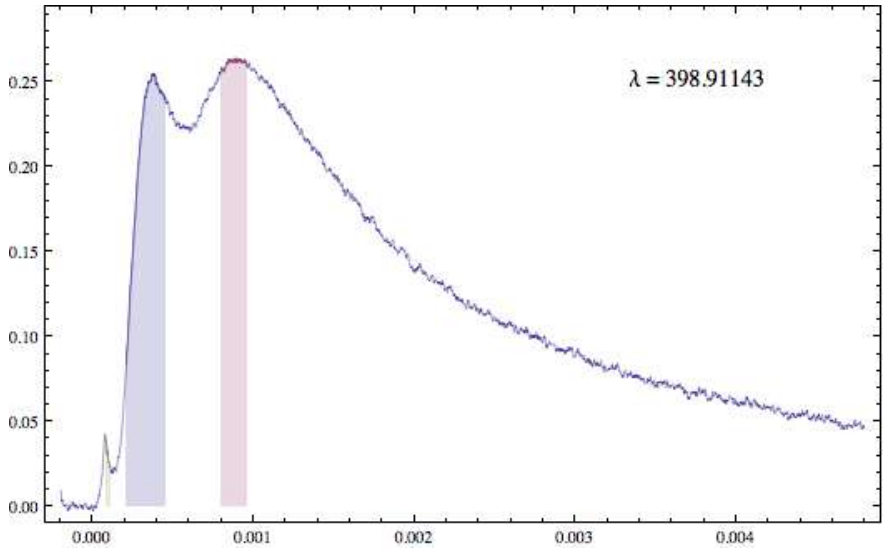

Figure C.4: Trimodal absorption TOF profile for Yb beam on the ^{1}74Yb peak. Data is taken at 2 sccm with 100% ablation power. The colors highlight the three peaks with rather different timescales. Data was analyzed by integrating the absorption signal within the colored areas.

The resulting spectra are plotted in Figure C.4.

Appendix D

Schematics

D.1 Cryostat sections

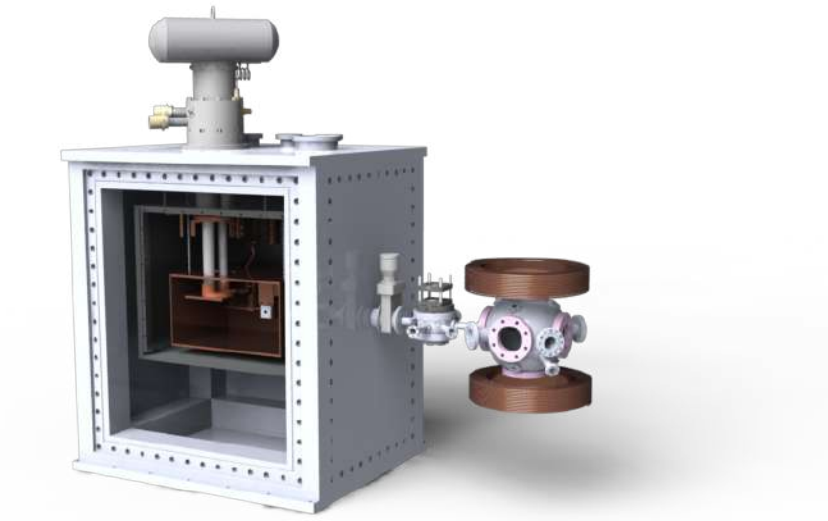

Figure D.1

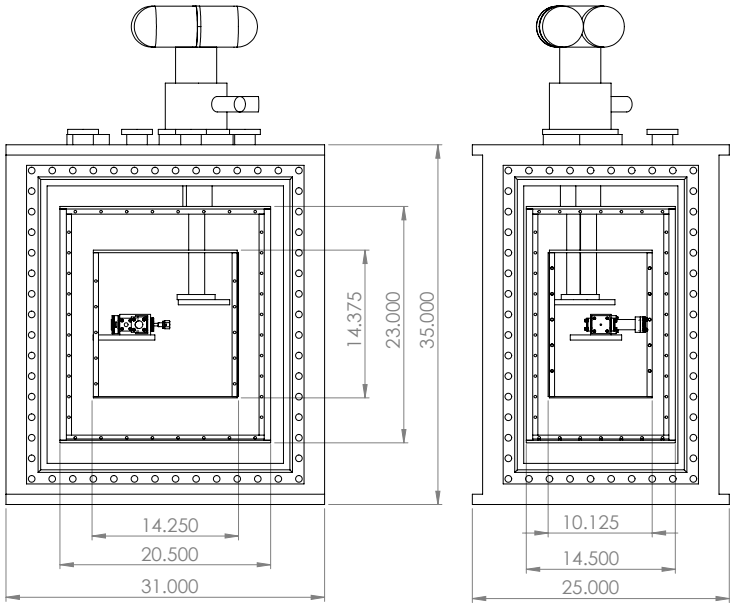

Figure D.2

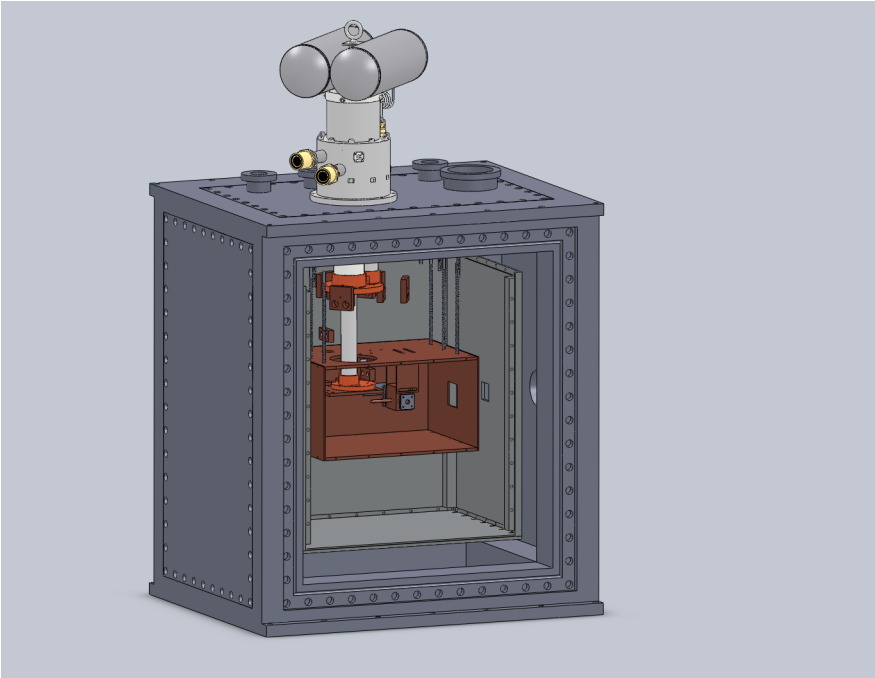

Figure D.3

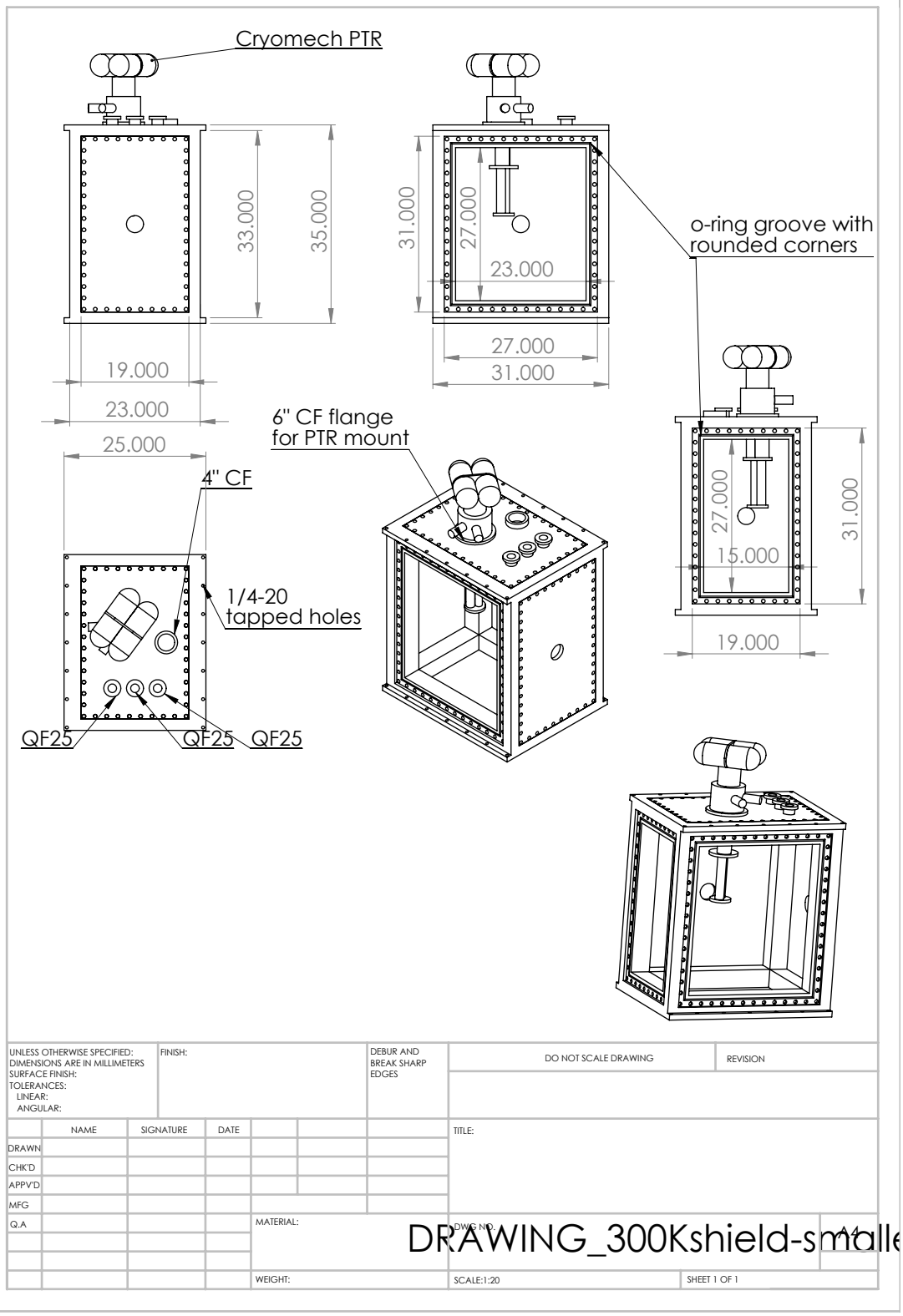
Cryomech PTR
33.000
35.000
19.000
23.000
25.000
4" CF
1/4-20
tapped holes
QF25
QF25
QF25
6" CF flange
for PTR mount
31.000
27.000
23.000
27.000
31.000
o-ring groove with
rounded corners
27.000
15.000
31.000
19.000
UNLESS OTHERWISE SPECIFIED:
DIMENSIONS ARE IN MILLIMETERS
SURFACE FINISH:
TOLERANCES:
LINEAR:
ANGULAR:
FINISH:
DEBUR AND
BREAK SHARP
EDGES
DO NOT SCALE DRAWING
REVISION
NAME
SIGNATURE
DATE
TITLE:
DRAWN
CHK'D
APPV'D
MFG
Q.A
MATERIAL:
DWG NO.
A4
WEIGHT:
SCALE:1:20
SHEET 1 OF 1
DRAWING_300Kshield-smalle

Figure D.4

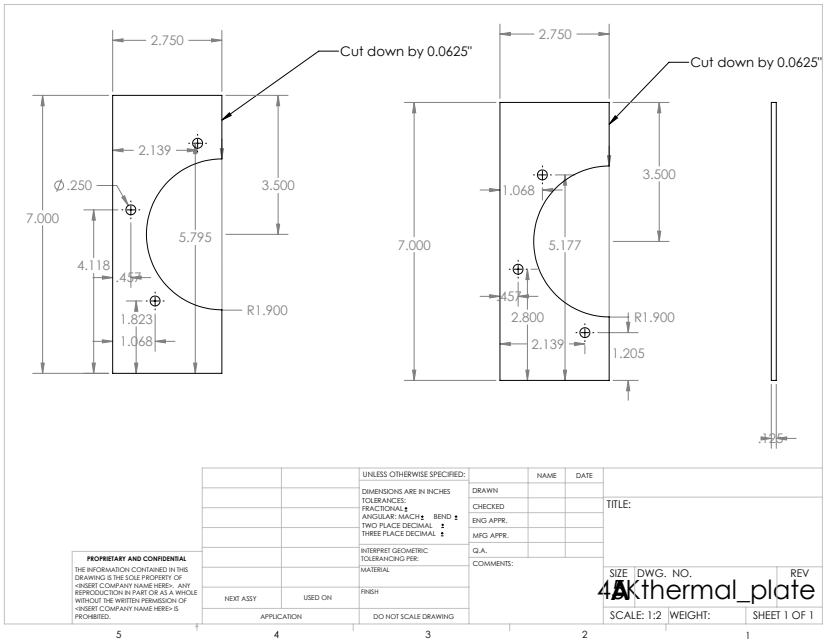

Figure D.5

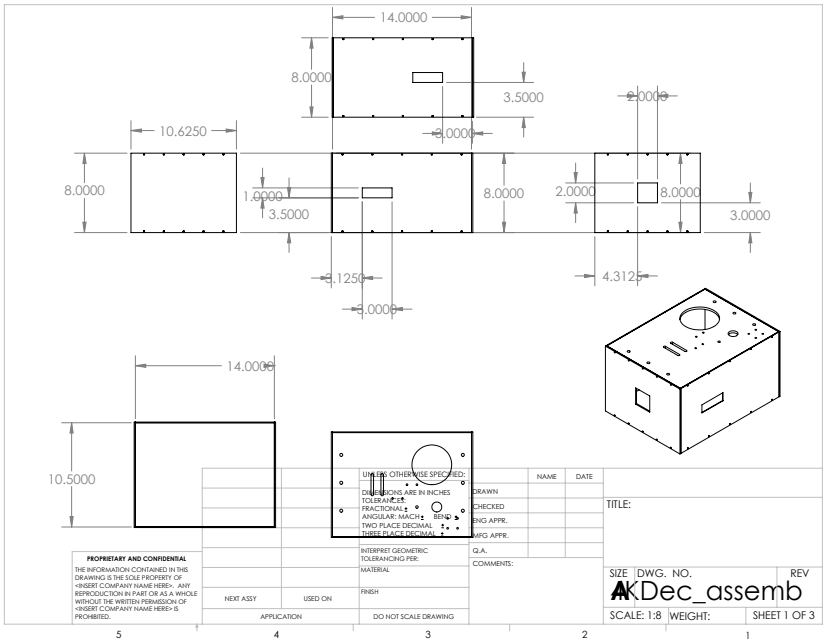

Figure D.6

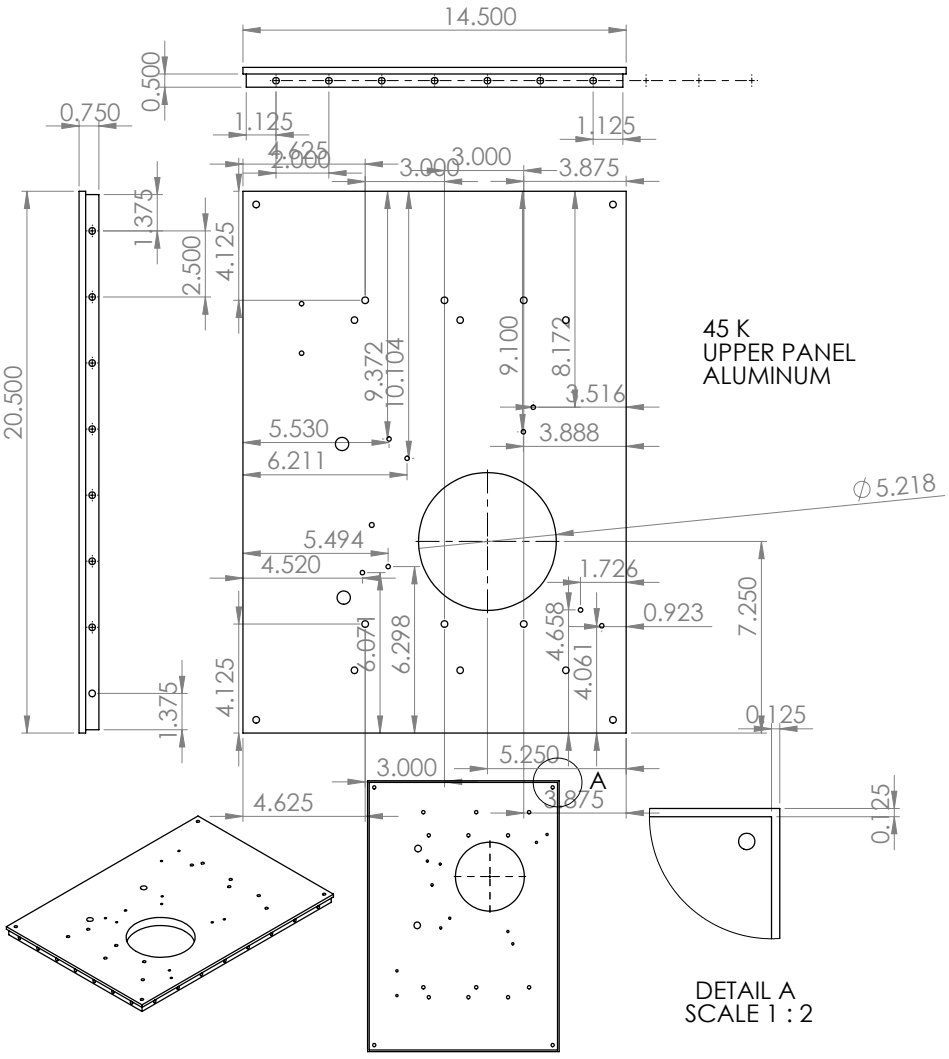
14.500
0.500
0.750
1.125
1.125
4.625
2.000
3.000
3.000
3.875
1.375
2.500
4.125
20.500
9.372
10.104
9.100
8.172
3.516
3.888
5.530
6.211
45 K
UPPER PANEL
ALUMINUM
∅5.218
5.494
4.520
1.726
0.923
7.250
6.071
6.298
4.658
4.061
4.125
1.375
0.125
3.000
5.250
A
4.625
3.875
0.125
DETAIL A
SCALE 1 : 2

Figure D.7

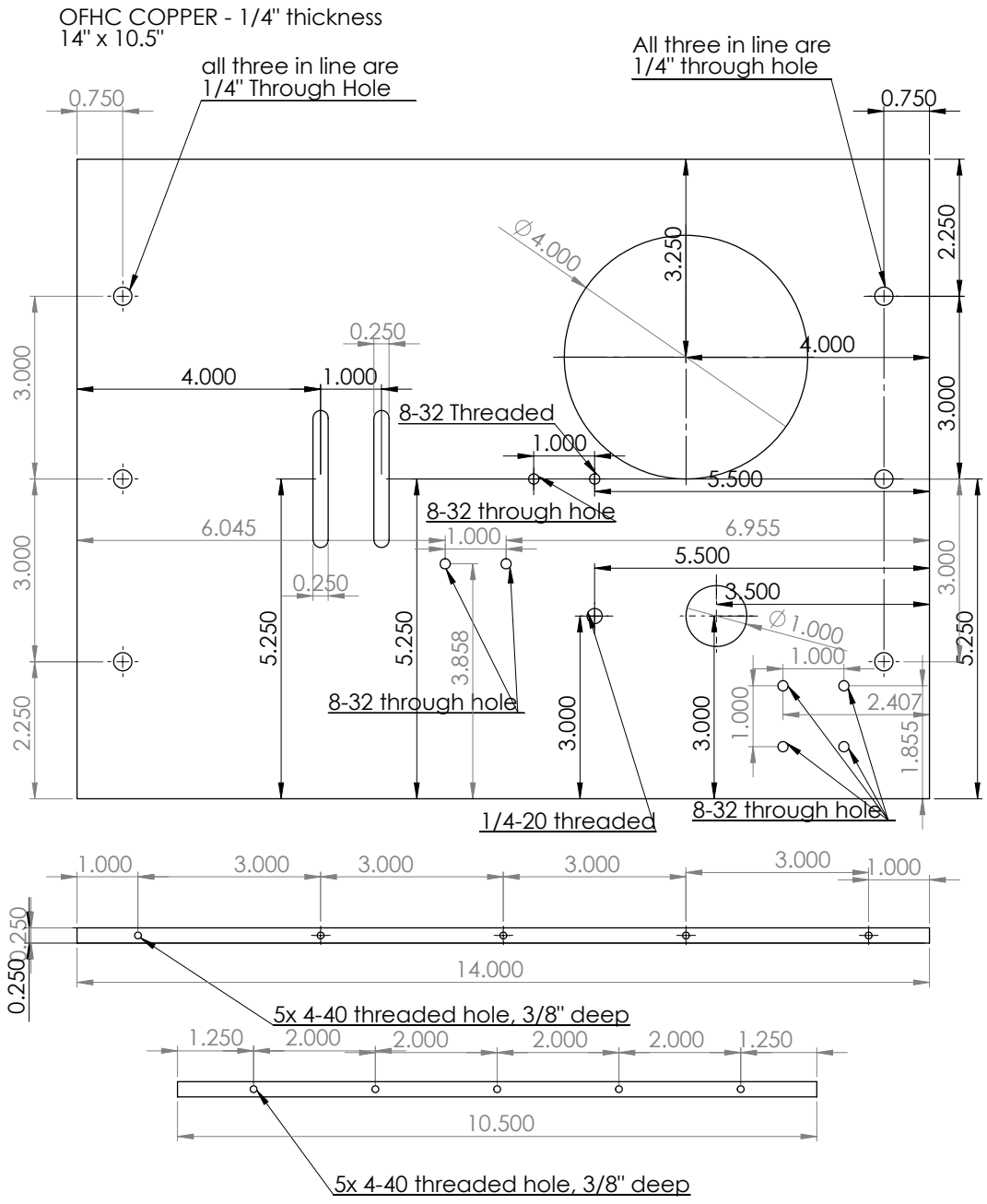
OFHC COPPER - 1/4" thickness
14" x 10.5"
all three in line are
1/4" Through Hole
All three in line are
1/4" through hole
0.750
0.750
Ø4.000
3.250
2.250
4.000
0.250
4.000
1.000
3.000
8-32 Threaded
1.000
3.000
5.500
8-32 through hole
6.045
1.000
6.955
5.500
3.000
0.250
3.500
Ø1.000
5.250
5.250
3.858
5.250
1.000
8-32 through hole
2.407
2.250
3.000
3.000
1.000
1.855
1/4-20 threaded
8-32 through hole
1.000
3.000
3.000
3.000
3.000
1.000
0.250
0.250
14.000
5x 4-40 threaded hole, 3/8" deep
1.250
2.000
2.000
2.000
2.000
1.250
10.500
5x 4-40 threaded hole, 3/8" deep

Figure D.8

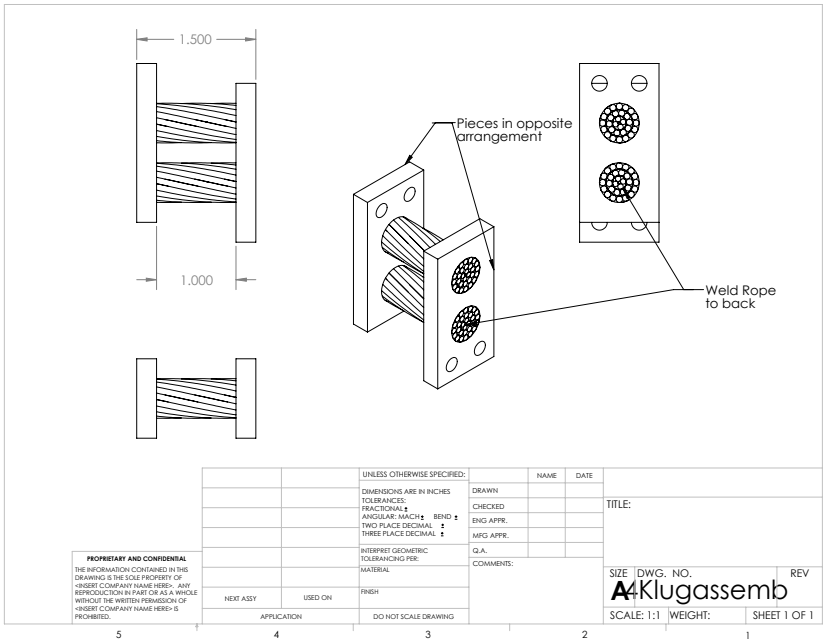

Figure D.9

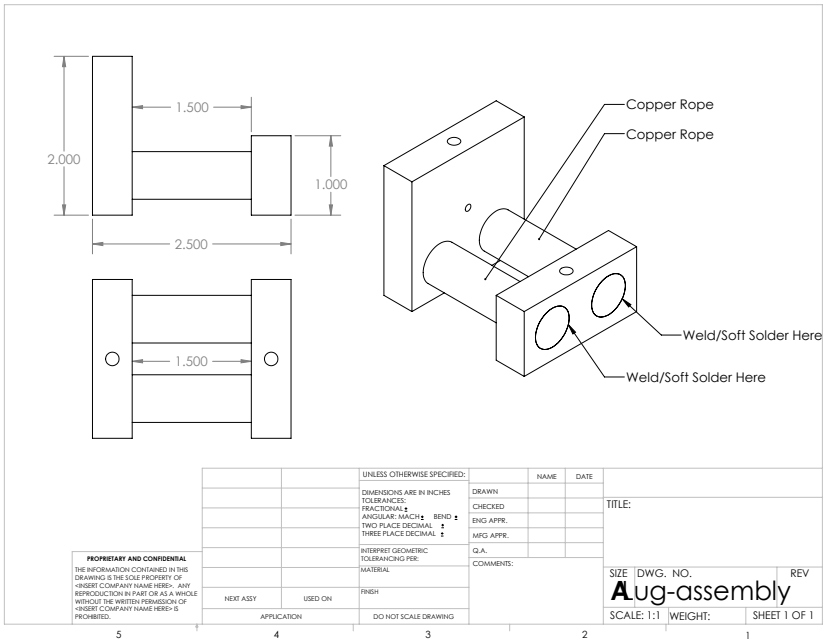

Figure D.10

D.2 Cell Designs

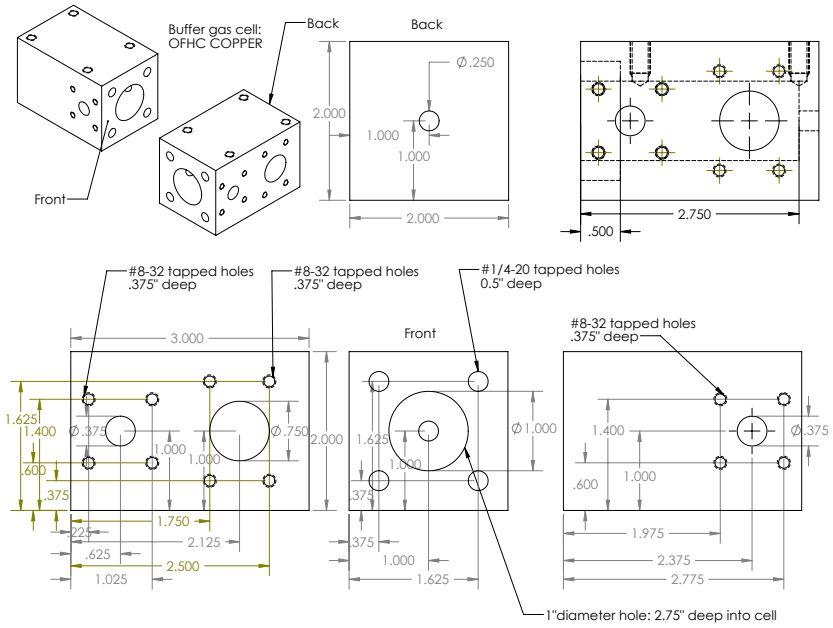

Figure D.11

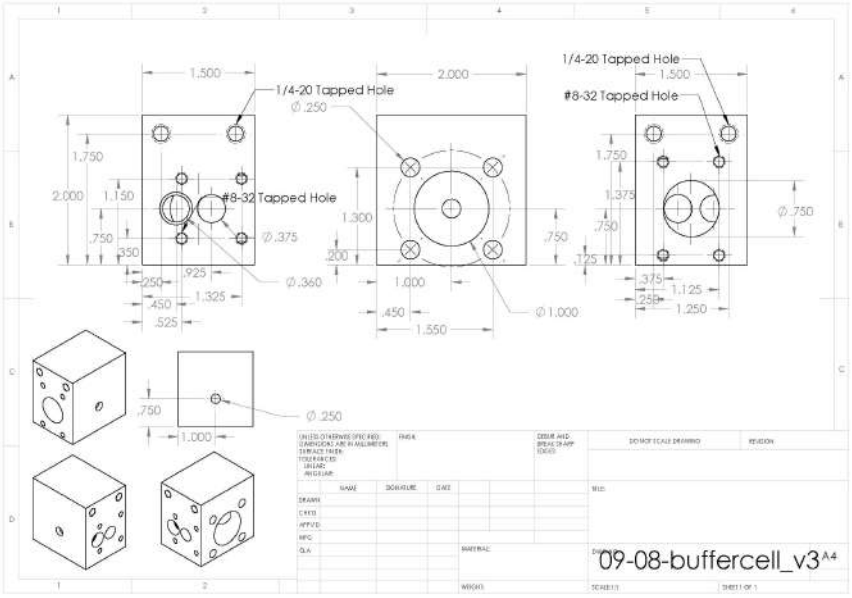

Figure D.12

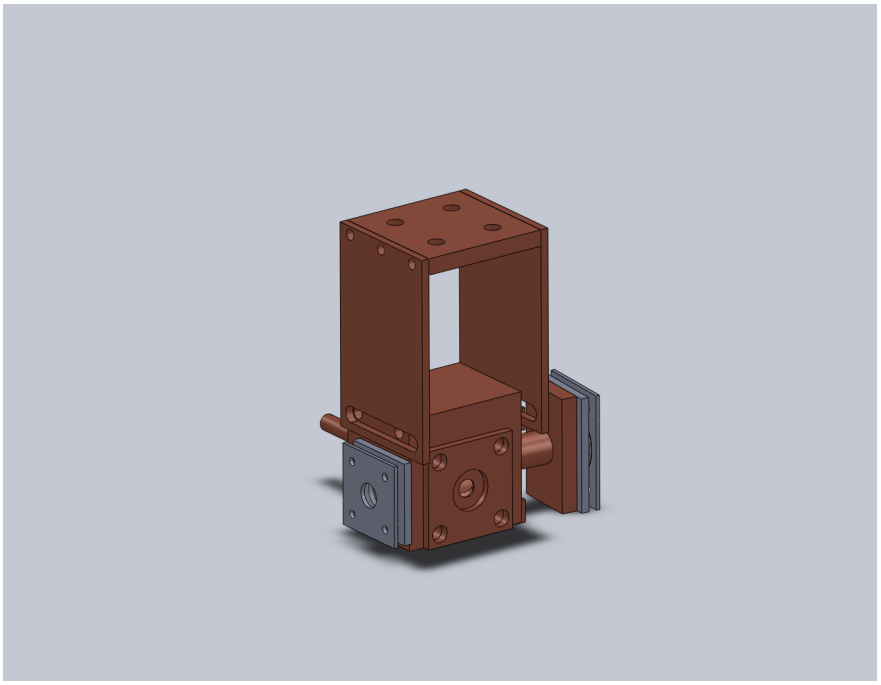

Figure D.13

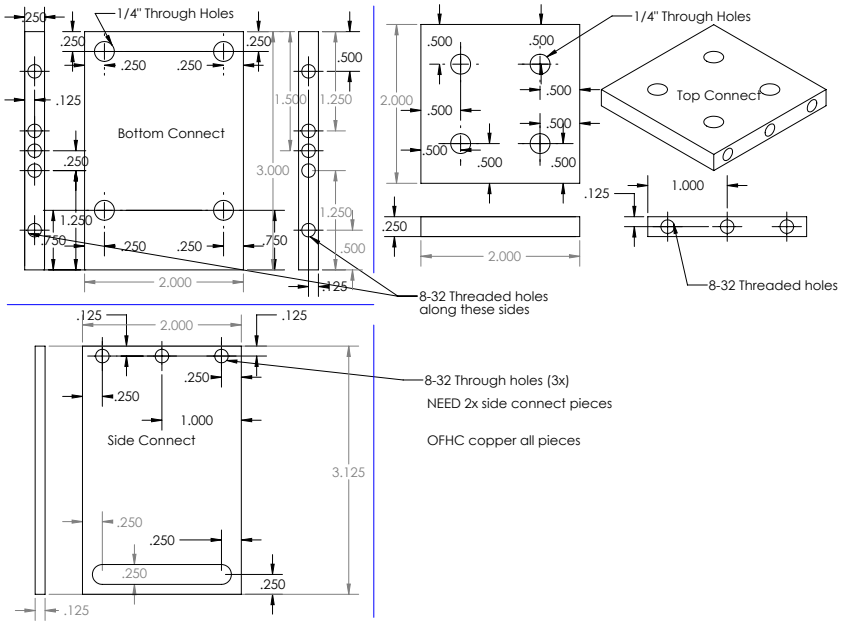

Figure D.14

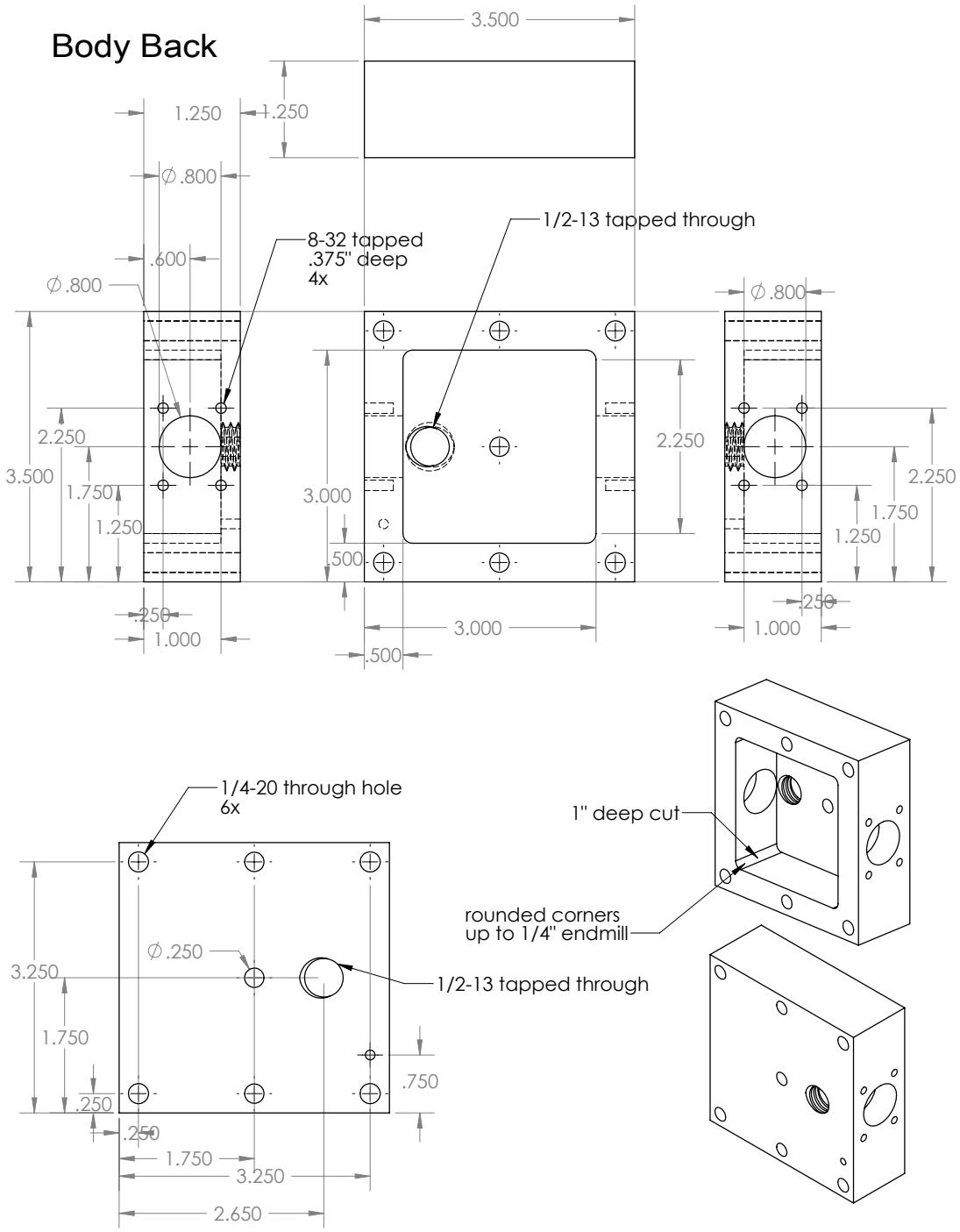
Body Back
3.500
1.250
1.250
∅.800
8-32 tapped
.375" deep
4x
1/2-13 tapped through
.600
∅.800
∅.800
2.250
3.500
1.750
1.250
3.000
2.250
.500
2.250
1.750
1.250
.250
1.000
3.000
.500
.250
1.000
1/4-20 through hole
6x
1" deep cut
rounded corners
up to 1/4" endmill
∅.250
3.250
1/2-13 tapped through
1.750
.750
.250
.250
1.750
3.250
2.650

Figure D.15

Body Front Panel

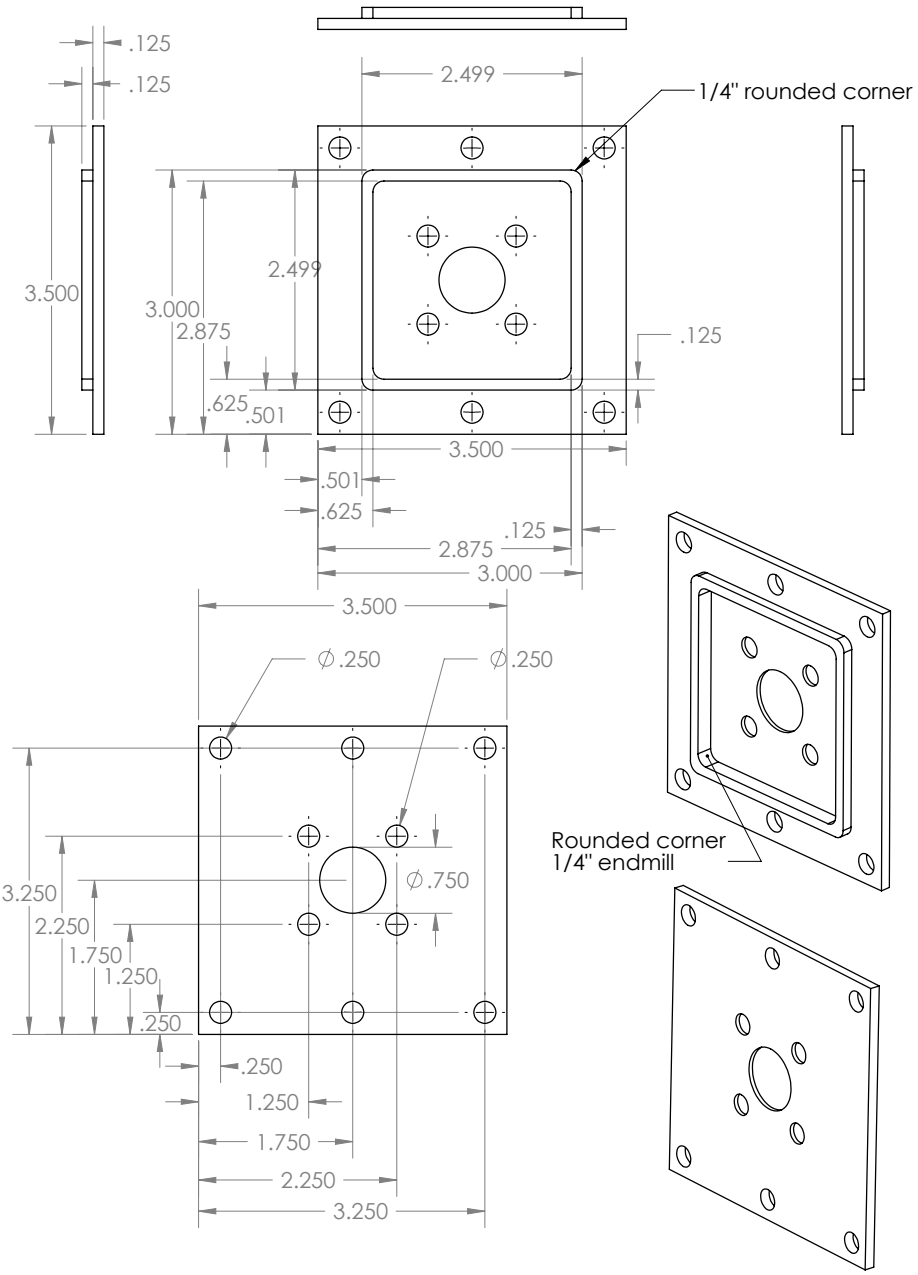

Figure D.16

pieces.PDF

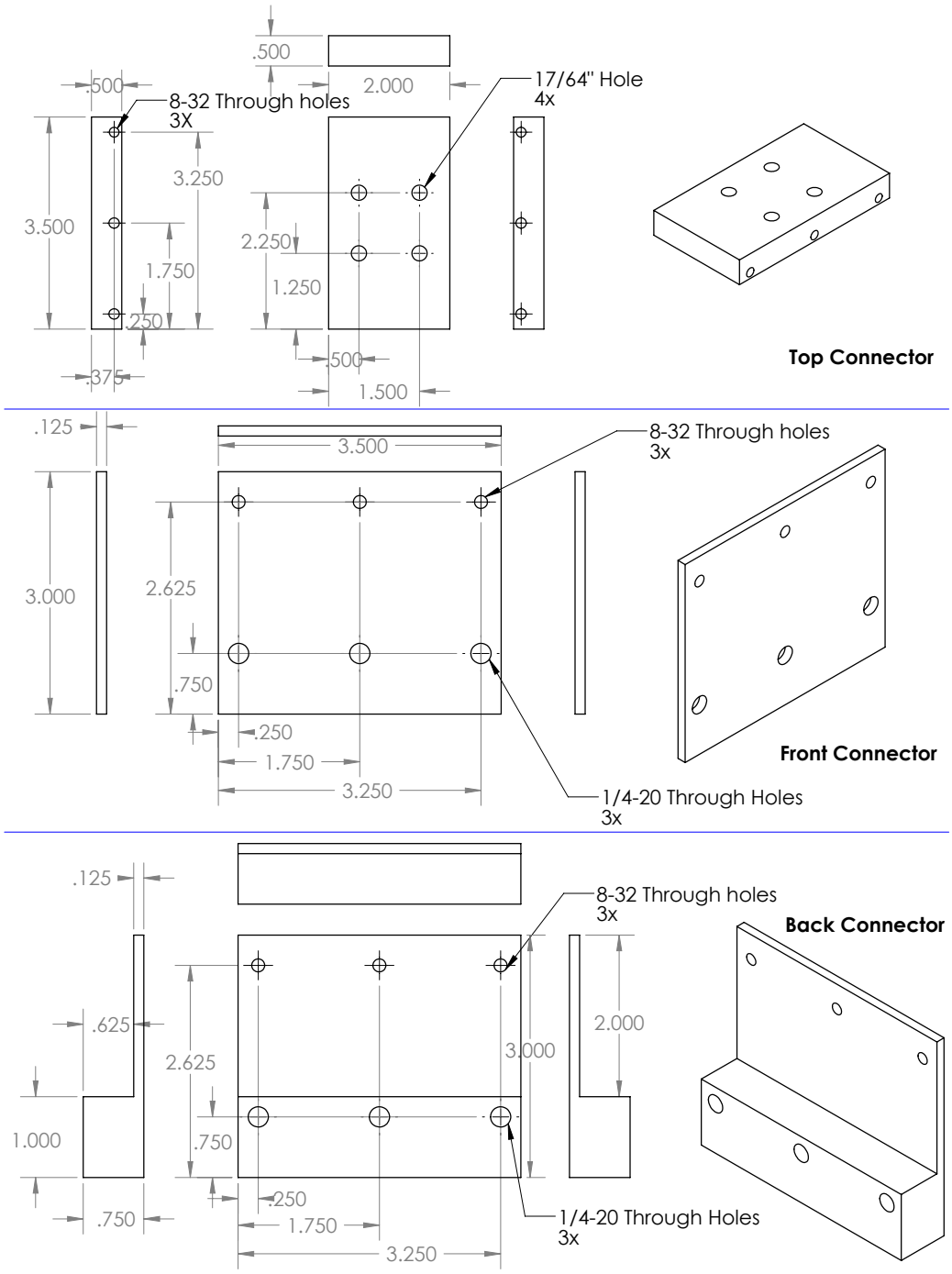

Figure D.17

Appendix E

Pictures

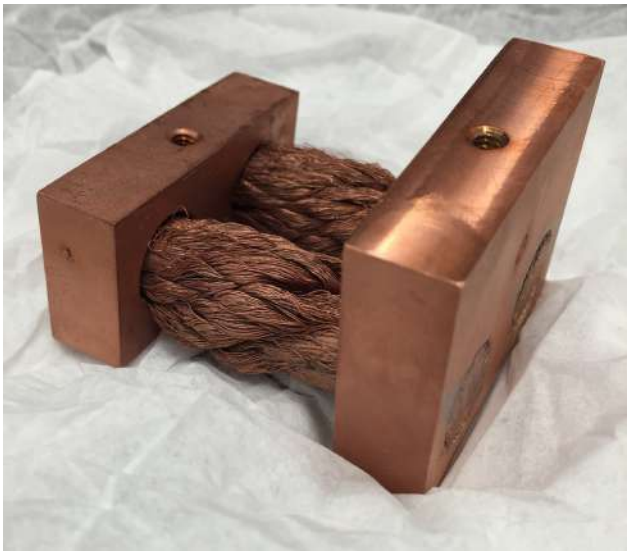

Figure E.1: Copper rope lug for thermal contact.

Figure E.2: Copper rope lug for thermal connection on the 4K stage.

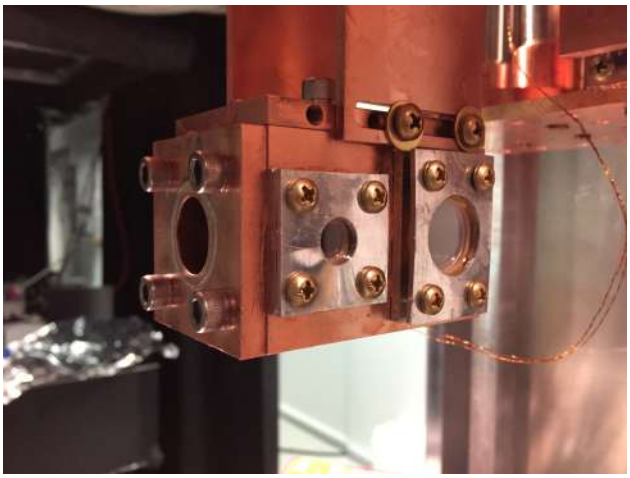

Figure E.3: Original buffer-gas cell V1.

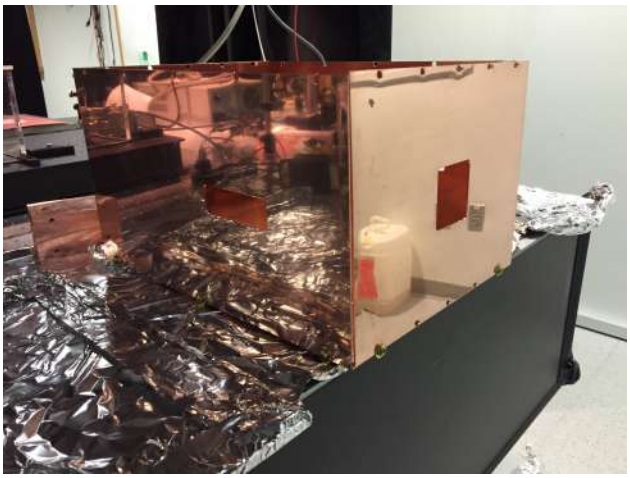

Figure E.4: 4K shield box showing reflective surfaces.

Figure E.5: Soldered copper bobbin for He gas thermalization.

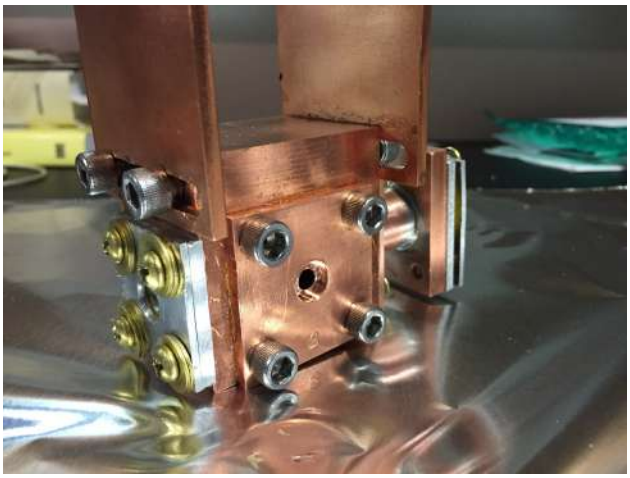

Figure E.6: Current buffer-gas cell V3 with best performance.

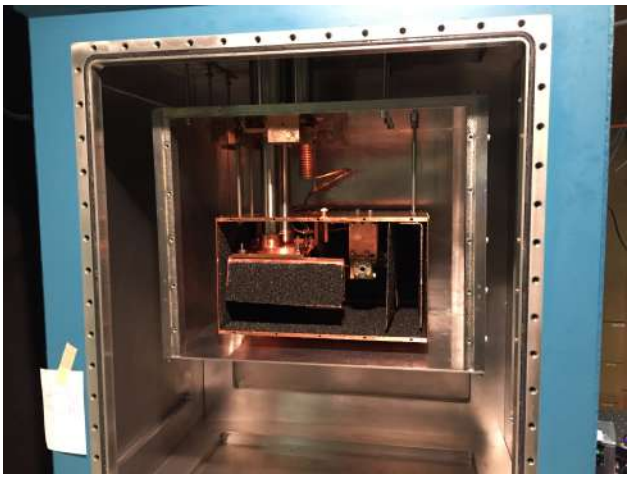

Figure E.7: Cryostat for buffer gas cooling.

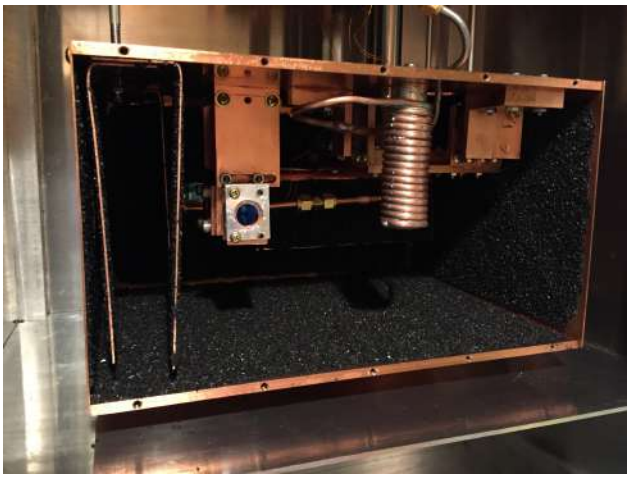

Figure E.8: Cell V3 in apparatus with coconut charcoal.

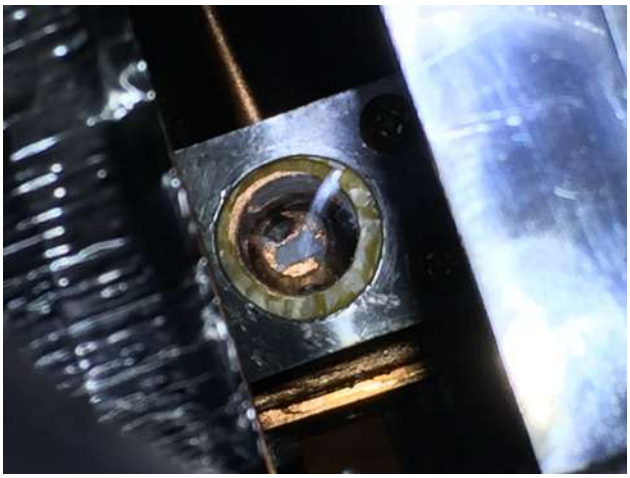

Figure E.9: BaH2 and Yb targets inside cell.

Bibliography

[1] J. F. Barry, D. J. McCarron, E. B. Norrgard, M. H. Steinecker, and D. DeMille. Magneto-optical trapping of a diatomic molecule. *Nature*, 512:286–289, 2014.

[2] S. Truppe, H. J. Williams, M. Hambach, L. Caldwell, N. J. Fitch, E. A. Hinds, B. E. Sauer, and M. R. Tarbutt. Molecules cooled below the Doppler limit. *Nat. Phys.*, 13:1173–1176, 2017.

[3] L. Anderegg, B. Augenbraun, E. Chae, B. Hemmerling, N. R. Hutzler, A. Ravi, A. Collopy, J. Ye, W. Ketterle, and J. M. Doyle. Radio Frequency Magneto-Optical Trapping of CaF with High Density. *Phys. Rev. Lett.*, 119(103201):1–5, 2017.

[4] B. J. Bloom, T. L. Nicholson, J. R. Williams, S. L. Campbell, M. Bishof, X. Zhang, W. Zhang, S. L. Bromley, and J. Ye. An optical lattice clock with accuracy and stability at the 10-18 level. *Nature*, 506(7486):71–75, 2014.

[5] L. W. Cheuk, M. A. Nichols, M. Okan, T. Gersdorf, V. V. Ramasesh, W. S. Bakr, T. Lompe, and M. W. Zwierlein. Quantum-gas microscope for fermionic atoms. *Phys. Rev. Lett.*, 114(19):1–5, 2015.

[6] I. Bloch. Ultracold quantum gases in optical lattices. *Nat. Phys.*, 1(1):23–30, 2005.

[7] J. Voit. One-dimensional Fermi liquids. *Reports Prog. Phys.*, 58(9):977–1116, 1995.

[8] F. Dalfovo, S. Giorgini, L. P. Pitaevskii, and S. Stringari. Theory of Bose-Einstein condensation in trapped gases. *Rev. Mod. Phys.*, 71(3):463–512, 1999.

[9] J. R. Anglin and W. Ketterle. Bose-Einstein condensation of atomic gases. *Nature*, 416(6877):211–218, 2002.

[10] B. H. McGuyer, M. McDonald, G. Z. Iwata, M. G. Tarallo, A. T. Grier, F. Apfelbeck, and T. Zelevinsky. High-precision spectroscopy of ultracold molecules in an optical lattice. *New J. Phys.*, 17, 2015.

[11] S. A. Moses, J. P. Covey, M. T. Miecnikowski, D. S. Jin, and J. Ye. New frontiers for quantum gases of polar molecules. *Nat. Phys.*, 13(1):13–20, 2017.

[12] L. D. Carr, D. DeMille, R. V. Krems, and J. Ye. Cold and ultracold molecules: science, technology and applications. *New J. Phys.*, 11(5):055049, may 2009.

[13] J. W. Park, S. A. Will, and M. W. Zwierlein. Ultracold Dipolar Gas of Fermionic Molecules in Their Absolute Ground State. *Phys. Rev. Lett.*, 114(205302):1–5, 2015.

[14] M. Aymar and O. Dulieu. The electronic structure of the alkaline-earth-atom (Ca, Sr, Ba) hydride molecular ions. *J. Phys. B*, 45:215103, 2012.

[15] M. D. Di Rosa. Laser-cooling molecules: Concept, candidates, and supporting hyperfine-resolved measurements of rotational lines in the A-X(0,0) band of CaH. *Eur. Phys. J. D*, 31(2):395–402, 2004.

[16] M. Gacesa and R. Côté. Photoassociation of ultracold molecules near a Feshbach resonance as a probe of the electron proton mass ratio variation. *J. Mol. Spectrosc.*, 300:124–130, 2014.

[17] The ACME Collaboration, J. Baron, W. C. Campbell, D. DeMille, J. M. Doyle, G. Gabrielse, and Y. V. Gurevich. Order of Magnitude Smaller Limit on the Electric Dipole Moment of the Electron. *Science*, 343, 2014.

[18] S. Chervenkov, X. Wu, J. Bayerl, A. Rohlfes, T. Gantner, M. Zeppenfeld, and G. Rempe. Continuous centrifuge decelerator for polar molecules. *Phys. Rev. Lett.*, 112(1):1–5, 2014.

[19] I. Kozyryev and N. R. Hutzler. Precision Measurement of Time-Reversal Symmetry Violation with Laser-Cooled Polyatomic Molecules. *Phys. Rev. Lett.*, 119(13):1–6, 2017.

[20] I. Kozyryev, L. Baum, K. Matsuda, B. L. Augenbraun, L. Anderegg, A. P. Sedlack, and J. M. Doyle. Sisyphus Laser Cooling of a Polyatomic Molecule. *Phys. Rev. Lett.*, 118(173201):1–6, 2017.

[21] B. H. McGuyer, M. McDonald, G. Z. Iwata, M. G. Tarallo, W. Skomorowski, R. Moszynski, and T. Zelevinsky. Precise study of asymptotic physics with subradiant ultracold molecules. *Nat. Phys.*, 11(1):32–36, 2015.

[22] M. G. Kozlov and L. N. Labzowsky. Parity violation effects in diatomic molecules. *J. Phys. B*, 28:1933–1961, 1995.

[23] E. B. Norrgard, E. R. Edwards, D. J. McCarron, M. H. Steinecker, D. DeMille, Shah Saad Alam, S. K. Peck, N. S. Wadia, and L. R. Hunter. Hyperfine structure of the $B^3\Pi_1$ state and predictions of optical cycling behavior in the X→B transition of TlF. *Phys. Rev. A*, 95(6):1–12, 2017.

[24] V. V. Flambaum and M. G. Kozlov. Enhanced Sensitivity to the Time Variation of the Fine-Structure Constant and m_p/m_e in Diatomic Molecules. *Phys. Rev. Lett.*, 99(15):150801, 2007.

[25] T. Zelevinsky, S. Kotochigova, and J. Ye. Precision test of mass-ratio variations with lattice-confined ultracold molecules. *Phys. Rev. Lett.*, 100(4):1–4, 2008.

[26] T. Fukuyama. Searching for New Physics Beyond the Standard Model in Electric Dipole Moment. *Int. J. Mod. Phys. A*, 27(16):1230015, 2012.

[27] Y. Nakai and M. Reece. Electric dipole moments in natural supersymmetry. *J. High Energy Phys.*, 2017(8), 2017.

[28] E. A. Hinds. Testing time reversal symmetry using molecules. *Phys. Scr.*, T70:34–41, 1997.

[29] S. Eckel, P. Hamilton, E. Kirilov, H. W. Smith, and D. Demille. Search for the electron electric dipole moment using Omega-doublet levels in PbO. *Phys. Rev. A*, 87(5):1–19, 2013.

[30] J. J. Hudson, D. M. Kara, I. J. Smallman, B. E. Sauer, M. R. Tarbutt, and E. A. Hinds. Improved measurement of the shape of the electron. *Nature*, 473(7348):493–496, 2011.

[31] J. Lim, J. R. Almond, M. A. Trigatzis, J. A. Devlin, N. J. Fitch, B. E. Sauer, M. R. Tarbutt, and E. A. Hinds. Ultracold molecules for measuring the electron's electric dipole moment. *arXiv:1712.02868*, 2017.

[32] I. E. Dzyaloshinskii, E. M. Lifshitz, and L. P. Pitaevskii. The general theory of van der Waals forces. *Adv. Phys.*, 10(38):165–209, 1961.

[33] A. I. Volokitin and B. N. J. Persson. Near-field radiative heat transfer and noncontact friction. *Rev. Mod. Phys.*, 79:1292–1327, 2007.

[34] J. G. Coelho, J. P. Pereira, and J. C. N. DeAraujo. The influence of quantum vacuum friction on pulsars . *arXiv:1604.00430*, 2016.

[35] P. Ben-abdallah, S. Biehs, and K. Joulain. Many-Body Radiative Heat Transfer Theory. *Phys. Rev. Lett.*, 107(114301):1–5, 2011.

[36] M. D. Lukin, M. Fleischhauer, R. Cote, L. M. Duan, D. Jaksch, J. I. Cirac, and P. Zoller. Dipole Blockade and Quantum Information Processing in Mesoscopic Atomic Ensembles. *Phys. Rev. Lett.*, 87(3):1–4, 2001.

[37] D. Comparat and P. Pillet. Dipole blockade in a cold Rydberg atomic sample. *J. Opt. Soc. Am. B*, 27(6):208–232, 2010.

[38] A. Browaeys, D. Barredo, and T. Lahaye. Experimental investigations of dipole dipole interactions between a few Rydberg atoms. *J. Phys. B*, 49(152001), 2016.

[39] D. Petrosyan and G. Kurizki. Scalable Solid-State Quantum Processor Using Subradiant Two-Atom States. *Phys. Rev. Lett.*, 89(20), 2002.

[40] G. Pupillo, A. Micheli, H. P. Buchler, and P. Zoller. Condensed Matter Physics with Cold Polar Molecules. *arXiv:0805.1896*, 2008.

[41] C. Chin, R. Grimm, P. Julienne, and E. Tiesinga. Feshbach resonances in ultracold gases. *Rev. Mod. Phys.*, 82(June), 2010.

[42] C. H. Wu, J. W. Park, P. Ahmadi, S. Will, and M. W. Zwierlein. Ultracold Fermionic Feshbach Molecules of $^{23}Na^{40}K$. *Phys. Rev. Lett.*, 109(085301), 2012.

[43] M. Heo, T. T. Wang, C. A. Christensen, T. M. Rvachov, D. A. Cotta, J. Choi, Y. Lee, and W. Ketterle. Formation of ultracold fermionic NaLi Feshbach molecules. *Phys. Rev. A*, 86(021602), 2012.

[44] J. J. Zirbel, K. Ni, S. Ospelkaus, J. P. D. Incao, C. E. Wieman, J. Ye, and D S Jin. Collisional Stability of Fermionic Feshbach Molecules. *Phys. Rev. Lett.*, 100(143201), 2008.

[45] K. Enomoto, K. Kasa, M. Kitagawa, and Y. Takahashi. Optical Feshbach Resonance Using the Intercombination Transition. *Phys. Rev. Lett.*, 101(203201), 2008.

[46] G. Thalhammer, M. Theis, K. Winkler, R. Grimm, and J. H. Denschlag. Inducing an optical Feshbach resonance via stimulated Raman coupling. *Phys. Rev. A*, 71(3):1–8, 2005.

[47] K. M. Jones, E. Tiesinga, P. D. Lett, and P. S. Julienne. Ultracold photoassociation spectroscopy : Long-range molecules and atomic scattering. *Rev. Mod. Phys.*, 78(June), 2006.

[48] G. Reinaudi, C. Osborn, M. McDonald, S. Kotochigova, and T. Zelevinsky. Optical Production of Stable Ultracold $^{88}Sr_2$ Molecules. *Phys. Rev. Lett.*, 109(11):1–5, 2012.

[49] W. C. Stwalley and H. Wang. Photoassociation of Ultracold Atoms: A New Spectroscopic Technique. *J. Mol. Spectrosc.*, 195:194–228, 1999.

[50] D. Wang, J. Qi, M. F. Stone, O. Nikolayeva, H. Wang, B. Hattaway, S.D. Gensemer, P. L. Gould, E. E. Eyler, and W. C. Stwalley. Photoassociative Production and Trapping of Ultracold KRb Molecules. *Phys. Rev. Lett.*, 93(243005), 2004.

[51] S. Dutta, J. Lorenz, A. Altaf, D. S. Elliott, and Y. P. Chen. Photoassociation of ultracold LiRb* molecules : Observation of high efficiency and unitarity-limited rate saturation. *Phys. Rev. A*, 89(020702):1–5, 2014.

[52] L. Dunoyer. Sur la realisation d'un rayonnement materiel d'origine purement thermique. *Le Radium*, 8(4):142–146, 1911.

[53] A. Kantrowitz and J. Grey. A high intensity source for the molecular beam. *Rev. Sci. Instrum.*, 22(5):328–332, 1951.

[54] N. R. Hutzler, H. I. Lu, and J. M. Doyle. The buffer gas beam: An intense, cold, and slow source for atoms and molecules. *Chem. Rev.*, 112(9):4803–4827, 2012.

[55] H. Metcalf and P. van der Straten. *Laser Cooling and Trapping*. Springer Science, New York, 1999.

[56] M. Yeo, M. T. Hummon, A. L. Collopy, B. Yan, B. Hemmerling, E. Chae, J. M. Doyle, and J. Ye. Rotational State Microwave Mixing for Laser Cooling of Complex Diatomic Molecules. *Phys. Rev. Lett.*, 114(22):1–5, 2015.

[57] X. Wang, M. Kirste, G. Meijer, and S. Y. T. Van De Meerakker. Stark deceleration of NO radicals. *Zeitschrift fur Phys. Chemie*, 227(11):1595–1604, 2013.

[58] T. E. Wall, J. F. Kanem, J. M. Dyne, J. J. Hudson, B. E. Sauer, E. A. Hinds, and M. R. Tarbutt. Stark deceleration of CaF molecules in strong- and weak-field seeking states. *Phys. Chem. Chem. Phys.*, 13:18991–18999, 2011.

[59] S. K. Tokunaga, J. M. Dyne, E. A. Hinds, and M. R. Tarbutt. Stark deceleration of lithium hydride molecules. *New J. Phys.*, 11(055038):0–14, 2009.

[60] D. Y. Balabanov and L. M. Duffy. Microstructured Stark Decelerator. *arXiv:1705.08570*, 2017.

[61] M. Strebel, F. Stienkemeier, and M. Mudrich. Improved setup for producing slow beams of cold molecules using a rotating nozzle. *Phys. Rev. A*, 81(3):1–12, 2010.

[62] L. Sheffield, M. S. Hickey, V. Krasovitskiy, K. D.D. Rathnayaka, I. F. Lyuksyutov, and D. R. Herschbach. Pulsed rotating supersonic source for merged molecular beams. *Rev. Sci. Instrum.*, 83(6), 2012.

[63] M. Gupta and D. Herschbach. A Mechanical Means to Produce Intense Beams of Slow Molecules. *J. Phys. Chem. A*, 103:10670–10673, 1999.

[64] H. Lu, J. Rasmussen, M. J. Wright, D. Patterson, and J. M. Doyle. A Cold and Slow Molecular Beam. *Phys. Chem. Chem. Phys.*, 13:18986–18990, 2011.

[65] T. Cremers, S. Chefdeville, N. Janssen, E. Sweers, S. Koot, P. Claus, and S. Y. T. Van De Meerakker. Multistage Zeeman decelerator for molecular-scattering studies. *Phys. Rev. A*, 95(4):1–15, 2017.

[66] N. J. Fitch and M. R. Tarbutt. Principles and Design of a Zeeman - Sisyphus Decelerator for Molecular Beams. *ChemPhysChem*, 17(22):3609–3623, 2016.

[67] B. Hemmerling, E. Chae, A. Ravi, L. Anderegg, G. K. Drayna, N. R. Hutzler, A. L. Collopy, J. Ye, W. Ketterle, and J. M. Doyle. Laser slowing of CaF molecules to near the capture velocity of a molecular MOT. *arXiv:1603.02787*, 49(17):1–6, 2016.

[68] J. F. Barry, E. S. Shuman, E. B. Norrgard, and D. Demille. Laser radiation pressure slowing of a molecular beam. *Phys. Rev. Lett.*, 108(10):1–5, 2012.

[69] M. G. Tarallo, G. Z. Iwata, and T. Zelevinsky. BaH molecular spectroscopy with relevance to laser cooling. *Phys. Rev. A*, 93(3), 2016.

[70] K. Moore and I. C. Lane. Quantitative theoretical analysis of lifetimes and decay rates relevant in laser cooling BaH. *Priv. Commun.*, 2017.

[71] I. Kopp, M. Kronekvist, and A. Guntsch. Rotational analysis of the A-X band system of BaH and BaD. *Ark. Fys.*, 32(19):371–405, 1966.

[72] O. Appelblad, L. E. Berg, L. Klynning, and J. W C Johns. Fourier transform spectroscopy of the $B^2\Sigma$-$X^2\Sigma$ transition of BaH. *Phys. Scr.*, 31(1):69–73, 1985.

[73] I. C. Lane. Production of ultracold hydrogen and deuterium via Doppler-cooled Feshbach molecules. *Phys. Rev. A*, 92(2):1–12, 2015.

[74] A. Collopy, Y. Wu, S. Ding, I. Finneran, L. Andregg, B. Augenbraun, J. Doyle, and J. Ye. An RF 3-D Magneto-Optical Trap for YO. In *Meet. Am. Phys. Soc.*, 2017.

[75] I. D. Setija, H. G. C. Werij, O. J. Luiten, M. W. Reynolds, T. W. Hijmans, and J. T. M. Walraven. Optical Cooling of Atomic Hydrogen in a Magnetic Trap. *Phys. Rev. Lett.*, 70(15):2257–2260, 1993.

[76] L.-E. Berg, K. Ekvall, A. Hishikawa, and S. Kelly. Radiative lifetime measurements of the $B^2\Sigma^+$ state of BaH by laser spectroscopy. *Phys. Scr.*, 55:269–272, 1997.

[77] G. Fabre, A. El Hachimi, R. Stringat, C. Effantin, A. Bernard, J. D'Incan, and J. Verges. The $H^2\Delta$ state of barium hydride. *J. Phys. B*, 20(9):1933–1944, 1987.

[78] A. Bernard, C. Effantin, J. D'Incan, G. Fabre, A. El Hachimi, R. Stringat, J. Verges, and R.F. Barrow. The 5d complex of barium hydride; BaH and BaD. *Mol. Phys.*, 62(3):797–800, 1987.

[79] J.D. Weinstein. Magnetic trapping of calcium monohydride molecules at millikelvin temperatures. *Nature*, 190(June):148–150, 1998.

[80] G. Z. Iwata, R. L. McNally, and T. Zelevinsky. High-resolution optical spectroscopy with a buffer-gas-cooled beam of BaH molecules. *Phys. Rev. A*, 96(2):1–7, 2017.

[81] M. H. Steinecker, D. J. Mccarron, Y. Zhu, and D. Demille. Improved Radio-Frequency Magneto-Optical Trap of SrF Molecules. *Chem. Phys. Chem.*, 17:3664–3669, 2016.

[82] T. Chen, W. Bu, and B. Yan. Structure, branching ratios, and a laser-cooling scheme for the 138BaF molecule. *Phys. Rev. A*, 94(6):063415, 2016.

[83] M. McDonald, B. H. McGuyer, G. Z. Iwata, and T. Zelevinsky. Thermometry via light shifts in optical lattices. *Phys. Rev. Lett.*, 114(2):1–5, 2015.

[84] B. H. McGuyer, M. McDonald, G. Z. Iwata, W. Skomorowski, R. Moszynski, and T. Zelevinsky. Control of Optical Transitions with Magnetic Fields in Weakly Bound Molecules. *Phys. Rev. Lett.*, 115(5):1–5, 2015.

[85] M. McDonald, B. H. Mcguyer, F. Apfelbeck, C. Lee, I. Majewska, R. Moszynski, and T. Zelevinsky. Photodissociation of ultracold diatomic strontium molecules with quantum state control. *Nature*, 535:122–126, 2016.

[86] M. McDonald, I. Majewska, C. H. Lee, S. S. Kondov, B. H. McGuyer, R. Moszynski, and T. Zelevinsky. Control of Ultracold Photodissociation with Magnetic Fields. *arXiv:1709.04527*, 2017.

[87] Mickey Patrick McDonald. *High precision optical spectroscopy and quantum state selected photodissociation of ultracold 88 Sr 2 molecules in an optical lattice*. PhD thesis, Columbia University, 2016.

[88] Florian Apfelbeck. *Photodissociation Dynamics of Ultracold Strontium Dimers*. Master's thesis, 2015.

[89] Christopher Butler Osborn. *The Physics of Ultracold Sr 2 Molecules : Optical Production and Precision Measurement*. PhD thesis, 2013.

[90] G. Reinaudi, C. B. Osborn, K. Bega, and T. Zelevinsky. Dynamically configurable and optimizable Zeeman slower using permanent magnets and servomotors. *J. Opt. Soc. Am. B*, 29(4):729, 2012.

[91] R. Grimm, M. Weidemuller, and Y. B. Ovchinnikov. Optical Dipole Traps. *Adv. At., Mol., Opt. Phys.*, 42:95–169, 2000.

[92] H. Katori, K. Hashiguchi, E. Y. Il'Inova, and V. D. Ovsiannikov. Magic wavelength to make optical lattice clocks insensitive to atomic motion. *Phys. Rev. Lett.*, 103(15):1–4, 2009.

[93] D. J. Wineland, C. Monroe, W. M. Itano, D. Leibfried, B. E. King, and D. M. Meekhof. Experimental issues in coherent quantum-state manipulation of trapped atomic ions. 103(3), 1997.

[94] Te. Ido and H. Katori. Recoil-Free Spectroscopy of Neutral Sr Atoms in the Lamb-Dicke Regime. *Phys. Rev. Lett.*, 91(5):053001, 2003.

[95] D. Leibfried, R. Blatt, C. Monroe, and D. Wineland. Quantum dynamics of single trapped ions. *Rev. Mod. Phys.*, 75(1):281–324, 2003.

[96] S. Blatt, J. W. Thomsen, G. K. Campbell, A. D. Ludlow, M. D. Swallows, M. J. Martin, M. M. Boyd, and J. Ye. Rabi spectroscopy and excitation inhomogeneity in a one-dimensional optical lattice clock. *Phys. Rev. A*, 80(5):1–11, 2009.

[97] R. H. Dicke. Coherence in Spontaneous Radiation Processes. *Phys. Rev.*, 93(1):99–110, 1954.

[98] M. Gross and S. Haroche. Superradiance: An essay on the theory of collective spontaneous emission. *Phys. Rep.*, 93(5):301–396, 1982.

[99] B. N. Chichkov, C. Momma, and S. Nolte. Femtosecond, picosecond and nanosecond laser ablation of solids. *Appl. Phys. A*, 115:109–115, 1996.

[100] D. Patterson, J. Rasmussen, and J. M. Doyle. Intense atomic and molecular beams via neon buffer-gas cooling. *New J. Phys.*, 11, 2009.

[101] S. M. Skoff, R. J. Hendricks, C. D. J. Sinclair, M. R. Tarbutt, J. J. Hudson, D. M. Segal, B. E. Sauer, and E. A. Hinds. Doppler-free laser spectroscopy of buffer-gas-cooled molecular radicals. *New J. Phys.*, 11(12):123026, 2009.

[102] C. Kittel and H. Kroemer. *Thermal Physics*. W.H. Freeman, New York, second edition, 1980.

[103] R. V. Krems, W. C. Stwalley, and B. Friedrich. *Cold Molecules*. Taylor and Francis Group LLC, Boca Raton, FL, 2009.

[104] S. M. Skoff, R. J. Hendricks, C. D. J. Sinclair, J. J. Hudson, D. M. Segal, B. E. Sauer, E. A. Hinds, and M. R. Tarbutt. Diffusion, thermalization, and optical pumping of YbF molecules in a cold buffer-gas cell. *Phys. Rev. A*, 83(2):023418, 2011.

[105] R. Kelly and R. W. Dreyfus. On the effect of Knudsen-layer formation on studies of vaporization, sputtering, and desorption. *Surf. Sci.*, 198(1-2):263–276, 1988.

[106] J. C. S. Kools, T. S. Baller, S. T. De Zwart, and J. Dieleman. Gas flow dynamics in laser ablation deposition Gas flow dynamics in laser ablation deposition. *J. Appl. Phys.*, 71(4547), 1992.

[107] M. Harnafi and B. Dubreuil. Characterization and analysis of the CO_2 laser-induced ablation of lithium target via laser-induced fluorescence and absorption spectroscopy of emitted atoms. *J. Appl. Phys.*, 69:7565–7571, 1991.

[108] W. Demtroder. *Laser Spectroscopy*. Springer, Berlin, 2008.

[109] J. K. G. Watson. Honl-London factors for multiplet transitions in Hund's case *a* or *b*. *J. Mol. Spectrosc.*, 252(1):5–8, 2008.

[110] U. Magg, H. Birk, and H. Jones. The ground state infrared spectrum of four isotopic forms of barium monohydride (BaH). *Chem. Phys. Lett.*, 149(3):321–325, 1988.

[111] G. Herzberg. *Spectra of Diatomic Molecules*. Van Nostrand, New York, 1950.

[112] R. DeCarvalho, J.M. Doyle, B. Friedrich, T. Guillet, J. Kim, D. Patterson, and J.D. Weinstein. Buffer-gas loaded magnetic traps for atoms and molecules: A primer. *Eur. Phys. J. D*, 7(3):289, 1999.

[113] W. W. Watson. Barium hydride band spectra in the near infrared. *Phys. Rev.*, 43(1):9–11, 1933.

[114] J. Brown and A. Carrington. *Rotational Spectroscopy of Diatomic Molecules*. Cambridge University Press, Cambridge, 2003.

[115] B. K. Stuhl, B. C. Sawyer, D. Wang, and J. Ye. Magneto-optical trap for polar molecules. *Phys. Rev. Lett.*, 101(24), 2008.

[116] R. Mulliken. The Interpretation of Band Spectra. Part IIc. Empirical Band Types. *Rev. Mod. Phys.*, 3(89), 1931.

[117] C. Day. Basics and Applications of Cryopumps. *Cern Accel. Sch. Proc. 'Vacuum Accel.*, pages 241–274, 2006.

[118] J.E. Jensen, W.A. Tuttle, R.B. Stewart, and H. Brechna. Thermal Conductivity Integrals of Solids at Low Temperatures. Technical report, 1980.

[119] G. Behrens, W. Campbell, D. Williams, and S. White. Guidelines for the Design of Cryogenic Systems. Technical Report 306, National Radio Astronomy Observatory, 1997.

[120] M. Q. Brewster. *Thermal Radiative Transfer and Properties*. John Wiley and Sons, New York, 1992.

[121] E. B. Norrgard, N. Sitaraman, J. F. Barry, D. J. McCarron, M. H. Steinecker, and D. Demille. In-vacuum scattered light reduction with black cupric oxide surfaces for sensitive fluorescence detection. *Rev. Sci. Instrum.*, 87(5), 2016.

[122] K. Liu and M. G. Littman. Novel geometry for single-mode scanning of tunable lasers. *Opt. Lett.*, 6(3):117, 1981.

[123] S. Truppe, H. J. Williams, N. J. Fitch, M. Hambach, T. E. Wall, E. A. Hinds, B. E. Sauer, and M. R. Tarbutt. An intense, cold, velocity-controlled molecular beam by frequency-chirped laser slowing. *New J. Phys.*, 19(022001), 2017.

[124] A. Bernard, C. Effantin, J. D'Incan, G. Fabre, R. Stringat, and R.F. Barrow. The 5d states of barium hydride; BaH and BaD. *Mol. Phys.*, 67(1):1–18, 1989.

[125] H. Lefebvre-Brion and R.W. Field. *Perturbations in the Spectra of Diatomic Molecules*. Academic Press Inc., Orlando, 1986.

[126] R. S. Ram, C. N. Jarman, and P. F. Bernath. Fourier transform emission spectroscopy of the $E^2\Pi$-$X^2\Sigma^+$ transition of BaH. *J. Mol. Spectrosc.*, 156(2):468–486, 1992.

[127] L. B. Knight and W. Weltner. Hyperfine Interaction and Chemical Bonding in MgH, CaH, SrH, and BaH molecules. *J. Chem. Phys.*, 54(1):3875–3884, 1971.

[128] B. E. Sauer, J. Wang, and E. A. Hinds. Laser-rf double resonance spectroscopy of ^{174}YbF in the $X^2\Sigma^+$ state: Spin-rotation, hyperfine interactions, and the electric dipole moment. *J. Chem. Phys.*, 105:7412–7420, 1996.

[129] M. R. Tarbutt. Magneto-optical trapping forces for atoms and molecules with complex level structures. *New J. Phys.*, 17(015007), 2015.

[130] J. Devlin, M.R. Tarbutt, D.L. Kokkin, and T.C. Steimle. Measurements of the Zeeman effect in the A2Π and B2Σ+ states of calcium fluoride. *J. Mol. Spectrosc.*, 317:1–9, 2015.

[131] T. E. Wall, J. F. Kanem, J. J. Hudson, B. E. Sauer, D. Cho, M. G. Boshier, E. a. Hinds, and M. R. Tarbutt. Lifetime of the $A(v' = 0)$ state and Franck-Condon factor of the $A-X$(0-0) transition of CaF measured by the saturation of laser-induced fluorescence. *Phys. Rev. A*, 78(6), 2008.

[132] C. I. Frum, J. J. Oh, E. A. Cohen, and H. M. Pickett. Rotational spectra of the $X^2\Sigma^+$ states of CaH and CaD. *Astrophys. J. Lett.*, 408:L61–L64, 1993.

[133] C. Corder, B. Arnold, and H. Metcalf. Laser cooling without spontaneous emission. *Phys. Rev. Lett.*, 114(4), 2015.

[134] M. R. Tarbutt, B. E. Sauer, J. J. Hudson, and E. A. Hinds. Design for a fountain of YbF molecules to measure the electron's electric dipole moment. *New J. Phys.*, 15(053034), 2013.

[135] M. Auzinsh, D. Budker, and S. M. Rochester. *Optically polarized atoms: understanding light-atom interactions*. Oxford University Press, Oxford, 1st edition, 2010.

[136] D. J. Berkeland and M. G. Boshier. Destabilization of dark states and optical spectroscopy in Zeeman-degenerate atomic systems. *Phys. Rev. A*, 65(3):033413, 2002.

[137] A. Stwertka. *A Guide to the Elements*. Oxford University Press, Oxford, 1996.

[138] W. F. Magie. *A Source Book in Physics*. Harvard University Press, Cambridge, Mass, 1969.

[139] T. W. Hansch, S. A. Lee, R. Wallenstein, and C. Wieman. Doppler-Free Two-Photon Spectroscopy of Hydrogen 1S-2S. *Phys. Rev. Lett.*, 34(6):307–309, 1975.

[140] D. G. Fried, T. C. Killian, L. Willmann, D. Landhuis, S. C. Moss, D. Kleppner, and T. J. Greytak. Bose-Einstein Condensation of Atomic Hydrogen. *Phys. Rev. Lett.*, 81(18):3811–3814, 1998.

[141] A. Beyer, L. Maisenbacher, A. Matveev, R. Pohl, K. Khabarova, A. Grinin, T. Lamour, D. C. Yost, T. W. Hänsch, N. Kolachevsky, and T. Udem. The Rydberg constant and proton size from atomic hydrogen. *Science*, 85(October):79–85, 2017.

[142] N. V. Vitanov, A. A. Rangelov, B. W. Shore, and K. Bergmann. Stimulated Raman adiabatic passage in physics, chemistry, and beyond. *Rev. Mod. Phys.*, 89, 2017.

[143] J. G. Danzl, M. J. Mark, E. Haller, M. Gustavsson, R. Hart, J. Aldegunde, J. M. Hutson, and H. C. Nägerl. An ultracold high-density sample of rovibronic ground-state molecules in an optical lattice. *Nat. Phys.*, 6:265–270, 2010.

[144] L. Veseth. Fine structure of the close-lying AΠ and BΣ states of BaH and BaD. *Mol. Phys.*, 25(2):333–344, 1972.

[145] S. Niggli and M. C E Huber. Transition probabilities in neutral barium. *Phys. Rev. A*, 35(7):2908–2918, 1987.

[146] H. J. Williams, S. Truppe, M. Hambach, L. Caldwell, N. J. Fitch, E. A. Hinds, B. E. Sauer, and M. R. Tarbutt. Characteristics of a magneto-optical trap of molecules Characteristics of a magneto-optical trap of molecules. *New J. Phys.*, 19(113035), 2017.

[147] E. L. Raab, M. Prentiss, A. Cable, S. Chu, and D. E. Pritchard. Trapping of Neutral Sodium Atoms with Radiation Pressure. *Phys. Rev. Lett.*, 59(23):2631–2634, 1987.

[148] D. Das, S. Barthwal, A. Banerjee, and V. Natarajan. Absolute frequency measurements in Yb with 0.08 ppb uncertainty: Isotope shifts and hyperfine structure in the 399-nm ${}^1S_0 \rightarrow {}^1P_1$ line. *Phys. Rev. A*, 72(032506), 2005.